Atmospheric Photochemistry, Surface Features, and Potential Biosignature Gases of Terrestrial Exoplanets

by

Renyu Hu

M.S. Astrophysics, Tsinghua University (2009)
Dipl.-Ing., Ecole Centrale Paris (2009)
B.S. Mathematics & Physics, Tsinghua University (2007)

Submitted to the Department of Earth, Atmospheric and Planetary Sciences
in partial fulfillment of the requirements for the degree of

Doctor of Philosophy in Planetary Sciences

at the

MASSACHUSETTS INSTITUTE OF TECHNOLOGY

June 2013

Author ....
Department of Earth, Atmospheric and Planetary Sciences
May 18, 2013

Certified by...
Sara Seager
Class of 1941 Professor of Planetary Science and Physics
Thesis Supervisor

Accepted by...
Robert van der Hilst
Schlumberger Professor of Earth and Planetary Sciences
Head, Department of Earth, Atmospheric and Planetary Sciences

Atmospheric Photochemistry, Surface Features, and Potential Biosignature Gases of Terrestrial Exoplanets

by

Renyu Hu

Abstract

The endeavor to characterize terrestrial exoplanets warrants the study of chemistry in their atmospheres. Here I present a comprehensive one-dimensional photochemistry-thermochemistry model developed from the ground up for terrestrial exoplanet atmospheres. With modern numerical algorithms, the model has desirable features for exoplanet exploration, notably the capacity to treat both thin and thick atmospheres ranging from reducing to oxidizing, and to find steady-state solutions starting from any reasonable initial conditions. These features make the model the first photochemistry-thermochemistry model applicable for non-hydrogen-dominated thick atmospheres on terrestrial exoplanets.

Using the photochemistry model, I explore the compositions of thin atmospheres on terrestrial exoplanets controlled by surface emission and deposition of gases. Highlights of my findings are: (1) oxygen and ozone may build up in 1-bar CO_2 atmospheres to levels that have conventionally been accepted as unique signatures of life, if there is no surface emission of reducing gases; (2) volcanic carbon compounds (CH_4 and CO_2) are likely to be abundant in terrestrial exoplanet atmospheres; but volcanic sulfur compounds (H_2S and SO_2) are chemically short-lived and therefore cannot accumulate in virtually any types of terrestrial exoplanet atmospheres.

Also using the photochemistry model, I explore the ranges of molecular compositions of thick atmospheres on terrestrial exoplanets. I find that carbon has to be in the form of CO_2 in a H_2-depleted water-dominated atmosphere, and that the preferred loss of light elements from an oxygen-poor and carbon-rich atmosphere leads to formation of unsaturated hydrocarbons (C_2H_2 and C_2H_4). These results imply that chemical stability has to be taken into account when interpreting the spectrum of a super Earth/mini Neptune like GJ 1214b.

Another intriguing category of terrestrial exoplanets is bare-rock exoplanets. I present the first theoretical framework to compute disk-integrated spectrum from a bare-rock exoplanet, taking into account the reflectivity and emissivity of solid minerals on the surface. I find that silicate surfaces lead to prominent spectral features in the 8 - 13 μm range, detectable by mid-infrared spectroscopy using transit. There-

fore transit spectroscopy is an independent method to confirm the rocky nature of an exoplanet.

Thesis Supervisor: Sara Seager
Title: Class of 1941 Professor of Planetary Science and Physics

Acknowledgments

I always feel fortunate to interact with great professors and peers who have made my education fruitful and pleasant at the Massachusetts Institute of Technology. I would like to express my sincere gratitude to those who helped me during the doctoral study.

This thesis would not be possible without the mentorship and tireless guidance from my thesis advisor, Professor Sara Seager. It was Professor Seager who introduced me to the exciting field of exoplanets and suggested me to work on the photochemistry of exoplanet atmospheres. Over the four years, Professor Seager has been incredibly helpful for my research, education, and career. I especially appreciate her efforts to help me build research toolkits, think strategically, write effectively, and learn the American culture. I will always be inspired by Professor Seagers scientific intuition and focus on the big picture.

I would like to especially thank Professor Maria Zuber who has advised me for another research project. Although the project with Professor Zuber is not included in this thesis, the education that I received working with Professor Zuber goes beyond the project and will go beyond my doctoral study. It was one of the greatest times in the years at MIT when I discussed weather on Mars with Professor Zuber almost every Thursday in my second year. I very much appreciate Professor Zuber for her dedicated guidance and mentorship on my scientific research and academic career.

I would also like to thank the members of my thesis committee for their advices on my study. I appreciate Professor Kerri Cahoy for her hands-on advisory, as well as her great efficiency in work that has set the norm for me. I appreciate Professor Bethany Ehlmann for her inspiration of new ideas on the surface characterization of terrestrial exoplanets. I appreciate Professor Cziczo for his perspective of cloud and aerosol microphysics that has made my knowledge more complete.

I have had the chance to interact with great researchers during my doctoral study. My sincere thank you goes to Professor James Kasting, Professor Susan Solomon, Professor Linda Elkins-Tanton, Professor Kerry Emanuel, and Professor Richard Binzel.

My study at MIT would not be as pleasant without the support and friendship

Contents

List of Figures

List of Tables

Chapter 1

Introduction

1.1 Terrestrial Exoplanets

1.1.1 Discovery

One of the most exciting discoveries made by astronomers in the past decade is terrestrial exoplanets[1]. Terrestrial exoplanets are first discovered by measuring the effect of the planets' gravity on the motion of their host stars via the Doppler shift of stellar spectra induced by the velocities of the stars along the line of sight (i.e., the radial velocity method; Rivera et al., 2005). Since then, the precision of the radial velocity measurement for bright stars has become closer and closer to the precision of 0.1 m s^{-1} required for detecting an Earth mass planet at the 1-AU orbit to a Sun-like star (referred to as a "true Earth analog"). As a result, the search for terrestrial exoplanets have been finding more and more terrestrial exoplanets that have smaller and smaller sizes (Udry et al., 2007; Forveille et al., 2009; Mayor et al., 2009; Vogt et al., 2010; Rivera et al., 2010; Dawson and Fabrycky, 2010; Howard et al., 2011; Bonfils et al., 2011). Recently, an Earth-mass terrestrial exoplanet was reported around α Centauri b, one of the closest stellar systems from Earth (Dumusque et al.,

---

[1]I define terrestrial exoplanets for this thesis as the planets outside the Solar System with masses within 10 times Earth's mass or with radii within 2 times Earth's radius. My definition of terrestrial exoplanets include Earth-sized and Earth-mass planets, as well as planets that are larger than Earth and considerably smaller than Neptune (super Earths).

2012).

Another method to discover terrestrial exoplanets is to observe the dimming of a star due to a planet passing in front of the star as viewed from Earth (i.e., the transit method). The signal of the transit is proportional to the ratio between the size of the planet and the size of its parent star. Earth transiting the Sun as viewed from another planetary system would have a transit signal of ∼80 part per million (ppm). Modern photometry technique has been able to provide this level of precision and therefore enabled the detection of terrestrial exoplanets via transits (Léger et al., 2009; Charbonneau et al., 2009; Winn et al., 2011; Demory et al., 2011). In recent years, the exoplanet community has witnessed an explosive increase of the number of terrestrial exoplanets discovered by transits, mostly as a result of the *Kepler* mission (Holman et al., 2010; Batalha et al., 2011; Lissauer et al., 2011; Cochran et al., 2011; Fressin et al., 2012; Gautier et al., 2012; Borucki et al., 2012; Muirhead et al., 2012; Batalha et al., 2013; Gilliland et al., 2013; Swift et al., 2013). The smallest transiting planets that have been confirmed are smaller than Mercury (Barclay et al., 2013).

The discovery of terrestrial exoplanets has impacted profoundly our inquiry of the Universe. As a milestone in the search for planets that might harbor life, terrestrial exoplanets are important subjects to study for three reasons: (1) the detection of terrestrial exoplanets provides a large ensemble of planets and planetary systems that enable comparative planetology of Earth-like planets beyond the Solar System; (2) terrestrial exoplanets may themselves be habitable if they receive appropriate heat from their parent stars; (3) characterization of atmospheres and surfaces of terrestrial exoplanets, starting from planets that are larger than Earths (referred to as "super Earths"), serves as the indispensable preparation of instrumentation, observation, and data interpretation techniques for eventually characterizing Earth-sized planets that are potentially habitable.

1.1.2 Population of Terrestrial Exoplanets in the Milky Way

A large number of stars in our interstellar neighborhood have terrestrial exoplanets. The occurrence rate of terrestrial exoplanets can be estimated based on the *Kepler*

observations, with correction of the geometric effect (due to the fact that the transit technique is only sensitive to those planets that pass in front of their host stars periodically), the incompleteness of detection, and the false positive of signals (Howard et al., 2012; Fressin et al., 2013). It has been estimated that ~ 30 % of stars in our interstellar neighborhood have terrestrial exoplanets that have radii within 2 times Earth's radius and orbital periods within 85 days (Fressin et al., 2013). The occurrence rate of exoplanets found by the *Kepler* transit survey is also consistent with the finding of radial velocity surveys that are sensitive to very different observational biases, supporting the fidelity of this result (Mayor et al., 2011; Howard et al., 2012; Figueira et al., 2012). The high occurrence rate of terrestrial exoplanets found by recent surveys warrants the investigation of the nature of these planets.

Super Earths and mini Neptunes, the planets that are larger than Earth but smaller than Neptune, are found to be common in the Milky Way. The Solar System does not have any planet in this size range, but both radial velocity surveys and transit surveys have found consistent results regarding the size distribution of planets outside the Solar System: the occurrence of planets increases as the radius decreases from Jupiter's radius to 2 times Earth's radius (Howard et al., 2012; Fressin et al., 2013). The increasing trend appears to be cutoff for planets having size similar to the Earth's size. Such a "plateau" in the occurrence rate for Earth-sized planets may reflect the underlying terrestrial planet population, or may be simply due to incompleteness of detection for planets as small as Earth (Howard et al., 2012; Fressin et al., 2013; Petigura et al., 2013).

The discovery of terrestrial exoplanets that are potentially habitable is dawning. A habitable planet is defined as a planet on the surface of which liquid water is stable. As the stellar radiation is the major heat source for a terrestrial exoplanet, the conventional habitable zone, the range of semi-major axes in which planets could be habitable, has been studied for main-sequence stars (Kasting et al., 1993). The conventional definition of the habitable zone relies upon the assumption that the planet has an N_2-dominated atmosphere with variable levels of CO_2 to provide appropriate levels of greenhouse effects. Such defined habitable zone around a Sun-like star is

evaluated most recently at 0.99 - 1.70 AU (Kopparapu et al., 2013). Recently the habitable zone has been considerably widened by including H_2-H_2 collision-induced absorption (Pierrehumbert and Gaidos, 2011) or lowering the water content in the atmosphere (Zsom et al., 2013). Both the radial velocity method and the transit method are more sensitive to planets that are closer to their parent stars. The amplitude of the radial velocity signal falls with the semi-major axis a as $a^{-1/2}$; the amplitude of transit signal does not depend on the semi-major axis, but the probability of transit due to the alignment between the star, the planet, and the observers is R_*/a, where R_* is the radius of the star. Several planets that are in the conventionally defined habitable zones of their host stars have been discovered by both the radial velocity method (Udry et al., 2007; Vogt et al., 2010; Pepe et al., 2011; Bonfils et al., 2011; Tuomi et al., 2013) and the transit method (Borucki et al., 2012; Borucki et al., 2013). The discovery of terrestrial planets in habitable zones is expected to accelerate as tens of planet candidates in habitable zones have been identified by *Kepler* (Batalha et al., 2013). A statistical quantity, $\eta_\oplus$, the frequency of terrestrial planets in habitable zones of their host stars, is estimated using *Kepler* observations to be ~ 15 % for cool stars (Dressing and Charbonneau, 2013) and 34 ± 14 % for FGK stars (Traub, 2012). Albeit the uncertainty in $\eta_\oplus$, it is reasonable to expect at least one potentially habitable terrestrial planet in our interstellar neighborhood in a few tens of parsecs[2].

One sweet spot to look for and characterize habitable terrestrial exoplanets is around M dwarf stars. M dwarf stars have sizes of a fraction of that of the Sun, and M dwarf stars are the most common type of stars in the neighborhood of the Sun (Salpeter, 1955). Recent surveys by *Kepler* have suggested that planets having radii within 2 times Earth's radius are more frequent around small M dwarfs than around FGK stars (Howard et al., 2012; Dressing and Charbonneau, 2013). Moreover, because M dwarfs are considerably sub-luminous compared with the Sun, the habitable zone around an M dwarf is much closer to the star than the habitable zone around a Sun-like star (Kasting et al., 1993). As a result, habitable planets around M dwarfs

---

[2]An astronomical unit for length, 1 parsec is equivalent to 3.09×10^{16} m or 3.26 light-years

would have higher transit probabilities and larger transit signals compared with their counterparts around FGK stars. The search for terrestrial exoplanets around nearby M dwarfs has been ongoing (e.g. Nutzman and Charbonneau, 2008), which has resulted in the discovery of a 2.7-$R_\oplus$ planet orbiting an M4.5 star only 13 parsecs away (GJ 1214b; Charbonneau et al., 2009).

1.1.3 Observations of Exoplanet Atmospheres

The atmosphere on an exoplanet can be analyzed by spectroscopy. If an exoplanet could be directly imaged, the light from the planet's atmosphere, either planetary thermal emission or reflection of the stellar light, could be analyzed via spectroscopy to determine the composition of its atmosphere. Such observations are extremely challenging due to the existence of a much stronger radiation source at close angular proximity (i.e., the host star). In fact, the first high-resolution spectrum of a directly imaged exoplanet (a nascent gas giant 40 AU from its host star) has recently been reported (Konopacky et al., 2013). A newly developed method to mitigate the weak signal of an exoplanet without spatially resolving the planet or nulling the stellar light is to make use the information of the planet's orbital motion. A correlation between the star's radial velocity and the radial velocity of a certain group of molecular lines (e.g., CO) may establish the existence of the molecule in the planet's atmosphere (Brogi et al., 2012; Rodler et al., 2012).

At current stage and in the near future, however, characterization of exoplanet atmospheres focuses on the planets that transit. The predictable on-and-off features of the planet's radiation when the planet passes behind its host star (referred to as "occultation") can be observed by monitoring the total light from the star-planet system in and out of transits (e.g. Seager and Sasselov, 1998; Seager et al., 2000). In addition, when the planet passes in front of its host star (referred to as "transit"), parts of the stellar radiation may transmit through the planet's atmosphere, and carry the information of the atmospheric composition (Seager and Sasselov, 2000). Soon after the first detection of an exoplanet atmosphere via transit (Charbonneau et al., 2002) and the first detection of thermal emission from an exoplanet atmosphere via

occultation (Charbonneau et al., 2005; Deming et al., 2005), both methods have been successful in characterizing extrasolar giant planets (e.g. Seager and Deming, 2010, and references therein). Recently, attempts to observe super Earth atmospheres are growing (e.g. Batalha et al., 2011; Gillon et al., 2012; Demory et al., 2012a), and the super Earth/mini Neptune GJ 1214b is being observed in as much detail as possible (e.g. Bean et al., 2010; Croll et al., 2011; Désert et al., 2011; Berta et al., 2012; de Mooij et al., 2012). Besides spectral characterization, exoplanet atmospheres have also been studied via the phase curves (e.g. Seager et al., 2000; Knutson et al., 2007), and the first observation of a phase curve from a terrestrial exoplanet can be expected for the near future (Demory et al., 2012b).

1.2 Physical Processes in Terrestrial Exoplanet Atmospheres

I explore the ranges of molecular compositions of terrestrial exoplanet atmospheres with models that compute key physical processes in the atmospheres. The purpose is to provide a tool to predict the amounts of component gases in the atmospheres of terrestrial exoplanets, and in the meantime quantify the links between the observables (e.g., abundances of trace gases and their spectral signatures) and the fundamental unknowns (e.g., geological and biological processes on the planetary surface, mixing and escape of atmosphere gases, heat sources from planetary interior and exterior). The ultimate goal is to enhance the ability to design and execute future missions to search for terrestrial exoplanets that might harbor life.

For this goal, I focuses on a snapshot perspective in this study. Two broad ways to consider planetary atmospheres are the evolution perspective and the snapshot perspective. An evolution model studies the formation and evolution of a planet's atmosphere in geological timescales. The evolution model is relevant to observations of an ensemble of similar planets at different stages of evolution, or to explain integrated features (usually isotopic features) in planetary atmospheres. Looking at a

much shorter timescale than geological timescales, I focus on the chemical compositions of major and trace gases in the atmosphere by seeking steady-state solutions according to appropriate boundary conditions. Such a snapshot model, when applied to study Earth's atmosphere, does not model the rise of oxygen (which could be studies by an evolution model), but would model the photochemical formation of ozone in an oxygen-rich background atmosphere and the oxidation of many other trace gases in the atmosphere. The snapshot model is relevant for prediction and interpretation of observations of individual atmospheres, because it is the atmospheric composition of both major and trace gases that determine the radiation properties of a terrestrial exoplanet[3]. Strickly speaking, a steady-state atmosphere is still evolving in the long term. Therefore, the steady state in this study is defined with respect to mixing: an atmosphere model is in the steady state if the variation timescale of the amounts of all gases in the atmosphere is significantly longer than the mixing timescale of the atmosphere.

Although not investigated in detail, an evolution perspective of atmospheres on terrestrial exoplanets provides some background for this study. For terrestrial exoplanets, the origins and evolution of their atmospheres should give rise of great diversity of their atmospheric compositions. The chemical diversity of terrestrial exoplanet atmospheres are likely to be considerably more significant than the diversity of atmospheres on gas giants. Gas giants have large masses and deep gravitational wells that could hold their primordial atmospheres against atmospheric loss; therefore the atmospheres on gas giants are hydrogen-rich, and they carry the information about where the planets were formed. However, as shown in Figure 1-1, terrestrial exoplanets may experience significant atmospheric evolution. The evolutionary history of an individual terrestrial exoplanet is highly uncertain, mostly due to the unknown early history of stellar X-ray and ultraviolet (UV) fluxes that would control the early atmospheric loss (e.g. Lammer et al., 2008, 2013; Cecchi-Pestellini et al., 2009). However, collectively, terrestrial exoplanets would have experienced atmospheric evolution to

---

[3]Atmospheric gases that are trace in amount are not necessarily minor in the planet's radiative properties. For example, trace gases H_2O and CO_2 in Earth's atmosphere provide the planet's most infrared absorption.
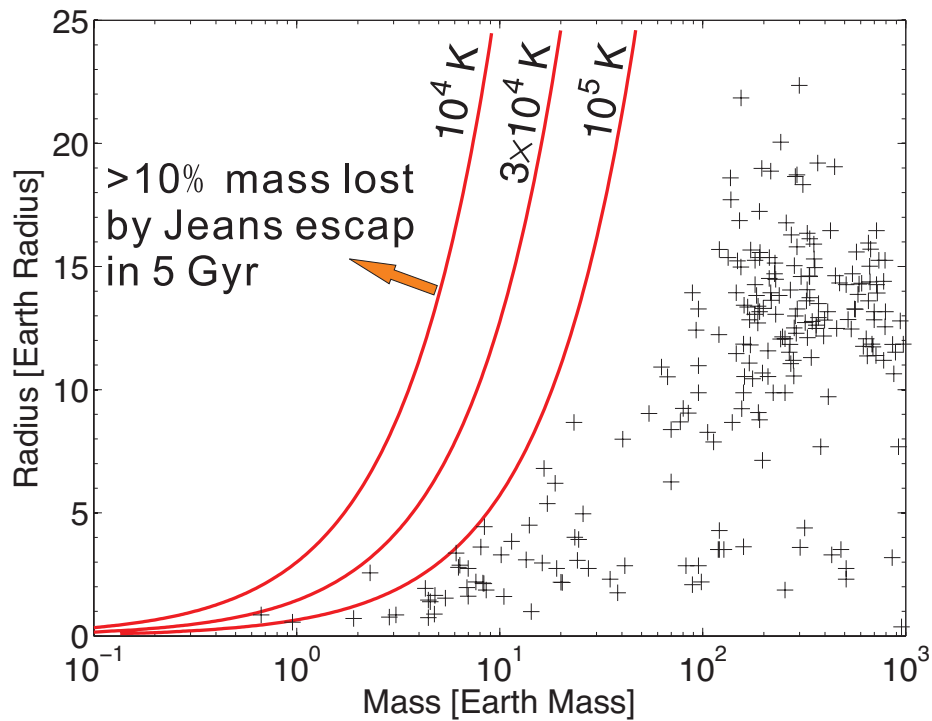
Figure 1-1: Masses and radii of confirmed exoplanets. Only confirmed exoplanets with mass and radius measurements are shown, and the data are from The Extrasolar Planets Encyclopedia (http://http://exoplanet.eu). The red lines show parameter regimes in which more than 10% of the planetary mass could be lost via Jeans escape in 5 billion years, for a number of typical exosphere temperatures. The population of terrestrial exoplanets intercepts with those lines, meaning that the atmospheres on terrestrial exoplanets may have experienced significant atmospheric evolution.

different extent, and their current atmospheres can be either primordial, or from secondary outgassing, or from both sources. These origins of atmospheres on terrestrial exoplanets imply a great chemical diversity ranging from hydrogen-rich to hydrogen-poor, from reducing to oxidizing. This diversity may be put into context by referring to the fact of the Solar System: atmospheres on all giant planets, including Jupiter, Saturn, Uranus, and Neptune, are hydrogen-rich; atmospheres on all small planets and moons, including Venus, Earth, Mars, and Titan, are highly evolved, probably sustained by outgassing or late delivery of volatiles, and have various compositions (e.g. Yung and Demore, 1999; de Pater and Lissauer, 2001).

Turning back to the snapshot perspective, a model for terrestrial exoplanet atmospheres should compute chemical reaction kinetics and transport in three pressure regimes: the low-pressure regime where photon-driven processes dominate; the intermediate regime where transport dominates; and the high-pressure regime where

thermochemical equilibrium dominates. Such a model is called "photochemistry-thermochemistry kinetic-transport model" or simply "photochemistry-thermochemistry model"[4].

A photochemistry-thermochemistry model is critical for the study of molecular compositions of any exoplanet atmosphere, including the atmospheres of terrestrial exoplanets. The overarching reason is that the composition of the observable part of an exoplanet atmosphere (0.1 mbar to 1 bar, depending on the wavelength) is controlled by the competition between chemical reaction kinetics and transport.

One process that controls the composition is chemical and photochemical reactions. The network of chemical reactions in the atmosphere may serve as sources for certain gases and sinks for the others. Chemical reactions occur when two molecules collide, and the reaction rates are therefore proportional to the number density of both molecules. Certain reactions would require a third body in the collision to remove excess energy or angular momentum. The rates of such termolecular reactions are therefore also dependent on the total number density of the atmosphere. Near the top of the atmosphere, photon-driven reactions contribute dominantly to the source and sink, as ultraviolet (UV) photons from the parent star that could dissociate molecules usually penetrate to the pressure levels of ~ 0.1 bar (e.g. Yung and Demore, 1999). The UV photodissociation produces reactive radicals that facilitate some reactions that are otherwise kinetically prohibited. One of the main goals of this work is to build a generic reaction network that includes bimolecular reactions, termolecular reactions, photodissociation reactions, and thermodissociation reactions for the study of terrestrial exoplanet atmospheres.

The other process that controls the composition is transport. Both large-scale mean flows and small-scale turbulence and instability can transport molecules in the atmosphere and affect the composition (e.g. Brasseur and Solomon, 2005; Seinfeld and Pandis, 2006). In this study, I focus on the transport in the vertical direction and

---

[4]Such models are sometimes called "photochemistry models" in the context of discriminating from thermochemistry models. However, this might cause confusion as the term "photochemistry model" usually implies that photochemical processes driven by parent-star irradiation are the dominant factor for molecular compositions in the modeled atmospheres.

explore the compositions of terrestrial exoplanet atmospheres as a function of altitude. Altitude is the most important dimension because the temperature and the pressure are strong function of altitude. The composition of Earth's atmosphere is primarily a function of altitude instead of longitude or latitude. Also, the vertically resolved compositions are critical for prediction and interpretation of spectra of a terrestrial exoplanet, because the spectra probe different altitudes of the atmosphere depending on the wavelength (Seager, 2010). The three-dimensional flows in the atmosphere, horizontal heat transport, and the interpretation of planetary orbital phase curves are not in the scope of this work.

The major mechanisms for vertical transport in an irradiated atmosphere on a terrestrial exoplanet include convection (the same mechanism required to transport heat), small-scale instability driven by shear of horizontal flows, and molecular diffusion. I follow the convention to capture the first two processes by the so-called "eddy diffusion coefficients" (e.g. Seinfeld and Pandis, 2006), and the last process by the molecular diffusion coefficients. I model the atmospheres on terrestrial exoplanets as gravitationally stratified, plan-parallel irradiated atmospheres in which vertical mixing is parameterized.

Eventually, the steady-state composition of a terrestrial exoplanet atmosphere is controlled by the boundary conditions. The upper boundary conditions are the fluxes of atmospheric escape or the material exchange fluxes between the neutral atmospheres and the ionospheres (not modeled) above. The lower boundary conditions depend on whether or not thermochemical equilibrium holds near the lower boundary. I therefore consider the following two categories of atmospheres on terrestrial exoplanets: thin atmospheres and thick atmospheres. The thick atmospheres are defined as the atmospheres that are thick enough to maintain thermochemical equilibrium at high pressures, and the thin atmospheres are defined as the atmospheres at the surface of which achieving thermochemical equilibrium is kinetically prohibited. I outline the key physical processes and the controlling factors of molecular compositions in the two categories of terrestrial exoplanet atmospheres in the following two sections.

1.2.1 Thin Atmospheres on Terrestrial Exoplanets

Thin atmospheres have a surface pressure that is too small to maintain thermochemical equilibrium. The main components of a thin atmosphere result from long-term geological evolution. For example, the N_2-O_2 atmosphere on Earth, the CO_2 atmosphere on Mars, and the N_2 atmosphere on Titan are results of long-term evolution (e.g. Kasting and Catling, 2003; Coustenis, 2005). For terrestrial exoplanets, the main components of their thin atmospheres can only be determined by observations, and the oxidation states of the thin atmospheres can range from reducing (e.g. H_2 atmospheres), to oxidized (e.g., N_2 and CO_2 atmospheres), to even oxic (O_2 atmospheres). One key challenge of this work is to design the photochemistry model to have sufficient flexibility to treat the atmospheres having very different oxidation states.

The dominant physical processes in thin atmospheres are photon-driven chemical reactions and vertical transport. The effects of UV photons are (1) directly dissociate the gases of interest, (2) produce reactive radicals (e.g., OH, H, O) that remove the gases of interest, (3) facilitate the conversion from emitted gases to photochemical products. The photon-driven chemical reactions are especially important for thin atmospheres because: (1) ultraviolet photons that cause photodissociation penetrate to the pressure levels of ~ 0.1 bar, relevant to the bulk part of a thin atmospheres (Yung and Demore, 1999); (2) in many cases, the photochemical processes in a thin atmosphere are irreversible. For example, the photochemical production of unsaturated hydrocarbons and haze from CH_4 occurs in the upper atmosphere of Titan, and the photochemical formation of C_2H_6 is irreversible and is therefore the dominant sink for CH_4 on Titan (Yung et al., 1984). This is in contrast to Jupiter's atmosphere, in which the photochemically formed C_2H_6 is converted back to CH_4 in deep atmosphere via pyrolysis (Strobel, 1969, 1973; Gladstone et al., 1996).

The fundamental parameters that define a thin atmosphere are the surface source (i.e., emission rates), the surface sink (i.e., deposition velocities of emitted gases and their photochemical products in the atmosphere) of trace gases (Yung and Demore, 1999; Seinfeld and Pandis, 2006), and in some cases, atmospheric loss to space. The

main task of my model, when applied to thin atmospheres, is to seek steady-state mixing ratios for trace gases of interest that are either emitted from the surface or produced by the chemical network in the atmosphere. The amounts of these trace gases are eventually controlled by the mass exchange between the surface and the atmosphere. It is important to study the amounts of trace gases by photochemistry models because an atmospheric spectrum may have strong features from spectroscopically active trace gases whose lifetime is controlled by the full chemical network in the atmosphere, and some of these trace gases may be hallmarks for specific atmospheric scenarios.

The fact that the surface emission and deposition controls the steady-state mixing ratios of trace gases in thin atmospheres on terrestrial exoplanets is pivotal to the ultimate goal of characterizing terrestrial exoplanets that might harbor life. Potential metabolic activities on a rocky planet emit a gas to the atmosphere that is otherwise not emitted or consume a gas that is otherwise not consumed. Both processes occur on Earth and regulate the composition of Earth's atmosphere. For example, Earth-based photosynthesis leads to the emission of O_2 that sustains a high O_2 mixing ratio in Earth's atmosphere; and Earth-based hydrogen-oxidizing bacteria provide an appreciable deposition velocity for H_2 from the atmosphere to the surface (e.g. Kasting and Catling, 2003; Kharecha et al., 2005; Seinfeld and Pandis, 2006). The photochemistry model provides the interface between the observables (atmospheric compositions) and the fundamental unknowns (surface source and sinks that may or may not be attributed to life); and the photochemistry model is therefore critical for determining the habitability of a terrestrial exoplanet and investigating whether a habitable planet is inhabited.

1.2.2 Thick Atmospheres on Terrestrial Exoplanets

A subset of terrestrial exoplanets will have thick atmospheres. At high pressures, collisions between molecules in the atmosphere become so frequent that the molecular composition proceeds to thermochemical equilibrium; in other words, the Gibbs free energy of the mixture of molecules is minimized, because the system tends to reach

the lowest energy state. Theoretical calculations show that Jupiter's atmosphere is in thermochemical equilibrium for pressures higher than ~ 1000 bar (e.g. Fegley and Lodders, 1994), and hot Jupiter HD 189733b's atmosphere is in thermochemical equilibrium for pressures higher than ~ 100 bar (e.g. Moses et al., 2011). Atmospheres on super Earths/mini Neptunes, similarly to the atmospheres on Jupiter and hot Jupiters, could obtain thermochemical equilibrium at depth if the atmosphere is thick enough to reach pressures higher than $10 \sim 1000$ bar. I suggest many super Earths/mini Neptunes may have thick atmospheres because: (1) the constraints on planetary compositions from the mass and the radius of a super Earth/mini Neptune (e.g. Rogers and Seager, 2010a) usually cannot exclude the possibility of a massive gas envelope; (2) population synthesis studies of planet formation have suggested planets that are more massive than Earth may accrete much more volatiles than Earth and are more likely to have thick atmospheres (e.g. Mordasini et al., 2012).

Some terrestrial exoplanets may have thick atmospheres that are not mainly composed of hydrogen. Super Earths and mini Neptunes are not as massive as gas giants; as a result they may have experienced more significant atmospheric loss than gas giants (Yelle, 2004; Yelle et al., 2008; Lammer et al., 2008, 2013). The result of atmospheric evolution on some super Earths should be preferential loss of light atoms (i.e., H and He) and enrichment of more heavy atoms (e.g., C, O, N, S). Recent observations of super Earth GJ 1214b have hinted that the planet has an atmosphere with a mean molecular mass significantly larger than that of a hydrogen-dominated atmosphere (e.g. Bean et al., 2010; Berta et al., 2012).

The super Earths and mini Neptunes being observed represent a new situation of atmospheric chemistry in the middle between extrasolar giant planets and Earth-like exoplanets, for which a self-consistent photochemistry-thermochemistry model applicable to non-H_2-dominated atmospheres has not yet been developed. When the atmosphere is not H_2-dominated (but could still contain hydrogen), the atmospheric chemistry, especially the transport quenching of key species, can be very different from the case of H_2-dominated atmospheres. For this work I aim at developing a photochemistry-thermochemistry model that can compute not only the trace gases,

but also the compositions of major gases in thick atmospheres of terrestrial exoplanets.

A photochemistry-thermochemistry model is critical for the study of molecular compositions of any thick atmospheres, including the thick atmospheres on super Earths. The reason is that the composition of the observable part of a thick atmosphere (0.1 mbar to 1 bar, depending on the wavelength) is controlled by both chemical reactions and vertical transport. For thick atmospheres there is a competition between chemical reactions that drive the system to thermochemical equilibrium and vertical transport that tends to mix the atmosphere bringing parts of the atmosphere to disequilibrium. The division between the thermochemical equilibrium regime and the transport-driven disequilibrium regime is the so called "quenching pressure". The quenching pressure has been worked out for H_2-dominated thick atmospheres on Jupiter and Saturn (Prinn and Barshay, 1977; Prinn and Olaguer, 1981; Fegley and Prinn, 1985; Yung et al., 1988; Fegley and Lodders, 1994), and brown dwarfs and hot Jupiters (Fegley and Lodders, 1996; Griffith and Yelle, 1999; Cooper and Showman, 2006; Line et al., 2010; Madhusudhan and Seager, 2011; Visscher and Moses, 2011; Moses et al., 2011). The key point is that although ultraviolet photons usually result in only minor perturbation on the compositions above 0.1 bar, a full photochemistry-thermochemistry model that treats chemical kinetics and vertical transport is required to compute the quenching pressure and the molecular composition in the observable part of a thick atmosphere.

The controlling factors of molecular compositions in thick atmospheres are the elemental abundance, the efficiency of vertical mixing, and the internal heat flux. The elemental abundance determines the molecular composition at thermochemical equilibrium, the efficiency of vertical mixing determines to which extent vertical transport brings up gases from the thermochemical equilibrium regime, and internal heat flux determines the temperatures at high pressures that affect the compositions at thermochemical equilibrium. The elemental abundance rather than the background molecular composition is a fundamental parameter in my models for thick atmospheres, because an arbitrary combination of molecules may not be chemically stable in thick atmospheres (a point that will be demonstrated in Chapter 5).

Before leaving this section, I emphasize that there is no prescribed boundaries in the planetary parameters such as mass, radius, and stellar properties, that divide the regime of thin atmospheres and the regime of thick atmospheres. However, in general, more massive planets would be able to accrete more volatile materials at their formation (Mordasini et al., 2012), and be more effective in preventing loss of its volatile envelope (see Figure 1-1, also see Yelle, 2004; Tian et al., 2005; Yelle et al., 2008; Lammer et al., 2008, 2013). Therefore, thick atmospheres are more likely to exist on super Earths and mini Neptunes, and thin atmospheres are more likely to exist on Earth-sized planets. Although I distinguish between thick atmospheres and thin atmospheres theoretically, it is so far difficult to discriminate between the two categories observationally. In the future, the surface pressure of a terrestrial exoplanet atmosphere may be derived from the pressure broadening of spectral features with high-resolution spectroscopy (Benneke and Seager, 2012).

1.3 Prospect of Terrestrial Exoplanet Characterization

Determination of the atmospheric compositions on terrestrial exoplanets is one of the most significant challenges facing astronomers. To achieve this goal, both advanced observational techniques and suitable targets are required (e.g. Deming et al., 2009). The ratio between the radiation from a terrestrial exoplanet and that from its parent star is in the orders of 10^{-10} in the visible wavelengths and 10^{-7} in the mid-infrared wavelengths. This means in the transit scenario, many observations of transits need to be stacked to lower the noise level in order to reveal the planet's signal (e.g. Seager and Deming, 2010; Deming et al., 2013); and in the direct imaging scenario, the stellar radiation has to be almost perfectly annihilated in order to reveal the planet (e.g. Kuchner and Traub, 2002; Lawson and Dooley, 2005; Trauger and Traub, 2007). Even with advanced observational techniques, atmospheric characterization of terrestrial exoplanets will be confined to nearby systems (e.g., within tens of parsecs

Guyon et al., 2006; Oppenheimer and Hinkley, 2009; Belu et al., 2011).

Full-sky surveys intended to discover terrestrial exoplanets around nearby main-sequence stars are being planed. The survey of terrestrial exoplanets around nearby systems are far from complete in several important areas: (1) Earth-mass planets around FGK stars have just become in the reach of the radial velocity method (Dumusque et al., 2012); (2) precise spectroscopic and photometric measurements of M dwarfs, despite of their dominant numbers in our interstellar neighborhood, have been long impeded by the faintness of these stars and the concentration of their radiation in the near-infrared wavelengths that are strongly contaminated by Earth's atmosphere (Nutzman and Charbonneau, 2008); (3) *Kepler*, although sensitive to Earth-sized planets, targets a small patch of sky and focuses on faint stars to maximize its scientific return (Batalha et al., 2010). One could expect rapid developments in all these areas. In particular, an all-sky space-based TESS mission (Transiting Exoplanet Survey Satellite) has recently been selected by NASA for launch in 2017 (Ricker et al., 2010). And, the CHaracterizing ExOPlanet Satellite (CHEOPS), also designed to search for terrestrial exoplanets around nearby bright stars, has been selected by ESA for launch in 2017 (Broeg et al., 2013). I expect a rapid growth in the number of terrestrial exoplanets that are suitable for follow-up observations of their atmospheres in the coming years.

The next-generation observation facility will allow thick atmospheres to be observed in great details, and even allow characterization of thin atmospheres on terrestrial exoplanets around late-type stars. Today's studies on hot Jupiters' atmospheres are flourishing with the *Hubble Space Telescope* and the *Spitzer Space Telescope* (see Seager and Deming, 2010, and references therein), but many detections of atmospheric molecules remain controversial (Deming et al., 2013). In 5 to 10 years, larger and more sophisticated facilities will allow measurements of molecular abundances and characterization of atmospheric chemistry in thick atmospheres of gas giants, and super Earths around M dwarf stars, to great detail (Traub et al., 2008; Kaltenegger and Traub, 2009; Belu et al., 2011; Benneke and Seager, 2012; van Boekel et al., 2012; Barstow et al., 2013). These anticipated facilities include the *James Webb*

Space Telescope (JWST) slated for launch in 2018 (Gardner et al., 2006), the *Exoplanet Characterization Observatory* (EChO) currently assessed for a possible launch in 2022 (Tinetti et al., 2012), and the giant 20- to 40-meter class ground-based telescopes that include the *Extremely Large Telescope* (Gilmozzi and Spyromilio, 2008), the *Giant Magellan Telescope* (Johns et al., 2012), and the *Thirty Meter Telescope* (Crampton and Simard, 2006).

In the more distant future, the community still holds hope that a direct-imaging space-based mission under the Terrestrial Planet Finder concept (e.g. Traub et al., 2006; Beichman et al., 2006; Levine et al., 2009) will enable Earth-like terrestrial exoplanets to be characterized. The technique of exoplanet direct imaging has been advancing rapidly and proceeding into spectroscopic observations of giant planets (Konopacky et al., 2013). A number of coronograph instruments are about to be mounted on state-of-the-art 10-m class telescopes, which will enable spectroscopic studies of extrasolar gas giants (e.g. Gemini Planet Imager, Chilcote et al., 2012). These ground-based efforts of direct imaging and spectroscopic measurements of exoplanets will pave the way to a future space-based direct-imaging mission that will allow characterization of true Earth analogs.

In all, the prospect of characterizing terrestrial exoplanet atmospheres is bright. What I focus on in this work is to develop a general atmosphere model for both thick and thin atmospheres on terrestrial exoplanets, and reveal the controlling physical factors for the atmospheric molecular compositions and the spectral features to be observed. The thesis is organized as follows. Chapter 2 describes my one-dimensional photochemistry-thermochemistry kinetic-transport model, and the numerical tests for model validation. Chapter 3 and Chapter 4 present the findings on thin atmospheres and thick atmospheres using the photochemistry-thermochemistry model. I additionally describe a general framework to compute disk-integrated spectra from bare-rock exoplanets and outline how to detect minerals on bare-rock exoplanet surfaces in Chapter 5. I conclude in Chapter 6.

Chapter 2

Photochemistry-Thermochemistry Model

2.1 Background

2.1.1 Photochemistry-Thermochemistry Models for Planets and Moons in the Solar System

One-dimensional photochemistry-thermochemistry models have long been used to understand the atmospheres of planets and moons in the Solar System (see Yung and Demore, 1999, and references therein), and these models and their networks of chemical reactions could serve as the foundation for exoplanet models. Photochemistry models have been very successful in understanding key physical and chemical processes in the atmospheres of Earth (e.g. Kasting et al., 1985; Zahnle, 1986; Brasseur and Solomon, 2005; Seinfeld and Pandis, 2006, and references therein), Mars (e.g. Yung and Demore, 1999; Zahnle et al., 2008), and the upper atmospheres of Venus (e.g. Krasnopolsky and Pollack, 1994; Zhang et al., 2012), Jupiter (e.g. Strobel, 1969, 1973; Gladstone et al., 1996), and Titan (e.g. Yung et al., 1984; Atreya et al., 2006; Lavvas et al., 2008a,b). Kinetic-transport models have been developed to study the deep atmospheres of Jupiter and Saturn (e.g. Prinn and Barshay, 1977; Prinn and Olaguer, 1981; Fegley and Prinn, 1985; Yung et al., 1988; Fegley and Lodders, 1994;

Visscher et al., 2010).

2.1.2 Photochemistry-Thermochemistry Models for Exoplanets

Photochemistry-thermochemistry models used for the study of exoplanets have been derived from the models designed for planets in the Solar System. After the discoveries of transiting hot Jupiters, the photochemistry-thermochemistry models were applied to study exoplanets. Liang et al. (2003), with a simplified chemical network that only treated hydrogen and oxygen species, suggested that, hot Jupiters have much higher H concentrations than Jupiter in their upper atmospheres driven by the photolysis of water. Zahnle et al. (2009a) and Line et al. (2010) investigated the hydrocarbon photochemistry in hot Jupiters' H_2-dominated atmospheres with a complete chemical network. Zahnle et al. (2009b) studied sulfur photochemistry in hot Jupiters' atmospheres, and suggested that H_2S photolysis becomes important at altitudes above the $\sim$100 Pa pressure level. Moses et al. (2011) studied atmospheric chemistry of HD 209458b and HD 189733b, the most well-characterized hot Jupiters, with a complete chemical network involving C, H, O, N species and derived observational signatures of disequilibrium processes in their atmospheres. Kopparapu et al. (2012) presented a photochemistry model of a possibly carbon-rich hot Jupiter, WASP-12b, and suggested that C_2H_2 and HCN, produced by photochemistry, may contribute significantly to the infrared opacity of its atmosphere. More recently, Miller-Ricci Kempton et al. (2012) presented the first analysis of photochemistry in a potential H_2-dominated atmosphere of mini Neptune GJ 1214b. In the meantime, the photochemistry models for certain types of terrestrial exoplanet thin atmospheres have been adapted based on models for Earth's atmosphere, to study the Earth-like atmospheres with M dwarfs as the parent star (Segura et al., 2005; Rugheimer et al., 2013), whether CO_2-dominated atmospheres could produce free oxygen photochemically (Selsis et al., 2002; Segura et al., 2007), and whether organic sulfur compounds could accumulate in N_2-dominated atmospheres (Domagal-Goldman et al., 2011).

A key challenge in developing a photochemistry model for terrestrial exoplanet atmospheres is handling the very wide range of plausible atmospheric compositions. The broad possibilities for terrestrial exoplanet atmospheric composition arise from the ideas for atmospheric origin. The atmospheres on terrestrial exoplanets may originate from the capture of nebular gases, degassing during accretion, and/or degassing from subsequent tectonic activity (Elkins-Tanton and Seager, 2008; Schaefer and Fegley, 2010). In principle, the atmospheres of terrestrial exoplanets may be reducing (H_2-rich), oxidized (N_2-rich, or CO_2-rich), or oxidizing (O_2-rich). It is also possible that some super-Earth atmospheres are water rich (Rogers and Seager, 2010a; Bean et al., 2010; Miller-Ricci Kempton et al., 2012). To date, photochemistry models are usually specific to certain types of atmospheres, because very different photochemical reactions dominate the chemistry of those atmospheres (for example in oxidized vs. reducing atmospheres). In particular, photochemistry of hydrogen-dominated atmospheres on terrestrial planets is yet to be explored; but hydrogen-dominated atmospheres may still create habitable surface temperature through collision-induced absorption (Pierrehumbert and Gaidos, 2011; Wordsworth, 2012).

For thick atmospheres on terrestrial exoplanets, the challenge is that the atmospheres may or may not be hydrogen-dominated. Instead of assuming a fixed hydrogen-helium background atmosphere as in previous models for gas giant atmospheres, my photochemistry-thermochemistry model for thick atmospheres on super Earths should compute not only the trace gases, but also the compositions of major gases in the atmosphere self-consistently. A subtle but important point is that the mean molecular mass that links the pressure scale to the altitude scale is *a priori* unknown for the atmospheres on super Earths. I have designed the photochemistry-thermochemistry model to be fully flexible in computing the main components of thick atmospheres on super Earths. In the model, the mean molecular mass is not a given, but belongs to the output. In this way, the model is uniquely suitable for exploration of atmospheric compositions on terrestrial exoplanets.

A second significant challenge for a terrestrial exoplanet photochemistry-thermochemistry model is the range of free parameters that describe key physical processes, namely ver-

tical diffusion, fluxes of surface emission, and rates of dry and wet deposition. While the fundamental equations of continuity that govern the atmospheric composition are the same, these coefficients must be kept as free parameters in order to explore the range of atmospheric mixing and the range of plausible surface conditions, which yield the wide variety of possible exoplanets' atmospheres. I am therefore motivated to develop a photochemistry-thermochemistry model that can be applied to study atmospheres of a wide range of redox states and that can handle the range of free parameters for physical processes in terrestrial exoplanet atmospheres.

During my doctoral study I have developed a photochemistry-thermochemistry model from the ground up from basic chemical and physical principles and using both established and improved computer algorithms, which have the capacity of modeling very different terrestrial exoplanet atmospheres in a consistent way. The design of the photochemistry-thermochemistry model aims at providing the maximum flexibility in treating atmospheres of very different pressures, compositions, and oxidation states. Besides stellar parameters and planetary parameters (mass, radius, etc.), the photochemistry-thermochemistry model accepts a series of input parameters including temperature structure of the atmosphere, dominant species and mean molecular mass of the atmosphere (for thin atmospheres), elemental abundances (for thick atmospheres), coefficients of vertical diffusion, fluxes of surface emission and fluxes of dry and wet depositions. These input parameters are treated as free parameters so that the photochemistry-thermochemistry model can simulate a wide range of surface pressures and atmospheric compositions.

2.2 A Photochemistry-Thermochemistry Model for the Study of Exoplanet Atmospheres

The purpose of the photochemistry-thermochemistry model is to compute the steady-state chemical composition of an exoplanetary atmosphere. The system can be described by a set of time-dependent continuity equations, one equation for each species

at each altitude. Each equation describes: chemical production; chemical loss; diffusion (contributing to production or loss); sedimentation (for aerosols only); and specified gains and losses on the lower and upper boundaries of the atmosphere. The lower boundary has assigned geological or biological source fluxes and assigned deposition rates of species for thin atmospheres and assigned thermochemical equilibrium compositions for thick atmospheres, and the upper boundary has diffusion-limited atmospheric escape, relevant for light species.

With the assumption of a one-dimensional plane-parallel atmosphere, the unknowns to be computed in the model are the number densities of each species at each altitude. Starting from an initial state, the system is evolved to the steady state in which production and loss are balanced for each species at each altitude. Because the removal timescales of different species are very different, the inverse Euler method is employed for the numerical time stepping. I allow the time step to be adjusted according to how fast the atmospheric components change (i.e., the variation timescale), and determine if the solution converges to the steady-state solution by evaluating the variation timescale for each species at each altitude, as well as the global production and loss balance for each species. Once the steady-state solution is found, I use a separate code to compute the exoplanet atmosphere spectrum for thermal emission, reflected stellar radiation, and transmission of stellar radiation.

I developed the photochemistry-thermochemistry model from the ground up, and tested the model in different pressure regimes. For the high pressures where thermochemical equilibrium dominates, I confirmed that my kinetic model that balances all forward and reverse reactions gives identical results compared with direct minimization of the global Gibbs free energy. For the intermediate pressures in which vertical transport dominates, I simulated the atmosphere of Jupiter and the atmosphere of hot Jupiter on HD 189733b, to compare with observations. I focused on reproducing the effect of vertical transport on the $CO \rightleftharpoons CH_4$ conversion in these atmospheres that have very different temperatures. For the low pressures where photochemistry dominates, I tested the model by reproducing the atmospheric compositions of Earth and Mars, in terms of globally-averaged 1D vertical mixing ratio profiles. These tests

of the model are described in more detail in Section 2.3.

The photochemistry-thermochemistry model is designed for exoplanet applications, and has features that are not needed for studies of individual Solar System objects but which are useful for study of potential exoplanet atmospheres. The most important feature that yields the capacity of treating reducing and oxidized atmospheres with the same code is the flexibility of choosing chemical species to be considered in photochemical equilibrium. The species that have lifetimes less than the numerical time step can be treated as being in photochemical equilibrium. My photochemistry-thermochemistry model features a "burn-in" period in which all species' number densities are rigorously computed and then those species that satisfy the lifetime condition are treated in equilibrium so that the computation can be optimized for speed. I have coded the Jacobian matrix for the implicit Euler method analytically, which improves the numerical rigor of the code. In this way my photochemistry-thermochemistry model can quickly find the steady-state solution of atmospheric composition starting from any sensible initial conditions for both reducing and oxidized atmospheres. I emphasize that the ability to compute atmospheric composition of different oxidation states and the elimination of the need of providing fine-tuned initial conditions are essential for exoplanet exploration, because the oxidation states are unknown for terrestrial exoplanets and there are no benchmark cases to provide common initial conditions.

Another important feature of my photochemistry-thermochemistry model is that it treats a wide range of free parameters for terrestrial exoplanets. I do not hardwire any model parameters that meant to be free for exoplanet exploration, including those parameters for planets, such as stellar spectrum and surface gravity, those parameters for atmospheres, such as the mean molecular mass, refractive indices, temperature profiles (which can also be self-consistently computed), and eddy diffusion coefficients, and those parameters that are specific to particular molecules, such as solubility, rainout rate, saturation vapor pressure, surface emission rate, and dry deposition velocity. The code thus has a clear structure that makes extensive parameter exploration possible.

The third important feature of my photochemistry-thermochemistry model is that I offer the flexibility of choosing a subset of chemical species and chemical reactions for the computation. It is in particular important for exoplanet exploration to be able to isolate a chemical system from the complex network of atmospheric chemistry; and my photochemistry-thermochemistry model responds to this need. I design the code to be able to include or exclude the effect of any species or reactions in the complex chemical network, in order to understand the fundamentals of atmospheric chemistry on terrestrial exoplanets. Also, I pay attention to the temperature range in which chemical kinetic rates and photochemical cross sections are valid. The temperature range of exoplanet atmospheres can be significantly larger than the Solar System planet atmospheres. I label the chemical reactions whose rates are measured only at low temperatures ($T < 400$ K) and the chemical reactions whose rates are measured only at high temperatures ($T > 1000$ K), and use them only at appropriate temperature ranges. In addition, I consider the temperature dependence of photochemical cross sections in the model. Finally, I include a basic aerosol formation scheme in the model, the computation of which only relies on the saturation pressure of relevant substances and a timescale of condensation and sublimation. The aerosol scheme is simple, but could easily be expanded to treat non-conventional aerosols in the atmosphere.

I now present the detailed formulation of the photochemistry-thermochemistry model.

2.2.1 Fundamental Equations

The coupled 1-dimensional continuity-transport equation that governs the chemical composition is

$$\frac{\partial n}{\partial t} = P - nL - \frac{\partial \Phi}{\partial z}, \qquad (2.1)$$

where n is the number density of a certain species (cm^{-3}), z is the altitude, P is the production rate of the species ($\mathrm{cm}^{-3}\ \mathrm{s}^{-1}$), L is the loss rate of the species (s^{-1}), and Φ is the upward vertical transport flux of the species ($\mathrm{cm}^{-2}\ \mathrm{s}^{-1}$). The flux can be

approximated by the eddy diffusion together with the molecular diffusion, as

$$\Phi = -KN\frac{\partial f}{\partial z} - DN\frac{\partial f}{\partial z} + Dn\left(\frac{1}{H_0} - \frac{1}{H} - \frac{\alpha_T}{T}\frac{dT}{dz}\right), \qquad (2.2)$$

where K is the eddy diffusion coefficient ($\text{cm}^2 \text{ s}^{-1}$), D is the molecular diffusion coefficient ($\text{cm}^2 \text{ s}^{-1}$), N is the total number density of the atmosphere, $f \equiv n/N$ is the mixing ratio of the species, H_0 is the mean scale height, H is the molecular scale height, T is the temperature (K), and α_T is the thermal diffusion factor (Banks and Kockarts, 1973; Levine, 1985; Krasnopolsky, 1993; Yung and Demore, 1999; Bauer and Lammer, 2004; Zahnle et al., 2006). The first term of Equation (2.2) represents eddy diffusion, and the last two terms represent molecular diffusion. The vertical transport flux is written in terms of the derivatives of the mixing ratio rather than in terms of the number density because this form is simpler and more straightforward to be implemented in numerical schemes. I show that Equation (2.2) is equivalent to the standard vertical diffusion equation in Appendix B.1.

The molecular diffusion coefficient D and the thermal diffusion factor α_T can be determined from the gas kinetic theory, but the eddy diffusion coefficient is a more speculative parameter and must be estimated empirically. For molecular diffusion, I use the following expressions in $\text{cm}^2 \text{ s}^{-1}$ for H and H_2 in a N_2-based atmosphere

$$
\begin{aligned}
D(\text{H}, \text{N}_2) &= \frac{4.87 \times 10^{17} \times T^{0.698}}{N}, \\
D(\text{H}_2, \text{N}_2) &= \frac{2.80 \times 10^{17} \times T^{0.740}}{N};
\end{aligned}
\qquad (2.3)
$$

and in a CO_2-based atmosphere

$$
\begin{aligned}
D(\text{H}, \text{CO}_2) &= \frac{3.87 \times 10^{17} \times T^{0.750}}{N}, \\
D(\text{H}_2, \text{CO}_2) &= \frac{2.15 \times 10^{17} \times T^{0.750}}{N};
\end{aligned}
\qquad (2.4)
$$

and in a H_2-based atmosphere

$$D(H, H_2) = \frac{8.16 \times 10^{17} \times T^{0.728}}{N}.$$ (2.5)

In Equations (2.3-2.5), T has a unit of K and N has a unit of cm^{-3}. The functional form of Equations (2.3-2.5) is derived from the gas kinetic theory and the coefficients are obtained by fitting to experimental data (Marrero and Mason, 1972; Banks and Kockarts, 1973). The expressions for molecular diffusion coefficients are valid for a wide range of temperatures, up to 2000 K, except for $D(H_2, CO_2)$ that is only valid at low temperatures, i.e., $T < 550$ K (Marrero and Mason, 1972). $D(H, CO_2)$ is assumed to be 1.8 times larger than $D(H_2, CO_2)$ (Zahnle et al., 2008). The thermal diffusion factor α_T is taken as a constant for H and H_2 as $\alpha_T = -0.38$ (Banks and Kockarts, 1973). The negative sign of α_T corresponds to the fact that the lightest molecules tend to diffuse to the warmest region.

The eddy diffusion coefficient is the major uncertainty in the 1-D photochemistry-thermochemistry model. For Earth's atmosphere, the eddy diffusion coefficient can be derived from the number density profile of trace gases (e.g. Massie and Hunten, 1981). The eddy diffusion coefficient of Earth's atmosphere is characterized by the convective troposphere and the non-convective stratosphere, which is not necessarily applicable for the exoplanets. The eddy diffusion coefficient may be typically parameterized as

$$K = K_T \qquad (z < z_T),$$
$$K = \min\left(K_H, \quad K_T\left(\frac{N(z_T)}{N}\right)^{1/2}\right) \qquad (z > z_T),$$ (2.6)

where K_T, K_H and z_T are independent parameters satisfying $K_H > K_T$. This formula is adapted from Yung and Demore (1999) with the requirement of continuity in K. My code can either import eddy diffusion coefficient from a file or specify eddy diffusion coefficient according to Equation (2.6).

The goal of the photochemistry-thermochemistry model is to obtain a steady-state solution of each species, or a set of $n(z)$, which makes the left hand side of the

43

Equation (2.1) vanish and satisfies the boundary conditions. Assuming N_x species in the model and N_l equally stratified layers of the atmosphere, I transform the continuity Equation (2.1) into a discrete form as

$$\frac{\partial n_i}{\partial t} = P_i - n_i L_i - \frac{\Phi_{i+1/2} - \Phi_{i-1/2}}{\Delta z}, \tag{2.7}$$

where the subscript i denotes physical quantities in the ith layer, and the subscripts $i + 1/2$ and $i - 1/2$ mean that the flux is defined at the upper and lower boundary of each layer. It is physically correct to define the flux term at the boundary of each layer, which is also crucial for numerically preserving hydrostatic equilibrium for an atmospheric transport scheme that uses number density as independent variables. According to Equation (2.2),

$$\begin{aligned}
\Phi_{i+1/2} &= -(K_{i+1/2} + D_{i+1/2})N_{i+1/2}\frac{f_{i+1} - f_i}{\Delta z} \\
&\quad + D_{i+1/2}\frac{N_{i+1/2}}{2}\left[\frac{(m_a - m)g}{k_B T_{i+1/2}} - \frac{\alpha_T}{T_{i+1/2}}\frac{T_{i+1} - T_i}{\Delta z}\right](f_{i+1} + f_i), \quad (2.8)
\end{aligned}$$

where m_a is the mean molecular mass of the atmosphere, m is the molecular mass of the species, g is the gravitational acceleration, and k_B is the Bolzmann constant. I have approximated $f_{i+1/2}$ by $(f_{i+1} + f_i)/2$ in Equation (2.2).

The combination of Equation (2.7) and (2.8) gives the following 2nd ordered centered discrete differential equation to be solved numerically,

$$\begin{aligned}
\frac{\partial n_i}{\partial t} &= P_i - n_i L_i + \left(k_{i+1/2}\frac{N_{i+1/2}}{N_{i+1}} - d_{i+1/2}\frac{N_{i+1/2}}{N_{i+1}}\right)n_{i+1} \\
&\quad - \left(k_{i+1/2}\frac{N_{i+1/2}}{N_i} + d_{i+1/2}\frac{N_{i+1/2}}{N_i} + k_{i-1/2}\frac{N_{i-1/2}}{N_i} - d_{i-1/2}\frac{N_{i-1/2}}{N_i}\right)n_i \\
&\quad + \left(k_{i-1/2}\frac{N_{i-1/2}}{N_{i-1}} + d_{i-1/2}\frac{N_{i-1/2}}{N_{i-1}}\right)n_{i-1}, \tag{2.9}
\end{aligned}$$

where

$$
\begin{aligned}
k_{i+1/2} &= \frac{K_{i+1/2} + D_{i+1/2}}{\Delta z^2}, \\
d_{i+1/2} &= \frac{D_{i+1/2}}{2\Delta z^2}\left[\frac{(m_a - m)g\Delta z}{k_{\mathrm{B}}T_{i+1/2}} - \frac{\alpha_{\mathrm{T}}}{T_{i+1/2}}(T_{i+1} - T_i)\right].
\end{aligned}
$$

In principle, $\partial n/\partial t = 0$ is equivalent to a set of $N_x N_l$ nonlinear algebraic equations. The set of nonlinear algebraic equations may be solved numerically by Newton-Raphson methods (Press et al., 1992). However, in practice, I find that Newton-Raphson methods require an initial guess to be in the vicinity of the solution. Instead, I treat the problem as a time-stepping problem by evolving the system according to Equation (2.9) to the steady state.

Implicit numerical methods are implemented to solve Equation (2.9). Due to the orders-of-magnitude differences in chemical loss timescales, the system is numerically stiff. I use the inverse-Euler method for the time stepping, as in most previous photochemistry models (e.g. Kasting et al., 1985; Nair et al., 1994; Zahnle et al., 2008). For each time step, it is needed to invert a matrix of dimension $N_x N_l$. As seen in Equation (2.9), the variation in any layer only depends on the number density in that layer and adjacent layers. As a result, the matrix is by nature block tridiagonal with a block dimension of N_x, which is solved efficiently by the Thomas algorithm (Conte and deBoor, 1972). The time step is self-adjusted in a way that the code updates the time step after each iteration according to the variation timescale of the whole chemical-transport system, i.e., the minimum variation timescale of each species at each altitude. As the system converges, larger and larger time steps are chosen.

The criterion of convergence to the steady-state solution is that the variation timescale of each species at each altitude is larger than the diffusion timescale of whole atmosphere, and the fluxes of gain and loss balance out for all species. The gain fluxes include surface emission, chemical production and condensation; whereas the loss fluxes include chemical loss, dry deposition, wet deposition, atmospheric escape, and condensation. I require that the ratio between the net global flux and

the column-integrated number density for all long-lived species is small compared to the diffusion timescale. This condition is very important in the determination of convergence. If any possible long-term trends of major species can be detected, I run the code for an extended time period to test the convergence rigorously.

2.2.2 Species in the Model

The current photochemistry-thermochemistry model can compute concentrations of 110 molecules or aerosols made of C, H, O, N, S elements. These species can be grouped into 5 groups according to their elemental compositions (Table 2.1). This species list contains molecular species that are important for the photochemical models of Earth's atmosphere (Seinfeld and Pandis, 2006), additional molecualar species that are important in the anoxic atmosphere of Titan (Yung et al., 1984), additional molecular species that are important in the hydrogen-dominated atmosphere of Jupiter (Gladstone et al., 1996), and additional sulfur species that are proposed in order to simulate sulfur photochemistry in the anoxic atmosphere of early Earth (Pavlov and Kasting, 2002). The species list should be adequate for simulations of oxygen, carbon, nitrogen, and sulfur photochemistry in atmospheres having wide ranges of oxidation state. Further expansion of the species list can be driven by specific scientific applications that one may consider.

I offer the flexibility to choose a subset of species for computation in the photochemistry-thermochemistry model. The purpose to use a subset of species instead of the full set of species is to focus on a tractable chemical network for a specific problem and in some cases, to speed up the computation. Since the computation time for each time step scales with N_x^3, decreasing the number of chemical species greatly reduces the computation time. If doing so, one should be cautious about the completeness of species in calculation. Species in different groups of Table 2.1 may interact with each other, and sometimes affect the steady-state composition in subtle ways. For example, it is well known that nitrogen species can form catalytic cycles that remove some of ozone in Earth's atmosphere (e.g. Seinfeld and Pandis, 2006), and only considering the Group I species (hydrogen and oxygen) will not allow to simulate this

Table 2.1: Species in the photochemistry-thermochemistry model

Group	Group Name	Species
I	Hydrogen and Oxygen	H_2, O_2, H_2O, O, $O(^1D)$, O_3, H, OH, HO_2, H_2O_2
II	Simple Carbon	CO_2, CO, CH_4, C, CH, CH_2, $^1CH_2$, CH_3, CH_2O, CHO, CH_3O, CH_3O_2, CHO_2, CH_2O_2, CH_4O, CH_4O_2, C_2, C_2H, C_2H_2, C_2H_3, C_2H_4, C_2H_5, C_2H_6, C_2HO, C_2H_2O, C_2H_3O, C_2H_4O, C_2H_5O
III	Nitrogen	N_2, N, NH, NH_2, NH_3, N_2H_2, N_2H_3, N_2H_4, N_2O, NO, NO_2, NO_3, N_2O_5, HNO, HNO_2, HNO_3, HNO_4, HCN, CN, CNO, HCNO, CH_5N, C_2H_2N, C_2H_5N, CH_3NO_2, CH_3ONO_2
IV	Sulfur	S, S_2, S_3, S_4, S_8, SO, SO_2, $^1SO_2$, $^3SO_2$, SO_3, H_2S, HS HSO, HSO_2, HSO_3, H_2SO_4, OCS, CS, CH_3S, CH_4S
V	Complex Carbon	C_3H_2, C_3H_3, CH_3C_2H, CH_2CCH_2, C_3H_5, C_3H_6, C_3H_7, C_3H_8, C_4H, C_4H_2, C_4H_3, C_4H_4, C_4H_5, $1\text{-}C_4H_6$, $1,2\text{-}C_4H_6$, $1,3\text{-}C_4H_6$, C_4H_8, C_4H_9, C_4H_{10}, C_6H, C_6H_2, C_6H_3, C_6H_6, C_8H_2
VI	Aerosol	H_2SO_4 aerosols, S_8 aerosols

effect in the model. As a general remark, the choice of species to be included in a photochemistry simulation depends on the scientific problem that one intends to solve. I here suggest the following general guidelines for future references: (1) it is advisable to select the species by the groups in Table 2.1; (2) one should verify that the products of the chemical reactions that have appreciable reaction rates based on the selected reactants are in the list of selected species; (3) for thin atmospheres one should consider the main atmospheric components and the main surface emission components in species selection; (4) for thick atmospheres one should consider the main elements of interest in species selection.

I also offer the flexibility to choose the "fast species" to be computed by photochemical equilibrium in each time step. As is common practice in the effort to reduce the stiffness of the system and improve the numerical stability, "fast" species with relatively short chemical loss timescales are computed directly from the diagnostic

equation, namely

$$n = \frac{P}{L},$$ (2.10)

which implies that photochemical equilibrium can be achieved within each time step. The choice of fast species varies with the atmospheric composition and should be considered on a case-by-case basis. The choices of "fast" species were usually hard-wired in previous photochemistry codes, which fundamentally limited their application to certain specific types of atmospheres (e.g., to Earth and to Mars). My photochemistry code offers the flexibility to adjust the choice of species in photochemical equilibrium, which yields the capacity of treating atmospheres having very different oxidation states with the same code. I evaluate P and L in Equation (2.10) at each time step using the number density of all species from previous time step and determine the number density of fast species according to Equation (2.10) after the current time step linearly. I neglect nonlinearity due to multiple species in photochemical equilibrium; as a result, I do not allow strongly inter-dependent species to be concurrently considered as in photochemical equilibrium, for example for S_2, S_3, and S_4. This approach yields stable convergence to the steady-state solution from virtually any initial test solutions. I always verify the mass balance of the steady-state solution.

2.2.3 Chemical Kinetics

I compiled a comprehensive list of chemical and photochemical reactions from the literature. The production and loss rates in Equation (2.7) are provided from all chemical and photochemical reactions that produce or consume the relevant molecule. I exhausted all possible reacting pairs between the species in the model, and included the latest experimental measurements or review recommendation values for these reactions. For expected reactions that currently do not have kinetic rate measurements, I adopted the postulated reaction rates from previous photochemistry investigations.

As a result, in the generic model, I have included 645 bimolecular reactions, 89 termolecular reactions, and 93 thermal dissociation reactions. I included the thermal dissociation reactions to make the photochemistry-thermochemistry model poten-

tially adaptable to simulate hot planets. I mainly used the updated reaction rates from the online NIST database (http://kinetics.nist.gov) and refer to the JPL publication (Sander et al., 2011) for the recommended rate when multiple measurements are presented in the NIST database. For termolecular reactions and dissociation reactions, I included both the low-pressure limit rates and the high-pressure limit rates when available, and used the complete formula suggested by the JPL publication (Sander et al., 2011) to compute the pressure dependency. The high-pressure limit rates are adopted from the NIST Kinetics database, and Baulch et al. (1994, 2005); Jasper et al. (2007); Moses et al. (2011).

I performed careful comparisons of my reaction lists and corresponding reaction rates with those used by previous photochemistry models including Nair et al. (1994), Pavlov and Kasting (2002), and Zahnle et al. (2008). Most of my reaction rates are the same as those used by other codes. For a dozen reactions, I find updated reaction rates listed in either the JPL publication or the NIST database updated after the publication of the cited photochemistry models. Also, for the general purpose of my photochemistry-thermochemistry model, I include the reactions that are very slow at low temperatures (i.e., 200 - 400 K) but may be become important at higher temperatures > 1000 K. In addition, a number of reactions that lack laboratory-measured rates may be important for low-temperature (i.e., 200 - 400 K) applications. For C>2 hydrocarbon-related reactions that do not have experimentally measured reaction rates, I adopted the rates from Yung and Demore (1999) which have been proved to be successful in reproducing the hydrocarbon chemistry in the atmospheres of Jupiter and Titan. Sulfur polymerization reaction rates still lack consistent experimental measurements, and I adopt the reaction rates proposed by Kasting (1990) and those proposed by Moses et al. (2002). Both sets of sulfur polymerization reaction rates are speculative and they are widely discrepant, the effect of which will be discussed later in the study of sulfur chemistry (Section 3.4). All chemical reactions and their reaction rates are tabulated in Table A.1.

Chemical reaction rates may sensitively depend on temperature. For all reaction rates I use the Arrhenius formula to account for the dependence on temperature when

the activation energy data are available, otherwise I adopted the value of experimental measurements, which are usually under $\sim$298 K. The reported reaction rates are usually valid in certain specific temperature ranges. For example, reaction rates recommended by the JPL publication (Sander et al., 2011) are the reactions relevant to Earth's atmosphere, in general valid within the small range of 200 - 300 K. Hence it may be problematic to extend the rate expressions to high-temperature cases, such as hot planets. At the high-temperature end, the valid temperature range for some of the reaction rates measured in the combustion chemistry is a few thousand K. These reactions may be important for modeling hot Jupiters (e.g. Moses et al., 2011), but they should not be included in the computation of low-temperature cases, e.g., for Earth-like planets. The low-temperature reactions and the high-temperature reactions are annotated in Table A.1. Moreover, most chemical reactions involving free radicals have very small activation energy, and thus weak temperature dependencies. Usually the reaction rates of free radicals are measured at room temperature and can be used in photochemistry models under different temperatures (Sander et al., 2011). Common atmospheric free radicals are: $O(^1D)$, OH, H, N, NH_2, N_2H_3, C, CH, CH_2, $^1CH_2$, CH_3, CHO, CHO_2, CH_3O, CH_3O_2, C_2, C_2H, C_2H_3, C_2H_5, C_2HO, C_2H_3O, C_2H_5O, CN, CNO, S, S_2, SO_3, HS, HSO, HSO_2, HSO_3, CH_3S and CS. For reactions with these molecules, if no activation energy is reported in the literature, I generally assume that the activation energy is negligible and their kinetic rates do not depend on temperature.

I have included the reverse equation for each forward equation tabulated in Table A.1, for the model to be applicable to the high-pressure regime in which thermochemical equilibrium holds. The reverse reactions are the reversal of the chemical reactions whose kinetic rates have been measured or computed for the studies of Earth and planetary atmospheres (chosen as forward reactions). The kinetic rates of reverse reactions (k_r) and forward reactions (k_f) are linked by the difference in the Gibbs free energy of formation ($\Delta_f G^\circ$) of the reactants and the products as

$$k_r = k_f \exp\left[\frac{\Delta_f G^\circ(\text{products}) - \Delta_f G^\circ(\text{reactants})}{RT}\right](k'_b T)^{n_p - n_r}, \qquad (2.11)$$

where R is the gas constant, $k'_b = 1.38065 \times 10^{-22}$ bar cm^3 K^{-1} is the Boltzmann constant, and n_p and n_r are the number of products and reactants, respectively. Equation (2.11) is derived by Visscher and Moses (2011) and is used to calculate the rates of the reverse reactions. The thermochemical data are taken from the NIST-JANAF database (Chase, 1998), Burcat and Ruscic (2005), and Visscher and Moses (2011). For a number of reactions, there are empirical measurement for both forward and reverse reactions, which provide an opportunity of validating the computation scheme. Whenever possible, I adopt the empirical kinetic rate that have the widest temperature range (i.e., define as the forward reaction), compute the reverse reaction rate, and compare the reverse rate with empirical measurements. For all tested reactions I find agreement within one order of magnitude.

2.2.4 Interaction with Radiation

Molecules in the atmosphere absorb ultraviolet (UV) and visible light from the host star. If the absorbed photon carries enough energy, the molecule may be photodissociated to form free radicals. The photodissociation rate is proportional to the number density of photons with UV and visible wavelengths at each altitude. For direct stellar radiation, the optical depth τ includes the contribution from molecular absorption τ_a, Rayleigh scattering τ_r, and aerosol particle extinction τ_m. For the multiple-scattered (diffusive) radiation, I use the δ-Eddington 2-stream method implemented based on the formulation of Toon et al. (1989). The actinic flux[1] of the diffusive radiation is $F_{\text{diff}} = 2(F^+ + F^-)$ where F^+ and F^- are the diffusive flux in the upward and downward direction. The photolysis flux at a certain altitude includes both the direct radiation and the diffusive radiation, i.e.,

$$F(\lambda\,,z) = F_0(\lambda)\exp\left[-\tau(\lambda\,,z)/\mu_0\right] + F_{\text{diff}}, \tag{2.12}$$

---

[1]The actinic flux is the quantity of light available to molecules at a particular point in the atmosphere and which, on absorption, drives photochemical processes in the atmosphere. It is calculated by integrating the spectral radiance over all directions of incidence of the light. The actinic flux is distinguished from the spectral irradiance in the way that it does not refer to any specific orientation because molecules are oriented randomly in the atmosphere.

where F_0 is the radiation flux at the top of the atmosphere where $\tau = 0$, and μ_0 is the angle of the path of sunlight. By default I assume the zenith angle of the star to be 57.3° (see Appendix B.2 for justification). The photodissociation rate is then

$$J(z) = \frac{1}{2} \int q(\lambda)\sigma_a(\lambda)L(\lambda, z)d\lambda, \tag{2.13}$$

where σ_a is the absorption cross section, $q(\lambda)$ is the quantum yield that is defined as the ratio between the yield of certain photodissociation products and the number of photons absorbed, and $L(\lambda, z)$ is the actinic flux with units of quanta cm^{-2} s^{-1} nm^{-1}. The 1/2 factor is included to account for diurnal variation of the incident photon flux (e.g. Zahnle et al., 2008), which is not used to model the dayside of a tidally locked planet, or to model very short-lived species (i.e., OH) during the daytime. The general-purpose model includes 70 photodissociation reactions. Different branches resulting from the photodissociation of one molecule are treated as different photodissociation reactions. The photodissociation reactions, the sources of data for cross sections and quantum yields, and the rates on the top of Earth's atmosphere are tabulated in Table A.2.

For the UV and visible cross sections and the quantum yields, I use the recommended values from the JPL publication (Sander et al., 2011) when available. I also use the cross sections from the MPI-Mainz-UV-VIS Spectral Atlas of Gaseous Molecules[2] when the JPL recommended values are not available or incomplete. There are a number of molecules of atmospheric importance that lack measurements for UV and visible cross sections or quantum yields, and I have estimated photolysis rates for them in the following way. The photodissociation timescale of S$_2$ has been measured to be ~ 250 s at 1 AU from the Sun (de Almeida and Singh, 1986), from which I estimate the photolysis rate of S$_2$. For other molecules that have no UV or visible-wavelength cross sections available in the literature, I assume their photolysis rates to be the same as another molecule that has similar molecular structure. For example, the photolysis rate of HNO is assumed to be the same as HNO$_2$ (Zahnle et al., 2008);

---

[2]www.atmosphere.mpg.de/spectral-atlas-mainz

the photolysis rate of HSO is assumed to be the same as HO_2 (Pavlov and Kasting, 2002); and the photolysis rate of N_2H_2 is assumed to be the same as N_2H_4.

It is useful to stress that sometimes the wavelength resolution has to be fine enough to correctly compute the photolysis rates using Equation (2.13). Two wavelength regions are of particular interest. One is the Lyman-alpha line at 121.6 nm. This is a single emission line that sometimes carries a significant fraction of near-ultraviolet radiative energy from the parent star (e.g. France et al., 2013). It is necessary to resolve this line, or to treat this line separately from the integration over wavelength, in order to correctly compute the contribution of the Lyman-alpha line to the photolysis rates. Important molecules that are affected by the Lyman-alpha line are H_2O, CH_4, and CO_2 (e.g. Brasseur and Solomon, 2005). The second important wavelength ranges that require special attention is the Schumann-Runge bands of molecular oxygen at 175-200 nm. In these bands, the cross section of molecular oxygen varies by more than 3 orders of magnitude in each 1 nm wavelength range, making it computationally intensive to correctly calculate the photolysis rate of O_2 and the penetration of photons in oxygen-rich atmospheres (important for the photolysis rates of other molecules including H_2O, N_2O, and CO_2). A number of techniques developed to approximate the Schumann-Runge bands is summarized in Brasseur and Solomon (2005). In my model, I find it adequate to use an ultraviolet wavelength resolution of 0.1 nm to largely approximate the effects of the Lyman-alpha line and the Schumann-Runge bands.

Temperature dependencies of photolysis cross sections and quantum yields are considered. Notably, at 200 K, compared to room temperature, N_2O, N_2O_5, HNO_3, OCS, CO_2 have smaller UV cross sections, leading to photolysis rates more than 10% lower; whereas NO_3 has a larger UV cross section, leading to a photolysis rate more than 10% higher. SO_2 has complex band structures in its UV spectrum and the cross sections depend on temperature as well. I take into account any other temperature dependencies reported for a gas at temperatures outside 290 - 300K (see Table A.2 for notes on temperature dependencies). In most cases, cross sections are also measured at lower temperature such as 200 K, primarily for Earth investigations (Sander et al.,

2011). I use linear interpolation to simulate cross sections between 200 and 300 K, and do not extrapolate beyond this temperature range. It is worthwhile noting that UV cross sections of almost all gases at temperatures significantly higher than room temperature are unknown, and temperature dependencies of cross sections are not considered in previous high-temperature photochemistry-thermochemistry models of hot exoplanets (e.g. Moses et al., 2011; Miller-Ricci Kempton et al., 2012). This may be a plausible simplification for gases without significant band structure in UV, but for gases such as H_2, CO_2 and SO_2, whose band structures are sensitive to temperature, extrapolation of cross sections to high temperature might induce significant errors. One needs to be cautious about the uncertainty of photolysis rate at temperatures much higher than room temperature.

Rayleigh scattering from atmosphere molecules introduces additional optical depth, particularly important for attenuation of UV radiation. The optical depth due to Rayleigh scattering is

$$\tau_r(\lambda, z) = \int_z^\infty N(z')\sigma_r(\lambda)dz',$$
(2.14)

in which the Rayleigh scattering cross section is (e.g. Liou, 2002)

$$\sigma_r(\lambda) = C_r \frac{8\pi^3(m_r(\lambda)^2 - 1)^2}{3\lambda^4 N_s^2},$$
(2.15)

where m_r is the real part of the refractive index of the molecule, C_r is a corrective factor to account for the anisotropy of the molecule, and N_s is the number density at the standard condition (1 atm, 273.15 K). The refractive index depends on the main constituent in the atmosphere. The refractive index of Earth's atmosphere is from Seinfeld and Pandis (2006); the refractive index of H_2 is from Dalgarno and Williams (1962); the refractive index of N_2 is from Cox (2000); the refractive index of CO_2 is from Old et al. (1971); and refractive indices of CO, and CH_4 are given in Sneep and Ubachs (2005). In principle the correction factor C_r depends on the molecule and the wavelength; but C_r is usually within a few percent with respect to the unity, except for $C_r \sim 1.14$ for CO_2 (Sneep and Ubachs, 2005). In the following I assume $C_r = 1.061$, the value for Earth's atmosphere at ~ 200 nm (Liou, 2002).

For the spectrum of a solar-type star (G2V), I use the Air Mass Zero (AM0) reference spectrum produced by the American Society for Testing and Materials[3]. The AM0 spectrum covers a wavelength range from 119.5 nm to 10 microns. The spectrum gives a Lyman alpha flux of 4×10^{11} photon $cm^{-2} s^{-1}$ on the top of Earth's atmosphere, corresponding to a low level of solar activity. For the extreme-UV spectrum, we use the average quiet-Sun emission provided by Curdt et al. (2004). I also use the simulated non-active M star spectrum from Allard et al. (1997) for quiet M stars.

2.2.5 Treatment of Aerosols

Microphysical processes involved in the formation of atmospheric aerosols are nucleation, condensational growth, and coagulation (e.g. Toon and Farlow, 1981; Seinfeld and Pandis, 2006). It is beyond the purpose of this work to simulate these microphysical processes in detail. For photochemically produced aerosols, the competition between coagulation and sedimentation mainly determines the particle size distribution. A complete treatment of the atmospheric aerosols involves solving the steady-state size distribution function (e.g. Seinfeld and Pandis, 2006).

For the photochemical model, I simplify the problem of atmospheric aerosols by assuming the particle diameter to be a free parameter. I adopt the lognormal distribution as

$$\frac{dN}{dD} = \frac{N_t}{\sqrt{2\pi} D \ln \sigma} \exp \left[- \frac{(\ln D - \ln D_0)^2}{2 \ln^2 \sigma} \right], \tag{2.16}$$

where dN is the number of particles per volume in the diameter bin dD, N_t is the total number density of particles, D_0 is the median diameter of the particles, and σ is the particle size dispersion (defined as the ratio of the diameter below which 84.1% of the particles lie to the median diameter). The lognormal distribution is a reasonable assumption because it provides a good fit to the particle size distribution measured in Earth's atmosphere (e.g. Seinfeld and Pandis, 2006), and a sensible particle size dispersion parameter for photochemically produced aerosols is in the range of 1.5 ~ 2.0 (e.g. Seinfeld and Pandis, 2006). What is important for the

---

[3]http://rredc.nrel.gov/solar/spectra/am0/

radiative transfer model and the photochemistry model is the surface area mean diameter D_S and the volume mean diameter D_V, respectively. The mean diameters are related to the median diameter as

$$D_S = D_0 \exp(\ln^2 \sigma), \tag{2.17}$$

$$D_V = D_0 \exp\left(\frac{3}{2}\ln^2 \sigma\right). \tag{2.18}$$

I use the surface area mean diameter D_S (referred to as "mean diameter" in the following) as the free parameter for specifying a particle size distribution, as it is relevant to the radiative properties of the particle population. The volume mean diameter D_V is useful in the conversion from mass concentration of the condensed phase (computed in the photochemistry model) to the number of aerosol particles for radiative transfer computation. This parameterization separates the complexity of aerosol formation from the photochemistry model, which allows to explore how the particle size affects the overall chemical composition.

I compute the production and loss rate of a molecule in the condensed phase (i.e., aerosols) based on its condensation timescale. When the molecule becomes supersaturated at a certain altitude, condensation can happen and aerosols form. The condensation/evaporation timescale is given by Hamill et al. (1977) and Toon and Farlow (1981) as

$$\frac{1}{t_c} = \frac{m}{\rho_\mathrm{p}}\left(\frac{2k_\mathrm{B}T}{\pi m}\right)^{1/2}\frac{n_\mathrm{g} - n_\mathrm{v}}{D_S}, \tag{2.19}$$

where t_c is the condensation/evaporation timescale, m is the mass of molecule, ρ_p is the particle density, k_B is the Boltzmann constant, T is the atmospheric temperature, n_g is the number density of the corresponding gas, and n_v is the saturated vapor number density at the corresponding pressure. The formula (2.19) is suitable for both condensation and evaporation processes. When $n_\mathrm{g} > n_\mathrm{v}$, the gas phase is saturated, so the condensation happens and $t_c > 0$. When $n_\mathrm{g} < n_\mathrm{v}$, the gas phase is unsaturated, so the evaporation is possible and $t_c < 0$. The production or loss rate of the molecule

in the condensed phase is

$$P = \frac{n_g}{t_c}, \qquad L = \frac{1}{t_c}. \tag{2.20}$$

I include gravitational settling in the mass flux term of the continuity-transport equation (Equation 2.1) for aerosol particles in addition to eddy mixing. The additional gravitational downward flux of the aerosol particle is

$$\Phi_F = -v_F n_c, \tag{2.21}$$

where v_F is the settling velocity of the particle in the atmosphere. The settling velocity is reached when the gravitational force is balanced by the gas drag. For aerosols with diameter of order of 1 μm, the settling velocity is reached within 10^{-5} s in Earth's atmosphere (Seinfeld and Pandis, 2006). Therefore I assume the falling velocity to be the settling velocity. The settling velocity can be derived from the Stokes' law (Seinfeld and Pandis, 2006) as

$$v_F = \frac{1}{18} \frac{D_S^2 \rho_p g C_c}{\mu}, \tag{2.22}$$

where g is the gravitational acceleration, μ is the viscosity of the atmosphere, and C_c is the slip correction factor related to the mean free path (λ) of the atmosphere as

$$C_c = 1 + \frac{2\lambda}{D_S} \left[1.257 + 0.4 \exp\left(-\frac{1.1 r_p}{\lambda} \right) \right]. \tag{2.23}$$

The treatment of photochemically produced aerosols described above is applicable to any molecules that could reach saturation as a result of photochemical production. In Earth's atmosphere, the photochemical aerosols include sulfate aerosols (H_2SO_4), sulfur aerosols (S_8), organic hazes, nitric acid aerosols (HNO_3), and hydrochloric acid aerosols (HCl). For now I have implemented sulfate aerosols (H_2SO_4) and sulfur aerosols (S_8) in my photochemistry code. These aerosols and water vapor are the common condensable materials at habitable temperatures that commonly exist in planetary atmospheres (e.g. Kasting et al., 1989; Pavlov et al., 2000; Seinfeld and

Pandis, 2006). The required data for including an aerosol species in the photochemistry model is the saturation vapor pressure. Saturation vapor pressure of H_2SO_4 is taken as recommended by Seinfeld and Pandis (2006) for atmospheric modeling, with a validity range of 150 - 360 K. S_8 is the stable form of elemental sulfur because the S_8 molecule has a crown-shape ring structure that puts least strain on the S-S bond among sulfur allotropes and the crown structure allows for considerable cross-ring interaction between nonbonded atoms (Meyer, 1976). Saturation pressure of S_8 is taken as the total sulfur saturation pressure against liquid sulfur at $T > 392$ K and solid (monoclinic) sulfur at $T < 392$ K tabulated and expressed by Lyons (2008). In addition to aerosols, I use Equation (2.19-2.20) to compute the process of condensation of water vapor in the atmosphere. I do not consider evaporation of condensed water in the atmosphere because water droplets may grow by aggregation and rapidly precipitate out (Seinfeld and Pandis, 2006). Saturation pressure of water is taken as that against ice at temperature lower than 273.16 K (Murphy and Koop, 2005), and that against liquid water at temperature higher than 273.16 K (Seinfeld and Pandis, 2006).

The optical effect of aerosols is treated by considering both scattering and absorption. Assuming a homogeneous sphere, the Mie theory (see van de Hulst, 1981, for a detailed description) computes extinction cross section (σ_{ext}), single scattering albedo (w_s) and asymmetric factor (g_{asym}), based on the following parameters: the refractive index of the material ($m_r + m_i i$), r_p, and the wavelength. I use the refractive index of S_8 aerosols from Tian et al. (2010) for the UV and visible wavelengths and from Sasson et al. (1985) for infrared (IR) wavelengths. I use the refractive index of H_2SO_4 aerosols (assumed to be the same as 75% sulfuric acid solution) from Palmer and Williams (1975) for UV to IR wavelengths, and Jones (1976) for far IR wavelengths.

2.2.6 Boundary Conditions

The atmospheric chemical composition of a terrestrial exoplanet is ultimately determined by boundary conditions. The upper boundary conditions describe the atmospheric escape. For thin atmospheres, the lower boundary conditions describe the

surface emission, the deposition of molecules and aerosols to the surface, or the presence of a large surface reservoir of certain molecule (e.g. H_2O). For thick atmospheres, the lower boundary conditions describe thermochemical equilibrium. The boundary conditions need to be properly provided to capture the physics of an exoplanet atmosphere.

The upper boundary conditions describe the atmospheric escape of an terrestrial exoplanet. The escape rates of exoplanet atmospheres are fairly uncertain depending on stellar soft X-ray and UV luminosity, exosphere chemistry, existence of magnitude fields, etc (e.g. Yelle et al., 2008; Tian, 2009). I thus provide the following options of specifying escape rates in the photochemistry-thermochemistry code:

Type 1: $\Phi_{N_l+1/2} = 0$, or no escape;

Type 2: $\Phi_{N_l+1/2} = n_{N_l} V_{\lim}$, where $V_{\lim}$ is the diffusion-limited escape velocity;

Type 3: $\Phi_{N_l+1/2}$ is a assigned nonzero value.

Here I use the same notation for flux as in Equation (2.7-2.8), such that the upper boundary condition replaces the flux at the upper boundary of the layer N_l in Equation (2.8). For the type 2 upper boundary condition (atmospheric escape), the diffusion-limited velocity ($V_{\lim}$) is

$$V_{\lim} = D_{N_l+1/2}\left(\frac{1}{H_0} - \frac{1}{H}\right),\tag{2.24}$$

where $D_{N_l+1/2}$ is the molecular diffusion coefficient evaluated at the top of the atmosphere. The diffusion-limited flux is the highest escape flux of an atmosphere in hydrostatic equilibrium (Hunten, 1974). For Mars, the Jeans escape of H_2 reaches the diffusion-limited flux when the exobase temperature is above 400 K (Zahnle et al., 2008). For modeling current atmospheres of Earth and Mars, I use the Type 2 upper boundary condition for the escape of H and H_2 in my model, and generally I assume no escape for all other species, i.e., the Type 1 upper boundary condition. The Type 3 upper boundary condition may be used when processes above the neutral atmosphere

are important. For example, an influx of atomic N can represent the photodissociation of N_2 in the upper atmosphere. The Type 3 boundary condition may also be used when hydrodynamic escape has to be considered.

The lower boundary conditions describe the interaction between the atmosphere and the surface, which includes surface emission and surface deposition. Mathematically, the three types of lower boundary conditions are:

Type 1: n_1 is assigned;

Type 2: $\Phi_{1/2} = -n_1 V_{\mathrm{DEP}}$ where V_{DEP} is molecule-specific dry deposition velocity;

Type 3: $\Phi_{1/2}$ is assigned.

Again I use the same notation for flux as in Equation (2.7-2.8), and $\Phi_{1/2}$ replaces the flux at the lower boundary of the layer 1 in Equation (2.8).

The Type 1 lower boundary condition presents a large reservoir at the lower boundary. For thin atmospheres, it is common to use this type of boundary conditions for water vapor to simulate the effect of a surface with oceans. This approach is equivalent to setting the relative humidity at the surface to be a constant. For thick atmospheres, the Type 1 lower boundary is used to mimic the atmosphere maintaining thermochemical equilibrium at high pressures. Note that specifying the Type 1 lower boundary condition means decreasing the number of free variables; n_1 is fixed as the lower boundary condition and is no longer considered as a variable in the main computation loop.

The Type 2 lower boundary condition specifies the dry deposition velocity, which is a key parameter that determines the chemical composition of the atmosphere and is a major unknown. The deposition velocity depends on both the dynamical properties of the lower atmosphere and the chemistry of the planet's surface. With the number density at the bottom layer (n_1) computed from the photochemistry-thermochemistry model, the interaction between the bottom layer of atmosphere and the surface consists of two steps: first, the molecular transport across a thin stagnant layer of air

adjacent to the surface, called the *quasi-laminar sublayer* ; second, the uptake at the surface (Seinfeld and Pandis, 2006). A parameterization of dry deposition velocity involving these two steps is described in Appendix B.3.

Physically the dry deposition requires a sink at the surface; for a gas without effective surface sink the dry deposition velocity should be zero. In particular, the surface deposition of a number of gases, including CO, H_2, CH_4, and NH_3, is primarily removed by microorganisms on Earth (e.g. Kharecha et al., 2005; Seinfeld and Pandis, 2006, Kasting, 2012, private communication), and the canonical values for their dry deposition velocities are not applicable for presumably abiotic planets. Take carbon monoxide for an example. If a planet has no ocean, there is no known reaction that can consume CO at the surface, and therefore the dry deposition velocity of CO for an abiotic desiccated planet should be zero (like Mars). If the surface has an ocean, the dissolved CO may be naturally and slowly converted into acetates by OH in sea water, or biologically converted into acetates at a much faster rate. The CO deposition velocity has been estimated to be 1.2×10^4 cm s^{-1} for the most efficient biological removal and $10^{-8} \sim 10^{-9}$ cm s^{-1} on an abiotic ocean planet (Kasting, 1990; Kharecha et al., 2005). For another example, it is common to use a fairly large dry deposition velocity for SO_2 (~ 1 cm s^{-1}) to study the sulfur cycle in Earth's marine atmosphere (e.g. Toon et al., 1987). In contrast, the dry deposition velocity is assumed to be zero, or reduced by an arbitrary factor of up to 1000, to mimic a putative Mars ocean that is believed to be saturated with dissolved SO_2 and other sulfur species (e.g. Halevy et al., 2007; Tian et al., 2010). In general, the dry deposition velocity depends on a broad context of planetary geochemistry, notably on the surface mineralogy, the acidity of ocean, and the surface pressure and temperature. Therefore it is critical for exoplanet exploration to understand the interaction between atmospheric chemistry composition of terrestrial exoplanets and the surface deposition.

In addition to the dry deposition at the surface, I also include the wet deposition throughout the atmosphere as a removal process for soluble species. I use the

parameterization of Giorgi and Chameides (1985) as

$$k_R(z) = f_R \times \frac{n_{\mathrm{H_2O}}(z) k_{\mathrm{H_2O}}(z)}{55 A_V [L \times 10^{-9} + (H'RT(z))^{-1}]}, \tag{2.25}$$

where f_R is a reduction factor adjustable in the model, $k_{\mathrm{H_2O}}$ is the precipitation rate taken to be 2×10^{-6} s^{-1}, A_V is the Avogadro's number, L is the liquid water content taken to be 1 g m^{-3} in the convective layer near the surface, and H' is the effective Henry's Law constant measuring the solubility of the molecule in the unit of mol dm^{-3} atm^{-1}. The effective Henry's law constant may differ from the standard Henry's law constant when taking into account dissociation in the aqueous phase (Giorgi and Chameides, 1985; Seinfeld and Pandis, 2006). In the model we use the effective Henry's Law constant published in Giorgi and Chameides (1985) as well as the standard Henry's Law constants from the NIST Chemistry Webbook[4]. Since the parameterization of Equation (2.25) is primarily for modeling Earth's atmosphere, the specific reduction factor f_R could be applied when it is reasonable to believe the hydrological cycle is reduced on an exoplanet (e.g. Tian et al., 2010).

The Type 3 lower boundary condition has assigned flux that represents the surface emission. Note that the dry deposition (Type 2) and assigned flux (Type 3) lower boundary conditions can be used at the same time, but assigned number density (Type 1) boundary condition over-rules other lower boundary conditions. For example, SO_2 may be deposited to the surface at a rate proportional to the number density of the bottom layer, and also be emitted from the surface to the atmosphere at an assigned flux.

I finish this section with a definition of the so-called "redox balance", the requirement of which arises when the fixed mixing ratio lower boundary condition (Type-1) is used in the photochemistry-thermochemistry model. Following Kasting and Brown (1998), Zahnle et al. (2006), and Segura et al. (2007), I define H_2O, N_2, CO_2, SO_2 as redox neutral, and assign the redox number ($\mathcal{R}$) of any H-O-C-N-S molecule as the

---

[4]http://webbook.nist.gov/chemistry/

number of hydrogen in excess, i.e.,

$$\mathcal{R}(H_{a_1}O_{a_2}N_{a_3}C_{a_4}S_{a_5}) = a_1 - 2a_2 + 4a_4 + 4a_5. \tag{2.26}$$

Note that my definition of the redox number differs from Zahnle et al. (2006) and Segura et al. (2007) in the way that I count the number of H and they count the number of H_2. With my definition, for example, the redox number of H_2S is 6, and the redox number of H_2SO_4 is -2. The redox balance says that the total redox influx to the atmosphere (i.e., surface emission) should be balanced by the total redox outflux from the atmosphere (i.e., atmospheric escape, dry deposition, and wet deposition), otherwise the atmosphere is being oxidized or reduced. The redox balance is equivalent to the conservation of total budget of hydrogen in the atmosphere, and is equivalent to the conservation of the total number of electrons in the atmosphere. One might consider the redox balance to be redundant. The redox balance is indeed redundant if the lower and upper boundary conditions for all species are specified in fluxes (and not in mixing ratios). In many applications, however, it is useful to use the Type-1 lower boundary condition, which specifies mixing ratio. In that case, the mass conservation would not necessarily guarantee the redox balance. After all, an imbalance in the redox budget for a steady-state solution indicates bugs in chemistry kinetics, unphysical boundary conditions, or solutions that have not yet converged. I explicitly check the redox balance for all my model outputs.

2.2.7 Coupling with Radiative Transfer Model

The photochemistry-thermochemistry model requires temperature-pressure profiles as input parameters. The dominant process that determines the temperatures of a terrestrial exoplanet atmosphere is the balance between heating from exterior (stellar radiation) and interior and cooling of the atmosphere (Liou, 2002). For thick atmospheres, a grey-atmosphere assumption (i.e., mean opacities in stellar radiation wavelengths and in thermal emission wavelengths) provides reasonably good estimate for the temperature-pressure profiles (Guillot, 2010). Therefore, for thick atmospheres

I compute the temperature-pressure profiles using the formulation of Guillot (2010) with the grey-atmosphere assumption. The temperature-pressure profiles are also adjusted according to the appropriate adiabatic lapse rate to account for the onset of convection (see Miller-Ricci et al., 2009).

The temperature profiles depend on the atmospheric compositions. For thick atmospheres, I compute the temperature profiles based on the atmospheric compositions that obey the thermochemistry equilibrium. I use the method of minimizing the total Gibbs free energy as described in Miller-Ricci et al. (2009) to compute the thermochemical equilibrium composition. The thermochemistry routine and the temperature profile routine are inter-dependent, so they are used iteratively to achieve a stratified atmospheric composition and temperature-pressure profile that obey thermochemical equilibrium, radiative-convective equilibrium, and hydrostatic equilibrium. The temperature-pressure profile and the composition at the lower boundary, are then provided to the full kinetic-transport model to seek the steady-state solution.

For thin atmospheres I use the photochemistry model in a "stand-alone" mode with the temperature-pressure profiles adopted. The grey-atmosphere formulation of Guillot (2010) is not applicable to thin atmospheres because it assumes that all radiative energy from the parent star is deposited in the atmosphere, which is usually not the case for a thin atmosphere. In principle, one could couple the photochemistry model with a radiative-convective climate model to seek fully self-consistent solutions for both atmospheric compositions and temperature profiles (e.g. Segura et al., 2007). However, such computation is expensive and therefore can only be performed for a limited set of scenarios. I am here more concerned with the chemical lifetime of trace gases in thin atmospheres with a wide range of oxidation states than an accurate account for the atmospheric temperatures. In my model for thin atmospheres the near-surface temperature and the stratospheric temperature are two independent assigned parameters, and the temperature profiles are then assumed to be adiabatic in the troposphere and constant in the stratosphere. Such assumed temperature profiles are adopted for the conventional estimation of the habitable zones (Kasting et al., 1993). More details regarding the temperature profiles for thin atmosphere

64

simulations can be found in Section 3.2.3.

After the photochemistry-thermochemistry simulation converges to a steady state, I compute synthetic spectra of the modeled exoplanet's atmospheric transmission, reflection and thermal emission with a line-by-line radiative transfer code developed based on the concept outlined by Seager and Sasselov (2000); Seager et al. (2000); Miller-Ricci et al. (2009); Madhusudhan and Seager (2009). Opacities are based on molecular absorption with cross sections computed from the HITRAN 2008 database (Rothman et al., 2009), molecular collision-induced absorption when necessary (Borysow, 2002), Rayleigh scattering, and aerosol extinction are computed based on the Mie theory (van de Hulst, 1981). The transmission is computed for each wavelength by integrating the optical depth along the limb path, as outlined in Seager and Sasselov (2000). The reflected stellar light and the planetary thermal emission are computed by the δ-Eddington 2-stream method (Toon et al., 1989).

The emergent spectrum of a terrestrial exoplanet can be significantly affected by aerosols and clouds in the atmosphere. The effect of aerosols and clouds on the emergent spectra is to mask molecular spectral features and confine the observable mass column of the gases of interest to that above the aerosol and cloud layer (e.g. Seager, 2010). The effect of potential cloud layers on the remote sensing of an Earth-like atmosphere has been studied by Des Marais et al. (2002). In my model, I include the contribution of opacities from photochemical aerosols, the concentration of which are calculated in the photochemistry model, in the computation of synthetic spectra. However, water clouds in the atmosphere of a planet having oceans will have highly variable vertical and horizontal distribution (i.e., weather), and this distribution that determines the overall radiative effects of water clouds cannot be treated with my one-dimensional model. Therefore, it is important to additionally consider the presence of water clouds for the atmospheres in which water is expected to condense. A temporary solution, demonstrated by Des Marais et al. (2002), is to include a cloud layer at the lowest-temperature altitude for a fraction of the planet (e.g., 50%) in the calculation of the synthetic spectra.

2.3 Model Testing

The photochemistry-thermochemistry model is applicable to the low pressures where photochemistry dominates, the intermediate pressures where vertical transport dominates, and the high pressures where thermochemical equilibrium dominates. I have tested the model in these three pressure regimes as follows.

For the high-pressure regime where thermochemical equilibrium dominates, I have confirmed that the kinetic model that balances all forward and reverse reactions gives identical results compared with direct minimization of the global Gibbs free energy. This straightforward mathematical validation implies that the calculation of reverse reaction rates is correct and the model is applicable for the regime of thermochemical equilibrium.

For the intermediate- and low-pressure regimes in which photochemical processes or vertical transport are important, direct mathematical validation for the model is not possible, because the steady-state solution is unknown. Instead, I seek to test my model by reproducing the results of planetary observations.

First, for the low-pressure regime where photochemical processes dominate, I have tested the photochemistry model by computing atmospheric compositions of current Earth and Mars. For Earth's atmosphere, my photochemistry model produces mixing ratios for ozone and important carbon and nitrogen species that are consistent with mid-latitude observations. In particular, for O_3 and CH_4, the model predictions are within the scatter ranges of spacecraft measurements of these gases in about 15 days that span 40 degrees in latitude (Figure 2-2). Also for Earth's atmosphere, my photochemistry model, using the globally averaged emission rates of trace gases as the input parameters, predicts the steady-state amounts of these gases (e.g., OH, CO, H_2S, SO_2) near the surface that are consistent with our knowledge of Earth's troposphere. For Mars, my photochemistry model predicts the amounts of long-lived and vertically well mixed species (O_2 and H_2) that are consistent with latest observations, confirming the odd hydrogen-driven stability of Mars's atmosphere. The model predictions are within the uncertainties of latest observational constraints. These re-

sults indicate that the photochemistry model provides an adequate description of the photochemical processes in the thin atmospheres on Earth and Mars.

Second, for the intermediate-pressure regime in which vertical transport dominates, I have simulated the atmosphere of Jupiter and the atmosphere of the most well-characterized hot Jupiter, HD 189733b, to compare with observations. In particular, the photochemistry-thermochemistry model predicts the mixing ratio of CO in the deep atmosphere of Jupiter that is consistent with the latest observation, reproducing the well known transport-driven enhancement of CO for Jupiter.

2.3.1 Transport-Only Model for an Earth-like Atmosphere

As a test of the transport-related schemes in the photochemistry model, I first consider a transport-only case. In theory, for species whose removal timescales are significantly larger than their transport timescales, such as CO_2 in Earth's atmosphere, their mixing ratios do not change with altitude, i.e., they are well-mixed.

I deliberately turn off the chemical network and compute a model using Earth's temperature profile to test the eddy diffusion transport, molecular diffusion transport, condensation, and rainout schemes of my chemical-transport model. A valid transport model should preserve hydrostatic equilibrium, predict well mixed mixing ratios for long-lived species, and predict a mixing ratio gradient for species that is rapidly removed in the atmosphere. I have verified that the transport scheme, although written in terms of number density rather than mixing ratio, preserves hydrostatic equilibrium. The fact that the code maintains hydrostatic equilibrium indicates that the transport scheme is numerically correct. I verify that long-lived species are well mixed, such as CO_2 throughout the atmosphere, as shown in Figure 2-1. I assign a mixing ratio for CO_2 at the surface and the code is able to predict a well-mixed vertical profile. I also verify that for H_2 molecular diffusion tends to increase the mixing ratio when the molecular diffusion coefficient is comparable with the eddy diffusion coefficient (i.e., the homopause; see Figure 2-1). With a diffusion-limited escape, the effect of molecular diffusion and the effect of escape on the H_2 vertical profile near the homopause largely cancel out (Figure 2-1), consistent with the definition of

diffusion-limited escape. I also show the behavior of H_2S, a poorly mixed species, to compare with well-mixed CO2. In this simplified model the only way to remove H_2S is photolysis, which requires photons with wavelengths shorter than 260 nm. Most of the photons in this wavelength range are effectively shielded by the major species O_2, so that removal rate of H_2S by photolysis near the surface is smaller than that in the stratosphere (see Figure 2-1).

Water vapor content in a rocky exoplanet's atmosphere is controlled by the water reservoir at the planetary surface, vertical transport, and condensation. In the photochemistry model, the mixing ratio of water vapor at the surface is assigned according to appropriate temperature-dependent relative humidity. Water vapor can be transported up into the atmosphere by eddy diffusion, and as the temperature decreases the atmosphere may become supersaturated in water as the altitude increases. For an Earth-like planet atmosphere, it is appropriate to assume a water vapor mixing ratio of 0.01 at the surface (which corresponds to a relative humidity of about 60%). The condensation scheme becomes effective when water vapor is supersaturated, which keeps the water vapor profile along the saturation profile. Such an approach to computing the atmosphere water vapor content is commonly adopted by other previously described photochemistry models of terrestrial planets (e.g. Nair et al., 1994; Yung and Demore, 1999; Zahnle et al., 2008).

The one-dimensional transport model tends to saturate the tropopause and over-predict the amount of water vapor in the stratosphere. In fact, when using the US Standard Atmosphere 1976 as the temperature profile, the tropopause temperature is 217 K, much warmer than the required "cold trap" temperature (~ 200 K) in order to maintain a dry stratosphere (water vapor mixing ratio in a few ppm). Common 1-D transport-condensation schemes may over-predict the amount of water vapor above the cold trap by a few orders of magnitude, and therefore over-predict the strength of HO_x cycle in the stratosphere. This is a well known problem in modeling Earth's atmosphere, mainly due to spatial and temporal variability of tropopause temperatures (K. Emmanuel, 2012, private communication). Tropospheric convection is most effective in transporting water vapor in tropics, where the tropopause temperature

68
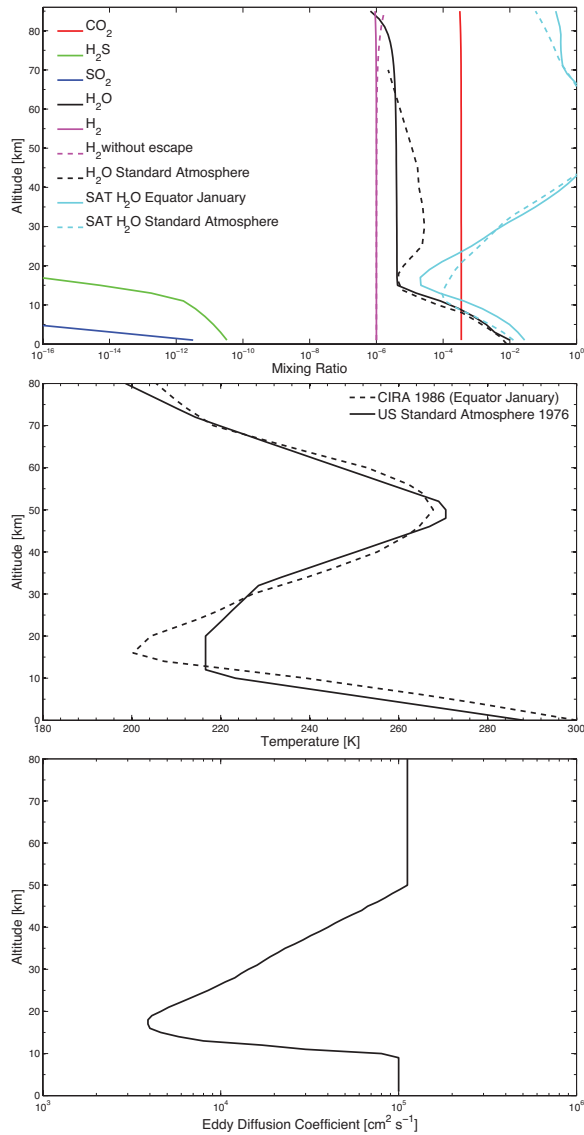
Figure 2-1: Numerical tests of the transport and condensation schemes of the photochemistry code. Only vertical transport via eddy diffusion, molecular diffusion (for H_2 only), dry deposition, wet deposition, condensation of water vapor, diffusion-limited escape of H_2, and photolysis of CO_2, H_2O, H_2, SO_2 and H_2S are considered for an Earth-like atmosphere. I omit all chemical kinetics to exclusively test the transport-related schemes. H_2S and SO_2 are the only sulfur compounds in this test and they are considered as removed once photo-dissociated or deposited. The atmosphere has the temperature-pressure profile of COSPAR International Reference Atmosphere (CIRA) 1986 at the equator in January, as shown by the dashed line on the middle panel, and major constituents of 20% O_2 and 80% N_2. Also on the middle panel I plot the temperature profile of US Standard Atmosphere 1976 for comparison. I adopt the eddy diffusion coefficient empirically derived from vertical profiles of trace gases (Massie and Hunten, 1981), shown in the lower panel. The boundary conditions are set as follows: CO_2 mixing ratio at the surface 350 ppm; H_2O mixing ratio at the surface 0.01; H_2 mixing ratio at the surface 1 ppm; SO_2 surface emission flux 9.0×10^9 cm^{-2} s^{-1}; H_2S surface emission flux 2.0×10^8 cm^{-2} s^{-1}. Water vapor in the atmosphere is limited by condensation. Steady-state mixing ratios are shown on the left panel, and the solid and dashed lines for H_2 show the situations with and without escape. Light blue lines on the left panel are saturation mixing ratios of water vapor with two temperature profiles. I verify that long-lived species, such as CO_2, are well-mixed in the atmosphere.

is the lowest and the number density of water vapor at the tropopause is the lowest compared with other latitudes. It is therefore likely that the tropopause is highly unsaturated as a global average. I reproduce the correct mixing ratio of water vapor at the cold trap (i.e., 4 ppm at ~ 20 km in the middle latitudes) by using a temperature profile of the equatorial region in January and limiting the water vapor saturation ratio to within 20% (Figure 2-1). The classic Manabe-Wetherald relative humidity profile for 1-D photochemistry models of Earth's atmosphere also has 20% relative humidity at the tropopause (Manabe and Wetherald, 1967).

As a result of water vapor condensation and rain, soluble gases are removed from the atmosphere by wet deposition (rainout). One should expect to see a decreasing slope in mixing ratio of the species being rained out, which depends on the rainout rate, itself dependent on the solubility of the species. For example, SO_2 is much more soluble than H_2S, so that SO_2 is more effectively rained out in the troposphere and cannot accumulate in the troposphere (see Figure 2-1).

2.3.2 Present-Day Earth

I compute a photochemical model to simulate the present-day Earth's atmosphere, and compare my results with mid-latitude observations. I focus on comparing with mid-latitude observations because (1) for long-lived species the mid-latitude abundances tend to represent the global means due to meridional mixing (Brasseur and Solomon, 2005); (2) for short-lived species the atmosphere in the middle latitudes resembles to the greatest degree the temperatures and the solar angle assumed for the one-dimensional model.

The purpose of this comparison is to verify that the photochemistry model adequately describes the key photochemical processes in Earth's atmosphere. The most important photochemical process in Earth's atmosphere is formation of the ozone layer, which leads to the temperature inversion in the stratosphere (e.g. Seinfeld and Pandis, 2006). Another important process is the coupled hydrological cycle and surface emission and deposition of CH_4, NO_x (i.e., NO and NO_2) and SO_2 that controls the tropospheric chemistry. Therefore, the reproduction of the composition of current

Earth's atmosphere is a comprehensive test of various aspects of the photochemistry model.

Molecular Composition

I model the atmosphere on Earth from 0 to 86 km altitude as 43 equally spaced layers, starting with a nominal 80% N_2 and 20% O_2 composition and a well-mixed CO_2 of 350 ppm. I adopt the temperature profile of the 1976 US Standard Atmosphere, and fix the water vapor mixing ratios below 20 km to the water vapor content of the 1976 US Standard Atmosphere (Seinfeld and Pandis, 2006). The water vapor mixing ratios above 20 km are computed by the photochemistry model. The resulting water vapor profile has a mixing ratio of 7.8×10^{-3} at the surface, 4 ppm at 20 km, and 7 ppm at 50 km, resembling the typical water vapor profile in the middle latitudes (e.g. Jucks et al., 1998). The eddy diffusion coefficient is adopted from Massie and Hunten (1981), who have derived it from vertical profiles of trace gases including CH_4 and N_2O. I enhance the eddy diffusion coefficient in the troposphere of Massie and Hunten (1981) by a factor of 3 to improve mixing in the troposphere. The incoming solar radiation is cut off for wavelengths shorter than 100 nm to account for the thermosphere absorption. The photolysis rates at the top of the atmosphere are tabulated in Table A.2. Key trace species are assigned emission rates from the surface according to typical global values (Seinfeld and Pandis, 2006). Emission rates and dry deposition velocities of these species are tabulated in Table 2.2. Results of the photochemistry model in comparison with observations are shown in Table 2.2, Figure 2-2, and Figure 2-3.

My models adequately simulate the photochemical processes in Earth's stratosphere. First, formation of the ozone layer is correctly predicted. The modeled vertical distribution of O_3 is consistent with the low- and mid-latitude measurements by the Halogen Occultation Experiment (HALOE), as shown in Figure 2-2. The modeled ozone profile is well within the scatter ranges for observations spanning about 15 days covering latitudes from -10° to -50°. The model over-predicts the amount of O_3 at 70 km by a factor of about two, which may be an effect of meridional transport.

Table 2.2: Test of the photochemistry model for Earth's atmosphere. For the surface emission and dry deposition velocities, measured surface mixing ratios are compared to the photochemistry model results.

Species	Surface Emission[a] (molecule cm^{-2} s^{-1})	V_{DEP} (cm s^{-1})	Surface Mixing Ratio Measured[e]	Modeled
CO	3.0×10^{11}	1.2×10^{-4}[b]	40-200 ppb	175 ppb
CH$_4$	1.3×10^{11}	0.002[b]	700-1745 ppb[f]	1607 ppb
NH$_3$	7.7×10^9	1[d]	0.1-10 ppb	0.1 ppb
N$_2$O	1.0×10^9	0[b]	276-315 ppb[f]	317 ppb
NO	7.0×10^9	0.016[b]	0.02-10 ppb[g]	0.03 ppb
SO$_2$	9.0×10^9	1[c]	30-260 ppt	160 ppt
OCS	5.0×10^7	0.01[d]	510 ppt	200 ppt
H$_2$S	2.0×10^8	0.015[c]	1-13 ppt	7.1 ppt
H$_2$SO$_4$	7.0×10^8	1[d]	5-70 ppt[h]	4.0 ppt[h]

[a] Typical globally averaged emission rates are taken from Seinfeld and Pandis (2006).
[b] Typical dry deposition velocities are taken from the compilation of Hauglustaine et al. (1994).
[c] Typical dry deposition velocities are taken from the compilation of Sehmel (1980).
[d] Dry deposition velocities are assumed by considering the solubility and reactivity of gases (see Appendix B.3).
[e] Mixing ratios at the surface are taken from Seinfeld and Pandis (2006).
[f] Ranges are from the preindustrial mixing ratio to the present-day value.
[g] Ranges are mixing ratio of NO$_x$ at the planetary boundary layer.
[h] Mixing ratio of SO$_4^{2-}$ in both gaseous and aqueous phases.
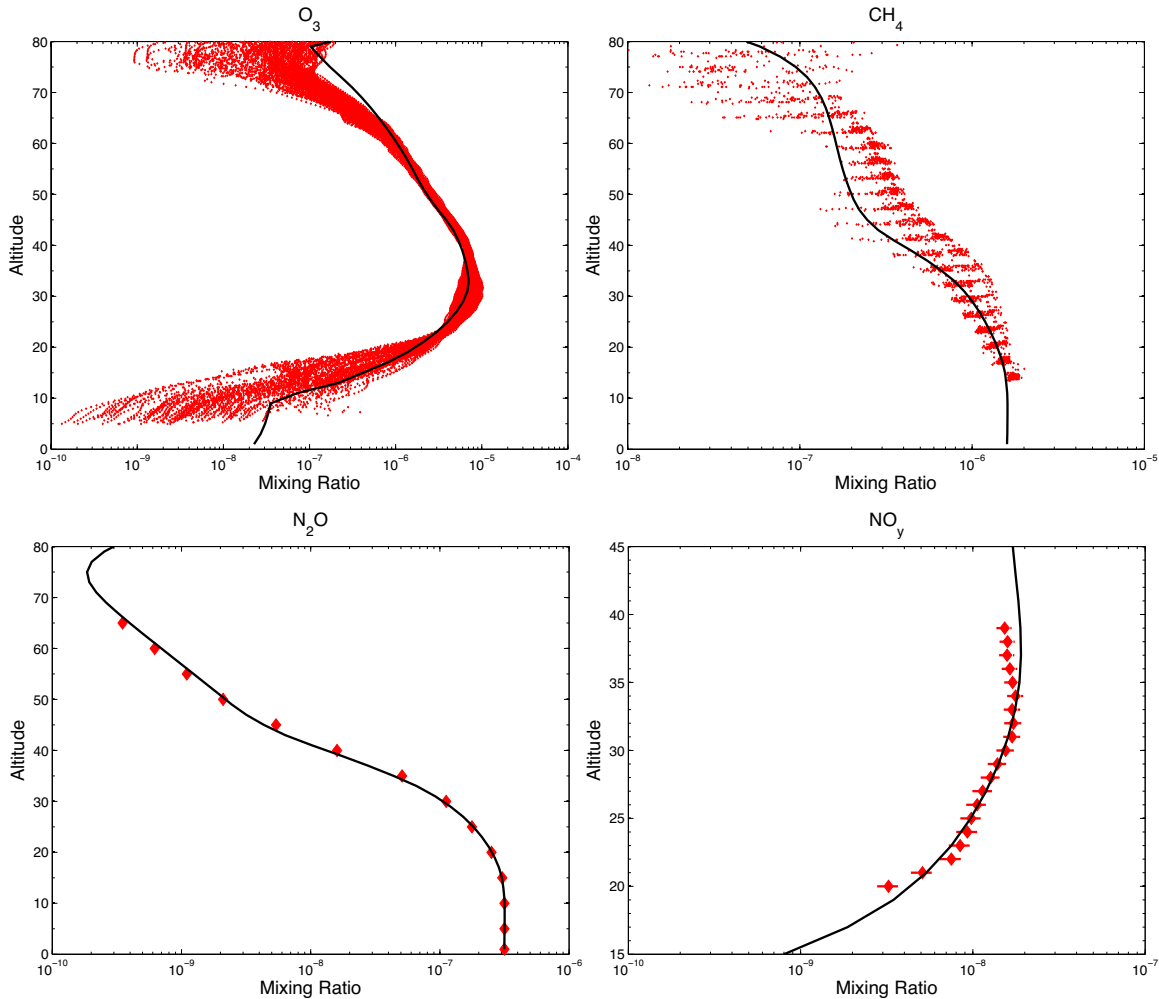
Figure 2-2: Mixing ratio profiles of ozone and important carbon and nitrogen species in Earth's atmosphere predicted by the photochemistry model in comparison with observations (red dots). The input parameters of the photochemistry model is described in the text and Table 2.2. CH_4, N_2O, and NO_y are selected because they have lifetimes of years in the lower stratosphere and days in the upper stratosphere, which makes them ideal tracers to test the one-dimensional model. The observation data for comparison are: (1) a large number of vertical distribution profiles for O_3 and CH_4 measured by the Halogen Occultation Experiment (HALOE) on the Upper Atmosphere Research Satellite (UARS) spacecraft (Russell et al., 1993) in April, 2005 over latitudes of 10°-50° in the southern hemisphere; (2) globally averaged mixing ratios of N_2O compiled by Massie and Hunten (1981); (3) mixing ratios of NO_y from balloon observations at the latitude of ∼35°N in September, 1993 (Sen et al., 1998). My photochemistry model is able to predict the correct abundances for O_3 and globally distributed species including N_2O, CH_4, and NO_y in Earth's atmosphere.
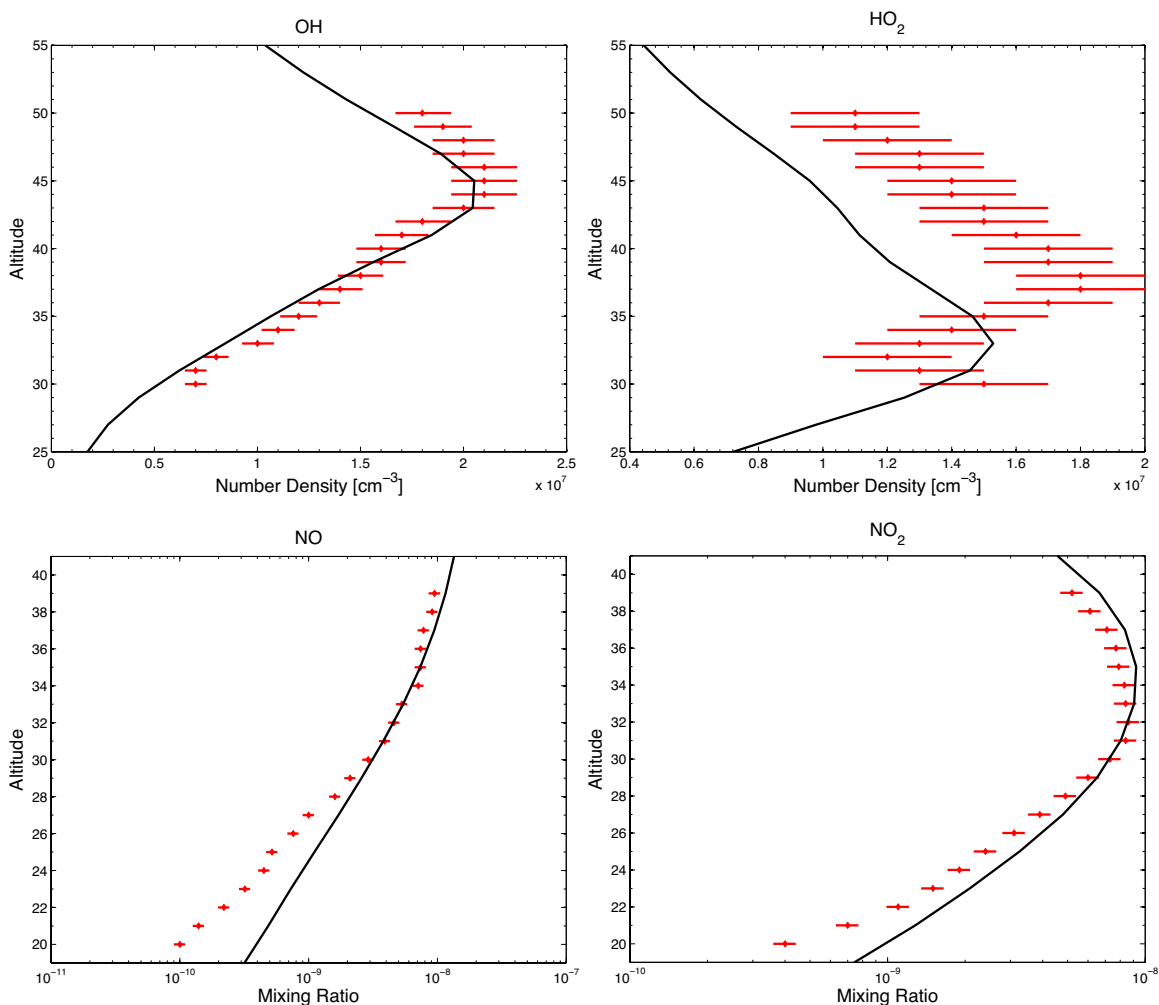
Figure 2-3: Mixing ratio profiles of important short-lived radicals in Earth's stratosphere predicted by the photochemistry model in comparison with observations. The photochemistry model is the same model shown in Table 2.2 and Figure 2-2, except that for HO_x species, the photochemistry model is re-run without the 0.5 factor in the photolysis rate calculation (Eq. 2.13) because the observations were taken during the daytime and HO_x has lifetimes of less than 1 minute in the stratosphere. The data shown on the figure are: (1) number densities of OH and HO_2 from balloon observations in Fairbanks, AK in 1997 (Jucks et al., 1998); (2) mixing ratios of NO and NO_2 from balloon observations at the latitude of $\sim$35°N in 1993 (Sen et al., 1998). Despite the one-dimensional nature of my photochemistry model, it predicts the amounts of short-lived species in the stratosphere roughly consistent with mid-latitude observations.

Second, for important carbon and nitrogen species in the stratosphere that have life-times longer than 1 day, including N_2O and CH_4, and the odd nitrogen family NO_y[5], my model produces correct altitude gradient of their mixing ratios (Figure 2-2). The vertical distributions of these gases in the stratosphere are controlled by the competition between vertical mixing and removal by photolysis (for N_2O), reactions with OH and $O(^1D)$ (for CH_4), and rainout (for NO_y). The fact that the model prediction agrees with the mid-latitude or globally averaged observations indicates that the photochemistry model contains a correct account of these processes.

I also compare the modeled abundances of short-lived radicals in the stratosphere with mid-latitude observations (Figure 2-3). The lifetime in stratosphere is in the order of minutes for HO_x (OH and HO_2) and ranges from minutes to days depending on altitude for NO_x (NO and NO_2). Therefore, to compare with individual observations, *local* models rather than *global* models should be used. Still, I find that my global one-dimensional model is roughly consistent with typical observations of these short-lived species in the middle latitudes (Figure 2-3). The model under-predicts the amount of HO_2 by about 50% in the upper stratosphere, which remains an unsolved problem for standard photochemistry models (Jucks et al., 1998). The model over-predicts the amounts of NO and NO_2 in the lower stratosphere by a factor of two or three, which is due to the fact that I do not include chlorine species in the model but $ClONO_2$ is known to be an important reservoir of odd nitrogen in Earth's lower stratosphere (Brasseur and Solomon, 2005). Overall, the photochemistry model is able to simulate the key aspects of photochemical processes in Earth's stratosphere.

Turning to the troposphere, the key element of the tropospheric chemistry is the production of the hydroxyl radical OH, because OH is the major removal pathway for most species emitted from the surface. It has been established that OH in Earth's troposphere is produced by reactions between $O(^1D)$ and H_2O, and $O(^1D)$ is produced by photolysis of O_3 (Seinfeld and Pandis, 2006). In turn, the main source of tropospheric ozone is the NO_x cycle, with non-negligible effects of HO_x cycle and

---

[5]The odd nitrogen family NO_y is defined as the sum of N, NO, NO_2, NO_3, N_2O_5 (2 times), HNO_3, and HNO_4.

hydrocarbon chemistry as well. The photochemistry model predicts that the surface ozone mixing ratio is 20 ppb, and the surface OH number density is 7.5×10^5 cm^{-3}, very close to the commonly accepted OH number density of 1.0×10^6 cm^{-3}. I also confirm that the steady-state mixing ratios of major trace gases near the surface are consistent with ground measurements (see Table 2.2). The main removal mechanism of CO, CH$_4$, and NH$_3$ is through reactions of OH, and N$_2$O is long-lived in the troposphere and is transported up to the stratosphere. Considering the significant spatial and temporal variability of the amount of OH, I conclude that the photochemistry model correctly computes the chemistry in Earth's troposphere.

The photochemistry model also correctly treats the sulfur chemistry in Earth's atmosphere (see Table 2.2). Most of sulfur-bearing emission, if not deposited, is oxidized in multiple steps in the troposphere and eventually converted into sulfate. Sulfite (S^{4+}) and sulfate (S^{6+}) are soluble in water and effectively removed from the atmosphere by rainout. The photochemistry models simulate these processes, and find steady-state mixing ratios of sulfur-bearing species (e.g., H$_2$S and SO$_2$) consistently with the ground measurements. The models also predict the saturation of sulfate and the formation of sulfate aerosols as expected. The modeled mixing ratio of sulfate is slightly lower than tropospheric observations. Additional numerical tests reveal that the steady-state mixing ratio of sulfate is sensitive to the specific parameterization of rainout.

Transmission and Reflection Spectra

Using the molecular composition of Earth's atmosphere given by the photochemistry model, I simulate the transmission and reflection spectra of Earth and compare them with observation spectra from a lunar eclipse (Pallé et al., 2009). My model is able to correctly predict the main features of water vapor in near-infrared low-resolution spectra of Earth (Figure 2-4). There is a mismatch of band-center location for the water band at 1.4 μm between the modeled reflection spectrum and the observed reflection spectrum, but this mismatch does not exist between the modeled transmission spectrum and the observed transmission spectrum. The O$_2$ absorption at 760 nm
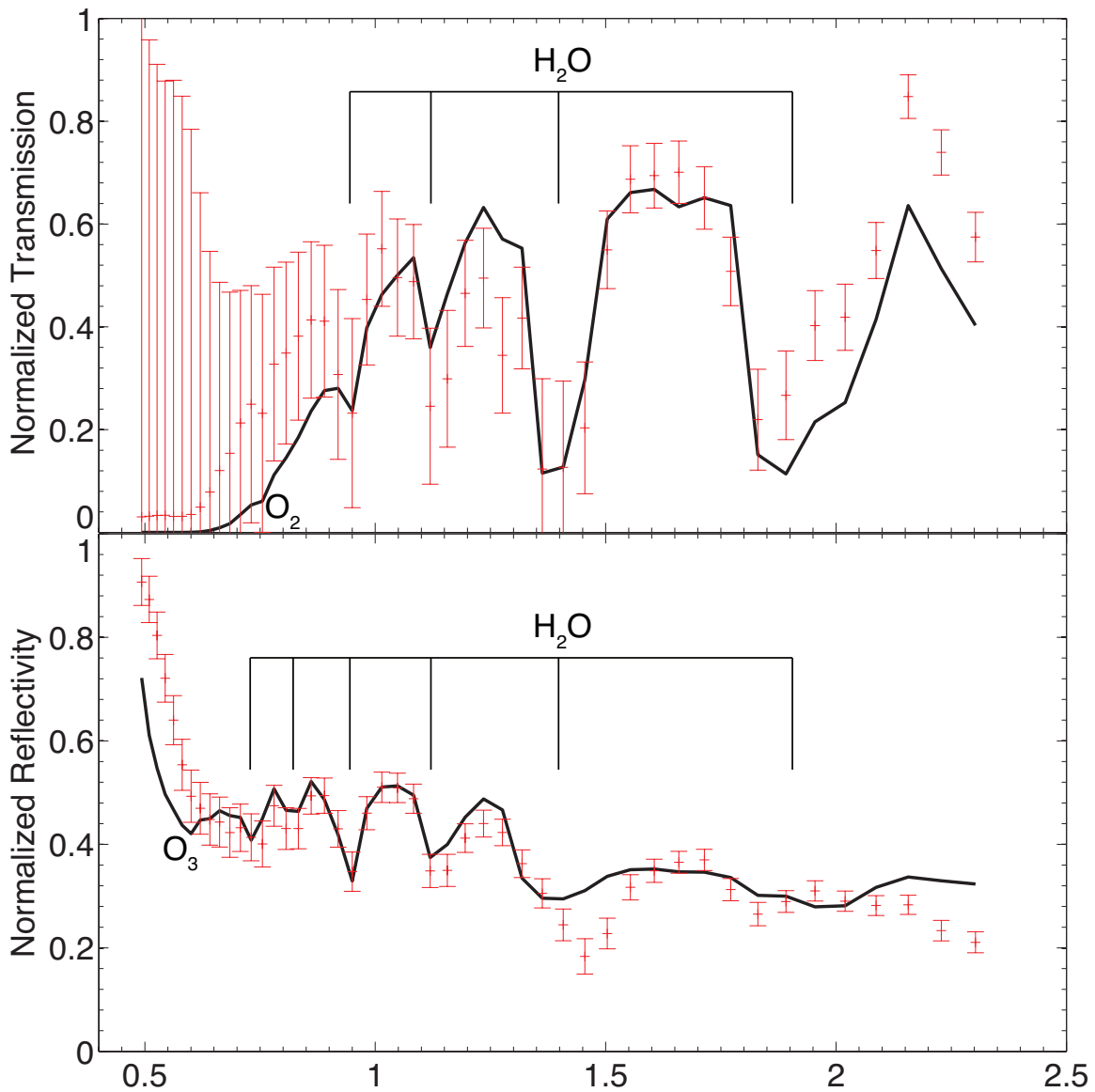
Figure 2-4: Modeled Earth's transmission and reflection spectra in comparison with observation spectra from a lunar eclipse. The observation spectra shown in red are from the lunar eclipse observations of Pallé et al. (2009). High-resolution spectra are binned down to a spectral resolution of 30 to mimic future terrestrial exoplanet observations. The error bars are assigned by assuming a signal-to-noise ratio of 20 for the highest flux band and scaling for other bands according to the photon noise limit. Observations with similar quality can be expected for an Earth-like exoplanet around a nearby M dwarf star with *JWST* (Belu et al., 2011). The modeled spectra are based on the simulated molecular composition of Earth's atmosphere. The transmission spectrum is calculated for the light rays that have tangent altitudes between 0 and 11 km, to be roughly compared with the measurements by the lunar eclipse (see García Muñoz et al., 2012, for a detailed discussion of the geometry of lunar eclipse observations of Earth spectra). The reflection spectrum is calculated by the $\delta-$Eddington 2-stream approximation. My photochemistry model and radiative-transfer model are able to predict the main features in the transmission and reflection spectra of Earth. Remaining discrepancies are discussed in the text.

is deep and narrow in the high-resolution transmission spectrum (Pallé et al., 2009), but the spectral contrast will be greatly reduced at low resolutions, as predicted by my model (Figure 2-4).

There are some discrepancies between my calculation and the Earth spectra obtained from the lunar eclipse. At short wavelengths, the lunar eclipse spectra show greater Rayleigh scattering features than the modeled spectra (Figure 2-4). Also, the modeled reflection spectrum shows the Chappuis band of O_3 around 600 nm, but this feature is masked in the lunar eclipse spectrum probably by the strong Rayleigh scattering features extended over the entire visible wavelengths. This discrepancy may be due to the fact that the Earth spectra obtained from the lunar eclipse are based on the light rays refracted and bended by Earth's atmosphere, and these light rays contain more Rayleigh scattering contribution than straight light rays assumed in my model (García Muñoz et al., 2012). A detailed reproduction of the lunar eclipse spectra will have to involve tracking the refracted light rays in Earth atmosphere (García Muñoz and Pallé, 2011). At long wavelengths, the lunar eclipse spectra by Pallé et al. (2009) are somewhat puzzling. The observed spectra show that Earth's atmosphere is much more transparent in the K band than in the J band and H band, but the reflectivity of Earth in the K band is at a minimum (see Figure 2-4). I do not find an apparent explanation for the observed spectra at wavelengths longer than 2 μm. One potential issue of the lunar eclipse spectra is the inhomogeneous reflectivity of the lunar surfaces due to distribution of mafic minerals (see Chapter 5). The transmission spectrum from lunar eclipse observations relies on the ratio between reflection from a surface in umbra and reflection from another surface in penumbra, which will be sensitive to the lunar surface features if the two reflecting surfaces on the Moon are different, especially around 2 μm where absorption due to some surface minerals (i.e., pyroxene) can be strong.

To summarize, I test the photochemistry model by reproducing the chemical composition of current Earth's atmosphere (see Table 2.2 and Figure 2-2). The photochemistry model is successful in predicting the formation of the ozone layer, treating key chemical cycles in both the stratosphere and the troposphere, computing oxida-

tion of hydrocarbon and sulfur-bearing species in the troposphere, and transporting long-lived species from the troposphere to the stratosphere. These aspects involve all chemical kinetics, photolysis, and transport processes, which not only verify that the photochemistry model is suitable for applications in oxidizing atmospheres, but also allows my model to be applied to other atmospheric scenarios.

2.3.3 Present-Day Mars

I test the photochemistry model by simulating the atmospheric composition of present-day Mars. The current atmosphere of Mars is a thin CO_2-dominated atmosphere and its bulk chemical composition is known from extensive observations (see Krasnopolsky, 2006, and references therein). I test the photochemistry code by reproducing the observed mixing ratios of long-lived species CO, O_2, and H_2 (Table 2.3), and also comparing with previous model results regarding Martian atmosphere photochemistry. Key parameters and results of the present-Mars atmosphere model are shown in Table 2.3 and Figure 2-5.

For all long-lived photochemically produced species in Mars's atmosphere (CO, O_2, and H_2), my photochemistry model predicts a mixing ratio consistent with observed values (Table 2.3). In particular, for O_2, the model prediction is within the uncertainties of the latest observations (Table 2.3). The modeled mixing ratio of CO is somewhat lower than the observed value, but the discrepancy is less than $2 - \sigma$. For the species that are short-lived and have strong seasonal and latitudinal variation (H_2O_2 and O_3), my photochemistry model predicts a mixing ratio in the range of the observed variations (Table 2.3). I emphasize that it is important to use temperature-dependent UV cross sections for modeling the photolysis and UV penetration in the Martian environment (see Anbar et al., 1993, for an error analysis of temperature-dependence of CO_2 in the Martian atmosphere).

My photochemistry model reproduces the most important aspect of Martian atmospheric photochemistry: the stabilization of the CO_2 atmosphere by H, OH, and HO_2 (commonly referred to as odd hydrogens). Odd hydrogens, as catalysts, facilitate the recombination of photochemically produced CO and O_2 and maintain the CO_2

Table 2.3: Test of the photochemistry model for Mars's atmosphere. For the upper boundary flux and dry deposition velocities, measured mixing ratios of major trace gases on Mars are compared to the model predictions.

Species	Upper Boundary Flux[a] (molecule cm^{-2} s^{-1})	V_{DEP}[b] (cm s^{-1})	Column Averaged Mixing Ratio	
			Measured	Modeled
O_2	0	0	1400$\pm$200 ppm[c]	1545 ppm
CO	-2.0 $\times$ 10^7	0	980$\pm$150 ppm[d]	572 ppm
CO			800-1600 ppm[e]	
H_2	3.6 $\times$ 10^8	0	15$\pm$5 ppm[f]	23 ppm
H_2O_2	0	0.02	0 $\sim$ 40 ppb[g]	18 ppb
O_3	0	0.02	0 $\sim$ 120 ppb[g]	18 ppb

[a] H_2 upper boundary flux is computed from diffusion-limited escape velocity after finding the steady state. Besides tabulated values, influx of N of 2.0 $\times$ 10^6 molecule cm^{-2} s^{-1}, NO of 2.0 $\times$ 10^7 molecule cm^{-2} s^{-1}, and outflux of O of 2.0 $\times$ 10^7 molecule cm^{-2} s^{-1}, are considered as input to the model.

[b] Dry deposition velocity is assumed to be 0.02 for reactive species, including H, O, O(^{1}D), O_3, OH, HO_2, H_2O_2, CHO_2, CH_2O_2, CH_3O_2, CH_4O_2, NH_3, NO_3, N_2O_5, HNO_3, and HNO_4 (e.g. Zahnle et al., 2008). Dry deposition velocity is assumed to be zero for all other species.

[c] The global mixing ratio of O_2 is from *Herschel* observations by Hartogh et al. (2010b).

[d] The global mixing ratio of CO is from *Herschel* observations by Hartogh et al. (2010a).

[e] Strong seasonal and latitudinal variations of the CO mixing ratio are observed by Krasnopolsky (2007).

[f] This is the inferred mixing ratio of H_2 for altitudes below 100 km based on the observations of mixing ratios of H_2 for altitudes higher than 100 km, from Krasnopolsky and Feldman (2001).

[g] Data are taken from the compilation of Krasnopolsky (2006). Mixing ratios of O_3 and H_2O_2 have significant diurnal, seasonal and latitudinal variations.
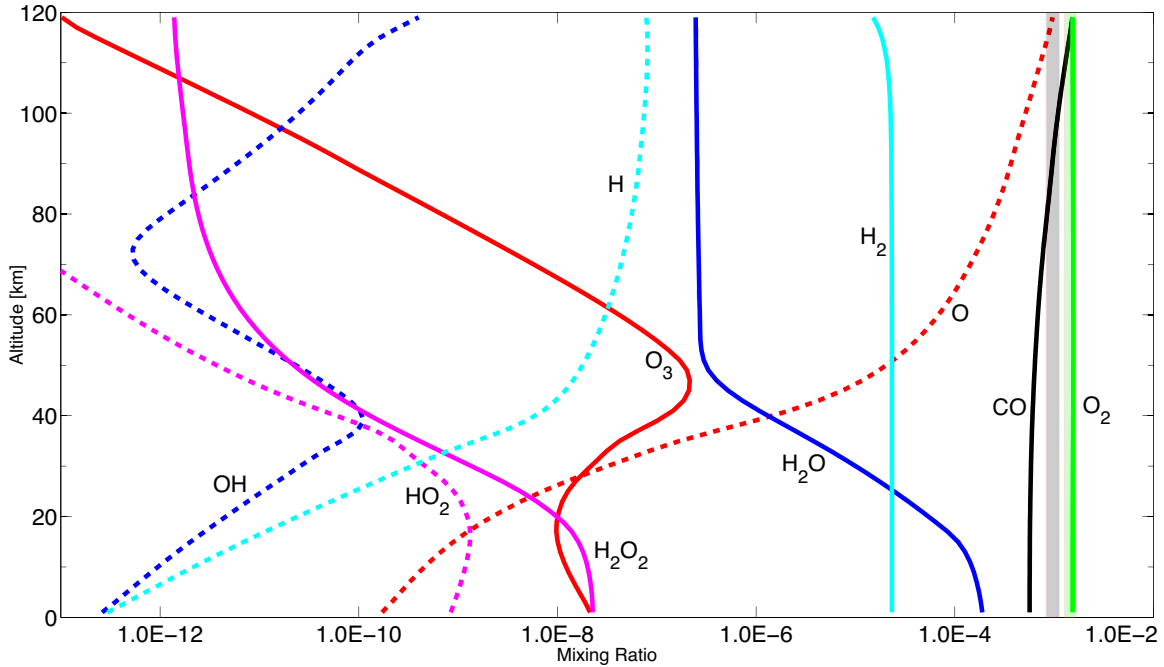
Figure 2-5: Profiles of key molecules in Mars's atmosphere predicted by the photochemistry model compared with observations. The constraints on the mixing ratios of O_2 and CO in Mars's atmosphere from the recent *Herschel* observations are shown by semi-transparent rectangles (Hartogh et al., 2010a,b). Note that the observational constraints are applied to the full atmospheric column, because no vertically resolved data are available. The chemical-transport model is computed with a 2-km grid from 0 to 120 km. For the photolysis rates, an unattenuated solar flux at 1.524 AU and a surface albedo of 0.1 are used, and the UV cross sections are computed at 200 K when their temperature dependencies are available from laboratory measurements. All C, H, O, N species and relevant reactions are computed. Termolecular reaction rates are multiplied by 2.5 to account for CO_2 being the third body (e.g. Zahnle et al., 2008). The eddy diffusion coefficient is assumed to have a profile as Equation (2.6) with $K_T = 10^6$ cm^2 s^{-1}, $K_H = 10^8$ cm^2 s^{-1} and $z_T = 20$ km. The atmospheric temperature profile is assumed to be the globally averaged profile as suggested by Zahnle et al. (2008): surface temperature 210 K, lapse rate of 1.4 K km^{-1} until 50 km and then isothermal of 140 km up to 120 km. The relative humidity at the surface is fixed at 0.19, and the water vapor is transported up into atmosphere by eddy mixing, limited by condensation. The maximum saturation of water vapor of 60% is imposed, which gives a column number density of 9.8 precipitable microns, corresponding to the observed water vapor content in Mars's atmosphere (e.g. Maltagliati et al., 2011). Wet deposition is reduced compared to Earth, with the rainout factor assumed to be 0.01 in the model. My photochemistry model reproduces the CO_2-stabilization effect by odd hydrogens in Mars's atmosphere, with the mixing ratios of O_2 and CO in rough agreement with the observed values.

dominance of the Mars' atmosphere (e.g. McElroy and Donahue, 1972; Nair et al., 1994; Krasnopolsky, 2006; Zahnle et al., 2008). A pure CO_2 atmosphere is unstable against photolysis, because CO_2 can only be restored with a slow three-body reaction $CO + O + M \longrightarrow CO_2 + M$ (e.g. Yung and Demore, 1999). Odd hydrogen species, including H, OH and HO_2, are produced by photolysis of water vapor; and trace amounts of odd hydrogens can effectively stabilize the CO_2-dominated atmosphere. Nonetheless, one-dimensional photochemistry models tend to over-address the problem, predicting amounts of CO, O_2 and O_3 several times smaller than the observed values (e.g. Nair et al., 1994; Krasnopolsky, 2006). By considering a slow dry deposition of H_2O_2 and O_3 to the surface, Zahnle et al. (2008) are able to predict the amount of O_2 that matches observations. I adopt the assumptions of Zahnle et al. (2008), and confirm the finding of appropriate amounts of O_2 (see Table 2.3 and Figure 2-5). I therefore reproduce the photochemical stability of the current Martian atmosphere. The modeled mixing ratio of CO is still somewhat lower than the observed value. Taking the face value, it is 40% lower. So the "overshooting" problem still persists to some extent.

The timescale of CH_4 removal can also be used for model testing. Rapid variation (over several years) of the amount of CH_4 in Mars' atmosphere has been reported (e.g. Mumma et al., 2009), but the modeling of coupled general circulation and gas-phase chemistry find no known gas-phase chemistry path that allow such a rapid removal (e.g. Lefèvre and Forget, 2009). Based on the fiducial model of Mars' atmosphere, the loss timescale for CH_4 is computed to be about 240 years, within the same order of the magnitude of Lefèvre and Forget (2009).

To summarize, I have tested the photochemistry model by reproducing the atmospheric compositions of current Earth and Mars. I find that the model gives consistent results compared to observations and previous photochemistry models. All physical and chemical processes that are important for molecular compositions in thin atmospheres, including photolysis, chemical reactions, transports, condensation, and deposition are rigorously tested in these examples.

2.3.4 Jupiter and Hot Jupiters

I have tested my photochemistry-thermochemistry model by simulating the C-H-O chemistry in the deep atmosphere of Jupiter. The most important feature in Jupiter's atmosphere that is relevant for this investigation is the enhancement of CO mixing ratio in the observable parts of the atmosphere due to vertical transport. My model correctly predicts this enhancement in comparison with the observed mixing ratio of CO (Figure 2-6). I have also compared the simulated CO mixing ratios with those of the latest model for Jupiter's deep atmosphere (Visscher et al., 2010) and found agreement within a factor of 2. The remaining discrepancy may be due to updated kinetic rates of several reactions that I have adopted. Compared with reaction rates used in Visscher et al. (2010); Moses et al. (2011), I found that the rates for reaction $CH_3O \longrightarrow CH_2O + H$ have updated recommended values and the discrepancy in these rates can account for the minor discrepancy in the $CO \rightleftharpoons CH_4$ conversion rates between my models and the models of Visscher et al. (2010). I have taken for this reaction the low-pressure limit rate from Baulch et al. (1994) and the high-pressure limit rate from Curran (2006); both recommended values are based on extensive literature reviews.

To test the $CO \rightleftharpoons CH_4$ conversion computation for a warmer planet than Jupiter, I have simulated the H_2-dominated atmosphere on hot Jupiter HD 189733b and compared my predictions with the molecular compositions derived from observations (Figure 2-7). I find agreement in the amounts of CH_4 and CO_2 at the pressure levels of 0.001-1 bar between my models and the interpretation of observations of Madhusudhan and Seager (2009). Due to limited data available for exoplanets including HD 189733b, the observational constraints on the molecular composition are poor. To further test my model, I have compared my results with a similar suite of simulations by Visscher and Moses (2011) and found agreement to within a factor of 2. The efficiency of vertical mixing affects the steady-state mixing ratios of methane and other hydrocarbons significantly in the observable parts of the atmosphere.

Furthermore, I have also compared my results with the main features of H_2-
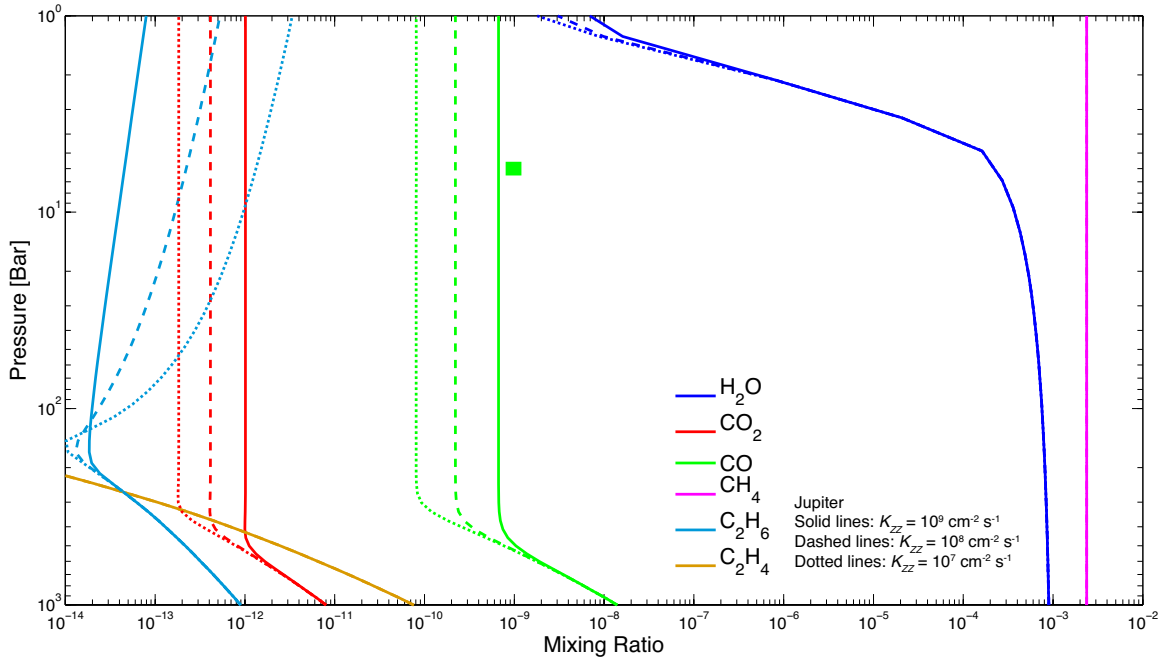
Figure 2-6: Modeled compositions of the deep atmosphere of Jupiter in comparison with observations. The mixing ratios of H_2O, CH_4, CO, CO_2, C_2H_6, and C_2H_4 are shown as a function of the atmospheric pressure, for eddy diffusion coefficients ranging from 10^7 to 10^9 cm^2 s^{-1} according to free-convection and mixing-length theories (Gierasch and Conrath, 1985; Visscher et al., 2010). The temperature profile is adopted from Galileo probe measurements and Cassini CIRS measurements (Seiff et al., 1998; Simon-Miller et al., 2006). The abundance of CH_4 is assigned to be consistent with measurements of the Galileo probe at pressure levels deeper than 10 bar (Wong et al., 2004), and the abundance of H_2O at the bottom is assigned to be the solar abundance. The computed mixing ratios of CO are compared with the measurements by high-resolution spectroscopy at 6 bar (Bézard et al., 2002, see thick horizontal bar on the figure). The model is able to predict reasonably well the degree of enhancement of CO in Jupiter's atmosphere due to vertical transport.
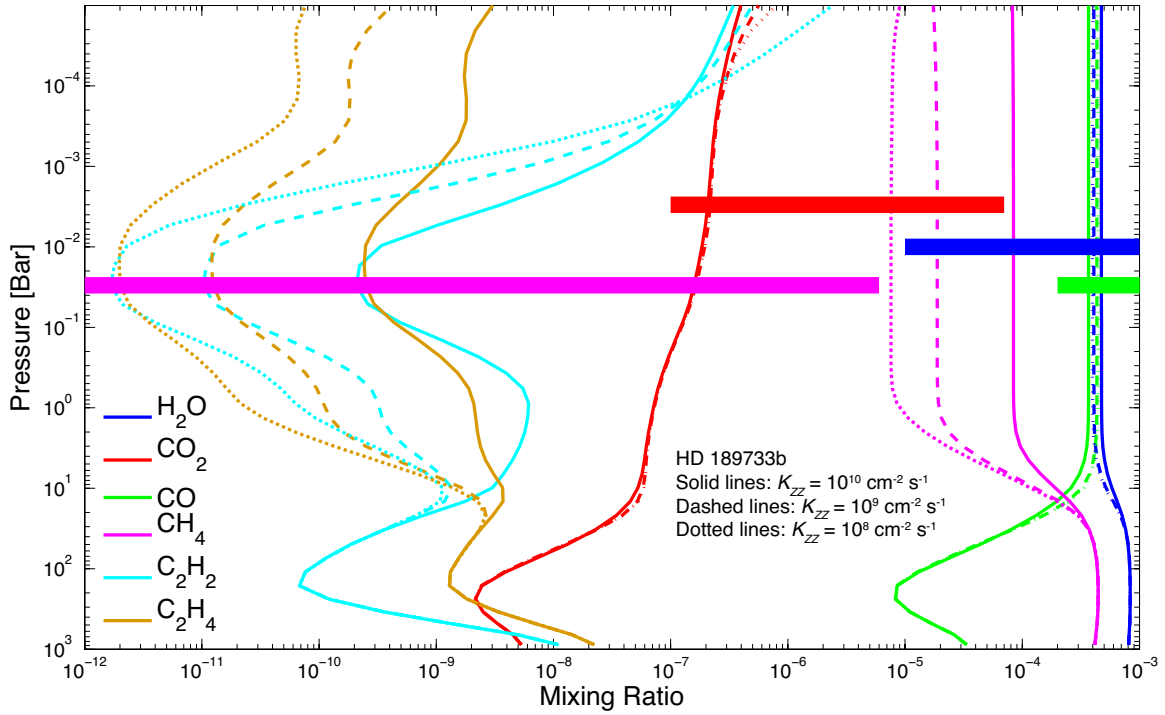
Figure 2-7: Mixing ratios of common molecules in simulated atmospheres of hot Jupiter HD 189733b. The mixing ratios of H_2O, CH_4, CO, CO_2, C_2H_2, and C_2H_4 are shown as a function of the atmospheric pressure for three eddy diffusion coefficients. The temperature profiles are the adopted dayside averaged temperature profiles in Moses et al. (2011) . The mixing ratios of H_2O, CH_4, CO, and CO_2 inferred from *HST* and *SPITZER* observations by (Madhusudhan and Seager, 2009) are shown with thick horizontal bars for comparison. The pressure levels at which these bars are placed are arbitrarily chosen within 10^{-3} - 1 bar for illustration. My simulations agree with the interpretation of observations for HD 189733b, and the upper limit of CH_4 mixing ratio could places an upper limit on the eddy diffusion coefficient of the planet.

dominated atmospheres simulated by Miller-Ricci Kempton et al. (2012) for super Earth GJ 1214b. For a solar elemental abundance, I simulate the steady-state atmosphere on GJ 1214b with C, H, O, N chemistry. My simulations compare nicely with Miller-Ricci Kempton et al. (2012) in both qualitative and quantitative behaviors of H_2O, CH_4, NH_3 and N_2. I also find photochemical HCN formation in the upper part of atmosphere, similar to Miller-Ricci Kempton et al. (2012). However, I find 1-order-of-magnitude higher concentration of HCN and 1-order-of-magnitude lower concentration of C_2H_2 and C_2H_4 than Miller-Ricci Kempton et al. (2012). This is probably because I have included a more complete set of chemical and photochemical reactions that allows the formation of C-N bond as Moses et al. (2011), and then a larger fraction of CH_3 from methane photolysis is converted into HCN instead of forming C_2H_2 and C_2H_4.

In summary, I have tested the photochemistry-thermochemistry model in the low-pressure regime in which photochemical processes dominate, the intermediate-pressure regime in which vertical transport dominates, and the high-pressure regime in which thermochemical equilibrium holds. The photochemistry-thermochemistry model is therefore suitable for exploration of molecular compositions in both thin and thick atmospheres on terrestrial exoplanets.

2.4   Uncertainties and Limitations of the Model

Despite the efforts to include as much fundamental physics as possible, the photochemistry-thermochemistry model remains partly empirical. The model replies on a large number of empirical parameters that can only be determined experimentally for a limited set of physical environments. Often in the exoplanet applications one has to extrapolate to the conditions for which these parameters have not been empirically studied before. Therefore, one should be aware of the inherited uncertainties of the photochemistry-thermochemistry model. I here list the most important sources of model uncertainties.

1. Uncertainties in the ultraviolet cross sections and photolysis quantum yields of some molecules, and their temperature dependencies. For example, the cross sections of CH_4, NH_3, and SO_2 have not been measured at temperatures significantly higher than the room temperature.

2. Uncertainties in the reaction rates. The chemistry of certain sulfur species and complex carbon species (Group IV and V in Table 2.1) are poorly understood. Many reactions involving short-lived species are only measured at the room temperature (see Table A.1). It is also possible that a reaction unimportant for Earth (therefore its rate is not measured) becomes important in a very different environment on exoplanets.

3. Uncertainties in the eddy diffusion coefficients. The eddy diffusion coefficients in the atmosphere of an exoplanet can only be estimated to the precision of several orders of magnitude based on limited understanding of heat transfer and flow patterns in the atmosphere.

4. Uncertainties in the atmospheric temperature-pressure profile. The temperature-pressure profile can be calculated by radiative transfer models; however, due to unknown components in the atmosphere, the temperature-pressure profile estimate can be off by several tens of K, if not greater.

5. Uncertainties in the dry deposition velocities. The dry deposition velocities depend on the surface properties of an exoplanet, which is unknown. Extrapolation based on the dry deposition velocities measured on Earth is often the only feasible solution.

6. Uncertainties in the aerosol formation mechanisms and precipitation processes. The particle shape and size of atmospheric aerosols will be more complex then what is assumed in this model. Notably, coagulation of particles, scavenging of particles by cloud droplets, and the three-dimensional distribution of clouds are not treated in this model. These factors will affect the radiative transfer in the atmosphere.

7. Uncertainties in the atmospheric escape rates. The atmospheric escape rates can range by many orders of magnitude for a planet depending on the X-ray and extreme ultraviolet flux of its parent star, and the escape rates may affect the composition of the upper atmosphere.

Besides the model uncertainties listed above, one fundamental limitation of the photochemistry-thermochemistry model is that the model approximates the atmosphere with one-dimensional plane-parallel geometry whereas three-dimensional processes may be important in real atmospheres. Transport in an atmosphere will have vertical and horizontal components and for some species the latitudinal, seasonal, and even diurnal variations are important (e.g. Seinfeld and Pandis, 2006). The one-dimensional model, when taking globally averaged temperature-pressure profile and radiation levels, provides a proxy to the globally average abundances for long-lived species (like CO, O_2, and H_2 in Mars's atmosphere). Also, the one-dimensional model can simulate the chemistry of very short-lived species when taking local temperature profiles and radiation levels (like OH and HO_2 in Earth's atmosphere). Nonetheless, the species that have chemical lifetime comparable to the atmospheric advection timescale can be significantly affected by the horizontal flows in the atmosphere (e.g. Brasseur and Solomon, 2005). Identifying these species with the one-dimensional model, however, will help motivate further efforts to couple the one-dimensional model to the general circulation model.

Albeit the uncertainties and limitations, the photochemistry-thermochemistry model will be effective in providing physical insights for understanding exoplanet atmospheres. Due to limited spectral resolution, near-future observations of exoplanet atmospheres will only provide order-of-magnitude constraints on the mixing ratios of atmospheric trace gases. The photochemistry-thermochemistry model will most likely to be incurred when a certain gas is found to be out of equilibrium by several orders of magnitude. In this case, the interplay of chemical network, vertical transport, and radiative transfer simulated by the one-dimensional photochemistry-thermochemistry model will be very useful to explain the new phenomenon. Another area in which the photochemistry-thermochemistry model will be useful is to predict molecular

components that can be expected for terrestrial exoplanet atmospheres. This kind of investigation includes the order-of-magnitude estimate of chemical lifetimes of species of interest in wide ranges of atmospheric scenarios, the order-of-magnitude quantification of required surface emission flux for a biosignature gas candidate to build up in the atmosphere, and the predication of the first-order chemical phenomena that could occur in terrestrial exoplanet atmospheres.

One should also realize that understanding the atmosphere on an exoplanet will be a process that takes multiple steps. As more observations are accumulated, and perhaps more experimental studies are carried out motivated by first-order photochemistry modeling, the ability to simulate the atmospheres on terrestrial exoplanets using the current framework will be improved. Such improvement has been constantly occurring for the study of Earth's atmosphere and in some limited ways for the study of Solar System planet's atmosphere. In some cases, observations and photochemistry modeling together will help to put new constraints on empirical parameters (e.g., reaction rates) in the model (see Nair et al., 1994, for an example of improving photochemistry models for Mars's atmosphere). The photochemistry-thermochemistry model will serve as a pivotal tool to ultimately understand the physics and chemistry in exoplanet atmospheres.

Chapter 3

Thin Atmospheres on Terrestrial Exoplanets

3.1 Background

Terrestrial exoplanets with thin atmospheres are important because those planets hold the most interest on the path to finding and characterizing planets that might harbor life. The concentrations of trace gases in thin atmospheres on terrestrial exoplanets are controlled by the component gas emission from the surface and subsequent sinks in the atmosphere (chemical reactions initiated by UV photolysis). Even with a trace amount, some gases may leave significant footprints in the planet's spectra, for instance H_2O, CO_2, and O_3 in Earth's atmosphere. In contrast to giant exoplanets where the atmospheric composition is mainly controlled by the elemental abundance, the steady-state compositions of terrestrial exoplanets' thin atmospheres are mainly controlled by photochemical processes. For thin atmospheres, the photochemistry-thermochemistry model reduces to a photochemistry model.

In this chapter, I use the comprehensive photochemistry model to explore chemical compositions of terrestrial exoplanet thin atmospheres, ranging from reducing to oxidizing, with all key non-equilibrium processes taken into consideration, including photolysis, chemical kinetics, vertical diffusion of molecules, atmospheric escape, dry and wet deposition, and condensation and sedimentation of concern condensable

species. The goal is to make use of the atmospheric chemistry model to quantify the link between the fundamental unknowns (e.g., geological sources, biological sources, mixing rates, and escape rates) and the observables (e.g., abundances of trace gases and their spectral signatures).

3.2 Exoplanet Benchmark Scenarios

I now present three benchmark atmospheric scenarios of rocky exoplanets and summarize the effects of key photochemistry processes. The goal is to provide baseline models to assess the stability of molecules in different kinds of atmospheres in order to: identify the dominant stable molecules; calculate the lifetime of spectrally significant gases; and identify the amounts of the main reactive species that control molecule lifetimes. The benchmark cases are also intended to serve as the test cases for independent photochemistry models for rocky exoplanet atmospheres.

The key to assess molecular stability is the oxidation power of the atmosphere - the ability to reduce or oxidize a gas in the atmosphere. The main reactive species are linked to the oxidation power of the atmosphere. In an oxidizing atmosphere, OH and O are created by photochemistry and are the main reactive radicals. In a reducing atmosphere, H, also created by photochemistry, is the main reactive species. Although it is expected that the atmospheric composition of exoplanets will be highly varied, based on the nearly continuous range of masses and orbits of exoplanets, the primary dimension of chemical characterization for terrestrial exoplanet atmospheres shall be their oxidation states. The redox power, in turn, is controlled by both the main component in the atmosphere (e.g., H_2, N_2, and CO_2) and the surface emission and deposition of trace gases (i.e., H_2, CH_4, and H_2S), as shown in Table 3.1. In the extreme cases of the atmospheric redox state, i.e., the H_2-dominated atmospheres and the O_2-rich atmospheres, the atmospheric redox power is surely reducing or oxidizing for a wide range of surface emission or deposition. However, for an intermediate redox state, the atmosphere would be composed of redox-neutral species like N_2 and CO_2, and the redox power of the atmosphere can be mainly controlled by the emission

Table 3.1: Redox power of atmospheres on rocky exoplanets

Type	Main Component	Redox Power	Reactive Species	Solar-System analogs	Note
Reduced	H_2, CO	Reducing	H	None	H_2-dominated atmospheres can be both reducing and oxidizing for very high CO_2 emission rates (Section 3.3).
Oxidized	N_2, CO_2	Weakly reducing	H, OH, O	None	The redox power is mainly controlled
		Weakly oxidizing	H, OH, O	Mars, Venus	by the surface emission of trace gases.
Oxic	O_2	Highly oxidizing	OH, O	Earth	

and the deposition fluxes of trace gases from the surface. The higher the emission of reducing gases is, the more reducing the atmosphere becomes.

For the benchmark cases, I have chosen three endmembers in terms of atmospheric oxidizing power. The scenarios are a reducing ($90\% H_2$-$10\% N_2$) atmosphere, a weakly oxidizing N_2 atmosphere ($> 99\% N_2$), and a highly oxidizing ($90\% CO_2$-$10\% N_2$) atmosphere. In this section I consider Earth-like volcanic gas composition that consists of CO_2, H_2, SO_2, CH_4, and H_2S, with emission rates comparable to current Earth. I also assume that the planet surface has a substantial fraction of its surface covered by a liquid water ocean so that water is transported from the surface and buffered by the balance of evaporation/condensation. Key assumptions of the parameters of the three atmospheric scenarios are summarized in Table 3.2 and rationals of important model parameters are given later in § 3.2.3.

I now describe the key results of the three atmosphere scenarios, for the 1-bar atmosphere on an Earth-size and Earth-mass habitable rocky exoplanet around a Sun-like star. I also describe qualitatively the behaviors of the atmospheres in the habitable zone of a quiet M dwarf, based on my numerical explorations. Mixing ratios of emitted gases, photochemical products, and reactive species in the three scenarios are tabulated in Table 3.3 and shown in Figure 3-1. Schematic illustrations of key non-equilibrium processes in the three scenarios are shown in Figure 3-2. I start with a qualitative overview of the key results, and then present the chemical properties of the three benchmark scenarios.

Table 3.2: Basic parameters for the terrestrial exoplanet benchmark scenarios. The benchmark scenarios are H_2, N_2, CO_2 atmospheres on habitable terrestrial exoplanets with Earth-like volcanic emissions. Note that I do not consider any known biosignature gas emission or biotic contribution to the dry deposition velocities.

Parameters	Reducing	Weakly Oxidizing	Highly Oxidizing
Main component	90%H_2, 10%N_2	> 99%N_2	90%CO_2, 10%N_2
Mean molecular mass	4.6	28	42.4
Planetary parameters			
Stellar type	G2V	G2V	G2V
Semi-major axis	1.6 AU	1.0 AU	1.3 AU
Mass	$M_\oplus$	$M_\oplus$	$M_\oplus$
Radis	$R_\oplus$	$R_\oplus$	$R_\oplus$
Temperature profile			
Surface temperature	288 K	288 K	288 K
Surface pressure	10^5 Pa	10^5 Pa	10^5 Pa
Tropopause altitude	120 km	13.4 km	8.7 km
Temperature above tropopause	160 K	200 K	175 K
Maximum altitude	440 km	86 km	51 km
Eddy diffusion coefficient			
In the convective layer	6.3×10^5 cm^2 s^{-1}	1.0×10^5 cm^2 s^{-1}	6.8×10^4 cm^2 s^{-1}
Minimum	2.5×10^4 cm^2 s^{-1}	3.9×10^3 cm^2 s^{-1}	2.7×10^3 cm^2 s^{-1}
Altitude for the minimum	107 km	17.0 km	11.6 km
Near the top of atmosphere	7.1×10^5 cm^2 s^{-1}	1.1×10^5 cm^2 s^{-1}	7.6×10^4 cm^2 s^{-1}
Water and rainout			
Liquid water ocean	Yes	Yes	Yes
Water vapor boundary condition	$f(H_2O) = 0.01$	$f(H_2O) = 0.01$	$f(H_2O) = 0.01$
Rainout rate[a]	Earth-like	Earth-like	Earth-like
Gas emission[b]			
CO_2	3×10^{11} cm^{-2} s^{-1}	3×10^{11} cm^{-2} s^{-1}	N/A
H_2	N/A	3×10^{10} cm^{-2} s^{-1}	3×10^{10} cm^{-2} s^{-1}
SO_2	3×10^9 cm^{-2}	3×10^9 cm^{-2}	3×10^9 cm^{-2}
CH_4	3×10^8 cm^{-2} s^{-1}	3×10^8 cm^{-2}	3×10^8 cm^{-2}
H_2S	3×10^8 cm^{-2}	3×10^8 cm^{-2}	3×10^8 cm^{-2}
Dry deposition velocity[c]			
H_2	0		
CH_4	0		
C_2H_6	1.0×10^{-5} (Assumed)		
CO	1.0×10^{-8} cm s^{-1} (Kharecha et al., 2005)		
CH_2O	0.1 cm s^{-1} (Wagner et al., 2002)		
CO_2	1.0×10^{-4} cm s^{-1} (Assumed)		
O_2	0		
O_3	0.4 cm s^{-1} (Hauglustaine et al., 1994)		
H_2O_2	0.5 cm s^{-1} (Hauglustaine et al., 1994)		
H_2S	0.015 cm s^{-1} (Sehmel, 1980)		
SO_2	1.0 cm s^{-1} (Sehmel, 1980)		
S_8(A)	0.2 cm s^{-1} (Sehmel, 1980)		
H_2SO_4(A)	0.2 cm s^{-1} (Sehmel, 1980)		

[a] Rainout rates for H_2, CO, CH_4, C_2H_6, and O_2 are generally assumed to be zero to simulate an ocean surface saturated with these gases on an abiotic exoplanet.

[b] The volcanic gas emission rates from the planetary surface are assigned for each model scenario. H_2O emission is not explicitly considered because the surface has a large water reservoir, i.e., an ocean.

[c] Here I list the dry deposition velocities (with references) for emitted gases and their major photochemical byproducts, and dry deposition velocities that are important for the mass and redox balance of the atmosphere. Dry deposition velocities are assumed to be identical for the three scenarios. C_2H_6 dry deposition velocity is assumed to take into account the loss of carbon due to organic haze formation and deposition. CO_2 dry deposition velocity is assumed such that the steady-state mixing ratio of CO_2 in H_2 and N_2 atmospheres is in the order of 100 ppm.

Table 3.3: Atmospheric compositions of terrestrial exoplanet benchmark scenarios. For the surface emission in 1-bar H_2-, N_2-, and CO_2-dominated atmospheres, mixing ratios of emitted gases, photochemical products and reactive agents are computed by the photochemistry model.

Scenario	Column Averaged Mixing Ratio		
	Emitted Gases	Photochemical Products[a]	Reactive Agents[b]
Reducing 90%H_2, 10%N_2	CO_2: 8.9×10^{-5} SO_2: 9.9×10^{-12} CH_4: 5.9×10^{-6} H_2S: 9.1×10^{-10}	CO: 8.0×10^{-6} C_2H_6: 4.7×10^{-10} S_8: 3.5×10^{-10} CH_2O: 2.9×10^{-10} CH_4O: 5.6×10^{-11}	H: 2.1×10^{-9} OH: 2.0×10^{-14} O: 1.2×10^{-11} O(^{1}D): 2.2×10^{-21}
Weakly oxidizing N_2	CO_2: 1.3×10^{-4} H_2: 4.5×10^{-4} SO_2: 8.9×10^{-12} CH_4: 3.1×10^{-5} H_2S: 1.1×10^{-14}	CO: 1.7×10^{-7} C_2H_6: 9.0×10^{-9} CH_4O: 1.4×10^{-9} O_2: 3.4×10^{-10} S_8: 3.0×10^{-10} CH_2O: 4.0×10^{-11} C_2H_2: 1.5×10^{-11}	H: 1.2×10^{-9} OH: 9.3×10^{-14} O: 6.5×10^{-10} O(^{1}D): 1.8×10^{-20}
Highly oxidizing 90%CO_2, 10%N_2	H_2: 1.0×10^{-3} SO_2: 1.6×10^{-10} CH_4: 3.7×10^{-5} H_2S: 1.4×10^{-10}	CO: 7.7×10^{-3} O_2: 6.4×10^{-7} C_2H_6: 6.1×10^{-10} H_2O_2: 3.7×10^{-10} H_2SO_4: 5.0×10^{-11} CH_2O: 2.5×10^{-12}	H: 6.0×10^{-11} OH: 7.8×10^{-15} O: 2.0×10^{-8} O(^{1}D): 3.0×10^{-18}

a

Species produced in the atmosphere from the emitted volcanic gases via photochemistry and subsequent series of chemical reactions, listed in the order of decreasing abundance. S_8 and H_2SO_4 mixing ratios include both the gas phase and the condensed phase; whereas the condensed phase is found to contain more than 85% of mass.

bCommon reactive agents in the atmosphere are H, OH, O, O(^{1}D). I list the abundance of these gases in all three scenarios for as useful reference for the future assessment of chemical lifetime of trace gases.
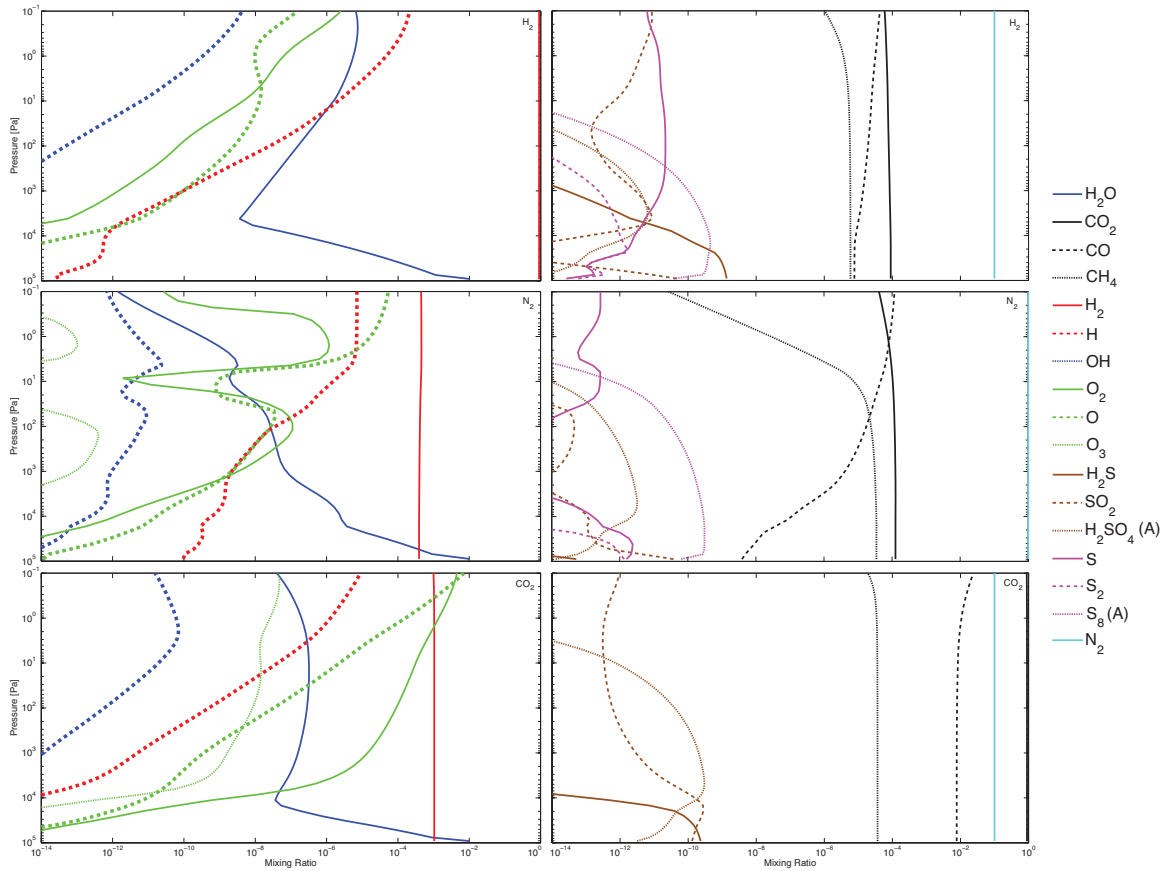
Figure 3-1: Compositions of the three benchmark scenarios of rocky exoplanet atmospheres tabulated in Table 3.2. The left column shows mixing ratios of H and O species, and the right column shows mixing ratios of N, C, and S species. From top to bottom, the three panels correspond to the reducing (H_2-dominated), oxidized (N_2-dominated), and highly oxidized (CO_2-dominated) atmospheres. The vertical scales are expressed in pressure, which allows comparison between different scenarios that have very different mean molecular masses, and hence the altitude difference for a given pressure change. I highlight the profiles of three reactive species, H, OH, and O by thick lines.
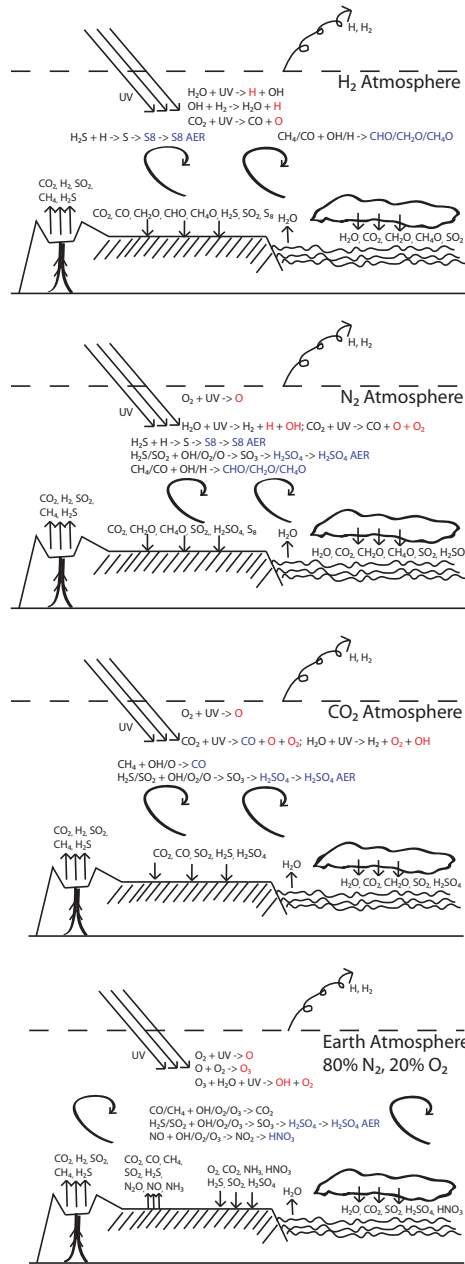
Figure 3-2: Schematic illustrations of key non-equilibrium processes in the 3 scenarios of rocky exoplanet atmospheres considered in this chapter (Table 3.3), in comparison with the current Earth. From top to bottom, the four panels correspond to the H_2, N_2, CO_2 atmospheres, and the atmosphere of Earth. The red color highlights the reactive radicals in each atmospheric scenario, and the blue color highlights the major photochemical products in the atmosphere.

3.2.1 General Results

I here list the main findings on general chemistry properties of thin atmospheres on habitable terrestrial exoplanets.

Atomic hydrogen (H) is a more abundant reactive radical than hydroxyl radical (OH) in anoxic atmospheres. Atomic hydrogen is mainly produced by water vapor photodissociation; and in anoxic atmospheres the main ways to remove atomic hydrogen is its recombination and reaction with CO. This is in contrast to oxygen-rich atmospheres (e.g., current Earth's atmosphere) in which H is quickly consumed by O_2. As a result, removal of a gas by H is likely to be an important removal path for trace gases in an anoxic atmosphere. Atomic oxygen is the most abundant reactive radical in CO_2-dominated atmospheres. Due to the photochemical origin of the reactive species including H, OH, and O, their abundances in the atmosphere around a quiet M dwarf are 2 orders of magnitude lower than their abundances around a Sun-like star.

Dry deposition velocities of long-lived compounds, notably major volcanic carbon compounds including methane, carbon monoxide, and carbon dioxide, have significant effects on the atmospheric oxidation states. The specific choice of dry deposition velocities for emitted gases and their major photochemical byproducts in the atmosphere is critical to determine the atmospheric composition and the redox power on terrestrial exoplanets.

Volcanic carbon compounds (i.e., CH_4 and CO_2) are chemically long-lived and tend to be well mixed in terrestrial exoplanet atmospheres, whereas volcanic sulfur compounds (i.e., H_2S and SO_2) are short-lived. CH_4 and CO_2 have chemical lifetime longer than 10,000 years in all three benchmark atmospheres ranging from reducing to oxidizing, implying that a relatively small volcanic input can result in a high steady-state mixing ratio. The chemical lifetime CO, another possible volcanic carbon compound, ranges from 0.1 to 700 years depending on the OH abundance in the atmosphere.

Abiotic O_2 and O_3, photochemically produced from CO_2 photolysis, can build up

in the 1-bar CO_2-dominated atmosphere if volcanic emission rates of reducing gases (i.e., H_2 and CH_4) is more than one order of magnitude lower than current Earth's volcanic rates. Abiotic O_2 can therefore be a false positive for detecting oxygenic photosynthesis, but the combination of O_2/O_3 and reducing gases remains rigorous biosignature.

3.2.2 Chemistry of H_2-, N_2-, and CO_2-Dominated Atmospheres

H_2-Dominated Atmospheres

The main reactive agent in the H_2-dominated atmosphere is atomic hydrogen (H). The abundance of atomic hydrogen is five orders of magnitudes higher than that of hydroxyl radical (Figure 3-1). The source of both H and OH is water vapor photodissociation. In the H_2-dominated atmosphere, most of the OH molecules produced from water vapor photodissociation react with H_2 to reform H_2O and produce H through the reactions:

$$H_2O + h\nu \longrightarrow H + OH, \qquad (C\,1)$$

$$OH + H_2 \longrightarrow H + H_2O. \qquad (C\,2)$$
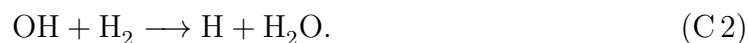
Therefore the abundance of atomic hydrogen is much higher than that of OH. It is noted that H production via water photodissociation is much more efficient than the direct photodissociation of H_2, which requires radiation in wavelengths less than 85 nm. As water vapor is the primary source of H and OH in anoxic atmospheres, the amounts of H and OH depends on the mixing ratio of water vapor above the cold trap, which is in turn sensitively controlled by the cold trap temperature. Water vapor mixing ratio spans 3 orders of magnitudes for the cold trap temperature ranging in 160 - 200 K; consequently, the number densities of H and OH in the atmosphere can easily vary by one order of magnitude, depending on the cold trap temperature. The removal of atomic hydrogen is mainly by recombination to H_2, which can be more

efficient with the presence of CO, via

$$H + CO + M \longrightarrow CHO + M, \qquad (C\,3)$$

$$H + CHO \longrightarrow CO + H_2. \qquad (C\,4)$$
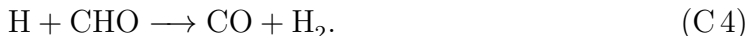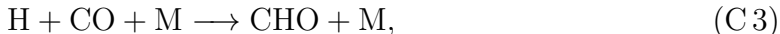
As a result of low OH abundance in the H_2-dominated atmosphere, both CH_4 and CO are long-lived and therefore well mixed (Figure 3-1). Part of CH_4 emitted from the surface is slowly oxidized in the atmosphere into methanol, which gives methane a chemical lifetime of 8×10^4 years. CO is produced by CO_2 photodissociation in the benchmark model; it is emitted by volcanoes on Earth at a much lower rate than CO_2, but it can presumably be the main carbon-bearing gas produced by volcanoes if the upper mantle is more reduced than the current Earth's (e.g. Holland, 1984). I find that CO is long-lived in the H_2 atmosphere as well.

The lack of efficient atmospheric sink of CH_4 and CO in the H_2 atmosphere implies that surface sink, if any, is the major sink for these two carbon compounds. CH_4 and CO should have zero or very small dry deposition velocities on an abiotic planet, so they can build up to significant amounts in the H_2 atmosphere (Figure 3-1). If a nonzero deposition velocity is adopted for CH_4 and CO, their steady-state mixing ratios will be much lower than the benchmark model. For example, using a deposition velocity for CH_4 standard on Earth (~ 0.01 cm s^{-1}) results in a mixing ratio of less than 1 ppb for CH_4, compared to a mixing ratio of 6 ppm in the benchmark model. The dry deposition velocity is indeed the controlling factor for the steady-state abundance of the long-lived carbon compounds. In comparison, the emitted sulfur compounds (H_2S and SO_2) are short-lived. In the H_2 atmosphere, sulfur emission from the surface is readily converted to elemental sulfur aerosols (S_8) in the atmosphere.

N_2-Dominated Atmospheres

Both reducing radicals (i.e., H) and oxidizing radicals (i.e., O and OH) are relatively abundant in the N_2 atmosphere compared with the H_2 atmosphere (Figure 3-1). Like in H_2-dominated atmospheres, H abundance is orders of magnitude larger than OH

abundance, because most of OH molecules from water photolysis react with H_2 to reform H_2O and produce H. The molecular hydrogen that consumes OH and boosts H is emitted volcanically, so a general N_2 atmosphere can be more oxidizing (i.e., having lower H and higher OH) if there is a lower volcanic H_2 emission rate and mixing ratio than the benchmark model.

An important feature of the N_2-dominated atmosphere is that both H and OH are relatively abundant near the surface. Comparing the N_2-dominated atmosphere with the H_2-dominated atmosphere (Figure 3-1), I find that both the OH and the H number densities are higher near the surface due to the lower H_2 number density. The relatively high OH number density leads to relatively fast removal of CO by

$$CO + OH \longrightarrow CO_2 + H, \qquad\qquad (C\,5)$$

as shown in Figure 3-1. With a low CO abundance the recombination of H via reactions (4-3-C 4) is inefficient. Counter-intuitively, a high OH number density helps preserve H in this specific case. This example shows the complexity and the nonlinearity of an atmospheric chemical network. The feature of simultaneous high OH and H abundances near the surface is sensitive to the specification of surface hydrogen emission and eddy diffusion coefficients (see section 3.2.3 for relevant rationale).

The chemical lifetimes of CH_4 and CO mainly depend on the amount of OH. In the N_2 atmosphere, CH_4 is well mixed because its chemical lifetime is long. CH_4 is photodissociated and oxidized slowly in the atmosphere into methanol (CH_4O) with a chemical lifetime of $\sim 6 \times 10^4$ years. The photolysis of methane is a secondary source of atomic hydrogen, which concentrates at the pressure level of 10 Pa. Interestingly, methane photolysis causes the apparent trough of O_2 mixing ratio profile at ~ 10 Pa. It is the shielding of the UV radiation that dissociates methane by methane itself that determines this pressure level (see Appendix B.4 for an analytical formula for assessing the pressure level at which the photolysis of a certain gas is important).

CO_2 is actively photodissociated into CO and O in the upper atmosphere, but most of the CO produced is efficiently converted back to CO_2 by reacting with OH

(reaction C5). In equilibrium the net chemical removal of CO_2 is minimal, so the CO_2 mixing ratio is still set by the balance between emission and deposition.

Sulfur-bearing gases emitted from the surface are effectively converted into elemental sulfur and sulfuric acids. Elemental sulfur, mainly in the condensed phase (i.e., aerosols), is the major sulfur-bearing species in the steady state because of relatively high H_2 mixing ratio in the benchmark model. In separate numerical simulations I find that sulfuric acid aerosols may outnumber elemental sulfur aerosols when the H_2 emission is reduced by more than 1 order of magnitude and the atmosphere is more oxidizing than the benchmark model.

CO_2-Dominated Atmospheres

CO_2 photodissociation produces CO, O, and O_2. Atomic oxygen is the most abundant reactive radicals in the CO_2-dominated atmosphere (Figure 3-1), because H is readily removed by O_2 and OH is readily removed by CO. As a result of low H and OH, CO is long-lived in the atmosphere and can build up to very high mixing ratios in the atmosphere depending on its dry deposition velocity; and CH_4 emitted from the surface is also long-lived in the atmosphere with a chemical lifetime of $\sim 6 \times 10^4$ years. The steady-state abundance of CO and CH_4 is therefore controlled by their dry deposition velocities. Most of the emitted SO_2 is deposited to the surface, because there are very few OH or O radicals near the surface. A small fraction of the SO_2 is transported upwards and converted into sulfuric acid aerosols in the radiative layer.

3.2.3   Rationale of Model Parameters

I here provide rationale for the specification of the atmospheric temperature profile, the eddy diffusion coefficients, and the dry deposition velocities.

First, the surface temperatures for the three scenarios are assumed to be 288 K, and the semi-major axis of the planet is adjusted according to appropriate amounts of greenhouse effect. The semi-major axis around a Sun-like star for H_2-, N_2-, and CO_2-dominated atmospheres is found to be 1.6 AU, 1.0 AU, and 1.3 AU. I have

compared the planetary thermal emission flux and the incidence stellar flux to determine the semi-major axis, a similar procedure as Kasting et al. (1993) taking into account CO_2, H_2O, and CH_4 absorption, H_2 collision-induced absorption, and 50% cloud coverage and a Bond albedo of 30%. The temperature profiles are assumed to follow appropriate dry adiabatic lapse rate (i.e., the convective layer) until 160 K (H_2 atmosphere), 200 K (N_2 atmosphere), and 175 K (CO_2 atmosphere) and to be constant above (i.e., the radiative layer). I simulate the atmosphere up to the altitude of about 10 scale heights, or the pressure level of 0.1 Pa. The adopted temperature profiles are consistent with significant greenhouse effects in the convective layer and no additional heating above the convective layer for habitable exoplanets. The results discussed above do not change significantly if these temperature profiles are changed by several tens of K.

Second, I have used eddy diffusion coefficients empirically determined on Earth and scaled the values to account for different mean molecular masses. The eddy diffusion coefficient at a certain pressure level is assumed to be that of current Earth's atmosphere at the same pressure level (see Figure 2-1), scaled by 6.3, 1.0, and 0.68 for the H_2-, N_2-, and CO_2-dominated atmospheres, respectively to account for different dominant molecules. I have roughly scaled the eddy diffusion coefficient assuming $K \propto H_0$ where H_0 is the atmospheric scale height. The reasoning of the scaling is as follows. According to the mixing length theory, $K \propto lw$, where l is the typical mixing length and w is the mean vertical velocity. The mixing length is a fraction of the pressure scale height (e.g. Smith, 1998). The mean vertical velocity is related to the vertical convective energy flux, as $F \propto pw$, where p is the pressure (e.g. Lindzen, 1990). For a certain planet F should have the same order of magnitude for different atmosphere compositions. As the scaling is applied from pressure surface to pressure surface, I have roughly $K \propto H_0$. The scaling is an approximation and I only intend to provide a consistent description of eddy diffusion for atmospheres with very different mean molecular mass. The eddy diffusion coefficients for the three scenarios are also consistent with their temperature profiles, featuring minima near the tropopause. The general results discussed above are not sensitive to the variation

of eddy diffusion coefficients by an order of magnitude.

Third, the typical deposition velocity on Earth is sometimes not directly applicable for terrestrial exoplanets, because the major surface sink of a number of gases (notably, H_2, CH_4, CO) on Earth is actually microorganisms. In this paper I focus on the scenarios assuming no biotic contribution in neither surface emission nor surface deposition. For H_2 and CH_4, a sensible dry deposition velocity without biotic surface sink is zero (J. Kasting, 2012, private communication). For CO_2, the dry deposition velocity should match with the timescale of weathering and carbonate formation, which is 10,000 years (Archer, 2010). For CO, the rate limiting step for converting CO into bicarbonate has been proposed to the hydration of CO in the ocean, which corresponds to a deposition velocity of $1.0 \times 10^{-9} \sim 10^{-8}$ cm s^{-1} (Kharecha et al., 2005). The adopted or assumed values of dry deposition velocities are tabulated in Table 3.2.

For completeness, I now comment on my assumptions for nitrogen chemistry and organic haze in the photochemistry model. I do not track the bulk nitrogen cycle, instead assuming 10% N_2 for H_2- and CO_2-dominated atmospheres. My model does not treat abiotic nitrogen fixation by lightning (see Kasting and Walker, 1981; Zahnle, 1986; Tian et al., 2011, for specific analysis), so N_2 is considered as inert in my models. I include the formation of elemental sulfur aerosols and sulfuric acid aerosols in my models; but I do not include the less-understood hydrocarbon chemical network for hydrocarbon molecules that have more than 2 carbon atoms or the formation of hydrocarbon haze. Organic haze may be formed in anoxic atmospheres based on methane photolysis and hydrocarbon polymerization. The number density of hydrocarbons that have more than 4 carbon atoms (usually considered to be condensable) is ~ 4 orders of magnitude smaller than the number density of C_2H_6 at the steady state (e.g. Allen et al., 1980; Yung et al., 1984; Pavlov et al., 2001). To account for the loss of carbon due to possible organic haze formation and deposition, I apply an *ad hoc* dry deposition velocity of 1.0×10^{-5} cm s^{-1} for C_2H_6. This small velocity results from a scaling based on typical sub-micron particle deposition velocity (~ 0.2 cm s^{-1}) and the number density ratio of C_4 hydrocarbons and C_2H_6 (e.g. Yung et al.,

1984). An accurate treatment for organic haze is not the purpose of this paper, because the efficiency of haze formation depends on oxidation states of atmospheres, stellar UV radiation, and a number of less-understood reaction rates. Nonetheless, for all simulated scenarios, the carbon loss due to haze formation is less than 1% of the methane emission flux; therefore I do not expect my simplification of organic haze formation would impact the results.

3.3 Redox-Controlling Effects of Surface Emission and Deposition

One of the main results I found using the photochemistry model is the controlling effects of surface emission and deposition of trace gases on the general redox power of a thin atmosphere. This is a profound finding because, in addition to the main components, the minor components in the thin atmosphere also can affect the chemical lifetimes of gases of interest. Here I provide two conjugated examples to further illustrate this point: the redox controlling effect of CO_2 emission and deposition in H_2-dominated atmospheres, and the redox controlling effect of H_2 and CH_4 emission and deposition in CO_2-dominated atmospheres.

3.3.1 Redox-Controlling Effects of CO_2 in H_2-Dominated Atmospheres

CO_2 is fairly long-lived and therefore well mixed in H_2-dominated atmospheres, meaning that the reduction of CO_2 in H_2-dominated atmospheres is not efficient (Figure 3-1). For a deposition velocity of 10^{-4} cm s^{-1}, only 1/3 of emitted CO_2 is reduced in the modeled atmosphere, and the rest is deposited to the surface by dry and wet deposition. It is the balance between surface emission and surface deposition that sets the steady-state mixing ratio of CO_2.

The steady-state amount of a long-lived species in a thin atmosphere can be

directly estimated by the mass balance between emission and deposition, viz.,

$$F = f_1 = \frac{n_1}{N_1} = \frac{\Phi_{1/2}}{V_{\mathrm{DEP}} N_1},\tag{3.1}$$

where the overall mixing ratio (F) is the same as the near-surface mixing ratio (f_1), and $\Phi_{1/2}$ is the surface emission rate. For CO_2 in the H_2-dominated atmosphere, using Equation (3.1), with $V_{\mathrm{DEP}}(CO_2) = 1 \times 10^{-4}$ cm s^{-1}, one can estimate that the steady-state mixing ratio to be 1.3×10^{-4}, only 50% more than the result of the full photochemical model (8.9×10^{-5}; see Table 3.3 and Figure 3-1). The discrepancy is because not all emitted CO_2 is balanced by surface deposition; in fact about $1/3$ of emitted CO_2 is photochemically reduced in the atmosphere. In all, the steady-state mixing ratio of a long-lived volcanic gas that is primarily removed by surface deposition is inversely proportional to its dry deposition velocity.

Figure 3-3 shows the mixing ratio of CO_2, as well as the mixing ratios of reducing radicals (H) and oxidizing radicals (O), in the benchmark H_2-dominated atmosphere for increasing CO_2 emission rates. The photochemical simulations show that the mixing ratio of CO_2 increases with the emission rate of CO_2 linearly, consistent with Equation (3.1). With separate simulations I have verified that the mixing ratio of CO_2 is inversely proportional to the dry deposition velocity of CO_2. Furthermore, one may notice that for the same emission flux and dry deposition velocity, the amount of CO_2 in the atmosphere decreases with increasing UV photon flux (Figure 3-3). This is because for more intense UV radiation, the production of H in the atmosphere via reactions (C 1-C 2) is enhanced, and then a larger fraction of emitted CO_2 can be reduced in the atmosphere.

The key feature illustrated by Figure 3-3 is that, as a result of increasing CO_2 emission rate (or decreasing CO_2 deposition velocity), the amount of oxidizing radicals (i.e., O) in the atmosphere increases, and the atmosphere become more oxidizing. The main source of O in the atmosphere is the photodissociation of CO_2; thus the amount of O is almost proportional to the amount of CO_2 (Figure 3-3), and then proportional to the ratio $\Phi_{1/2}/V_{\mathrm{DEP}}$ for CO_2 (Eq. 3.1). For a CO_2 emission rate 100 times more

106
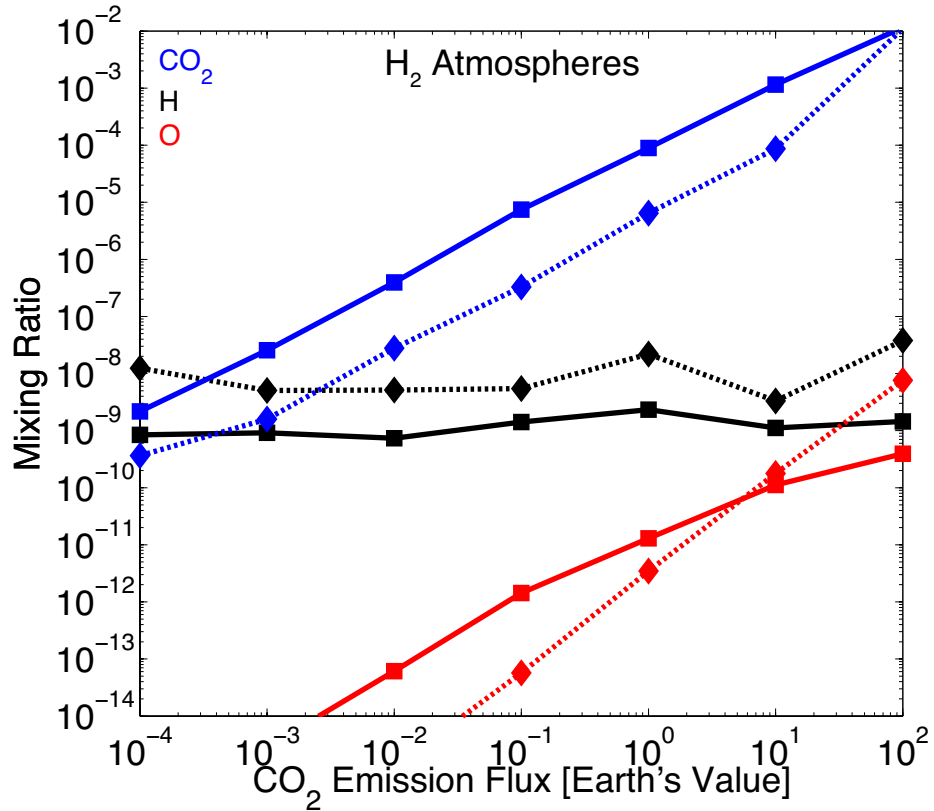
Figure 3-3: Effects of the surface emission of CO_2 on the compositions of H_2-dominated atmospheres on rocky exoplanets. The simulated planet is a Earth-sized planet at 1.6 AU from a Sun like star, with a variety of CO_2 emission fluxes, and other parameters the same as tabulated in Table 3.2. Mixing ratios of CO_2, H, and O are shown in the figure; and the solid lines correspond to Solar-like UV photon flux, and dashed lines correspond to 100 times higher UV photon flux (in 100-300 nm). The amount of oxidizing radicals (i.e., O) in the atmosphere increases for increasing CO_2 emission rates.

than Earth's volcanic emission rate, the mixing ratio of CO_2 in the H_2-dominated atmosphere can be as high as 10^{-2}, and the mixing ratio of O can be comparable to the mixing ratio of H. This result implies that the H_2-dominated atmosphere is usually reducing; but for elevated CO_2 emission rates or very low CO_2 dry deposition velocities, CO_2 may build up in the H_2-dominated atmosphere, and the atmosphere can be both reducing and oxidizing.

3.3.2   Redox-Controlling Effects of H_2 and Abiotic Formation of O_2 in CO_2-Dominated Atmospheres

I have demonstrated in the last section that the emission and deposition of CO_2 affects significantly the redox power of the H_2-dominated atmosphere. Now I turn to consider the redox controlling effects of H_2 in CO_2-dominated atmospheres. This study is particularly important because of its relevance to the abiotic formation of free O_2 in CO_2-dominated atmosphere. I will revisit in this section whether photochemically produced O_2 can cause false positives for inferring oxygenic photosynthesis using atmospheric O_2.

Oxygen and ozone are the most studied biosignature gases for terrestrial exoplanet characterization (e.g. Owen, 1980; Angel et al., 1986; Leger et al., 1993, 1996; Beichman et al., 1999; Snellen et al., 2013). One of the main concerns of using O_2/O_3 as biosignature gases is that O_2 may be produced abiotically from photodissociation of CO_2. A number of authors have studied the abiotic production of oxygen in terrestrial atmospheres, either for understanding prebiotic Earth's atmosphere (e.g. Walker, 1977; Kasting et al., 1979; Kasting and Catling, 2003), or for assessing whether abiotic oxygen can be a false positive for detecting photosynthesis on habitable exoplanets (Selsis et al., 2002; Segura et al., 2007). Selsis et al. (2002) found that photochemically produced oxygen can build up in CO_2-dominated atmospheres without any surface emission or deposition. The results of Selsis et al. (2002) was challenged by Segura et al. (2007), who had additionally considered the surface emission of reducing gases including H_2 and CH_4, and concluded that abiotic oxygen CO_2 photodissociation is

Table 3.4: Mixing ratios of O_2 and O_3 and redox budget for CO_2-dominated atmospheres on rocky exoplanets having different surface emission of reducing gases. The redox number for each species is defined according to Equation (2.26). In the redox balance, all values have unit of molecule cm^{-2} s^{-1}, and defined as positive for hydrogen flux into the atmosphere. The redox budget for my atmosphere models is balanced, meaning that the atmosphere is not becoming more oxidized or reduced.

Chemical species	CO$_2$-dominated atmospheres		
	$\Phi_{1/2}(H_2) = 3 \times 10^{10}$ cm s^{-1}	$\Phi_{1/2}(H_2) = 3 \times 10^{9}$ cm s^{-1}	No H$_2$ Emission
Column-averaged mixing ratio			
O$_2$	6.4E-7	3.8E-6	1.3E-3
O$_3$	7.0E-11	3.7E-10	1.3E-7
Redox balance			
Atmospheric escape			
H	-7.0E+8	-2.4E+8	-1.2E+6
H$_2$	-5.9E+10	-5.8E+9	-2.0E+6
Surface emission			
H$_2$	6.0E+10	6.0E+9	0
CH$_4$	2.4E+9	2.4E+9	0
H$_2$S	1.8E+9	1.8E+9	1.8E+9
Dry and wet deposition			
O$_3$	0	6.3E+4	1.1E+10
HO$_2$	3.1E+4	7.8E+7	1.2E+8
H$_2$O$_2$	1.7E+5	1.5E+9	2.7E+9
CO	-3.7E+9	-5.6E+9	-1.5E+10
CH$_2$O	-1.3E+6	-7.2E+4	0
OrganicHaze	-2.0E+6	-8.1E+1	0
H$_2$S	-4.9E+8	-2.5E+8	-3.2E+8
H$_2$SO$_4$	1.2E+8	6.3E+7	2.9E+7
Balance	4.9E+3	-9.5E+2	-1.3E+3

not likely to build up in the atmosphere on an planet having active hydrological cycle.

I find that the steady-state number density of O_2 and O_3 in the CO_2-dominated atmosphere is mainly controlled by the surface emission of reducing gases such as H_2 and CH_4, and without surface emission of reducing gas photochemically produced O_2 can build up in a 1-bar CO_2-dominated atmosphere. In addition to the benchmark model, I have simulated CO_2-dominated atmospheres with relatively low and zero emission rates of H_2 and CH_4 (Table 3.4 and Figure 3-4). The O_2 mixing ratio near the surface increases dramatically in 1-bar CO_2 atmospheres when the emission of reducing gases decreases. O_2 is virtually nonexistent at the surface for the Earth-like emission rates of H_2 and CH_4; but O_2 mixing ratio can be as high as 10^{-3} if no H_2 or CH_4 is emitted (Figure 3-4). In particular, if no H_2 or CH_4 is emitted, the O_3 column integrated number density can reach one third of the present-day Earth's atmospheric levels (Table 3.4), which constitutes a potential false positive.
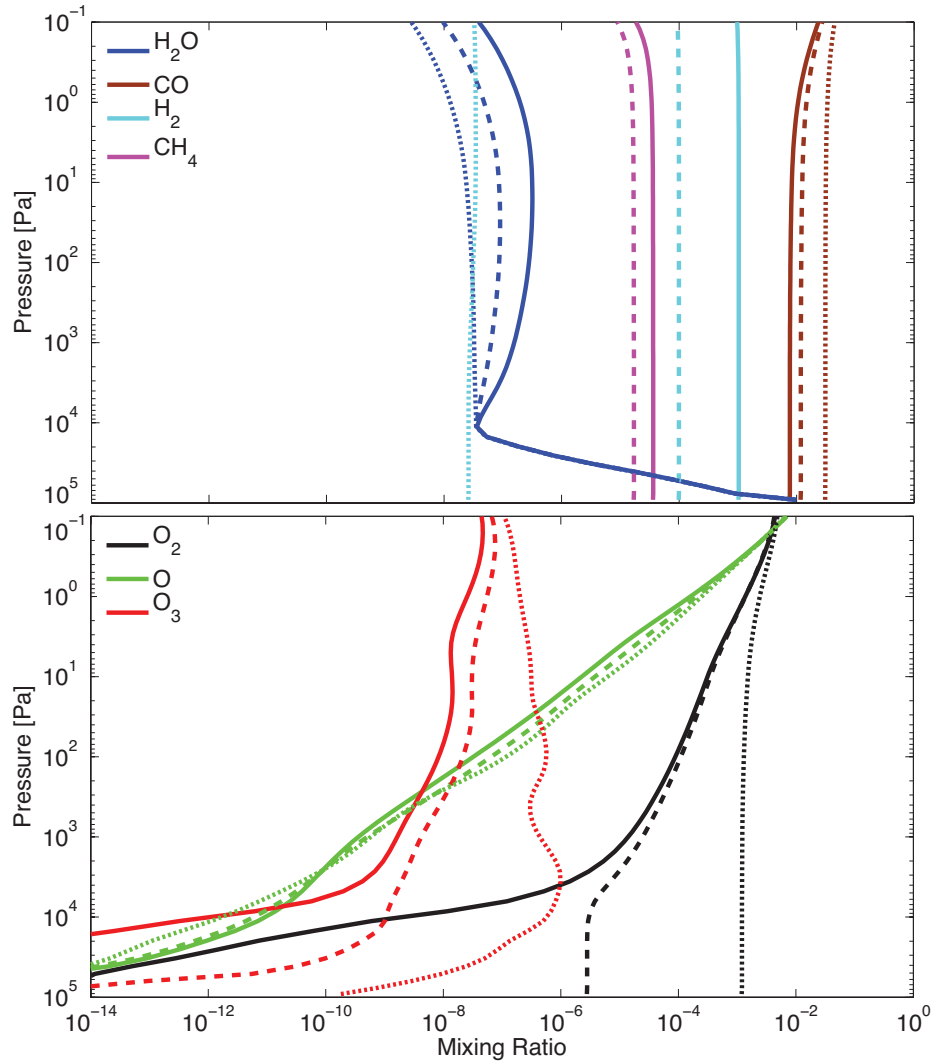
Figure 3-4: Effects of the surface emission reducing gases on CO_2-dominated atmospheres of rocky exoplanets. The upper panel shows mixing ratios of H_2O, CO, H_2, and CH_4, and the lower panel shows mixing ratios of O_2, O, and O_3. The solid lines show the chemical composition of the benchmark scenario whose parameters are tabulated in Table 3.2. In particular the emission rate of H_2 is 3×10^{10} cm^{-2} s^{-1}. The dashed lines show the chemical composition of the same scenario, but with an H_2 emission rate of 3×10^9 cm^{-2} s^{-1}; and the dotted lines show the chemical composition for zero emission of H_2 and CH_4. I find a dramatic increase of O_2 and O_3 mixing ratios as a result of a decrease of the surface emission of reduced gases.

In the 1-bar CO_2-dominated atmosphere O_3 can potentially build up to a false-positive level even on a planet with active hydrological cycle. Segura et al. (2007) have based their conclusion on simulations of 20% CO_2 1-bar atmospheres with and without emission of H_2 and CH_4 and simulations of 2-bar CO_2 atmospheres with emission of H_2 and CH_4. I have been able to reproduce all results of Segura et al. (2007) quantitatively to within a factor of two. Where my models differ from Segura et al. (2007) is that my model successfully simulated high CO_2 1-bar atmospheres with minimal volcanic reducing gas emission (Figure 3-4). This is a parameter space that Segura et al. (2007) did not cover, but I find that this is the parameter space for high abiotic O_2.

This result implies that one should exercise caution to use spectral features of O_2 as a probe of oxygenic photosynthesis on a terrestrial exoplanet. The risk of false positive described here would affect the inference of photosynthesis via O_2 features detected in the visible wavelengths, potentially by either the *Terrestrial Planet Finder - Coronagraph* (e.g. Beichman et al., 2006) or the cross-correlation method applied to high-resolution spectroscopy on the 40-meter class telescopes (Snellen et al., 2013). The risk of false positive is however not relevant to the detection of O_3 (a photochemical derivative of O_2) features in the mid-infrared, because the O_3 feature would be masked by strong CO_2 features and therefore not detectable for CO_2-dominated atmospheres (Selsis et al., 2002). Eventually, the risk of false positive may be mitigated by detecting both O_2 features and CH_4 features. A methane mixing ratio of ~ 10 ppm would imply a surface source of reducing gases that could prevent the abiotic build-up of O_2 (Figure 3-4).

3.4 Sulfur Chemistry in Terrestrial Exoplanet Atmospheres

3.4.1 Background

Sulfur gases emitted from the surface and their photochemical products significantly shape the spectra of rocky bodies in the Solar System. The most striking feature of Venus' atmosphere is a high planetary albedo due to thick H_2SO_4 clouds. Photochemistry models of the Venusian atmosphere have been developed and the formation of H_2SO_4 in the dry CO_2-dominated atmosphere have been simulated (e.g. Yung and Demore, 1982; Zhang et al., 2012; Krasnopolsky, 2012). The latest photochemistry model of Venus' atmosphere has assumed a constant mixing ratio of SO_2 (i.e., ~ 10 ppm) at the altitude of 47 km (implying significant source of SO_2 from below) and predicted the formation of H_2SO_4 at the altitudes around 66 km (Zhang et al., 2012; Krasnopolsky, 2012). Io, the innermost moon of Jupiter, is believed to have very intensive and variable volcanic activity with SO_2 emission, and the Io's atmosphere is dominated by photolysis of SO_2 and subsequent formation and polymerization of elemental sulfur (Moses et al., 2002). On early Earth, the sulfur chemistry may have been very different from now, featuring the formation of sulfur aerosols as well as sulfate aerosols as the atmosphere was anoxic (e.g. Kasting et al., 1989; Pavlov and Kasting, 2002; Kasting and Catling, 2003; Zahnle et al., 2006). The formation of insoluble sulfur aerosols is believed to be critical for the record of mass independent fractionation that timed the rise of oxygen in Earth's atmosphere (e.g. Farquhar et al., 2000; Pavlov and Kasting, 2002; Zahnle et al., 2006). In addition, organosulfur compounds, such as dimethyl sulfide (DMS) and methanethiol (CH_3SH), have also been suggested to be biosignatures of the early Earth (Pilcher, 2003). The greenhouse effect of SO_2 has been suggested to have contributed to the warming of early Mars (e.g. Halevy et al., 2007), a proposition that has been challenged by photochemistry studies that predict sulfur and sulfate aerosol formation as a result of SO_2 emission on early Mars and the anti-greenhouse effect of these aerosols (Tian et al., 2010).

Terrestrial exoplanets could have a wide range of sulfur gas emission. Sulfur gases are common volcanic gases on Earth, and in some scenarios may be more prevalent on exoplanets. Sulfur is a major building block for rocky planets and the abundance of sulfur is about one sixteenth that of carbon in the Solar System (Lodders, 2003). On present-day Earth, sulfur compounds, mainly in the form of H_2S and SO_2, are dominant volcanic gases in additional to hydrogen, oxygen and carbon emissions. In the Earth's magma, the dissolved sulfur has a weight percentage ranging from 10^{-4} to 10^{-2} (e.g. Wallace and Edmonds, 2011) and degassing of sulfur compounds as the magma decompresses when rising to the surface provides a global volcanic sulfur flux of about 3×10^9 S cm^{-2} s^{-1} (Seinfeld and Pandis, 2006). 90% of current Earth's sulfur emission is in the form of SO_2, whereas the H_2S/SO_2 ratios for individual volcanoes vary widely between 0.01 and 1 (see Holland, 2002, and references therein). An intriguing fact is that the amounts of sulfur compounds in Earth's atmosphere is extremely low despite the substantial emission rates, due to very short chemical timescales. On Earth, the lifetime of H_2S and SO_2 in the troposphere is only 2 days, which makes the mixing ratio of these gases in the atmosphere very small (Seinfeld and Pandis, 2006). In Earth's troposphere, the main sink of H_2S is the reaction with the hydroxyl radical OH (Lelieveld et al., 1997), and the main sink of SO_2 is the removal by dry and wet deposition.

Another reason that H_2S and SO_2 photochemistry is interesting is that Earth-based biological processes involve sulfur compounds. There are multiple ways that life can produce H_2S, including the reduction of sulfate (e.g. Watts, 2000) and the disproportionation of sulfur compounds of intermediate oxidation states (e.g. Finster, 2008). In general, 10 to 50 percent of the global H_2S emission on Earth is as a metabolic byproduct, whereas over 70% percent of natural SO_2 emission is volcanic, although on modern Earth 90% of atmospheric SO_2 is anthropogenic (Seinfeld and Pandis, 2006). Understanding the atmospheric response to H_2S and SO_2 emission will allow me to examine whether or not H_2S is a potential biosignature gas on a terrestrial exoplanet.

Previous investigation of sulfur photochemistry in the context of terrestrial exo-

planets has been very limited. Sulfur compounds are generally not considered in most models of terrestrial exoplanet atmospheres. Des Marais et al. (2002) describe the spectral features of certain molecules such as H_2O, N_2O, O_3 and CH_4 in terrestrial exoplanets. Miller-Ricci et al. (2009) present spectra of super Earths under equilibrium chemistry with photochemistry estimates and without considering sulfur compounds. Zahnle et al. (2009b) investigate sulfur photochemistry in hot Jupiters and suggest that HS and S_2 can be generated photochemically from H_2S. Kaltenegger and Sasselov (2010) study the effect of H_2S and SO_2 on the terrestrial planetary spectra and suggest that 1-10 ppm SO_2 has potentially detectable spectral features that could indicate active volcanism. Kaltenegger and Sasselov (2010), however, do not link the surface emission of sulfur gases to the mixing ratio of sulfur species via photochemistry involving sulfur compounds, or consider formation of aerosols. Domagal-Goldman et al. (2011) study the chemistry of organic sulfur compounds that are strongly linked to biology (e.g., CH_3SH) in anoxic N_2 atmospheres and suggest that the most detectable feature of organic sulfur gases is their indirect photochemical product, ethane. Moreover, the fate of surface emission of sulfur compounds, e.g., H_2S and SO_2, is yet to be explored for H_2-dominated atmospheres. H_2-dominated atmospheres, like N_2 or CO_2 atmospheres with water vapor, could also maintain a habitable temperature at the surface through collision-induced absorption (Pierrehumbert and Gaidos, 2011; Wordsworth, 2012).

In all, it is still largely unknown whether or not H_2S and SO_2 spectral features can be observed in the future in the atmosphere of an exoplanet and whether or not the emission rate of sulfur compounds on a terrestrial exoplanet can be inferred. In this section I use the photochemistry model to investigate the atmospheric chemistry resulting from H_2S and SO_2 surface emission in atmospheres having very different oxidation states ranging from reducing to oxidizing.

3.4.2 Photochemistry Model Setup

The photochemistry model is used to study the sulfur chemistry in atmospheres ranging from reducing to oxidizing on terrestrial exoplanets. I therefore select H_2-

dominated atmospheres as the representative cases for reducing atmospheres, and N_2- and CO_2-dominated atmospheres as the representative cases for oxidized atmospheres that could be both reducing and oxidizing. With the photochemistry model, I simulated the chemical composition of H_2-, N_2-, and CO_2-dominated atmospheres, with sulfur compounds emitted from the surface at various rates. Parameters for the atmospheric models are the same as for the benchmark scenarios tabulated in Table 3.2, except that I vary the emission rates and the deposition velocities of H_2S and SO_2 for this study.

I select a subset of species from the generic model for this study. The gaseous molecules considered are H, H_2, O, $O(^1D)$, O_2, O_3, OH, HO_2, H_2O, H_2O_2, CO_2, CO, CH_2O, CHO, C, CH, CH_2, $^1CH_2$, CH_3, CH_4, CH_3O, CH_4O, CHO_2, CH_2O_2, CH_3O_2, CH_4O_2, C_2, C_2H, C_2H_2, C_2H_3, C_2H_4, C_2H_5, C_2H_6, C_2HO, C_2H_2O, C_2H_3O, C_2H_4O, C_2H_5O, S, S_2, S_3, S_4, SO, SO_2, $^1SO_2$, $^3SO_2$, SO_3, H_2S, HS, HSO, HSO_2, HSO_3, H_2SO_4, and S_8, and the aerosols considered are S_8 aerosols and H_2SO_4 aerosols. This set of species is comprised of common H, O, and C bearing species and photochemical products of H_2S and SO_2 emission. I assume a constant H_2O relative humidity at the surface of 60% to mimic the supply of water vapor from a liquid water ocean. To reduce the stiffness of the system and improve the numerical stability, "fast" species with relatively short chemical loss timescales are computed directly from the photochemistry equilibrium. I consider in this work $O(^1D)$, $^1CH_2$, C_2H, $^1SO_2$, and $^3SO_2$ as fast varying species. As such, the photochemistry model rigorously finds steady-state composition of the atmosphere starting with initial compositions without any sulfur compounds. Once the model converged to the steady state, I checked explicitly the mass conservation of O, H, C, N, S atoms and verified the choice of fast species to have been appropriate. It is required that all models to balance mass flux within 10^{-3} for convergence, and typically my models balance mass flux to 10^{-6}. I have also explicitly checked the redox (i.e., hydrogen budget) balance, and required the models to balance redox flux to 10^{-3}.

An important factor that strongly influences the atmospheric sulfur chemistry is the formation and sedimentation of aerosols. Photochemically produced H_2SO_4

and S_8 may condense to form aerosols if their concentrations exceed their vapor saturation concentrations. I consider the average aerosol particle diameter, a key parameter that determines the aerosols' dynamical and optical properties, to be a free parameter. On Earth, the ambient aerosol size distribution is dominated by several modes corresponding to different sources. The "condensation submode", formed from vapor condensation and coagulation, has an average diameter of $\sim 0.4\ \mu$m (Seinfeld and Pandis, 2006). On Venus, the Mode 1 particles with an an average diameter of $\sim 1.0\ \mu$m dominate the upper cloud (e.g. Carlson et al., 1993). On Titan, the photochemical aerosols in the stratosphere have mean diameters in the range of 0.1 - 1 μm (Rages et al., 1983). I treat the particle diameter a free parameter, and explore the effects of varying the particle diameter from 0.1 to 10 μm. The dry deposition velocity of aerosols is assumed to be 0.2 cm s^{-1}, a sensible deposition velocity of particles having diameters between 0.1 and 1 μm (Sehmel, 1980; Seinfeld and Pandis, 2006). The extinction cross sections of H_2SO_4 and S_8 molecules in aerosols for various mean particular diameters are shown in Figure 3-5.

Elemental sulfur aerosols and sulfuric acid aerosols have different optical properties at the visible and infrared (IR) wavelengths. In the visible, S_8 aerosols have a larger cross section than H_2SO_4 aerosols (Figure 3-5). For wavelengths less than 400 nm S_8 aerosols are both reflective and absorptive. In the infrared, the cross section of S_8 aerosols drops significantly with increasing wavelength unless the mean diameter is in the order of 10 μm. In contrast, H_2SO_4 aerosols have an enhancement of absorption at the MIR wavelengths (5-10 μm) for all particle sizes (Figure 3-5).

3.4.3 Sulfur Chemistry in Reducing and Oxidizing Atmospheres

I now briefly describe the most important processes of sulfur chemistry that occur in reducing and oxidizing atmospheres on rocky exoplanets. The primary sulfur emission from the planetary surface would be SO_2 and H_2S; they are either deposited back to the surface via dry or wet deposition, or converted into other forms of sulfur

116
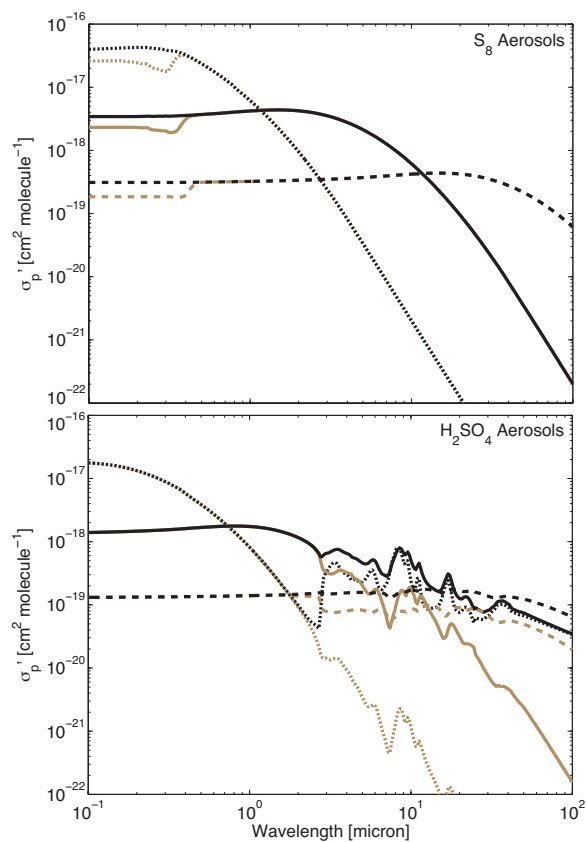
Figure 3-5: Extinction cross sections (black lines) and scattering cross sections (orange lines) of H_2SO_4 and S_8 per molecule in the condensed phase. The dotted, solid, and dashed lines are cross sections for the mean particle diameter of 0.1, 1, 10 μm, respectively. The size distribution of aerosol particles is assumed to be lognormal with a dispersion $\sigma = 2$.

compounds in the atmosphere by photochemical reactions. One of the main purposes here is to study the fate of sulfur gases emitted from the surface and their possible photochemical byproducts in the atmosphere.

The fate of sulfur gases emitted from the surface is mainly controlled by the redox power of the atmosphere. It is already known that sulfur gas emissions are effectively oxidized into sulfate, the most oxidized form of sulfur, in the oxic atmospheres such as the Earth's (e.g. Seinfeld and Pandis, 2006). In anoxic atmospheres, which include the reduced atmospheres and the oxidized atmospheres, previous studies have shown that both elemental sulfur and sulfate could be formed (Kasting, 1990; Pavlov and Kasting, 2002; Zahnle et al., 2006). I use H_2-dominated atmospheres as the representative cases for reducing atmospheres, and N_2- and CO_2- dominated atmospheres as the representative cases for oxidized atmospheres that could be both reducing and oxidizing.

Reducing H_2-Dominated Atmospheres

Both H_2S and SO_2 emitted from the surface are efficiently converted into elemental sulfur in reducing H_2 atmospheres. The major chemical pathways for sulfur compounds in the H_2-dominated atmosphere and the results of photochemistry model simulations are shown in Figure 3-6. Atomic hydrogen produced from photodissociation of water vapor and H_2S itself is the key reactive species that converts H_2S and SO_2 into elemental sulfur. The primary chemical loss for H_2S in the atmosphere is via

$$H_2S + h\nu \longrightarrow HS + H, \tag{C6}$$

and

$$H_2S + H \longrightarrow HS + H_2. \tag{C7}$$

The HS produced can then react with H again or with itself to produce elemental sulfur. HS can also react with S to produce S_2. The primary chemical loss for SO_2 in the atmosphere is photodissociation that produces SO. SO can be either photodissociated to elemental sulfur, or be further reduced to HS via HSO by H or

118

CHO and then converted to elemental sulfur (see Figure 3-6).

The S and S_2 molecules produced in the atmosphere will polymerize to form S_8, and S_8 will condense to form aerosols if it is saturated in the atmosphere. Due to its ring structure, S_8 is stable against photodissociation. S_8 is a strong UV absorber (Kasting, 1990). Therefore, S_8 aerosols, if produced in the atmosphere, can effectively shield UV photons so that H_2S and SO_2 may accumulate beneath the aerosol layer (see the case for a sulfur emission rate 300 times higher than Earth's current volcanic sulfur emission rate shown in Figure 3-6).

The primary source of atomic hydrogen is the photolysis of H_2O, which occurs above the altitudes of $\sim 10^3$ Pa pressure level. The atomic hydrogen can be then transported by eddy diffusion to the pressure level of $\sim 10^4$ Pa to facilitate the removal of H_2S and SO_2 and the production of elemental sulfur. Additional numerical simulations show that an increase of the eddy diffusion coefficient by one order of magnitude can increase the yield of elemental sulfur by about 20%, because the transport of atomic hydrogen becomes more efficient. A secondary source of atomic hydrogen is photolysis of H_2S (reaction C 6). This secondary source for atomic hydrogen is particularly important when the host star is a quiet M dwarf, because a quiet M dwarf produces few photons that could dissociate water[1]. For planets around quiet M dwarfs the photolysis of H_2S could be the main source of atomic hydrogen in their atmospheres. Additional numerical simulations show that in the habitable zone of a quiet M dwarf having an effective temperature of 3100 K, H_2S photolysis alone can produce enough atomic hydrogen to drive the formation of elemental sulfur in the atmosphere.

I here comment on the uncertainty of photochemistry models regarding the yield of S_8. In this study, I have assumed polymerization of elemental sulfur proceeds via

$$S + S \longrightarrow S_2 \,, \tag{C 8}$$

$$S + S_2 \longrightarrow S_3 \,, \tag{C 9}$$

---

[1]Water is principally dissociated by photons in the 150 - 200 nm wavelength range, whereas H_2S is principally dissociated by photons in the 200 - 260 nm wavelength range.
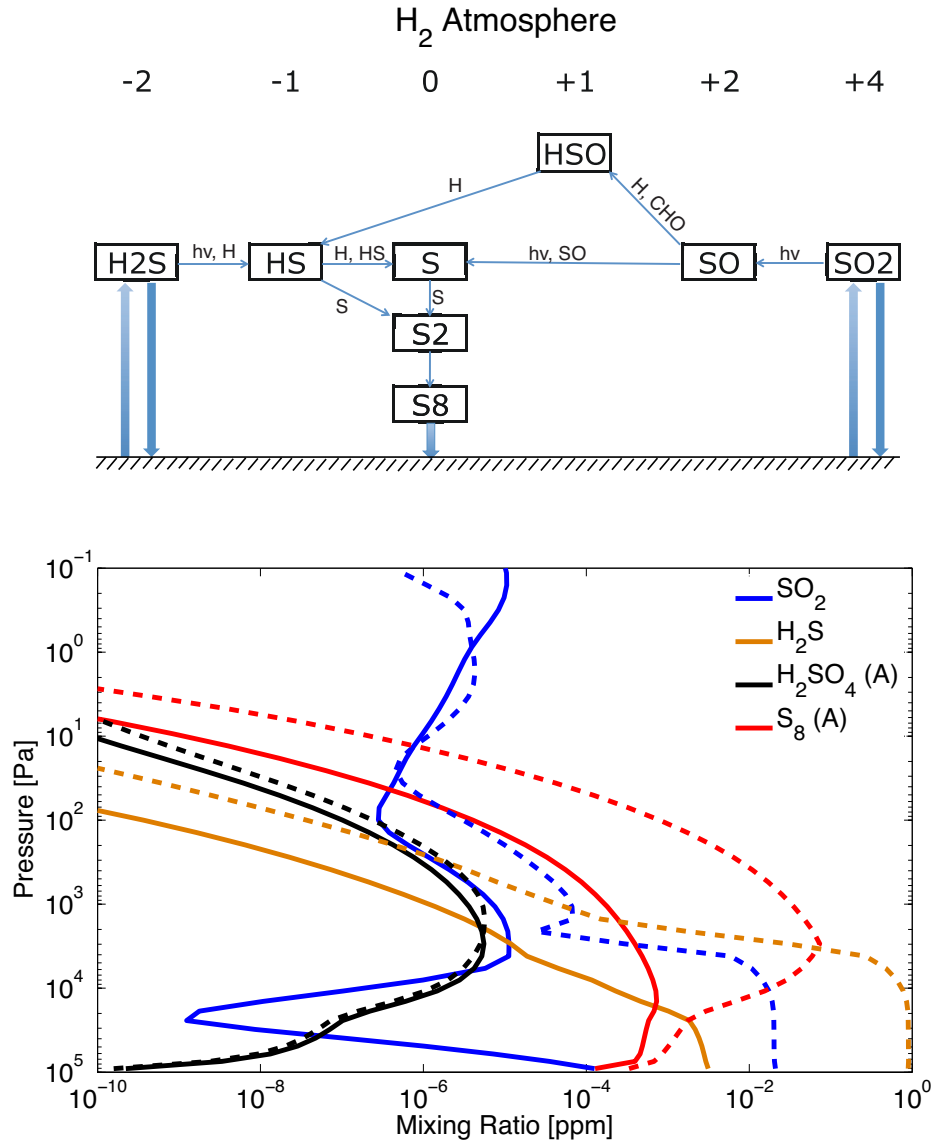
Figure 3-6: Formation of elemental sulfur aerosols in reducing H_2-dominated atmospheres on an Earth-sized rocky planet in the habitable zone of a Sun-like star. The upper panel schematically illustrates the chemical pathways from the primary sulfur emission (i.e., H_2S and SO_2) to elemental sulfur, in which sulfur compounds are located according to their oxidation states labeled on the top of the figure. The thin arrows show the major chemical pathways in the atmosphere, and the thick arrows show the major surface-atmosphere interactions. The lower panel shows the results of photochemistry simulations, with total surface sulfur emission of 10^{10} (solid lines) and 10^{12} (dashed lines) $cm^{-2}\,s^{-1}$, i.e, 3 and 300 times higher than the Earth's volcanic sulfur emission rate. The H_2S/SO_2 ratio in the sulfur emission is 0.5 and the particle mean diameter is 0.1 μm. Other model parameters are tabulated in Table 3.2. UV photons and atomic hydrogen effectively convert H_2S and SO_2 into elemental sulfur, and elemental sulfur aerosols shield UV photons so that H_2S and SO_2 may accumulate below the aerosol layer if the sulfur emission is more than 300 times higher than the Earth's volcanic emission rate.

$$S + S_3 \longrightarrow S_4 , \qquad\qquad (C\,10)$$

$$S_2 + S_2 \longrightarrow S_4 , \qquad\qquad (C\,11)$$

$$S_4 + S_4 \longrightarrow S_8 . \qquad\qquad (C\,12)$$

I have also included photodissociation for S_2, S_3, and S_4. However, the reaction rates of sulfur polymerization (reactions $C\,8$ - $C\,12$) have not been well established by laboratory studies, and previous authors have adopted different rate constants for these reactions. In particular, Kasting (1990) and Pavlov and Kasting (2002) have used 3-order-of-magnitude lower rates for reactions ($C\,8$ - $C\,9$) and 1-order-of-magnitude lower rates for reactions ($C\,10$ - $C\,12$), compared with Moses et al. (2002). In this work, I have adopted the reaction rates of Moses et al. (2002) for elemental sulfur reactions. My sensitivity tests show that adopting the reaction rates of Kasting (1990) would result in about 3 to 10 times less S_8. I have chosen a higher sulfur polymerization rates for nominal models because: (1) the chemical pathways of reactions ($C\,8$ - $C\,12$) are probably not complete and there may be other pathways to form S_8; (2) S_2, S_3, and S_4 may condense as suggested by Lyons (2008) and the polymerization may still proceed in the condensed phase to S_8. Experimental studies are encouraged to settle this important uncertainty.

Oxidized N_2 and CO_2-Dominated Atmospheres

H_2S and SO_2 gases emitted from the surface can be converted into both elemental sulfur (S_8) and sulfuric acid (H_2SO_4) in the oxidized (but anoxic) atmospheres such as N_2- and CO_2-dominated atmospheres. The major chemical pathways that lead to formation of both elemental sulfur and sulfuric acid, and the results of photochemistry model simulations are shown in Figure 3-7. The production of elemental sulfur aerosols involves UV photons and atomic hydrogen, as does in reducing H_2 atmospheres; whereas the production of sulfuric acid requires oxidizing species, notably OH and O_2. These reactive species, either reducing or oxidizing, are produced from photolysis of water and CO_2. In particular, the source of OH, responsible for con-

verting SO_2 to sulfuric acid in the atmosphere, is the photodissociation of H_2O. As a result, the amount of UV photons that are capable of dissociating water controls the yield of H_2SO_4. For example in the habitable zone of a quiet M dwarf the yield of H_2SO_4 is much reduced compared with solar-like stars by at least one order of magnitude.

The photochemically produced S_8 and H_2SO_4 may condense to form aerosols in the atmosphere if saturated. As a result, aerosols in the atmospheres provide a UV shield that enables the accumulation of H_2S and SO_2 beneath the layer of aerosols. In particular for an Earth-sized planet in the habitable zone of a Sun-like star, when the surface emission rate is more than two-orders-of-magnitude higher than the current Earth's volcanic sulfur emission rate, photochemical aerosols in the atmosphere lead to substantial UV shielding for accumulation of H_2S and SO_2, as shown in Figure 3-7. I find that only when sulfur emission is highly elevated with respect to current Earth could H_2S or SO_2 accumulate to the order of parts per million mixing ratio in the N_2 and CO_2 atmospheres.

The relative yield between elemental sulfur and sulfuric acid is controlled by the redox power of the atmosphere. In general, more sulfuric acid aerosols and less elemental sulfur aerosols are anticipated in a more oxidizing atmosphere. The redox power of the atmosphere, in turn, is determined by both the main constituent and the reducing gas emission. CO_2-dominated atmospheres are more oxidizing than N_2-dominated atmospheres as photodissociation of CO_2 leads to atomic oxygen. Therefore the primary sulfur emission is more likely to be converted to sulfuric acid in CO_2-dominated atmospheres than in N_2-dominated atmospheres (see Figure 3-7). Surface emission of reducing gases, including H_2, CH_4, CO, and H_2S, alters the redox budget of the atmosphere and therefore increases the relative yield of elemental sulfur versus sulfuric acid aerosols (e.g. Zahnle et al., 2006). As shown in Figure 3-7, when the sulfur emission rate increases, both N_2 and CO_2 atmospheres become more and more reducing (because H_2S is reducing), which results in a dramatic increase of elemental sulfur production in the atmosphere. Furthermore, the H_2S/SO_2 ratio in the sulfur emission affects its contribution to the redox power of the atmosphere and then
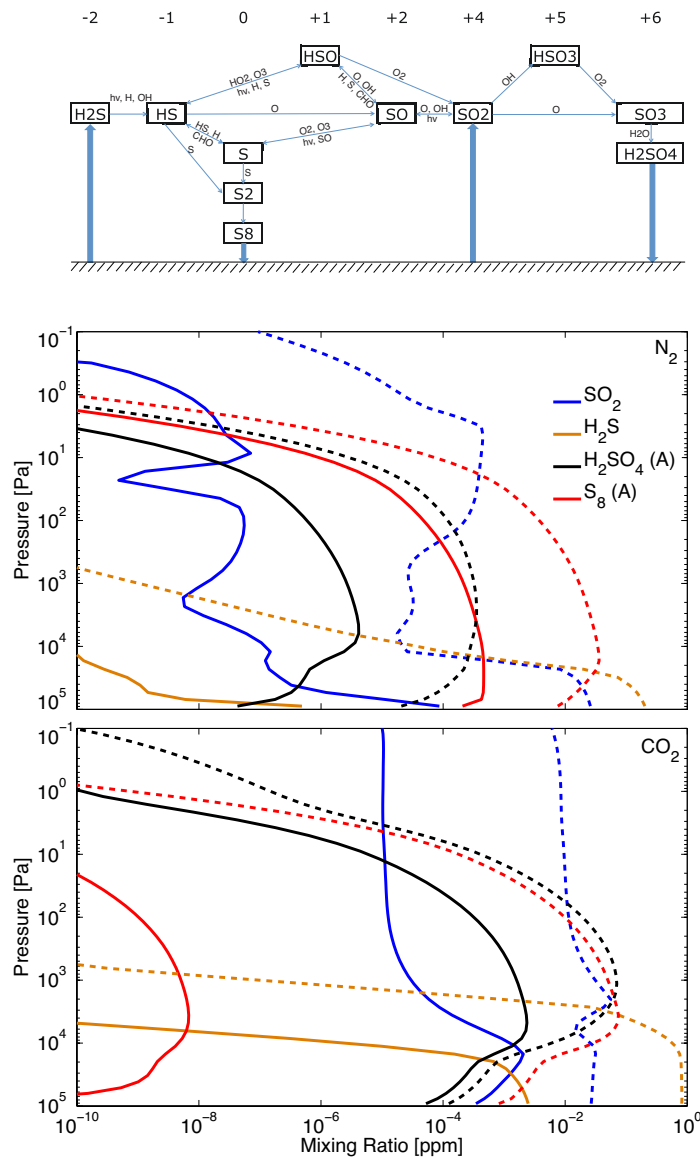
Figure 3-7: Formation of elemental sulfur and sulfuric acid aerosols in oxidized N_2-
and CO_2-dominated atmospheres on an Earth-sized rocky planet in the habitable zone
of a Sun-like star. Similar to Figure 3-6, the upper panel schematically illustrates the
chemical pathways from the primary sulfur emissions (i.e., H_2S and SO_2) to elemental
sulfur and sulfuric acid. For double arrows the label above the arrow indicates the
oxidizing agents, and the label below the arrow indicates the reducing agents. The
lower two panel shows the results of photochemistry simulations for N_2- and CO_2-
dominated atmospheres, respectively. The total surface sulfur emission is 10^{10} (solid
lines) and 10^{12} (dashed lines) cm^{-2} s^{-1}, i.e, 3 and 300 times higher than the Earth's
volcanic sulfur emission rate. The H_2S/SO_2 ratio in the sulfur emission is 0.5 and the
particle mean diameter is 0.1 μm. Other model parameters are tabulated in Table 3.2.
Both elemental sulfur aerosols and sulfuric acid aerosols are formed in the oxidized
and anoxic atmospheres. The origins of the principle reducing agents (H and CHO)
and the principle oxidizing agents (OH, O and O_2) is photodissociation of H_2O and
CO_2. The apparent depletion of SO_2 at the pressure level of 10 - 100 Pa in the N_2
atmosphere (the blue solid line in the middle panel) is due to the production of atomic
hydrogen by methane photodissociation at this pressure level.
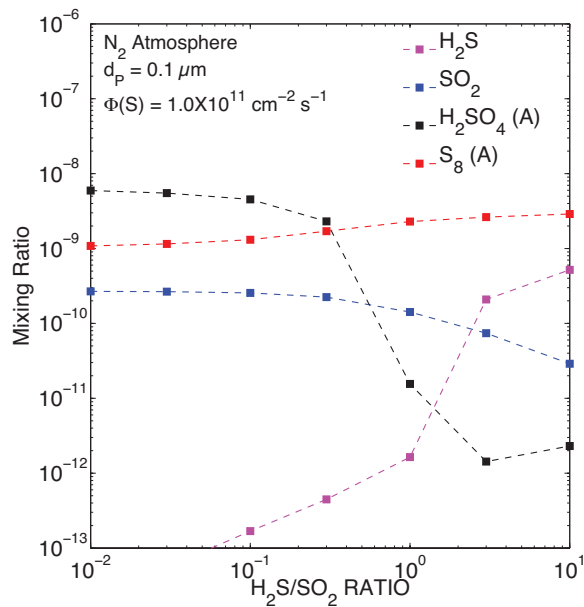
Figure 3-8: Correlation between the aerosol composition and the composition of sulfur emissions in the weakly oxidizing N_2 atmosphere on an Earth-sized rocky planet in the habitable zone of a Sun-like star. The total surface emission rate is 10^{11} cm^{-2} s^{-1}, or 30 times the Earth's volcanic sulfur emission rate, and the particle mean diameter is 0.1 μm. Other model parameters are tabulated in Table 3.2. As a larger fraction of surface sulfur emission is in the form of H_2S, the amount of S_8 aerosols in the atmosphere increases, and the amount of H_2SO_4 aerosols in the atmosphere decreases dramatically.

the relative abundances of the two types of aerosols in the atmosphere significantly. As a result of the increase in the H_2S/SO_2 emission ratio, the amount of S_8 aerosol in the atmosphere increases, and the amount of H_2SO_4 in the atmosphere decreases dramatically (see Figure 3-8). For an Earth-like planet having an N_2 atmosphere, if the H_2S/SO_2 emission ratio is less than 0.1 (as is the case for current Earth; Holland, 2002), the dominant type of aerosols in the atmosphere is sulfate; whereas elemental sulfur aerosols become the dominant type if the H_2S/SO_2 emission ratio is larger than 1.

3.4.4 Results

Optically Thick Aerosols from Sulfur Emission

The main finding is that on terrestrial exoplanets having atmospheres ranging from reducing to oxidizing, the primary sulfur emission from the surface (e.g., H_2S and SO_2) is chemically short-lived. The sulfur emission leads to photochemical formation of

elemental sulfur (S_8) and sulfuric acid (H_2SO_4), which would condense to form aerosols if saturated in the atmosphere. In reducing atmospheres (e.g., H_2 atmospheres), S_8 aerosols are photochemically formed based on H_2S and SO_2 emission; and in oxidized atmospheres (e.g., N_2 and CO_2 atmospheres), both S_8 and H_2SO_4 aerosols may be formed (see Figure 3-9). In general, the higher the surface sulfur emission, the more aerosols exist in the atmosphere (see Figure 3-9).

As a result of photochemical production of elemental sulfur and sulfuric acid, terrestrial exoplanets with a habitable surface temperature (e.g., $270 \sim 320$ K) and substantial sulfur emission from the surface are likely to have hazy atmospheres. Here I use "hazy" to describe an atmosphere that has significant aerosol opacities at visible wavelengths (e.g., 500 nm). Even with an Earth-like surface sulfur emission, 1-bar H_2-dominated atmospheres on habitable rocky exoplanets are hazy with S_8 aerosols (see Figure 3-9). If the sulfur emission rate is $30 \sim 300$ times more than the Earth's current volcanic sulfur emission rate, photochemical S_8 aerosols become optically thick at visible wavelengths in oxidized atmospheres including N_2 and CO_2 atmospheres (see Figure 3-9).

The key parameters that determine the aerosol opacity in the atmosphere are the surface sulfur emission rate, the dry deposition velocity, and the aerosol particle size. First, a higher surface sulfur emission rate leads to more sulfur and sulfate aerosols in anoxic atmospheres (e.g., Figure 3-9 and Figure 3-10). Second, larger dry deposition velocities of H_2S and SO_2 cause more rapid removal of these sulfur compounds from the atmosphere, which reduces the chance of converting them into condensable molecules (i.e., S_8 and H_2SO_4). Therefore, larger dry deposition velocities of H_2S and SO_2 result in lower aerosol loading and aerosol opacities in the atmospheres, as shown in Figure 3-11. Third, I find that the particle size has only secondary effects on the chemical composition of the atmosphere (i.e., by increasing the penetration of ultraviolet radiation), but has a primary effect on the aerosol optical depth. For mean particle diameter varying in the range of $0.1 \sim 1$ μm (i.e., typical particle sizes of photochemical aerosols on Earth (e.g. Seinfeld and Pandis, 2006) and Titan (e.g. Rages et al., 1983)), one does not see a notable variation in the yield of elemental
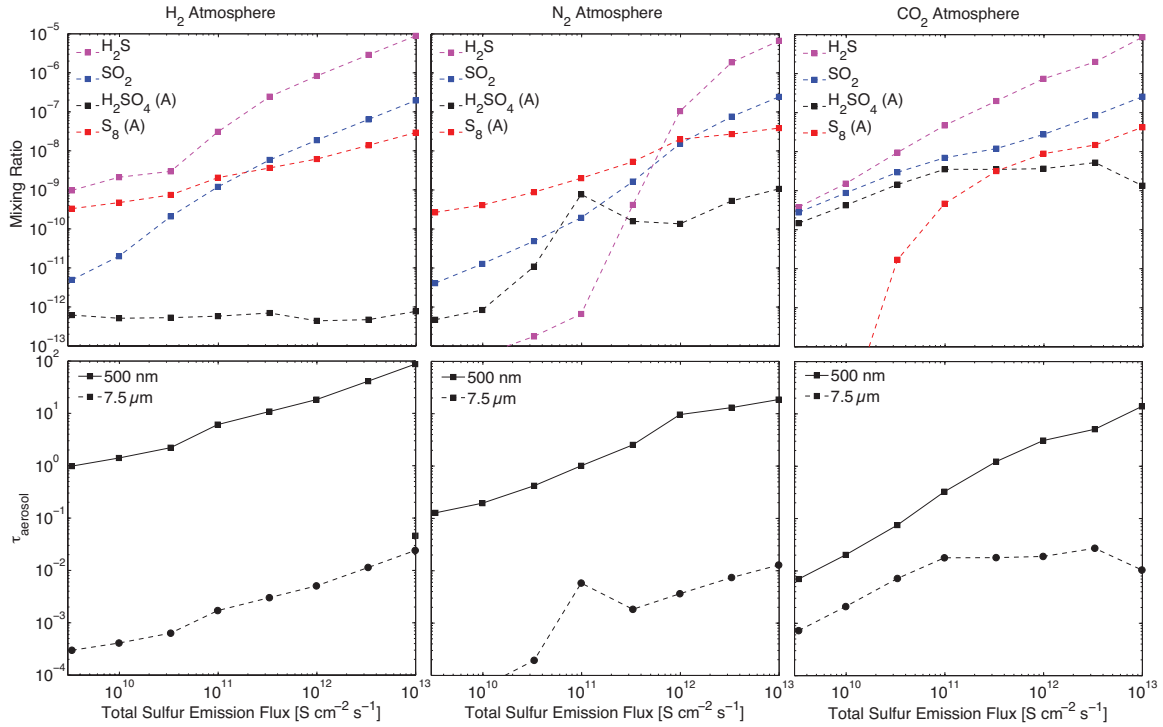
Figure 3-9: The relationship between the aerosol mixing ratios and aerosol opacities and the total sulfur emission rate. Column-integrated aerosol opacities at the 1-bar pressure level including both elemental sulfur aerosols and sulfuric acid aerosols at 500 nm (solid lines) and 7.5 μm (dashed lines) are shown in the lower panel. The planet is an Earth-sized rocky planet orbiting a Sun-like star, with reducing (H_2-dominated), weakly oxidizing (N_2-dominated), or highly oxidizing (CO_2-dominated) atmospheres. The aerosol particle mean diameter is assumed to be 0.1 μm, and the H_2S/SO_2 ratio of the surface emission is 0.5. Other model parameters are tabulated in Table 3.2. Sulfur emission 2-orders-of-magnitude larger than current Earth's volcanic sulfur emission ($\sim 3 \times 10^9$ S cm^{-2} s^{-1}) leads to substantial aerosol opacities in the visible wavelengths in N_2 and CO_2 atmospheres, and sulfur emission comparable with current Earth's volcanic sulfur emission leads to substantial aerosol opacities in the visible wavelengths in H_2 atmospheres. The wiggle in the concentration of sulfuric acid aerosols reflects the competition between two effects: more sulfur is available to be converted into sulfuric acid as the sulfur emission increases, but the atmosphere becomes more reducing and less oxidizing as the sulfur emission increases.
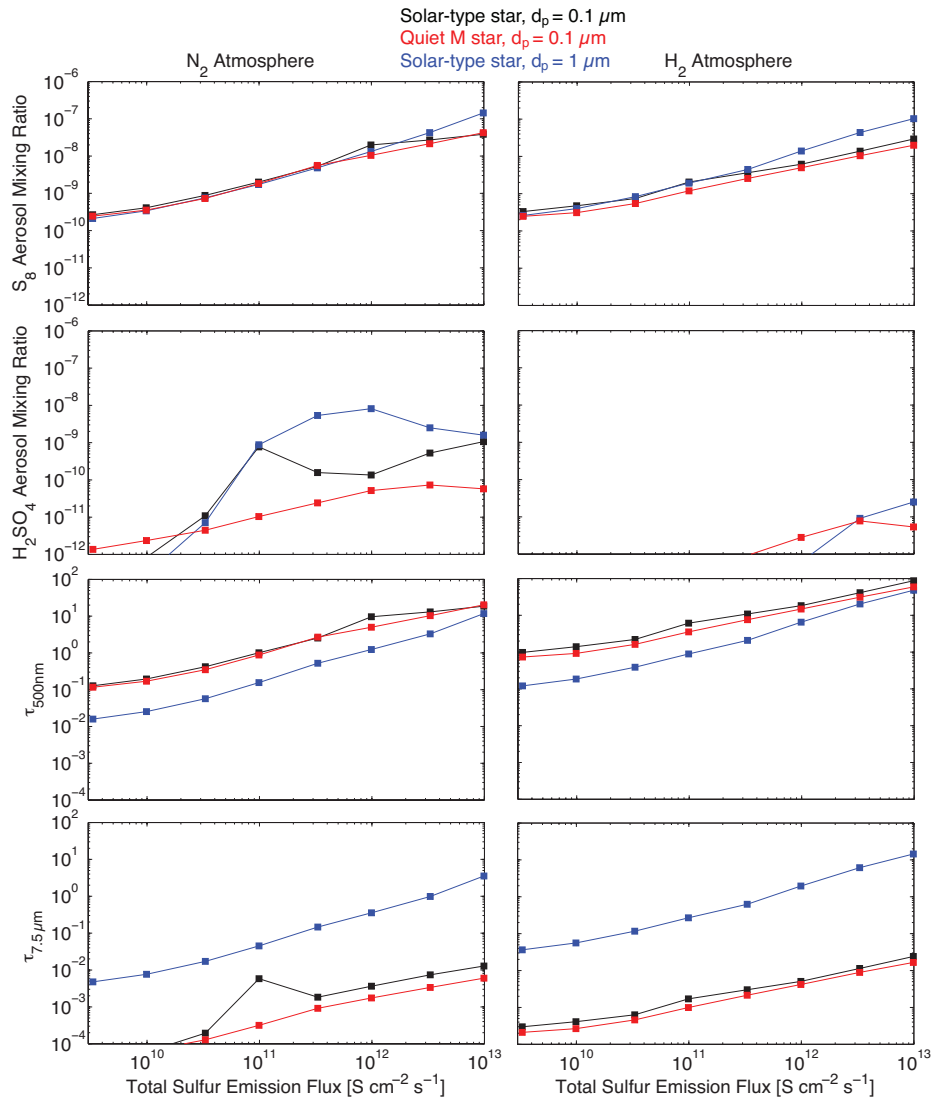
Figure 3-10: Aerosol mixing ratios and optical depths at the surface (1-bar pressure level) at 500 nm and 7.5 μm as a function of total sulfur emission rates, for an Earth-sized rocky planet orbiting a Sun-like star at 1 AU (black lines), a habitable planet around quiet M dwarf having effective temperature of 3100 K (red lines), and an Earth-sized rocky planet orbiting a Sun-like star at 1 AU with particle mean diameter of 1 μm (blue lines). The left column shows the case of weakly oxidizing N_2 atmospheres, and the right column shows the case of reducing H_2 atmospheres. The H_2S/SO_2 ratio in the sulfur emission is 0.5 and other model parameters are tabulated in Table 3.2. Decreasing UV photon flux has little effect on the S_8 formation, but results in a decrease of the amount of sulfuric acid aerosols, and therefore a decrease of MIR optical depth. Also, particle diameter variation in 0.1 $\sim$ 1 μm has little effect on the chemical composition, but for similar mass abundance a larger particle size results in a smaller optical depth in the visible wavelengths and a larger optical depth in the MIR wavelengths.
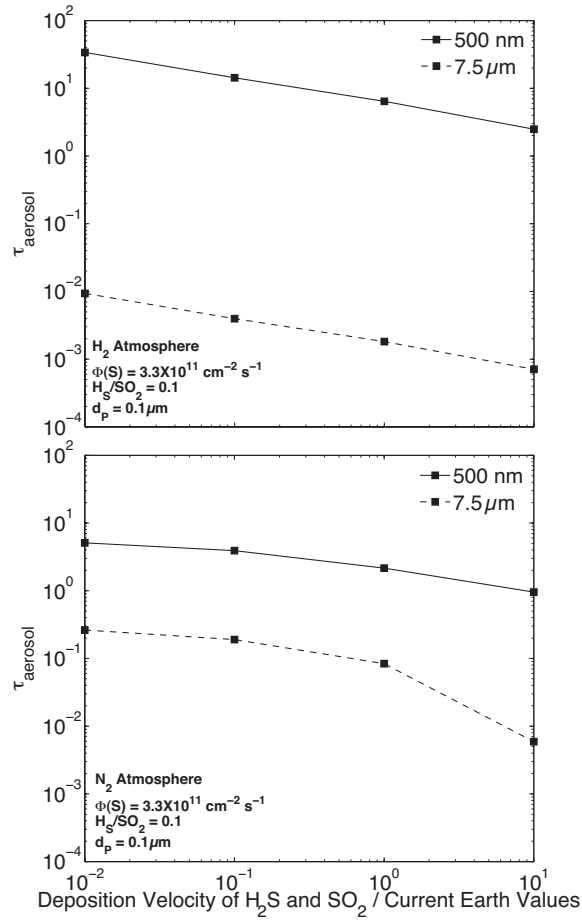
Figure 3-11: The relationship between the aerosol opacities (both S_8 and H_2SO_4 aerosols) at 500 nm and 7.5 μm in the H_2 and N_2 atmospheres and the H_2S and SO_2 dry deposition velocities. Model parameters are shown in the figure and tabulated in Table 3.2.
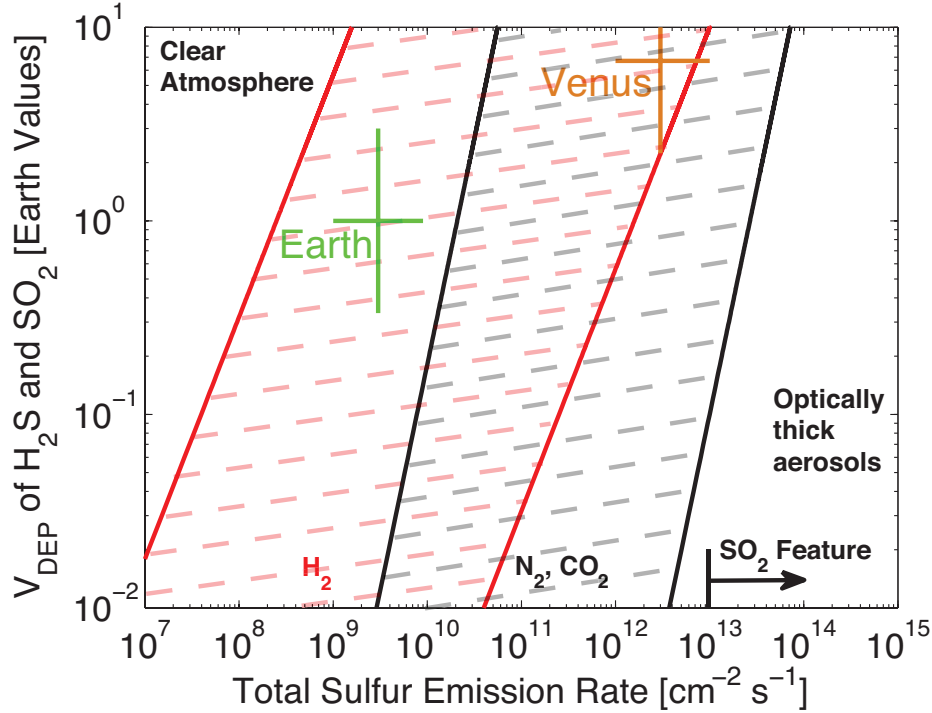
Figure 3-12: Formation of optically thick aerosols in atmospheres on rocky exoplanets in the habitable zone of their host star as a result of surface sulfur emission and deposition. The shaded areas are the parameter regime boundaries between a clear atmosphere and an optically thick atmosphere (defined as aerosol optical depth at 500-nm wavelength $\tau_{500nm} > 1$), for reducing (H_2) and oxidized (N_2 and CO_2) atmospheres. The upper-left corner of the parameter regime (small sulfur emission rates, large deposition velocities) leads to clear atmospheres; whereas the lower-right corner of parameter regime (large sulfur emission rates, small deposition velocities) leads to optically thick aerosols in the atmosphere composed of sulfur (S_8) and sulfate (H_2SO_4). The widths of the shaded boundary regime between clear atmospheres and optically thick atmospheres contain the uncertainties of: (1) the mean aerosol particle size ranging from 0.1 to 1 μm, (2) the H_2S/SO_2 ratio of the sulfur emission ranging from 0.01 to 10 (i.e., more H_2S leads to thicker haze), (3) the spectral type of the host star ranging from G2V to M5, (4) the strength of vertical mixing in the atmosphere by eddy diffusion ranging from 0.1 to 10 times Earth's value, and (5) the surface temperature ranging from 270 to 320 K. Earth and Venus are shown for a reference in the Solar System: Earth's volcanic sulfur emission and H_2S deposition velocity are plotted; and Venus' equivalent upward SO_2 flux and SO_2 deposition velocity at the altitude of 58 km are plotted (adapted from Krasnopolsky (2012)). Note that the equivalent SO_2 flux is a transfer rate across the 58-km altitude, and does not imply a surface emission rate. The SO_2 features at 7.5 μm and 20 μm requires a mixing ratio on the order of ppm to be spectrally significant, which corresponds to a sulfur emission flux of more than 10^{13} cm^{-2} s^{-1} due to rapid photochemical removal of SO_2 in the atmosphere.

sulfur, but one could see an enhancement of H_2SO_4 production with large particles (Figure 3-10). Even with the same aerosol abundances, however, micron-sized particles cause lower opacities at the visible wavelengths and higher opacities in MIR compared with submicron-sized particles (Figure 3-10).

I attempt to capture the effects of the three key parameters on the aerosol opacity in anoxic atmospheres on terrestrial exoplanets by fitting the following power-law formula, i.e.,

$$\tau = C\left(\frac{\Phi(S)}{10^{11} \text{ cm}^{-2} \text{ s}^{-1}}\right)^{a}\left(\frac{V_{\text{DEP}}}{V_{\text{DEP}}(\text{Earth})}\right)^{-b}\left(\frac{d_{\text{P}}}{0.1 \ \mu\text{m}}\right)^{-c}, \tag{3.2}$$

where τ is the vertical optical depth due to aerosols at 1 bar, $\Phi(S)$ is the total sulfur emission rate, $V_{\text{DEP}}/V_{\text{DEP}}(\text{Earth})$ is the dry deposition velocities of H_2S and SO_2 with respect to current Earth values, d_{p} is the mean particle diameter of aerosols, a, b, and c are positive numbers, and C is a constant that covers other uncertainties. I have fit the empirical relation (3.2) through an extensive parameter exploration using photochemistry models (see Figure 3-9 - 3-11 for examples) and determined the values of C, a, b and c for H_2-dominated reducing atmospheres and for N_2- and CO_2-dominated oxidized atmospheres. I summarize graphically the parameter regime in which sulfur emission leads to a hazy atmosphere in Figure 3-12. Here I use $\tau_{500\text{nm}}$ and $\tau_{7.5\mu\text{m}}$ as the representatives for aerosol opacities at visible wavelengths and MIR wavelengths; due to the complex nature of the extinction cross sections of aerosol particles (Figure 3-5), it is not practical to fold the full wavelength dependency into the empirical formula. Also, I find that it is always true that $\tau_{500\text{nm}} \sim 0$ for mean particle diameter in the order of 10 μm and $\tau_{7.5\mu\text{m}} \sim 0$ for mean particle diameter in the order of 0.1 μm.

For H_2 atmospheres, and mean particle diameter d_{P} in the the range of $0.1 \sim 1$ μm,

$$\tau_{500\text{nm}} = 1 \sim 20\left(\frac{\Phi(S)}{10^{11} \text{ cm}^{-2} \text{ s}^{-1}}\right)^{0.5}\left(\frac{V_{\text{DEP}}}{V_{\text{DEP}}(\text{Earth})}\right)^{-0.4}\left(\frac{d_{\text{P}}}{0.1 \ \mu\text{m}}\right)^{-0.6}, \tag{3.3}$$

and for d_P in the the range of $1 \sim 10$ μm,

$$\tau_{7.5\mu m} = 0.1 \sim 1 \left(\frac{\Phi(S)}{10^{11} \text{ cm}^{-2} \text{ s}^{-1}} \right)^{0.7} \left(\frac{V_{\text{DEP}}}{V_{\text{DEP}}(\text{Earth})} \right)^{-0.4} \left(\frac{d_P}{1.0 \ \mu m} \right)^{-1.5}. \quad (3.4)$$

For N_2 and CO_2 atmospheres, and d_P in the the range of 0.1 and 1 μm,

$$\tau_{500nm} = 0.1 \sim 3 \left(\frac{\Phi(S)}{10^{11} \text{ cm}^{-2} \text{ s}^{-1}} \right)^{0.7} \left(\frac{V_{\text{DEP}}}{V_{\text{DEP}}(\text{Earth})} \right)^{-0.3} \left(\frac{d_P}{0.1 \ \mu m} \right)^{-0.7}, \quad (3.5)$$

and for d_P in the the range of $1 \sim 10$ μm,

$$\tau_{7.5\mu m} = 0.01 \sim 0.1 \left(\frac{\Phi(S)}{10^{11} \text{ cm}^{-2} \text{ s}^{-1}} \right)^{0.8} \left(\frac{V_{\text{DEP}}}{V_{\text{DEP}}(\text{Earth})} \right)^{-0.5} \left(\frac{d_P}{0.1 \ \mu m} \right)^{-1.6}. \quad (3.6)$$

The constant C in Equations (3.3 - 3.6) spans about one order of magnitude, which covers the variation of the following model inputs:

- The H_2S/SO_2 ratio in the surface sulfur emission, ranging from 0.01 to 10;

- Temperature profiles deviating from the adopted temperature profile by ± 30 K that controls the mixing ratio of water vapor in the atmosphere by the cold trap;

- Stellar ultraviolet radiation received by the planet, ranging from the habitable zone of solar-like stars to the habitable zone of quiet M dwarfs with an effective temperature of 3100 K;

- Eddy diffusion coefficients ranging from 0.1 to 100 times the values of Earth's atmosphere;

- Sulfur polymerization reaction rates (reactions C 8 - C 12) ranging by one order of magnitude.

To summarize, I find that the emission of H_2S and SO_2 from the surface is readily converted into sulfur (S_8) and sulfate (H_2SO_4) in anoxic atmospheres of terrestrial exoplanets. The photochemical sulfur and sulfate would condense to form aerosols if

saturated in the atmosphere, which is likely to occur on a planet in the habitable zone of either a Sun-like star or a quiet M star. The aerosol layer is optically thick at the visible and NIR wavelengths if the surface sulfur emission is comparable to Earth's volcanic sulfur emission in the H_2 atmosphere, and more than $30 \sim 300$ times of the Earth's volcanic sulfur emission in other anoxic atmospheres, depending on the dry deposition velocities of sulfur compounds and particle size of the aerosols.

Spectral Features of SO_2, H_2S, and S_8 and H_2SO_4 Aerosols

The sulfur emission from surface shapes the spectra of terrestrial exoplanets at the visible and NIR wavelengths, mostly through the photochemical formation of S_8 and H_2SO_4 aerosols. I use the model outputs from the photochemistry models to compute the transmission, reflection, and thermal emission spectra of a terrestrial exoplanet with various levels of sulfur emission, and show examples of the computed spectra in Figure 3-13. Submicron-sized S_8 aerosols dominate the transmission and reflection spectra at wavelengths from visible up to 3 μm, if the sulfur emission is more than about two orders of magnitude higher than Earth's volcanic sulfur emission. In general, an atmosphere with high sulfur emission and therefore high aerosol loading generally exhibits a flat transmission spectrum (the H_2O features at NIR muted), and a high visible albedo (see Figure 3-13). Notably, S_8 aerosols are purely reflective at 500 nm but absorptive at 300 nm. The absorption edge of S_8 aerosols in 300 - 400 nm is evident in the reflection spectra for planets with enhanced sulfur emission (Figure 3-13), which is a potential diagnostic feature for S_8 aerosols.

Although opaque at visible wavelengths, the atmospheres with enhanced sulfur emission are likely to be transparent in the MIR wavelengths ($\lambda > 5$ μm). The spectral features of aerosols depend on their particle sizes, so one could consider two possibilities: if the particles are submicron-sized, the aerosol molecules have negligible cross sections at MIR (see Figure 3-5); or if the particles are micron-sized, the falling velocity of aerosol particles is large enough to rapidly remove aerosols from the atmosphere, as implied by Equation (3.4) and Equation (3.6) that are applicable for micron-sized particles. Therefore in both cases the aerosol opacities at MIR are

132
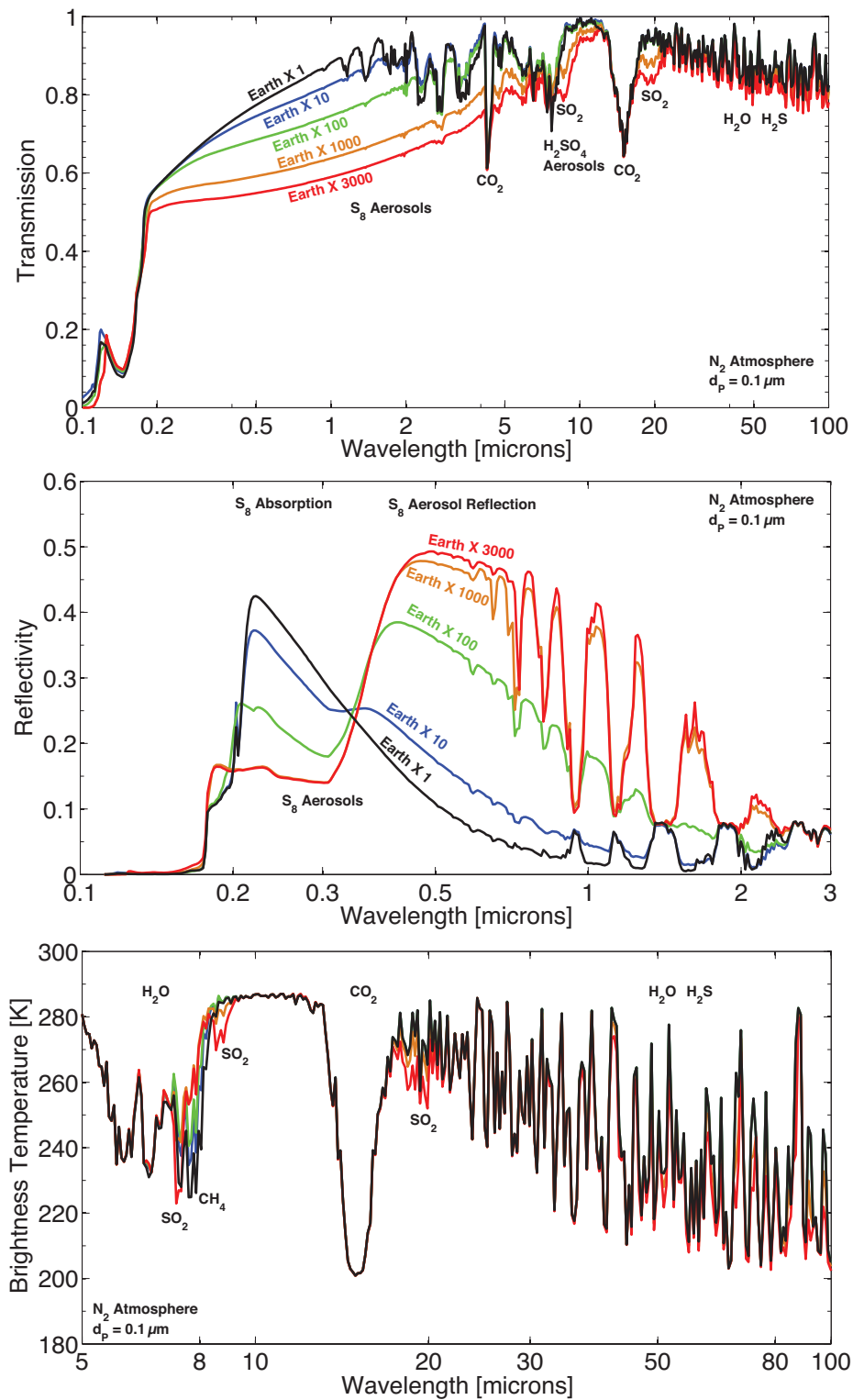
Figure 3-13: Transmission, reflection and thermal emission spectra of a terrestrial exoplanet with an N_2-dominated atmosphere with various surface sulfur emission up to 3000 times Earth's current volcanic emission (labeled in colors). The planet is an Earth-sized planet at the 1-AU orbit a Sun-like star, having surface temperature of 288 K. The H_2S/SO_2 emission ratio is 0.5, the aerosol particle diameter is assumed to be 0.1 μm, and other model parameters are tabulated in Table 3.2. The cross sections of S_8 and H_2SO_4 aerosols are shown in Figure 3-5.

minimal even for very high sulfur emission rates (see Figure 3-13 for examples of N_2 atmospheres, and H_2 atmospheres are qualitatively similar). The only exception, in which aerosols indeed affect MIR spectra, is the case of abundant H_2SO_4 aerosols. The main spectral effect of H_2SO_4 aerosols is absorption at MIR wavelengths ($5 \sim 10$ μm; Figure 3-13). However, the column-average mixing ratio of H_2SO_4 needs to be larger than 0.1 ppm in order to produce significant aerosol absorption at MIR. I find with numerical exploration that such a high abundance of H_2SO_4 aerosols is only possible in highly oxidizing CO_2-dominated atmospheres without reducing gas emission (see Section 3.3.2 for an example of such atmospheres). With reducing gas emission (i.e., H_2 and CH_4), it is unlikely that H_2SO_4 mixing ratio exceeds 0.01 ppm in anoxic atmospheres for a wide range of sulfur emission rates (see Figure 3-9). In summary the spectral effects of S_8 and H_2SO_4 aerosols should be minimal at MIR for most cases.

I now turn to consider the direct spectral features of H_2S and SO_2. It has been previously proposed that H_2S and SO_2 can be detectable on terrestrial exoplanets by their spectral features (Kaltenegger and Sasselov, 2010). However, my photochemistry models show that both H_2S and SO_2 are chemically short-lived in the atmospheres, which implies that that substantial surface emission is required to maintain a detectable level of either H_2S or SO_2 in the atmosphere. SO_2 has diagnostic absorption features at 7.5 μm and 20 μm (see Figure 3-13). For these features to be detectable the mixing ratio of SO_2 needs to be larger than 0.1 ppm, which corresponds to sulfur emission rates 1000 times more than current Earth's sulfur emission rates for H_2, N_2, and CO_2 atmospheres (see Figure 3-9). The spectral feature of H_2S is the pseudo-continuum absorption at wavelengths longer than 30 μm, which coincides with the rotational bands of H_2O. I find that the only scenario in which H_2S may be directly detected is the case with extremely high sulfur emission rates (i.e., 3000 times higher than the current Earth's sulfur emission rate) on a highly desiccated planet without liquid water ocean so that there is no water vapor contamination. I therefore conclude that direct detection of H_2S and SO_2 is tricky: they are chemically short-lived so that extremely large surface emission is required for a detectable mixing ratio in

the atmosphere, and their spectral features may be contaminated by other gases in the atmosphere.

Finally, I propose that the emission of sulfur compounds might be indirectly inferred by detecting sulfur and sulfate aerosols. My numerical exploration reveals a monotonic relationship between the abundance of aerosols in the atmosphere and the emission rates of sulfur compounds (see Figure 3-9), and the composition of aerosols is correlated with the H_2S/SO_2 ratio of the surface emission (see Figure 3-8). A combination of featureless low atmospheric transmission (large planet radius viewed in transits) and high planetary albedo (large planetary flux at the visible wavelengths viewed in occultations) may establish the existence of aerosols in the atmosphere. In particular, elemental sulfur (S_8) aerosols are absorptive at wavelengths shorter than 400 nm and therefore might be identified by the absorption edge (see Figure 3-13). Sulfate aerosols (H_2SO_4), if abundant in the atmosphere, lead to absorption features at the MIR wavelengths ($\lambda \sim 5$ - 10 μm). However, none of these features are uniquely diagnostic of certain types of aerosols. The identification of aerosol composition, therefore, is by no means straightforward. I learn from the Solar System exploration that the discriminating piece of information for aerosol identification comes from polarization of reflected stellar light. Historically, the bright clouds on Venus were identified to be mainly composed of H_2SO_4 droplets after the phase curve of the planet in polarized light had been observed (e.g. Young, 1973; Hansen and Hovenier, 1974). I therefore postulate that aerosol identification on terrestrial exoplanets and the inference of surface sulfur emission might require observation of polarized reflected light as a function of planetary illumination phase.

3.4.5 Can H$_2$S be a Biosignature Gas?

H$_2$S can be produced from several metabolic origins on Earth, and so is a candidate biosignature gas. Life on Earth can produce H$_2$S through sulfate reduction (when the environment is reduced) and sulfur disproportionation. Microorganisms can disproportionate sulfur compounds of intermediate oxidation states, including thiosulfate, sulfite, and elemental sulfur, into H$_2$S and sulfate (Finster, 2008). For example, dis-

proportionation of sulfite in the ocean is described by

$$4\,SO_3^{2-} + H^+ \longrightarrow 3\,SO_4^{2-} + HS^-, \qquad\qquad (C\,13)$$

in which the Gibbs free energy released is 58.9 kJ mol^{-1} sulfite. The sulfite reducers, including microorganisms in genus *Desulfovibrio* and *Desulfocapsa*, extract energy from the disproportionation (Kramer and Cypionka, 1989).

The effect of biotic H_2S production is the increase of the H_2S/SO_2 ratio of the surface sulfur emission. If the H_2S/SO_2 ratio in the volcanic sulfur emission is low (i.e., less than 0.1), sulfur disproportionation and sulfate reduction by life may increase the H_2S/SO_2 ratio significantly, which may lead to a change in the redox input to the atmosphere and therefore the dominant aerosol species in the atmosphere, as suggested by Figure 3-8. Specifically, for a habitable terrestrial exoplanet having a weakly oxidizing N_2 atmosphere, biotic production of H_2S in excess of the geological H_2S emission could result in a higher amount of S_8 aerosols and a much lower amount of H_2SO_4 aerosols in the atmosphere compared with a planet without life. Although it is currently not possible to distinguish different types of aerosols, H_2S could be a biosignature gas in the long term.

The geological production of H_2S, and the consequent risk of a false positive mis-identification of geological H_2S for biological H_2S, will be a major obstacle of confirming H_2S to be a biosignature gas. Sulfur is believed to be present in the mantle of all terrestrial planets, and what determines the H_2S/SO_2 ratio in the volcanic outgassing is the oxygen fugacity of the upper mantle, temperature of the location where magma degassing happens, water content in the conduit of magma, and gas content dissolved in the magma (e.g. Holland, 1984; Kasting et al., 1985; Holland, 2002; Burgisser and Scaillet, 2007). The current Earth volcanic emissions are oxidized, dominated by H_2O, CO_2 and SO_2 with minor contributions of H_2, CO and H_2S. This volcanic gas composition is consistent with a magma buffered by the quartz-fayalite-magnetite (QFM) equilibrium, i.e., a relatively oxidized upper mantle (Holland, 1984). As a global average, the volcanic H_2S/SO_2 emission ratio on Earth is 0.1 (Holland,

2002). However, if the mantle of a rocky exoplanet is much more reducing than that of the current Earth, significant geological source of H_2S can be expected (Holland, 1984; Kasting et al., 1985). As a result, it would be very hard to rule out a geological contribution to the H_2S emission flux by remote sensing.

In summary, although H_2S can be produced by energy-yielding metabolism, it is very unlikely to be a useful biosignature gas for three reasons. Firstly, H_2S itself is unlikely to be detectable directly by remote sensing because of its weak spectral features, and their contamination by the spectral features of water. Secondly, H_2S has a very short atmospheric lifetime, and so unrealistic emission rates are required to build up significant levels in any atmosphere. This second point could be overcome, in principle, by detecting S_8 aerosols in an anoxic atmosphere, and discriminating them from H_2SO_4 aerosols. Discrimination between sulfur and sulfuric acid aerosols is not possible with current equipment, but may be possible in the future through analysis of reflected light. Thirdly, however, H_2S suffers from a significant false positive risk, as geological sources can also produce H_2S, and the ratio of H_2S/SO_2 in geological emissions depends on mantle chemistry, the physical structure of the outgassing events, and the extent of surface reprocessing of vented sulfur gases. To infer that life was generating H_2S on a planet, this study shows that the observer would have to determine the S_8/H_2SO_4 aerosol ratio and have knowledge of the geological outgassing ratio of H_2S/SO_2 and have knowledge of the surface chemistry that might modulate the primary outgassing rate. This seems an unreasonable requirement.

3.5   Summary

Using the photochemistry model, I have investigated the main chemical processes and the lifetimes of key spectrally active species for terrestrial exoplanet thin atmospheres by simulating benchmark cases of atmospheres having redox states ranging from reducing to oxidizing. The most important general finding is that atomic hydrogen is a more abundant reactive radical than hydroxyl radical in anoxic atmospheres, and therefore reactions with atomic hydrogen are likely to be an important removal path-

137

way for spectrally important trace gases. The source of H and OH is water vapor photolysis in anoxic atmospheres, and the abundance of H in the atmosphere is always larger than the amount of OH because OH can react with H_2 or CO to produce H. In addition to atomic hydrogen, in weakly oxidizing N_2 atmospheres, OH, despite its lower abundance than H, is important in removing CH_4 and CO. In highly oxidizing CO_2 atmospheres, atomic oxygen is the most abundant reactive species.

The most intriguing finding is that the redox power of a thin atmosphere on a terrestrial exoplanet can be significantly affected by the surface emission and deposition of trace gases. In one example, I have demonstrated that a high CO_2 emission rate (or a low CO_2 deposition velocity) could make a H_2-dominated atmosphere both reducing and oxidizing. In another example, I have for the first time shown that it is the surface emission of reducing gases (e.g., CH_4 and H_2) that controls whether free oxygen can be photochemically formed in a CO_2-dominated atmosphere. Without surface emission of CH_4 or H_2, the photochemical processes can produce molecular oxygen that accumulates in a 1-bar CO_2-dominated atmosphere to the levels that have conventionally considered unique signature of life. This finding is in particular relevant for the design of a TPF-like mission via detecting O_2 feature in reflection. I suggest that simultaneous detection of oxygen and methane, instead of oxygen alone, would be a rigorous biosignature.

In general, I find that volcanic carbon compounds are long-lived and volcanic sulfur compounds are short-lived. Methane is always long-lived having chemical lifetime longer than 10,000 years, due to the scarcity of OH in anoxic atmospheres. In contrast to carbon species, volcanic sulfur compounds (i.e., H_2S and SO_2) are readily converted into either elemental sulfur (S_8) or sulfuric acid (H_2SO_4), which would condense to form aerosols if they are saturated in the atmosphere. For a planet in the habitable zone of a Sun-like star or a M star, Earth-like sulfur emission rates would result in optically thick aerosol layers in 1-bar H_2-dominated atmospheres; and a sulfur emission rate 2-orders-of-magnitude higher than the Earth's volcanic sulfur emission rate would result in optically thick aerosol layers in 1-bar N_2 and CO_2-dominated atmospheres. The composition of the photochemically produced aerosols mostly de-

pends on the redox state of the atmosphere: S_8 aerosols are formed in the reducing atmospheres (e.g., H_2 atmospheres), and both S_8 and H_2SO_4 aerosols are formed in the oxidized atmospheres that could be both reducing and oxidizing (e.g., N_2 and CO_2 atmospheres). Based on extensive numerical simulations, I provide empirical formulae that show the dependency of the aerosol optical depth on the surface sulfur emission rates, the dry deposition velocities of sulfur compounds, and the aerosol particle sizes.

Direct detection of H_2S and SO_2 is unlikely due to the rapid photochemical conversion from H_2S and SO_2 to elemental sulfur and sulfuric acid in atmospheres having a wide range of redox powers. For a terrestrial exoplanet with sulfur emitted from the surface at an enhanced rate, it is likely that at visible wavelengths the planet's atmosphere appears to be opaque due to the aerosol loading and that the planet has high visible albedo. However, for Earth-like planets with 1-bar atmospheres ranging from reducing to oxidizing, I find the effect of photochemical sulfur and/or sulfate aerosols in the MIR wavelengths is minimal, because micron-sized particles that interact with MIR photons have large gravitational settling velocities and therefore short atmospheric lifetime. Finally, as the aerosol composition is tightly related to the ratio of the H_2S versus SO_2 emission, although direct detection of H_2S and SO_2 by their spectral features is unlikely, their existence might be inferred by observing aerosol-related features in reflected light with future generation space telescopes.

The photochemistry models presented in this chapter are critical for prospecting the possible atmospheric composition that will eventually be characterized by a TPF-like mission. I have shown that volcanic carbon compounds including CH_4 and CO_2 are likely to be abundant in terrestrial exoplanet atmospheres; and I have also shown that an enhanced volcanic activity leads to formation of optically thick sulfur or sulfate aerosols. As for biosignatures, I here have shown that photochemically produced O_2 and O_3 can be a potential false positive biosignature in thick CO_2 atmospheres when there is no H_2 or CH_4 emitted from surface. More generally, the three benchmark models presented here can serve as the standard atmospheres for reducing, weakly oxidizing, and highly oxidizing atmospheres on habitable exoplanets

for assessing chemical lifetime of other potential biosignature gases.

Chapter 4

Thick Atmospheres on Terrestrial Exoplanets

4.1 Background

One of the most exciting discoveries of astronomy in recent years is the discovery of super Earths and mini Neptunes and the observation of their atmospheres. Thick atmospheres on super Earths are in the reach of current (if orbiting a nearby M dwarf) and next-generation observation facilities. In fact, two transiting super Earths and mini Neptunes are being observed in all possible ways (Bean et al., 2010; Croll et al., 2011; Bean et al., 2011; Désert et al., 2011; Berta et al., 2012; de Mooij et al., 2012; Demory et al., 2012a,b; Ehrenreich et al., 2012). More and more super Earths will be discovered and their atmospheres will be observed with the transit technique. In the future, direct imaging will allow the super Earths to be observed in reflected light and their atmospheres to be characterized in great detail (e.g., Maire et al. 2012).

I focus on thick atmospheres of hydrogen, carbon, and oxygen as they are likely to be the most important building blocks of super Earth atmospheres, and their relative abundance controls the molecular composition in thermochemical equilibrium. Though still debated (Fortney, 2012), stellar observations have suggested that the carbon versus oxygen elemental abundance ratio (i.e., the C/O ratio) of planet-hosting systems spreads over a wide range between 0.3 and 2.0 (Bond et al., 2010; Delgado

Mena et al., 2010; Petigura and Marcy, 2011). A significant fraction of planet-hosting systems may have C/O ratios larger than the solar C/O ratio (Petigura and Marcy, 2011; Fortney, 2012). Protoplanetary nebulae that are enriched in carbon have a different condensation sequence than the Solar System, which may lead to the formation of carbon-rich terrestrial planets, i.e. carbon planets (Lodders, 2004; Kuchner and Seager, 2005; Bond et al., 2010). Indeed, an atmosphere that has more carbon than oxygen have been suggested for a hot Jupiter (Madhusudhan et al., 2011a). For carbon planets that have carbon-rich atmospheres (but still H_2-dominated), a number of studies have anticipated high abundance of CO and scarcity of H_2O (Kuchner and Seager, 2005; Madhusudhan et al., 2011b; Kopparapu et al., 2012; Moses et al., 2013). After all, due to the uncertainty of planetary formation and evolution, the C/O ratio of the protoplanetary nebula does not necessarily align with that of planet formed therein, nor the C/O ratio of the planetary atmosphere necessarily aligns with that of the bulk planet mass. It is therefore plausible to consider super Earth atmospheres to have a wide range of C/O ratios, from much lower than the solar ratio (0.5) to much higher than unity.

4.2   Model Atmospheres

With the photochemistry-thermochemistry model, I explore the molecular compositions of thick atmospheres on warm and hot terrestrial exoplanets, with GJ 1214b and 55 Cnc e as the prototypes. I focus on the C-H-O chemistry in this work as they are the most common elements in the Universe. In a C-H-O system, the elemental abundance can be characterized by the hydrogen abundance (denoted as X_H) and the carbon versus oxygen ratio (denoted as X_C/X_O). I explore thick atmospheres being hydrogen-rich ($X_H > 0.7$), hydrogen-intermediate ($0.3 \leq X \leq H < 0.7$) and hydrogen-poor ($X_H < 0.3$); and I also explore the atmospheres with very different C/O ratios ranging from 0.1 to 10.

The unique feature that allows the model to explore thick atmospheres from hydrogen-rich to hydrogen-poor is that the model does not require specification

of the main component of the atmosphere (nor the mean molecular mass), and the model takes the elemental abundance as the input parameters. All previous photochemistry-thermochemistry models assume a specific dominant gas (and therefore mean molecular mass) and seek steady-state abundances of trace gases in the fixed background atmosphere. However, for applications to terrestrial exoplanets, one cannot assume any specific dominant gas, and the mean molecular mass needs to be self-consistently determined. I provide for the first time such a feature in my photochemistry-thermochemistry code. For the radiative transfer routine and the thermochemical equilibrium routine I use a pressure level grid so that a mean molecular mass is no longer required. The mean molecular mass is synthesized from the thermochemical equilibrium composition profile, and then used for the transformation from a pressure grid to a vertical altitude grid. This approach eliminates the need to specify a background atmosphere for kinetic-transport simulations of thick atmospheres, which makes my model uniquely suitable for applications to the study of super Earths and mini Neptunes.

For each simulation, I use the thermochemistry code and the radiative transfer code iteratively to compute the atmospheric temperature-pressure profiles and initial and boundary conditions, and then use the thermochemistry-photochemistry code to compute the steady-state molecular compositions from 10^3 bar to 10^{-8} bar. I verify that the lower boundary at 10^3 bar is sufficient to maintain thermochemistry equilibrium at the bottom layer for each simulation. I explore eddy diffusion coefficients ranging from 10^6 to 10^9 cm^2 s^{-1}, reasonable values for deep atmospheres according to the free-convection and mixing-length theories (Gierasch and Conrath, 1985; Visscher et al., 2010). The eddy diffusion coefficients are assumed to be constant throughout the atmosphere. Such assumption does not consider the possibility of a temperature inversion that may lower the eddy diffusion coefficients by more than 3 orders of magnitude at ~ 0.1 bar. My models may therefore under-estimate the amounts of potential photochemical products in the upper atmosphere; however this study is mainly concerned with the transport-driven disequilibrium in the deep atmosphere, for which my assumption regarding the eddy diffusion coefficient is sufficient.

For the stellar spectrum, I have used the latest *HST* measurement of UV flux of GJ 1214 (France et al., 2013) for the simulations of GJ 1214b like planets, and a black body spectrum of effective temperature 5200 K with additional Solar-like chromospheric emission for the simulations of 55 Cnc e like planets. I find suitable to assigned $O(^1D)$, C, and $^1CH_2$ to be "fast species" in the simulations for H_2-dominated cases, and $O(^1D)$, $^1CH_2$, C_2H, and CH_2O_2 to be "fast species" in the simulations for non-H_2-dominant cases.

4.3 Results

I provide a classification scheme of thick atmospheres on terrestrial exoplanets based on extensive simulations. The new types of non-H_2-dominated atmospheres are water-rich atmospheres, oxygen-rich atmospheres, and hydrocarbon-rich atmospheres. I reveal the molecules that could exist in abundance in these two types of atmospheres, and outline the means to observationally distinguish these two types of atmospheres via spectral features of hallmark molecules.

4.3.1 Chemical Classification of Thick Atmospheres on Terrestrial Exoplanets

I classify thick atmospheres on terrestrial exoplanets broadly into hydrogen-rich atmospheres, water-rich atmospheres, oxygen-rich atmospheres, and hydrocarbon-rich atmospheres, depending on the hydrogen abundance and the carbon to oxygen abundance ratio. The classification scheme focuses on the major gases in thick atmospheres. If a thick atmosphere is not H_2-dominated, the dominated gas at the potentially observable levels (1 $\sim$ 100 mbar) can be H_2O, CO_2, CO, CH_4, other hydrocarbons (C_2H_4 and C_2H_2), or even O_2. This is the first complete list of major molecular building blocks made of C, H, O elements for thick atmospheres on terrestrial exoplanets, and the proposition that unsaturated hydrocarbons including C_2H_2 and C_2H_4 can be the dominant gases in an exoplanet atmosphere is also the first.

Figure 4-1 summarizes the parameter regimes for each types of atmospheres based on the hydrogen abundance and the carbon to oxygen abundance ratio.

Before describing the non-H_2-dominated atmospheres, I first show that if $X_H > 0.7$, thick atmospheres of terrestrial exoplanets contain abundant (H_2) and therefore have the same chemical behaviors as atmospheres of gas giants. Previous thermo-chemistry and photochemistry results regarding the thick atmospheres on gas giants are valid in these cases, including: CH_4 is the dominant carbon species at equilibrium temperatures lower than 1400 K; CO is the dominant carbon species at equilibrium temperatures higher than 1400 K (Line et al., 2010; Visscher and Moses, 2011; Madhusudhan, 2012); and H_2O becomes scarce as the C/O exceeds 1 at high temperatures that favor CO over CH_4 (e.g. Kuchner and Seager, 2005; Kopparapu et al., 2012; Madhusudhan, 2012). I confirm all these behaviors in my simulations for terrestrial exoplanets having hydrogen-rich thick atmospheres (see Figure 4-2 and Figure 4-3). In particular, at the low temperatures where CH_4 is the dominant carbon carrier and H_2O is the dominant oxygen carrier, the ratio CH_4/H_2O is equal to the C/O ratio, and the eddy diffusion coefficients have no effects on the abundances of CH_4 or H_2O in the observable part of atmospheres.

Now I turn to non-H_2-dominated atmospheres. If the hydrogen abundance (X_H) is lower than 0.7, the atmosphere will contain abundant water vapor for low X_C/X_O, and hydrocarbons (i.e., CH_4, C_2H_2, and C_2H_4) for high X_C/X_O. The water-rich atmospheres occur for $X_C/X_O < 0.5$ and the hydrocarbon-rich atmospheres occur for $X_C/X_O > 2$. For the intermediate cases ($0.5 < X_C/X_O < 2$), the atmospheres may contain significant portions of H_2, CH_4, CO, CO_2, and H_2O concurrently, and their relative abundances depend on the temperatures in the atmosphere (Figure 4-1). A general trend in this regime in the middle is that as the temperature increases, CO becomes more and more a dominant gas rather than H_2O or CH_4 (see Figure 4-2 and Figure 4-3). If the hydrogen abundance (X_H) is lower than 0.3 (e.g., for an extremely evolved super Earth on which most atmospheric hydrogen has been lost), significant amounts of O_2 will build up in the atmosphere when $X_C/X_O < 0.5$. As shown in Figure 4-1, I classify thick atmospheres on terrestrial exoplanets according to
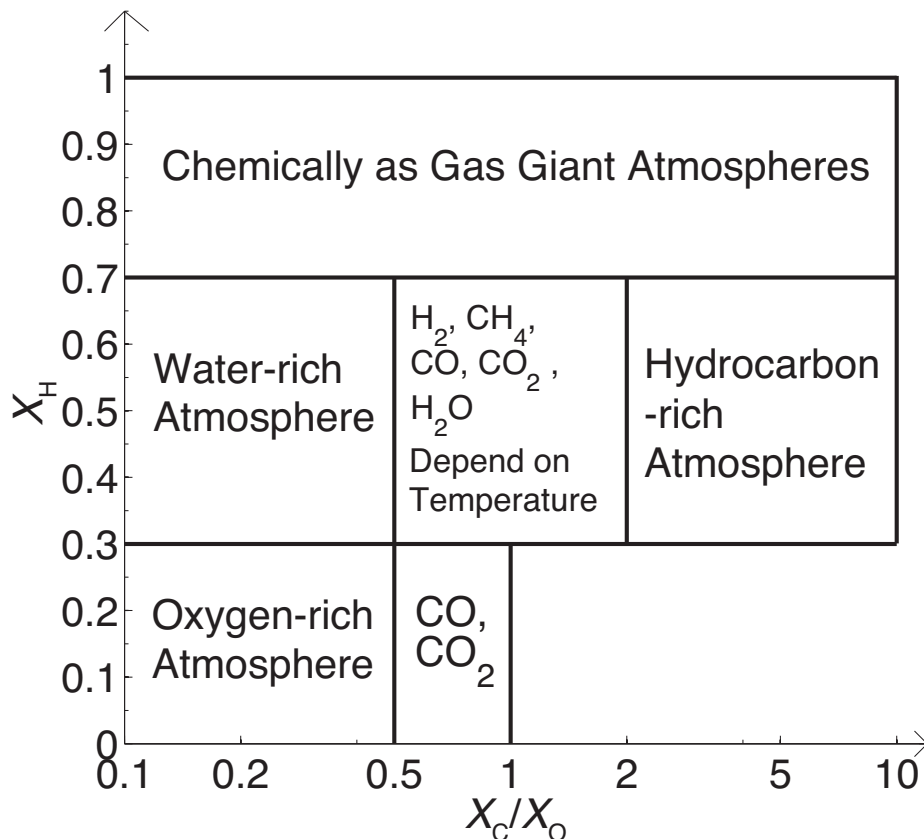
Figure 4-1: Chemical classification of thick atmospheres on terrestrial exoplanets. The classification is summarized based on extensive numerical exploration for exoplanets with equilibrium temperatures ranging from 500 to 2000 K, on a 2-dimensional grid that explores the hydrogen abundance and the carbon to oxygen abundance ratio in the atmosphere. Results of these simulations are also shown in subsequent figures. The main point is that, when H_2 is no longer the dominant component in the atmosphere, water-rich atmospheres, hydrocarbon atmospheres, and oxygen-rich atmospheres emerge, depending on the hydrogen abundance and the carbon to oxygen ratio. In the middle of these regimes is where H_2, CH_4, CO, CO_2, and H_2O can coexist, and their relative abundances are determined by the temperatures in the atmosphere.
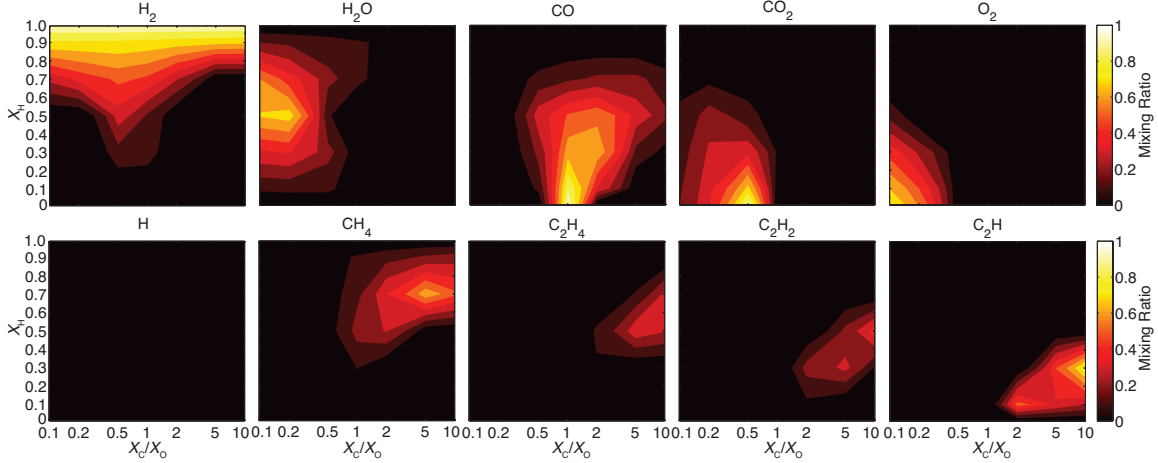
Figure 4-2: Mixing ratios of common molecules in thick atmospheres on a GJ 1214b like exoplanet. The simulated planet is a 6.5-$M_\oplus$ and 2.7-$R_\oplus$ planet at the 0.014-AU orbit of an M 4.5 star, corresponding to GJ 1214b. The mixing ratios of H_2, H_2O, CO, CO_2, O_2, H, CH_4, C_2H_4, C_2H_2, and C_2H are shown as a function of the H abundance and the C/O ratio in the atmospheres. The atmospheres have a temperature of 470 K at the top, $\sim$800 K at 1 bar, and $\sim$1300 K at 100 bar self-consistently computed with the composition assuming the interior heat flux to be $T_{int} = 20$ K. For photochemical calculations, I have used the latest HST measurement of UV flux of GJ 1214 (France et al. 2013), and explored the eddy diffusion coefficients ranging from 10^6 to 10^9 cm^2 s^{-1}. The mixing ratio shown in the figure is the vertically averaged mixing ratio for pressure levels from 1 to 100 mbar, to which transmission spectroscopy is sensitive. Water should not exist in the atmosphere with substantial amounts if $X_C/X_O > 1$ for a wide range of hydrogen abundance; hydrocarbons (CH_4 and C_2H_x) have high abundances in carbon-rich atmospheres; and molecular oxygen appears abundantly in the atmosphere only for hydrogen-poor and carbon-poor cases.

the hydrogen abundance and the carbon to oxygen abundance ratio, which includes hydrogen-rich atmospheres, water-rich atmospheres, oxygen-rich atmospheres, and hydrocarbon-rich atmospheres.

Non-H_2-dominated atmospheres differ from H_2-dominated atmospheres mostly in the dependency on the carbon to oxygen abundance ratio. In general, the composition of a non-H_2-dominated atmosphere is much more sensitive to carbon to oxygen abundance ratio than that of a H_2-dominated atmosphere (Figure 4-4). This is because when the atmosphere is not hydrogen-rich, the composition is first and foremost constrained by the limited supply of hydrogen. To better illustrate this point, let us consider how the H_2O versus CO abundance ratio depends on X_C/X_O for an example
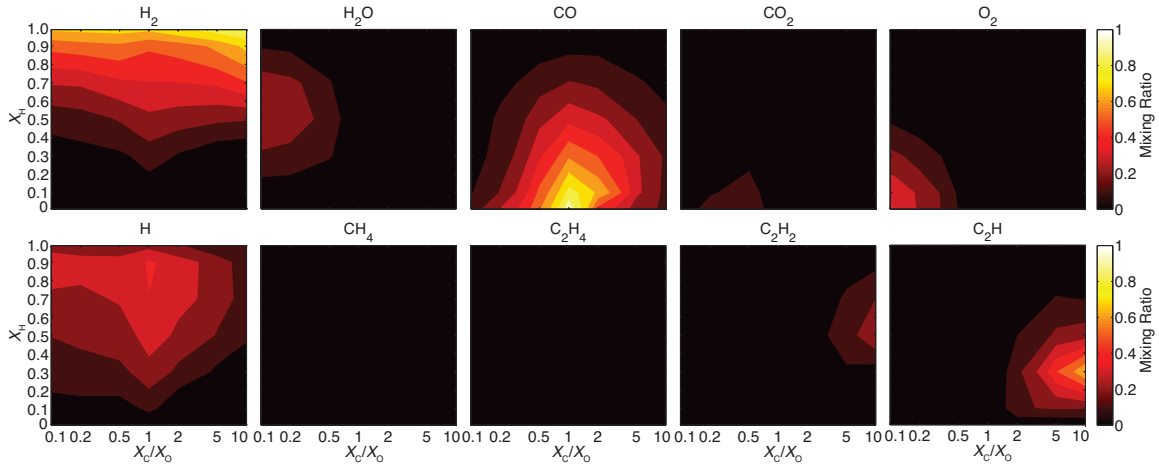
Figure 4-3: Mixing ratios of common molecules in thick atmospheres on a 55 Cnc e like exoplanet. The same format as Figure 4-2, but for a 8.6-$M_\oplus$ and 2.0-$R_\oplus$ planet at the 0.0156-AU orbit of a K0V star having an effective temperature of 5200 K, corresponding to 55 Cnc e. The atmospheres have a temperature of 2000-2200 K at the top, and 2500-3000 K at 100 bar self-consistently computed with the composition assuming the interior heat flux to be $T_{\mathrm{int}} = 20$ K. Compared with the GJ 1214b scenarios shown in Figure 4-2, CH_4 and C_2H_4 are not expected to exist in abundance in the atmosphere of 55 Cnc e; CO is the dominant gas in the atmosphere for a much wider parameter space; and C_2H and C_2H_2 become the thermochemically preferred hydrocarbons in the atmosphere.
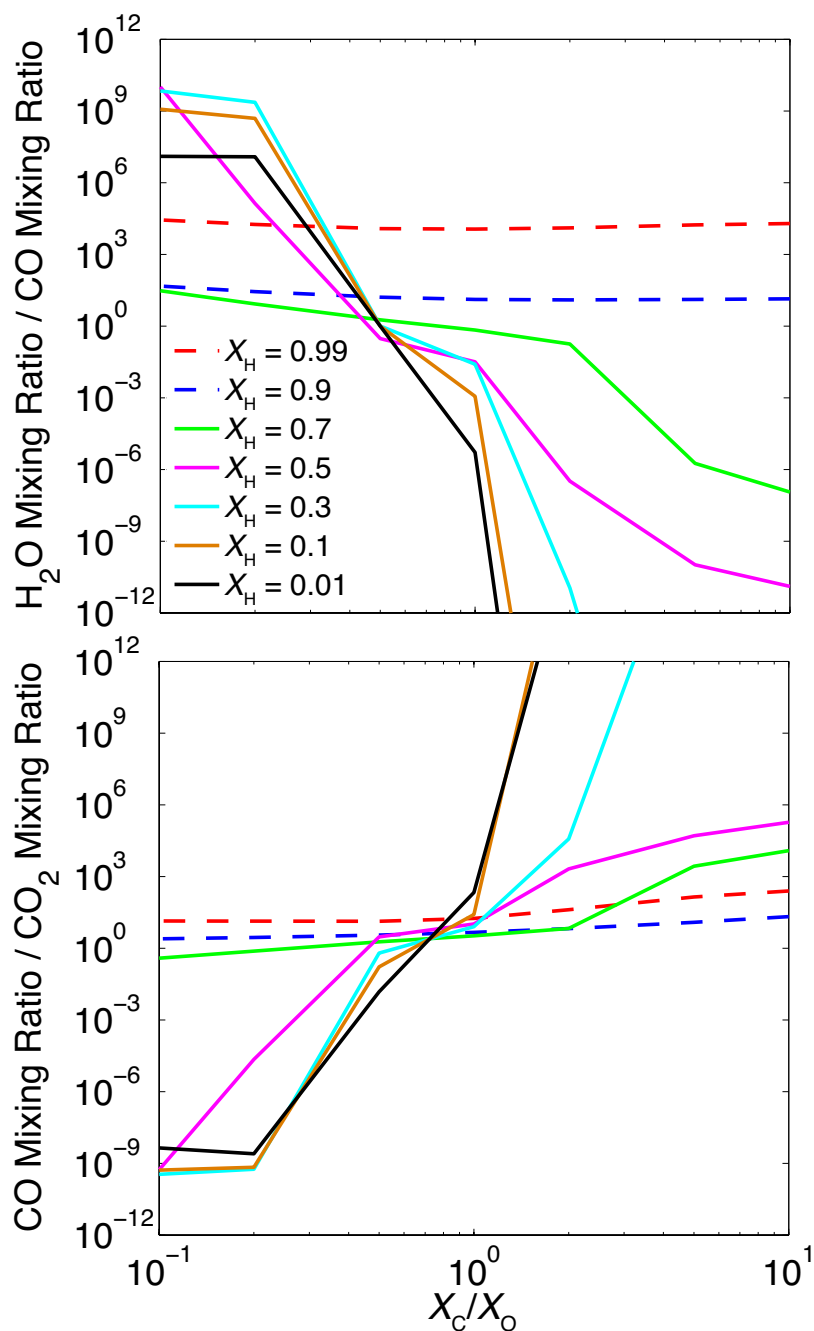
Figure 4-4: Key ratios of molecular abundances in thick atmospheres on a GJ 1214b like exoplanet as functions of the C/O ratio. Each color corresponds to a different hydrogen abundance, ranging from hydrogen-rich to hydrogen-poor. The hydrogen rich cases are shown in dashed lines, to be compared with the non-hydrogen-rich cases shown in solid lines. The C/O dependency for non-H_2-rich atmospheres is much more sensitive than for H_2-rich atmospheres.

(see the upper panel of Figure 4-4). For H_2-dominated atmospheres at temperatures less than ~ 1400 K, the main carbon-bearing species is CH_4, and CO is in equilibrium with H_2O; therefore the H_2O versus CO abundance ratio only has week dependency on X_C/X_O. However, for non-H_2-dominated atmospheres, CO must serve as one of the carbon carriers and then increasing X_C/X_O will result in more fractions of oxygen to be bound with carbon, and less fractions to be bound with hydrogen to form H_2O. In all, while the carbon to oxygen abundance ratio affects the amounts of trace gases in H_2-dominated atmospheres, the carbon to oxygen abundance ratio controls the abundances of major gases in non-H_2-dominated thick atmospheres.

Finally, in certain endmember scenarios for non-H_2-dominated thick atmospheres, I find that the elemental abundance uniquely determines the amounts of major components in the atmosphere, regardless of temperatures or efficiency of vertical mixing, and I derive analytical formulae of the molecular compositions for these cases. Table 4.1 tabulates an exhaustive list of parameter regimes of the elemental abundance, and the derived formulae for mixing ratios of major components in these regimes. The fundamental principle that I use here is simply that all H, C, and O atoms in the atmosphere have to be bound to form a limited set of thermochemically stable molecules (e.g., H_2, H_2O, CO_2, CO, CH_4, C_2H_4, C_2H_2, O_2, etc.), to the extent that molecular forms of C, H, and O elements are thermochemically preferred over atomic forms (which typically corresponds to an equilibrium temperature of less than ~ 2500 K). I find that in the cases of $X_C \ll 1$ and the cases of $X_H \ll 1$, the abundances of major gases in the atmosphere are uniquely determined by the elemental abundance (Table 4.1).

In the following two subsections, I present the results for the two new types of thick atmospheres on terrestrial exoplanets: water-rich atmospheres and hydrocarbon-rich atmospheres. Oxygen-rich atmospheres are described together with water-rich atmospheres as they both correspond to low X_C/X_O scenarios. I focus on the ranges of possible molecular compositions in these atmospheres, because it is the molecular compositions that control the observational properties of these atmospheres.

Table 4.1: Main components of thick atmospheres on terrestrial exoplanets as a function of the abundances of H, O, and C. The table lists all plausible combinations of H, O, and C, in the orders of one-element dominance, two-element dominance, and three-element dominances, except for the case of $X_H \ll 1$, $X_O \ll 1$, $X_C \sim 1$ as elemental carbon is not in the gaseous phase for the temperatures of interest. The main components are stable molecules made of H, O, and C, and the table is valid to the extent that the molecular forms are thermochemically favored over elemental forms.

Parameter Regime	Main Components	Mixing Ratio Formulae	Corresponding Classification
$X_H \sim 1$, $X_O \ll 1$, $X_C \ll 1$	H_2	$X_{H_2} \sim 1$	Hydrogen-rich atmospheres
$X_H \ll 1$, $X_O \sim 1$, $X_C \ll 1$	O_2	$X_{O_2} \sim 1$	Oxygen-rich atmospheres
$X_H \sim 1$, $X_O \sim 1$, $X_C \ll 1$, $X_H \geq 2X_O$	H_2, H_2O	$X_{H_2} = 1 - \frac{2X_O}{X_H}$, $X_{H_2O} = \frac{2X_O}{X_H}$	Water-rich atmospheres
$X_H \sim 1$, $X_O \sim 1$, $X_C \ll 1$, $X_H < 2X_O$	H_2O, O_2	$X_{H_2O} = \frac{2X_H}{X_H+2X_O}$, $X_{O_2} = \frac{2X_O-X_H}{X_H+2X_O}$	Water-rich atmospheres
$X_H \sim 1$, $X_O \ll 1$, $X_C \sim 1$	H_2, CH_4, C_2H_2, C_2H_4, C_2H	Temperature dependent	Hydrocarbon-rich atmospheres
$X_H \ll 1$, $X_O \sim 1$, $X_C \sim 1$, $X_C \leq X_O \leq 2X_C$	CO, CO_2	$X_{CO} = 2 - \frac{X_O}{X_C}$, $X_{CO_2} = \frac{X_O}{X_C} - 1$	CO-CO$_2$ atmospheres
$X_H \ll 1$, $X_O \sim 1$, $X_C \sim 1$, $X_O > 2X_C$	CO_2, O_2	$X_{CO_2} = \frac{2X_C}{X_O}$, $X_{O_2} = 1 - \frac{2X_C}{X_O}$	Oxygen-rich atmospheres
$X_H \sim 1$, $X_O \sim 1$, $X_C \sim 1$	H_2, H_2O, CH_4, CO, CO_2	Temperature dependent	

4.3.2 Ranges of Compositions of Water-Rich Atmospheres and Oxygen-Rich Atmospheres

I here present the results regarding water-rich and oxygen-rich thick atmospheres on terrestrial exoplanets. Water-rich atmospheres is in particular interesting because water is a substance fundamental for life. I have already shown that water-rich atmospheres emerge as an atmosphere with low X_C/X_O loses its most of its free hydrogen (Figure 4-1). For low X_C/X_O, the atmosphere is a mixture of H_2 and H_2O when $X_H \geq 2X_O$ and H_2O and O_2 when $X_H < 2X_O$ (Table 4.1). In this section, I study the possible ranges of mixing ratios for both the main components and the minor components in water-rich atmospheres. The main components are important because they are directly controlled by the elemental abundances and they serve as the background atmosphere; and the minor components are also important because they may lead to significant, if not dominant, spectral features and they provide means to characterize vertical mixing and internal heating of a terrestrial exoplanet.

Water-dominated atmospheres, defined as atmospheres in which water is the most abundant gas, only occur when $X_H \sim 2X_O$ and $X_C/X_O \ll 1$, a fairly small part of the parameter space of elemental abundances. Mixture of carbon, even at the solar X_C/X_O, would lead to the removal of most atmospheric water. As shown in
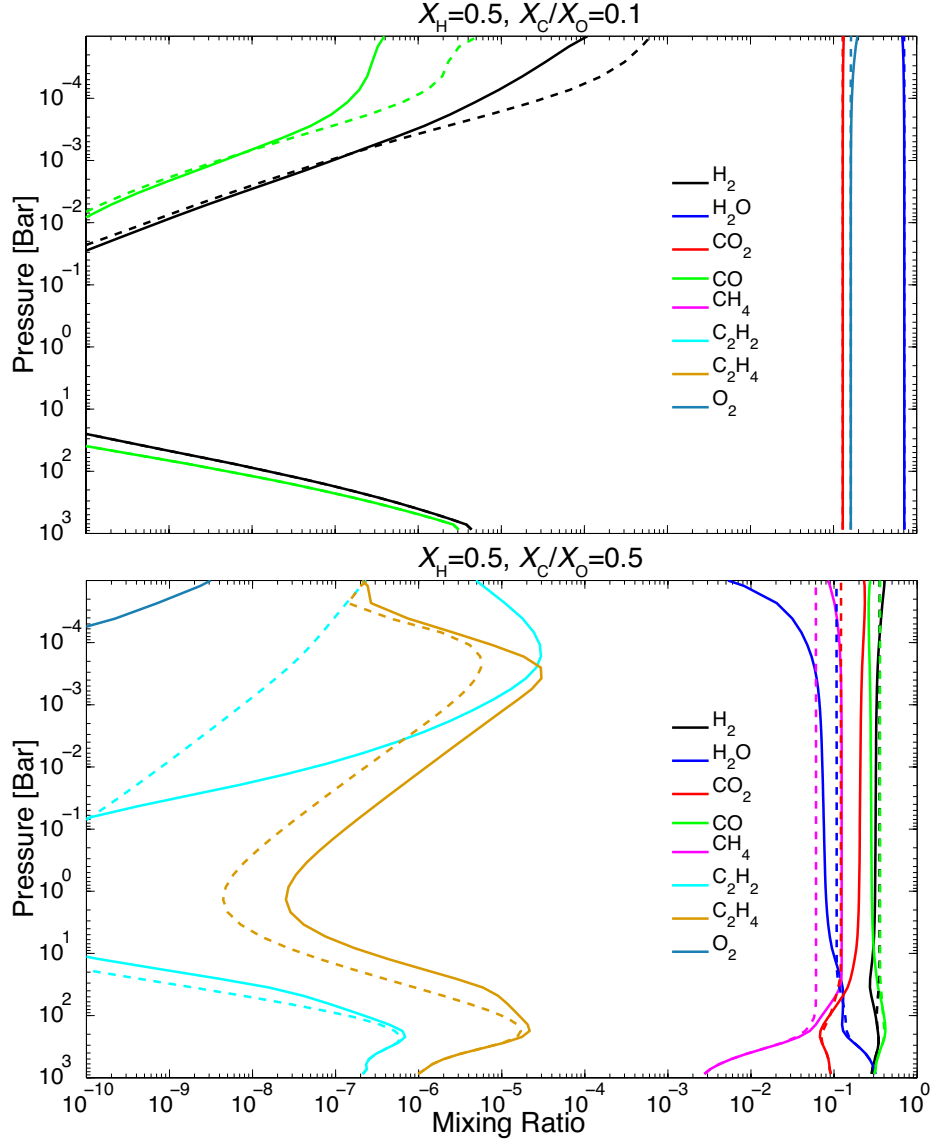
Figure 4-5: Molecular composition of water-rich atmospheres on GJ 1214b like super Earths/mini Neptunes. The simulated thick atmosphere has an adopted hydrogen abundance of 0.5 and a carbon to oxygen abundance ratio of 0.1 (top) and 0.5 (bottom). The planet is a GJ 1214b sized planet at the 0.014-AU orbit around an M4.5 star. With an internal luminosity of 20 K, the planet has a temperature of 470 K at the top of atmosphere, a temperature of ~ 810 K (left) and ~ 830 K (right) at the pressure level of 1 bar, and a temperature of ~ 1300 K at the pressure level of 100 bar. Results are shown for a vertical eddy diffusion coefficient of 10^6 cm^2 s^{-1} (solid lines) and 10^9 cm^2 s^{-1} (dashed lines). With a solar X_C/X_O, H$_2$, CO, CO$_2$, CH$_4$, and H$_2$O all have mixing ratio in the order of 0.1 at the pressure level of $0.1 \sim 10$ mbar, and the exact composition is sensitive to the eddy diffusion coefficient; whereas with $X_C/X_O = 0.1$, water vapor is the most abundant gas in the observable atmosphere with a mixing ratio of 0.71, and O$_2$ and CO$_2$ are the next abundant gases with mixing ratios of 0.16 and 0.13.

Figure 4-5, when $X_H = 0.5$, $X_C/X_O = 0.1$, the atmosphere is water dominated, with trace amount of carbon in the form of CO_2. The water vapor abundance decreases dramatically as the atmosphere is more carbon-rich (Figure 4-4). At the solar X_C/X_O, the atmosphere would be a mixture of H_2, CO, CO_2, CH_4, and H_2O, in which the water vapor mixing ratio is about 10% (Figure 4-5). Such an atmosphere is not water-dominated, but such an atmosphere shall still be considered water-rich, because a water vapor amount of even less than 10% would be very significant in the spectrum. A conceptual way to understand this result is that for a wide temperature range, oxygen atoms tend to be bound with carbon atoms whenever available. In summary, water-rich atmospheres exist when $X_C/X_O \leq 0.5$, but water-dominated atmospheres exist only when $X_C/X_O \ll 0.5$.

Furthermore, the mixing ratios of main components in the water-rich but not water-dominated atmospheres are affected by the temperatures and the efficiency of vertical mixing. As shown in Figure 4-5, the mixing ratios of CO_2, CH_4, and H_2O can vary by a factor of a few, for the eddy diffusion coefficients ranging from 10^6 to 10^9 cm^2 s^{-1}.

I now turn to consider the minor components in water-dominated atmospheres. The minor components of interest are, of course, the three stable forms of carbon, CH_4, CO, and CO_2. I here outline an analytical treatment for the carbon speciation in water-dominated atmospheres, which is also applicable to study the thermochemical speciation of other elements in a given mixture of gases. When $X_H \sim 1$, $X_O \sim 1$, $X_C \ll 1$, one may consider carbon as perturbation, and the atmosphere is primarily made of either H_2, H_2O, or H_2O, O_2, the mixing ratios of which are tabulated in Table 4.1. For carbon in a H_2-H_2O system, there are the following balanced reactions:

$$H_2O + CH_4 \rightleftharpoons 3\,H_2 + CO, \qquad\qquad (C\,14)$$

$$H_2O + CO \rightleftharpoons H_2 + CO_2. \qquad\qquad (C\,15)$$
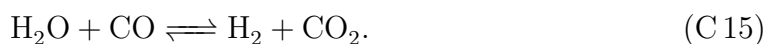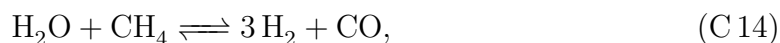
Let K_1 be the equilibrium constant of reaction (C 14), and K_2 be the equilibrium constant of reaction (C 15). Note that K_1 and K_2 only depend on the temperature.

153
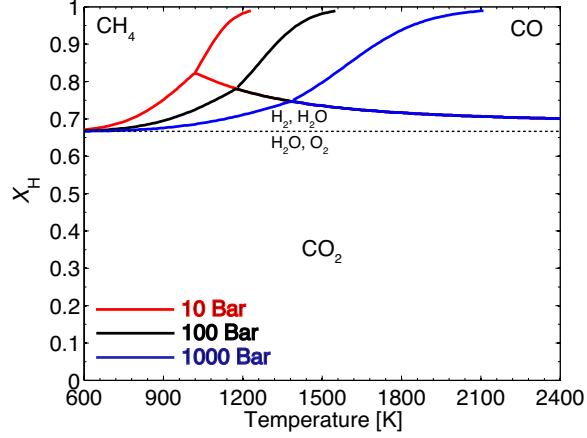
Figure 4-6: Carbon speciation in water-dominated thick atmospheres on terrestrial exoplanets. The main components of the atmosphere are either H_2 and H_2O ($X_H >$ $2/3$), or H_2O and O_2 ($X_H < 2/3$), and their mixing ratios depend on the hydrogen abundance X_H as tabulated in Table 4.1. The figure shows the parameter regimes in which CH_4, CO, and CO_2 is the main carbon carrier in the atmosphere. The boundaries between the regimes are computed using Equations (4.1-4.4), for a variety of pressures shown by different colors. As long as the atmosphere is depleted in molecular hydrogen, the main form of carbon is CO_2 regardless of temperature and pressure.

The *Law of Mass Action* reads

$$\frac{X_{CO}}{X_{CH_4}} = \frac{K_1}{P^2} \frac{X_{H_2O}}{X_{H_2}^3}, \tag{4.1}$$

$$\frac{X_{CO_2}}{X_{CO}} = K_2 \frac{X_{H_2O}}{X_{H_2}}, \tag{4.2}$$

in which X denotes the mixing ratio of a molecule, and P is the atmospheric pressure in the unit of bar. Similarly for a H_2O-O_2 system,

$$3\,O_2 + 2\,CH_4 \rightleftharpoons 4\,H_2O + 2\,CO, \tag{C 16}$$

$$O_2 + 2\,CO \rightleftharpoons 2\,CO_2. \tag{C 17}$$

154

There are

$$\frac{X_{\mathrm{CO}}}{X_{\mathrm{CH_4}}} = \sqrt{\frac{K_3}{P} \frac{X_{\mathrm{O_2}}^3}{X_{\mathrm{H_2O}}^4}}, \tag{4.3}$$

$$\frac{X_{\mathrm{CO_2}}}{X_{\mathrm{CO}}} = \sqrt{K_4 P X_{\mathrm{O_2}}}, \tag{4.4}$$

in which K_3 is the equilibrium constant of reaction (C 16), and K_4 is the equilibrium constant of reaction (C 17). The relative abundance of CH_4, CO, and CO_2 in thermochemical equilibrium in a predominantly hydrogen and oxygen atmosphere can be calculated with Equations (4.1-4.4), for a variety of temperatures and pressures. Figure 4-6 summarizes the result of this calculation.

I find that when the atmosphere is mainly a H_2-H_2O mixture ($X_{\mathrm{H}} > 2X_{\mathrm{O}}$), the main form of carbon is either CH_4 at low temperatures or CO at high temperatures (similar to gas giant atmospheres); when the atmosphere is mainly a H_2O-O_2 mixture ($X_{\mathrm{H}} < 2X_{\mathrm{O}}$), the main form of carbon is always CO_2, regardless of temperature (Figure 4-6; also see Figure 4-5 for an example). The transition from CH_4 to CO in a H_2-H_2O atmosphere depends on the temperature at the quenching pressure (i.e., the pressure at which the eddy mixing timescale is equal to the thermochemical equilibrium timescale) and the hydrogen abundance (see Figure 4-6). Therefore the abundances of CH_4 and CO can probe the efficiency of eddy mixing and the flux of internal heating. A higher quenching pressure (in other words more efficient eddy mixing) would lead to more CH_4 and less CO in the observable atmosphere. When the atmosphere is depleted in molecular hydrogen, however, the dominant form of carbon is always CO_2 to the extent that carbon is a minor constituent in the atmosphere ($X_{\mathrm{C}}/X_{\mathrm{O}} \ll 0.5$). In this case, the carbon speciation is insensitive to the effect of eddy mixing or the temperature structure of the atmosphere, and therefore cannot serve as the probe to these physical quantities. In particular, CH_4 is thermochemically prohibited to exist in abundance in a H_2-depleted water-dominated atmosphere; therefore, nonexistence of CH_4 can be an indicator for water dominance in the atmosphere.

Finally, I comment on the rise of free oxygen in the water-rich atmospheres. Pre-

vious discussions have shown that when $X_H < 2X_O$, one would expect the atmosphere to be a mixture of H_2O, O_2, and CO_2 (see Figure 4-2). The free oxygen in the atmosphere is basically the left-over oxygen after forming H_2O and CO_2; in other words, free oxygen is expected when $X_O > 0.5X_H + 2X_C$. The rise of free oxygen I present here is a result of the loss of hydrogen, rather than the photon-driven processes that only affects the upper atmosphere at $\sim 10^{-5}$ bar (see the upper panel of Figure 4-5 for an example). The caveat here is that I do not consider any material exchange between the atmosphere and the surface (if there is a surface). The oxygen build-up from hydrogen loss could be prevented by active volcanic release of reduced gases or oxidative weathering of the surface, a process that has been proposed to have operated on Venus (e.g. Kasting, 1997). A side point is that the OH radical would be very abundant in such H_2O-O_2-CO_2 atmospheres, with mixing ratios varying between 10^{-8} and 10^{-4}. As OH radicals remove most other gases in the atmosphere rapidly, such a high concentration of OH necessarily implies that the any gas that reacts with OH without reforming pathways is not expected to be able to accumulate in the atmosphere. The H_2O-O_2-CO_2 atmospheres on super Earths are likely to be highly oxidized, with all other elements in their most oxidized form.

4.3.3 Ranges of Compositions of Hydrocarbon-Rich Atmospheres

Another new type of thick atmospheres on terrestrial exoplanets I find is hydrocarbon-rich atmosphere. The hydrocarbon-rich atmospheres are the conjugate situation of the water-rich atmospheres; the difference here is that while the only stable "hydro-oxygen" is H_2O, there are many stable hydrocarbons. Based on my simulations, the potentially observable parts of a hydrocarbon-rich atmosphere may be composed of H_2, H, CH_4, C_2H_2, C_2H_4, and C_2H (Figures 4-2 and 4-3). As the number of possible molecules in hydrocarbon-rich atmospheres exceeds the number of major elements in the atmosphere (2), the main components are not uniquely set by the elemental abundance, and depend on other factors including the efficiency of vertical mixing
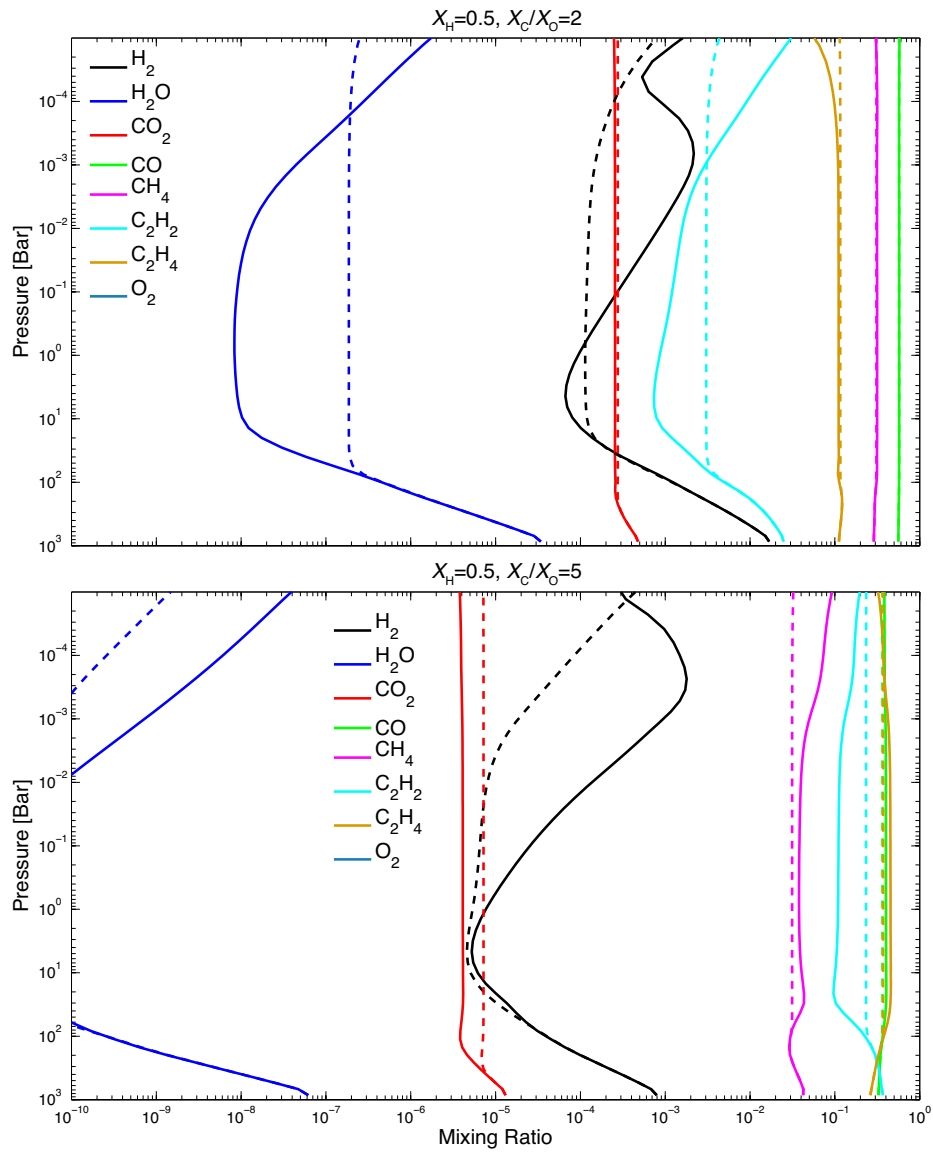
Figure 4-7: Molecular composition of hydrocarbon-rich atmospheres on GJ 1214b like super Earths/mini Neptunes, with same format as Figure 4-5. For $X_C/X_O > 1$, CO, CH_4, C_2H_2, and C_2H_4 all have mixing ratio in the order of 0.1 at the pressure level of $0.1 \sim 10$ mbar; and the exact compositions are sensitive to the eddy diffusion coefficient.
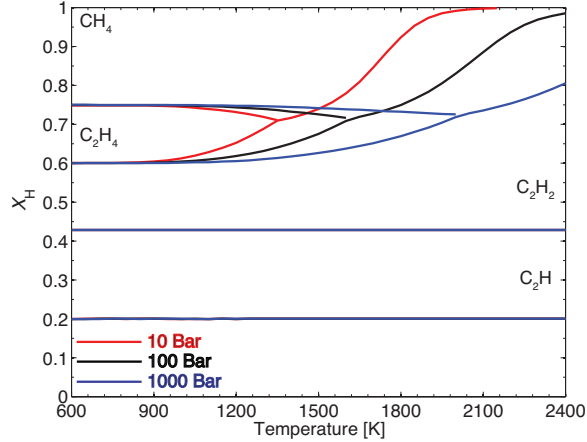
Figure 4-8: Carbon speciation in hydrocarbon-dominated thick atmospheres on terrestrial exoplanets. The atmosphere has hydrogen and carbon, and very little oxygen, i.e., $X_H + X_C = 1$ and $X_O \ll 1$. I compute the molecular composition in thermochemical equilibrium, and show on the figure the parameter regimes in which CH_4, C_2H_4, C_2H_2, and C_2H is the main carbon carrier in the atmosphere. The boundaries between the regimes are for a variety of pressures shown by different colors. The parameter regime of $X_H < 0.2$ corresponds to the formation of elemental carbon, which would condense and precipitate, and is therefore not physically plausible. The scarcity of hydrogen is the main driver for the formation of unsaturated hydrocarbons.

and the temperatures in the atmosphere.

For a terrestrial exoplanet having a carbon-rich thick atmosphere, unsaturated hydrocarbons can become the dominant carbon-bearing gases in the atmosphere if the atmosphere loses most of its free hydrogen. When the atmosphere has free hydrogen (i.e., $X_H > 4X_C$), carbon is in the most reduced form, CH_4, if the planet receives similar degree of irradiation as GJ 1214b (see Figure 4-2 and Figure 4-8). If $X_H < 4X_C$, the abundance of hydrogen in the atmosphere is not enough to saturate carbon, and C_2H_4 and C_2H_2 emerge as the main carbon carrier for decreasing hydrogen abundances (see Figure 4-2 and Figure 4-8). If the planet receives similar degree of irradiation as 55 Cnc e, CH_4 and C_2H_4 are not expected to exist in abundance in the atmosphere in any cases, instead C_2H_2 and C_2H would be the main carbon carrier (see Figure 4-3 and Figure 4-8).

The scarcity of hydrogen is the main driver for the formation of unsaturated hydrocarbon in oxygen-poor carbon-rich thick atmospheres of terrestrial exoplanets. I

158

systemize the speciation of carbon in hydrocarbon-rich atmospheres in Figure 4-8, for which I have used thermochemistry simulations (i.e., minimizing global Gibbs free energy) to compute the relative abundance of hydrocarbons for different hydrogen abundances X_H and temperatures and pressures. For an intermediate X_H, significant, even dominant amounts of C_2H_4 and C_2H_2 would be present in the atmosphere. For smaller and smaller X_H, the hydrocarbons in the atmosphere become less and less saturated (Figure 4-8). Interestingly, C_2H_6 cannot be the dominant carbon species in any cases. This is in contrast with the photochemical formation of unsaturated hydrocarbons (mostly in C_2H_6) in Jupiter's atmosphere (e.g. Gladstone et al., 1996) and Titan's atmosphere (e.g. Yung et al., 1984), which is driven by the photon-initiated dissociation of methane and is confined to pressures lower than 0.1 bar (i.e., the stratosphere). Here, the formation of unsaturated hydrocarbon is no longer a photochemical perturbation, but an inevitable result of hydrogen loss of the atmosphere. Unsaturated hydrocarbons can be the dominant gases in evolved oxygen-poor carbon-rich thick atmospheres on terrestrial exoplanets, and they lead to spectral features that allow unique identification of carbon-rich atmospheres.

The mixing ratios of CH_4, C_2H_2, and C_2H_4 in hydrocarbon-rich thick atmospheres on terrestrial exoplanets also depend on the efficiency of eddy mixing and likely on the internal heat flux. When the eddy mixing is more efficient, the quenching pressure becomes higher. If the planet has significant internal heat flux, the atmospheric temperature would increase with pressure adiabatically at depth, and then C_2H_2 is more favored than CH_4 or C_2H_4 as the carbon carrier (Figure 4-8; also see the lower panel of Figure 4-7). If the planet has negligible internal heat flux, the atmosphere below the radiative layer would be isothermal, and then as a result of increasing pressure and constant temperature, a greater eddy mixing coefficient would lead to more CH_4 in the observable part of the atmosphere. CH_4, C_2H_2, and C_2H_4 all have distinctive spectral features; and their relative abundance may provide a probe to the processes of eddy mixing and internal heating in the deep atmosphere of a super Earth that are otherwise not detectable.

The results above are valid for hydrocarbon-rich atmospheres, which typically

requires $X_C/X_O \geq 2$. If I loosen this requirement and consider the cases with $X_C/X_O \geq 1$, I find that the atmosphere is most likely to be dominated in CO. For $X_C/X_O \sim 1$, the abundance of unsaturated hydrocarbons in the non-H_2-dominated thick atmosphere of an exoplanet having similar temperatures as GJ 1214b would be at the level of 1000 ppmv in the observable part of the atmosphere, also significant in terms of driving spectral features. In all, I find that unsaturated hydrocarbons are abundant in non-H_2-dominated carbon-rich thick atmospheres on terrestrial exoplanets, and therefore they should be considered as one of the basic building blocks for terrestrial exoplanet atmospheres.

Finally I turn to the minor components in hydrocarbon-rich atmospheres. The main form of oxygen in hydrocarbon-rich atmospheres is invariably CO. Based on a thermochemical calculation similar to the previous section, assuming oxygen to be minor perturbation to a predominantly hydrogen and carbon atmosphere, I find that $X_{H_2O}/X_{CO} < 10^{-6}$ (also see Figure 4-4). This result is also verified by the photochemistry-thermochemistry simulations.

4.4   Application to Observations

I here present synthetic spectra based on the photochemistry-thermochemistry simulations in order to compare with current observations and to guide future observations. The results presented below are not only applicable to GJ 1214b and 55 Cnc e, but also applicable to terrestrial exoplanets that receive similar degree of heating from their parent stars.

4.4.1   GJ 1214b

Current observations of super Earth/mini Neptune GJ 1214b have shown a flat spectrum in transmission (Bean et al., 2010, 2011; Désert et al., 2011; Berta et al., 2012; de Mooij et al., 2012). The observed flat transmission spectrum has ruled out the scenario that the planet has a H_2-dominated clear atmosphere, but can be explained by an atmosphere having a mean molecular mass larger than 15. Using the photochemistry-

thermochemistry model, I find that as long as $X_H \leq 0.7$, the mean molecular mass of the observable part of the atmosphere is greater than about 15, and such an atmosphere would be consistent with current observations (Figure 4-9). All models with $X_H \leq 0.7$, regardless of the carbon to oxygen ratio, provide adequate fit to the current observations of GJ 1214b (Figure 4-9). The acceptable scenarios includes water-dominated atmosphere (upper panel of Figure 4-5), H_2-CO dominated atmosphere (lower panel of Figure 4-5), CO-CH_4 dominated atmosphere (upper panel of Figure 4-7), and C_2H_2-C_2H_4 dominated atmosphere (lower panel of Figure 4-7).

How could future observations distinguish these scenarios? Figure 4-10 shows the transmission spectra and the thermal emission spectra of the planet if its atmosphere has lost most of its hydrogen envelope. A number of diagnostic features indicating hallmark molecules for different atmospheric scenarios stand out, and these features will allow future characterization of super Earth/mini Neptune GJ 1214b, and other transiting super Earths and mini Neptunes with similar temperatures to be discovered. Out of a number of spectral features labeled in Figure 4-10, it is useful to stress the following three points.

First, a hydrocarbon-dominated atmosphere (i.e., the case of $X_C/X_O > 2$) can be uniquely identified by detecting the absorption bands of C_2H_2 at 1.0 and 1.5 μm in transmission. In particular, the C_2H_2 feature at 1.0 μm is not contaminated by other potential constituents in the atmosphere, and has a feature size comparable to that of the water features nearby (Figure 4-10). In addition, a hydrocarbon-rich atmosphere can be detected by the prominent absorption bands of C_2H_2 and C_2H_4 in 10-15 μm in thermal emission (Figure 4-10). The photochemistry-thermochemistry models show that C_2H_2 is expected to be abundant in a carbon-rich atmosphere of GJ 1214, and I suggest C_2H_2 as a main component and hallmark molecule for carbon-rich atmospheres on a GJ 1214b like exoplanet.

Second, a detection of the thermal emission would be highly complementary to the transmission spectroscopy. A hydrocarbon-rich atmosphere has little H_2O or CO_2, so its thermal emission spectrum should be dominated by the absorption bands of CH_4, C_2H_4, and C_2H_2 (Figure 4-10). A water-rich atmosphere has little methane or

161
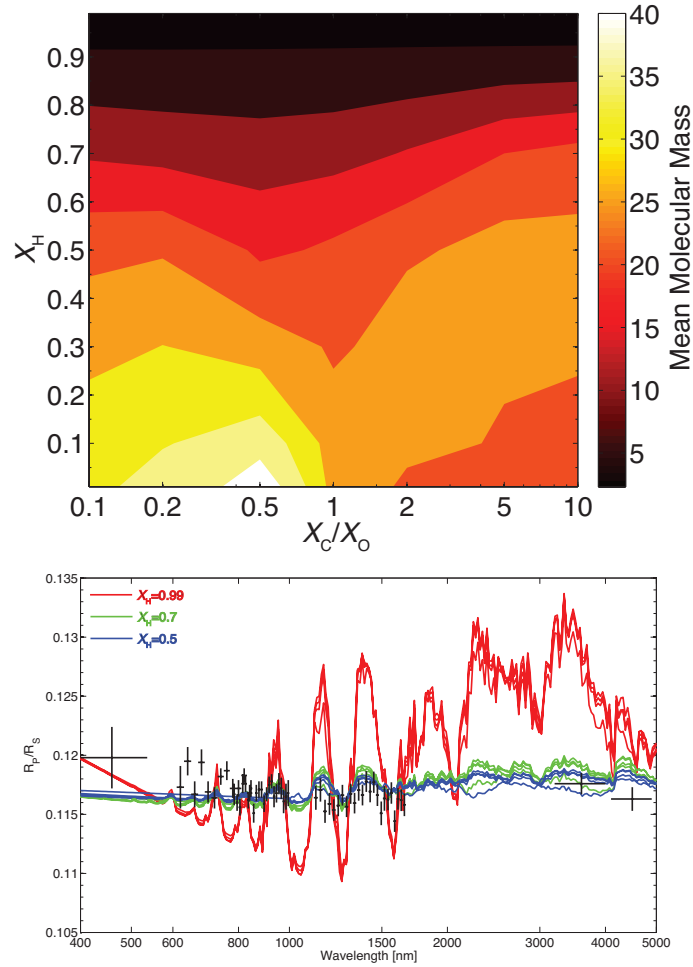
Figure 4-9: *Upper panel* Mean molecular masses of the observable part (pressure ranging from 1 mbar to 1 bar) of the modeled atmospheres of super Earth/mini Neptune GJ 1214 b. *Lower panel* Modeled transmission spectra of GJ 1214b in comparison with current observations. The synthetic spectra are computed based on the photochemistry-thermochemistry simulations, for $X_H = 0.99$ (red lines), 0.7 (green lines), and 0.5 (blue lines), respectively. For each X_H, I show the spectra corresponding the carbon to oxygen ratio of 0.1, 0.5, 1, and 2. Also plotted on the figure are the current observation data spanning from visible to mid-infrared wavelengths, from de Mooij et al. (2012); Bean et al. (2011); Berta et al. (2012); Désert et al. (2011) . The main point is that as long as $X_H \leq 0.7$, the mean molecular mass in the atmosphere would be greater than 15, regardless of the carbon to oxygen ratio, and the corresponding transmission spectrum would be flat enough to be consistent with current observations.
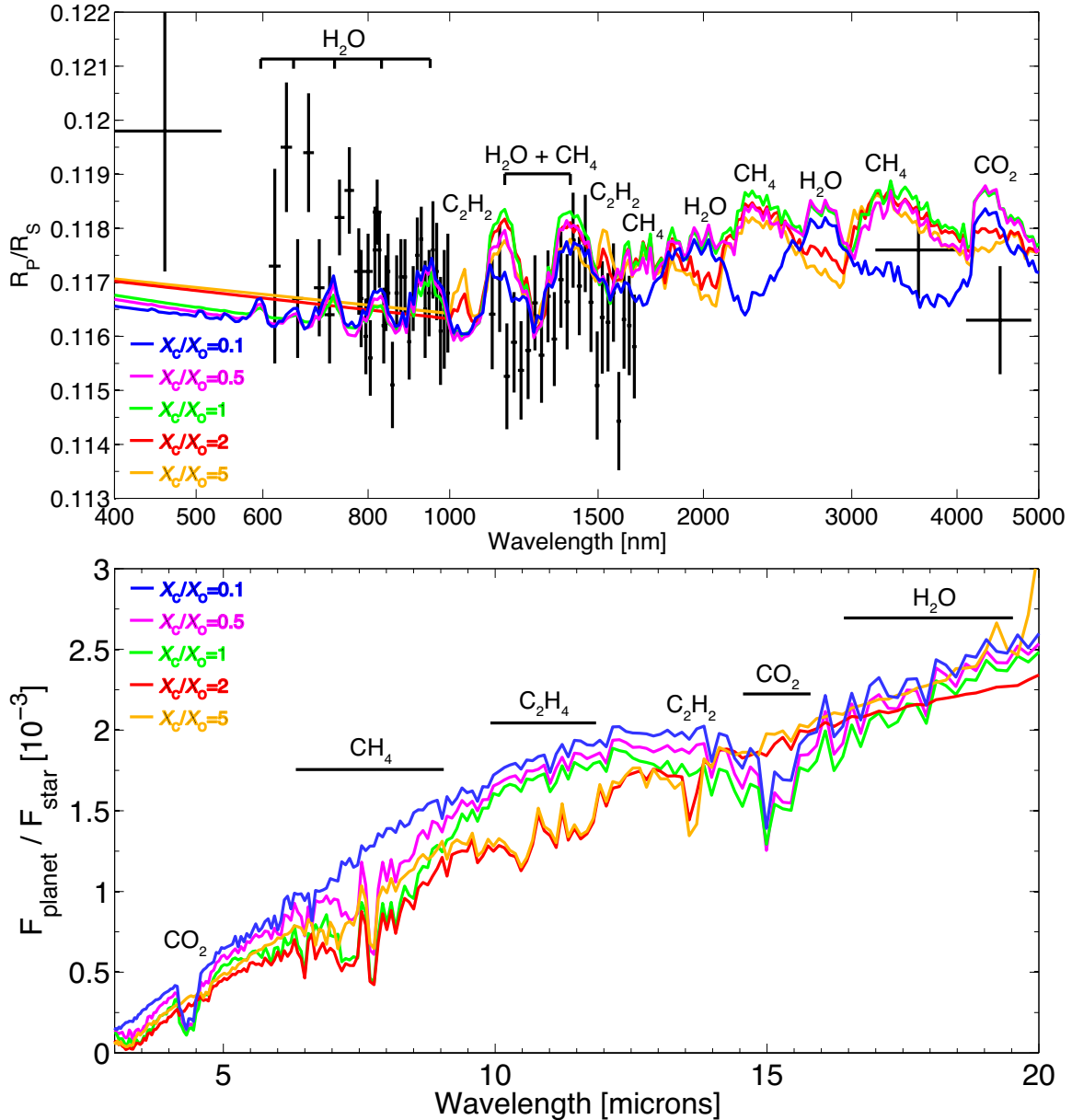
Figure 4-10: Molecular features in the transmission spectra and thermal emission spectra of non-H_2-dominated atmospheres on GJ 1214b based on my photochemistry-thermochemistry simulations. The simulated spectra are for $X_H = 0.5$ and a variety of carbon to oxygen ratio ranging from oxygen rich to carbon rich. Also plotted in the figure are the current observation data in transmission spanning from visible to mid-infrared wavelengths. The atmospheric scenarios with different carbon to oxygen ratios can be constrained via the spectral features of their hallmark molecules (see the highlights of the available spectral features in Section 4.4.1).

other hydrocarbons, so its thermal emission spectrum should only show the prominent absorption bands of CO_2 on top of the pseudo-continuum of H_2O absorption (Figure 4-10). Current attempts to observe the thermal emission of the planet with *SPITZER* have only yielded upper limits of 2.5×10^{-4} at 3.6 μm and 1.0×10^{-4} at 4.5 μm (Madhusudhan et al., 2010). The upper limit at the 4.5-μm band is of particular interest because such an upper limit could potentially imply the CO_2 absorption, rule out the scenarios of hydrocarbon-rich atmospheres, and support the scenarios of CO_2-H_2O atmospheres. Thermal emission spectra are likely to be observed by future infrared telescope in space, as the planet to star flux ratio will be within the reach of the *JWST*.

Third, a water-dominated atmosphere may be inferred from the nonexistence of methane absorption features. With transmission spectroscopy, a water-rich atmosphere (i.e., the case of $X_C/X_O \leq 0.5$) may be inferred based on the detection of water vapor absorption bands in the near-infrared. However, it would be very hard to establish that the atmosphere is mostly composed of water vapor based on water vapor features alone. Figure 4-10 shows that the atmosphere scenarios with X_C/X_O ranging from 0.1 to 1, which have the water vapor mixing ratio ranging from 70% to 5%, have almost identical water vapor features in 0.6-1.5 μm. The water vapor features would allow detection of *water-rich* atmospheres but not *water-dominated* atmospheres. The photochemistry-thermochemistry models show that a H_2-depleted water-dominated atmosphere must have CO_2 as the carbon carrier and must not have any significant amounts of CH_4. Therefore, a confirmed nonexistence of methane feature in either transmission or thermal emission (see Figure 4-10), in combination with a detection of water features, will provide sufficient evidence for a water-dominated atmosphere on a GJ 1214b like exoplanet.

4.4.2 55 Cnc e

The measured radius of super Earth 55 Cnc e (2.2 ± 0.1 R$_\oplus$) implies a volatile envelope on the planet (Gillon et al., 2012). For the measured mass of the planet, the planet's radius would be 1.5 $R_\oplus$ if it was completely composed of iron, or 1.9 $R_\oplus$ if

it was completely composed of $MgSiO_3$ estimated using of models of Zeng and Sasselov (2013); that is to say, the room for a potential atmosphere is maximally ~ 4000 km thick, or 30% of the observed planet radius. The planet's radius has also been measured by Winn et al. (2011) in the visible wavelengths to be $\sim 2\ R_\oplus$ (based on reanalysis by Gillon et al., 2012). Recently, the detection of the thermal emission of the planet in the *SPITZER* 4.5-μm band indicates a relatively high dayside temperature (2360 ± 300 K; Demory et al., 2012b).

Current observations of the thermal emission of 55 Cnc e in the *SPITZER* 4.5-μm band is likely to contain absorption features of either CO_2 in oxygen-rich scenarios, or CO in carbon-rich scenarios, if the planet has an atmosphere. I simulate the transmission spectra and thermal emission spectra of a 55 Cnc e like super Earth, assuming a thick atmosphere on the planet (Figure 4-11). Interestingly, the *SPITZER* 3.6-μm band (not yet observed), where the main CH_4 band falls into, is likely to probe deep into the atmosphere and has a higher brightness temperature than the 4.5-μm band, because methane is not expected to exist in significant amounts in such a high-temperature atmosphere according to my photochemistry-thermochemistry simulations.

For future observations of 55 Cnc e, a water-rich atmosphere can be detected in thermal emission with the absorption bands of H_2O and CO_2, and by transmission spectroscopy if the mean molecular mass is low (Figure 4-11). This is similar to the case of GJ 1214b that has a much lower temperature. A hydrocarbon-rich atmosphere on 55 Cnc e would result in prominent absorption bands of CO and C_2H_2, potentially detectable via thermal emission, and transmission if the mean molecular mass is low (Figure 4-11). Note that unlike the case of GJ 1214b, the nonexistence of methane feature cannot be interpreted as the water dominance. On 55 Cnc e, it is not expected to detect any methane feature regardless of the carbon to oxygen ratio.

The transmission spectroscopy of 55 Cnc e, if the planet has an extended H_2-rich atmosphere, is within reach of current observation facilities including VLT and *Hubble*. Especially, the diagnostic features of water-rich atmospheres (H_2O features) and the diagnostic features of hydrocarbon-rich atmospheres (C_2H_2 and CO features)
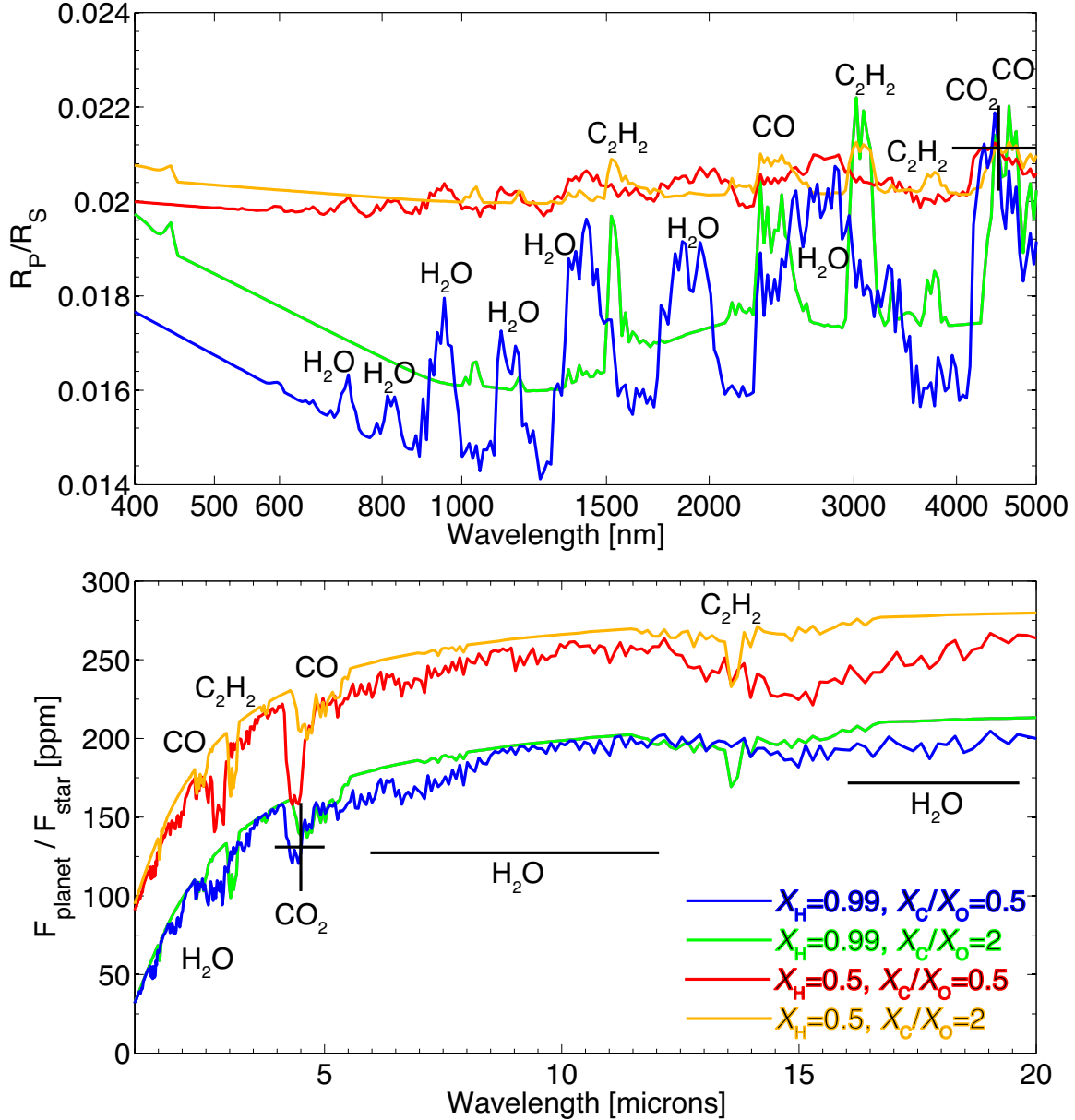
Figure 4-11: Modeled transmission spectra and thermal emission spectra of thick atmospheres on a 55 Cnc e like super Earth based on photochemistry-thermochemistry simulations. The presented spectra are for both H_2-dominated ($X_H = 0.99$) and non-H_2-dominated ($X_H = 0.5$) atmospheres with a variety of carbon to oxygen ratioS ranging from oxygen-rich to carbon-rich. Also plotted in the figure are the current observation data in transmission (Gillon et al., 2012) and in thermal emission (Demory et al., 2012a). The thermal emission spectra for the non-H_2-dominated scenarios are offset by 50 ppm for clarity. The cases of $X_H = 0.99$ would necessarily require the planet's interior to be mainly composed of iron, in order to satisfy the mass-radius constraints. The diagnostic features of water-rich atmospheres (H_2O features) and the diagnostic features of hydrocarbon-rich atmospheres (C_2H_2 and CO features) are well separated at near-infrared wavelengths.

are well separated in the near-infrared wavelengths in transmission spectra (Figure 4-11), which would enable straightforward characterization of the chemical compositions of the atmosphere.

4.5   Discussion

4.5.1   Finding Water-Dominated Thick Atmospheres May be Challenging

Water-dominated atmosphere, if discovered, would be an exciting environment in our interstellar neighborhood because of its reminiscence of a habitable world. In fact, one of preferred scenarios for the super Earth/mini Neptune GJ 1214b is that the planet has a signficant fraction of its mass as water based on mass-radius constraints (Rogers and Seager, 2010b) and that the planet has a water-dominated atmosphere based on the flat transmission spectrum (Bean et al., 2010, 2011; Berta et al., 2012). I study the range of atmospheric composition of GJ 1214b in detail using my photochemistry-thermochemistry model, and find that water-dominated atmosphere is far from being the only plausible solution to explain the flat transmission spectrum without incurring clouds. I show a range of possible scenarios, their transmission and thermal emission spectra, and outline a number of possible ways to distinguish them by future observations in the previous section.

For a more general discussion beyond GJ 1214b, I suggest that identifying a water-dominated atmosphere may be harder than previously expected. There are two reasons for this suggestion. The first reason is that water vapor features in the transmission spectra are not effective in distinguishing a water-dominated atmosphere versus a water-rich atmosphere. This has been shown by Benneke and Seager (2012) with a quantitative retrieval method for super Earth transmission spectra. This is also shown in Figure 4-10 as an example, in which atmospheric scenarios with water vapor mixing ratios ranging from 1% to 70% have similar sizes of water vapor features in the transmission spectra. The second reason is that the mixing ratio

of water vapor in a non-H_2-dominated atmosphere is highly sensitive to the carbon to oxygen ratio (Figure 4-4). In particular, for a solar carbon to oxygen ratio, a non-H_2-dominated atmosphere is not water-dominated, but such an atmosphere will have prominent water vapor features in its spectrum (Figure 4-5 and Figure 4-10). Therefore, identifying a water-dominated atmosphere not only involves measuring the water vapor features, but also require evaluating the carbon to oxygen ratio of the atmosphere, which warrants measurements of other gases in the atmosphere.

Moreover, a water-dominated atmosphere might be indigenously rare in nature. For a planet to have a water-dominated atmosphere, the planet has to start with an almost pure water ice envelope, with methane ice in the ice composition of no more than 20% by weight. I show in the section 4.3.2 that the carbon to oxygen ratio has to be less than 0.2, much smaller than the solar ratio, for a thick atmosphere to evolve into a water-dominated atmosphere. Such a condition on the planet's forming environment is quite confining, which might only be possible close to the snow line of a protoplanetary disk with a solar-like carbon to oxygen ratio. Studies of the condensation sequence of volatile ices from protoplanetary nebula gases have shown that the ice compositions sensitively depend on the carbon to oxygen ratio of the nebulae (e.g. Marboeuf et al., 2008; Johnson et al., 2012). Even for a planet-forming nabula with a solar carbon to oxygen ratio, the ice mixture should have $\sim 20\%$ carbon by weight (Marboeuf et al., 2008); and the carbon content in ice increases with increasing carbon to oxygen ratios of the nebulae, in particular for those with cold midplanes (Johnson et al., 2012). To summarize, one could expect the super Earths that are born as mini Neptunes to have a wide range of carbon to oxygen ratios in their atmospheres, and water-dominated atmosphere is one of many plausible atmospheric scenarios. This finding suggests that water-dominated atmospheres might be rare.

4.5.2 Chemical Stability of Atmospheric Gases

One useful application of my photochemistry-thermochemistry model is to verify the chemical stability of atmospheric gases. The "million model" approach has been developed to interpret the observations of exoplanet atmospheres (e.g. Madhusudhan

and Seager, 2009; Benneke and Seager, 2012). These methods seek best-fitted model spectra of planetary emission and transmission by exploring the full parameter space of molecular compositions. I have shown in this chapter that not all combinations of gases are chemically stable in thick atmospheres on terrestrial exoplanets. For example, I find that methane is not compatible with water-dominated atmospheres on GJ 1214b. Therefore, my photochemistry-thermochemistry model can be used in conjunction with the "million model" approach to eliminate a significant part of the parameter space, in terms of ruling out the unstable atmospheric scenarios, and strengthen the interpretation of observation spectra.

As a general study on the stability of gases in thick atmospheres, I additionally simulate atmospheres initially composed of all possible 50%-50% molecular binary combination of H_2, H_2O, CH_4, CO, and CO_2 for an exoplanet like GJ 1214b. For each scenario, I derive the elemental abundance from the initial composition for the model input. For example, to simulate a 50% H_2 50% CO atmosphere, I use an H:O:C ratio of 2:1:1. The thermochemistry-photochemistry model result is then compared with the initial molecular composition, to determine whether such an initial state is chemically stable.

I find that H_2 is compatible with all major stable gases of C, H, O elements, but H_2O is not compatible with equal amount of CH_4 and CO. An atmosphere mainly composed of H_2O and CO or CH_4 is not stable for GJ 1214b because of the following reactions:

$$H_2O + CH_4 \longrightarrow 3\,H_2 + CO. \tag{C 18}$$

$$H_2O + CO \longrightarrow H_2 + CO_2. \tag{C 19}$$
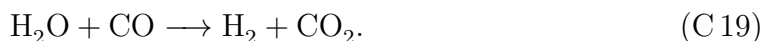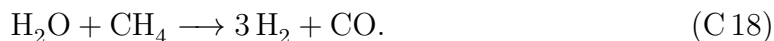
For the elemental abundance of H_2O-CO or H_2O-CH_4 combination, I find that CO and CH_4 can always reduce most of H_2O to H_2 (see Figure 4-12). Similarly, the CH_4-CO_2 combination has the same elemental abundance as the H_2-CO combination; the atmosphere will have the composition of H_2 and CO at the steady state, and the CH_4-CO_2 combination is not stable (and therefore not a plausible scenario). These results imply that chemical stability has to be taken into account when deriving atmospheric
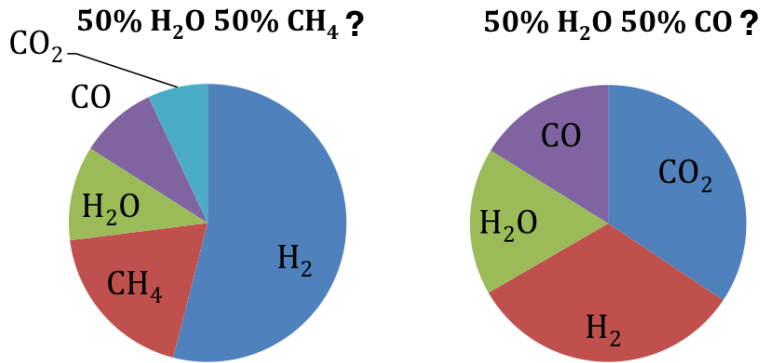
Figure 4-12: Mixing ratios of main components in the observable part of the atmosphere on a super Earth like GJ 1214b, based on photochemistry-thermochemistry simulations starting from an initial composition of 50% H_2O and 50% CH_4, and an initial composition of 50% H_2O and 50% CO. The initial compositions are not chemically stable because H_2O will oxidize CH_4 or CO in the mixture. Therefore 50% H_2O-50% CH_4, or 50% H_2O-50% CO, are not plausible scenarios for the atmosphere on GJ 1214b.

molecular compositions from spectra of super Earths and mini Neptunes.

4.5.3 Trace Gases as the Probe for Vertical Mixing and Internal Heating

Molecular compositions of a thick atmosphere at the pressure levels relevant to observations are controlled by vertical transport and chemical reactions at a deeper level. The idea of disequilibrium chemistry driven by vertical transport was originally proposed to explain the overabundance of CO and the deficit of NH_3 in Jupiter's atmosphere (Prinn and Barshay, 1977; Prinn and Olaguer, 1981) and used to explain chemical composition of Solar-System giant planets (e.g. Fegley and Prinn, 1985; Yung et al., 1988; Fegley and Lodders, 1994). Similar processes have also been suggested to operate on brown dwarfs and hot Jupiters (e.g. Fegley and Lodders, 1996; Griffith and Yelle, 1999; Cooper and Showman, 2006; Line et al., 2010; Madhusudhan and Seager, 2011; Visscher and Moses, 2011; Moses et al., 2011). In general, the chemical timescale of a certain molecule decreases with increasing pressure and temperature.

At the pressure levels where vertical transport timescale is shorter than the chemical kinetic timescale, the molecule is well mixed; at deeper levels in which the chemical timescale becomes shorter than the vertical transport timescale, the molecule's abundance is set by thermochemical equilibrium. Therefore, the molecule's abundance at observable pressure levels is set by thermochemical equilibrium at the level at which the vertical transport timescale equals the chemical kinetic timescale, i.e., the quenching level.

The most significant effects of vertical mixing are on the second most abundant carrier of major elements, and the most abundant carrier of minor elements. The abundances of the most abundant carriers of major elements, like H_2, H_2O, and O_2 in water-rich atmospheres, are determined by the constraints of elemental abundances. Indeed, the elemental abundance could uniquely determine the abundances of major components in some thick atmospheres (see Table 4.1). Based on the major composition set by the elemental abundance, relatively minor constituents in the atmosphere are indicators of the effects of eddy mixing and disequilibrium chemistry. The minor constituents can be either the carriers of minor elements, like carbon species in a water-rich atmosphere (Figure 4-5) and oxygen species in a hydrocarbon-rich atmosphere (Figure 4-7), or the second most abundant carriers of major elements, like C_2H_2 in a CO-CH$_4$ atmosphere (Figure 4-7).

Determining the major components and some of the minor components in atmospheres of super Earths and mini Neptunes like GJ 1214b via spectroscopy may offer a window to their deep atmospheres that are otherwise not detectable, and potentially enable the study of vertical mixing and internal heating on these planets. For a warm exoplanet like GJ 1214b, I find that for a wide range of composition, and an eddy diffusion coefficient ranging from $10^6 \sim 10^9$ cm^2 s^{-1}, the quenching pressure is $10 \sim 100$ bar. This is true for almost all types of atmospheres. What determines the abundance of the minor species is the interplay between eddy mixing that determines the quenching pressure, and the internal heat flux that determines the temperature at the quenching pressure. The so called "minor species", although low in absolute amounts, may have significant imprints in spectra and therefore be detectable. For

example, C_2H_2 in a CH_4 dominated atmosphere leads to prominent C_2H_2 features in both transmission and thermal emission (Figure 4-10). For a very hot super Earth like 55 Cnc e (equilibrium temperature higher than $\sim$ 2000 K), however, the atmosphere is very close to thermochemical equilibrium at all relevant pressure levels. For these planets, thermochemical equilibrium calculation would be efficient and adequate for studying the chemical properties of their atmospheres.

4.5.4 Atmosphere-Surface Exchange of Super Earths

A cumulative loss of hydrogen from atmospheres on super Earths would result in the build-up of oxygen, unsaturated hydrocarbons, and other thermochemical and photo-chemical products. In this study, I neglect the possible material exchange between the atmosphere and the surface of a super Earth. How would active atmosphere-surface exchange affect the atmospheric composition of a super Earth?

First, surface emission of reduced gases (e.g., H_2, CH_4, H_2S) and exposure of un-oxidized minerals (e.g., FeO) by volcanism can consume atmospheric oxygen and potentially prevent the formation of O_2-rich atmospheres. Without atmosphere-surface exchange, I predict some super Earths that form in oxygen-rich nebulae will have O_2-rich atmospheres due to loss of atmospheric hydrogen into the space. Such O_2-rich atmospheres may be short-lived due to atmosphere-surface exchange. A Solar-System example reminiscent of this process is Venus. If Venus starts with an ocean and loses its ocean during the runaway greenhouse phase, a scenario supported by the detection of an atmospheric D/H ratio $\sim$ 160 times higher than the terrestrial value (e.g. Don-ahue et al., 1982), a massive O_2-rich atmosphere up to 240 bars must have existed on Venus (Kasting, 1997). However, today's Venus atmosphere only has trace amounts of oxygen, which means that that much of oxygen has to be consumed over the history of Venus. Volcanic eruptions can release reduced gases (e.g., H_2, CH_4, H_2S) and expose unoxidized lithosphere (e.g., FeO), which can consume atmospheric oxygen. It has been estimated that volcanic eruption rates on Venus has to be a few times higher than the current volcanic eruption rate of Earth to consume the left-over O_2 in 100 million years (Fegley, 2008). For a super Earth to prevent the O_2 build up due

to hydrogen loss, the level of volcanic activity would need to be at least comparable to Earth's, depending on how strong the hydrogen loss is.

Second, surface emission of hydrogen and other reduced gases to the evolved atmosphere on a super Earth will be quickly removed by thermochemical reactions that yield energy. For example, in an oxygen-rich atmosphere, emitted hydrogen would react with free oxygen to form water, a process that yields chemical energy. For another example, in an evolved carbon-rich atmosphere, emitted hydrogen would react with unsaturated hydrocarbons to form more saturated forms of carbon, a process that also yields chemical energy. As shown in Figure 4-6 and Figure 4-8, the scarcity of hydrogen, driven by atmospheric loss, is the controlling factor for the major components in water-rich atmospheres and hydrocarbon-rich atmospheres. Therefore, hydrogen escape to the space could potentially results in a large chemical gradient between the atmosphere and the interior of the planet. Such chemical gradient could be exploited by chemotrophs (see Seager et al., 2012), if temperature is suitable, and lead to potential biosignature gases.

4.6 Summary

I have developed and tested a one-dimensional photochemistry-thermochemistry kinetic-transport model for the exploration of compositions of thick atmospheres on terrestrial exoplanets. The unique feature of my photochemistry-thermochemistry model is that my model can treat both H_2-dominated atmospheres and non-H_2-dominated atmospheres, and my model is able to compute the main components and the mean molecular mass of the atmosphere based on elemental abundances. This feature makes my model uniquely suitable for the exploration of super Earth atmospheres, which are expected to be have diverse chemical compositions.

Using the photochemistry-thermochemistry model, I have outlined a roadmap to characterize thick atmospheres on terrestrial exoplanets. Using the hydrogen abundance (X_H) and the carbon to oxygen abundance ratio (X_C/X_O) as the primary parameters, I classify thick atmospheres on terrestrial exoplanets into hydrogen-rich at-

mospheres, water-rich atmospheres, oxygen-rich atmospheres, and hydrocarbon-rich atmospheres. I find that when $X_H > 0.7$, the atmosphere has free hydrogen and chemically behaves like H_2-dominated atmospheres on gas giants. When $0.3 < X_H < 0.7$, the atmosphere is water-rich for small X_C/X_O and hydrocarbon-rich for large X_C/X_O. In the middle of these regimes the molecular compositions depend on temperature sensitively.

Water-dominated atmospheres, in which most molecules are water vapor, only exist for $X_C/X_O < 0.2$, suggesting that this kind of atmospheres could be rare. I find that in a H_2-depleted water-dominated atmosphere, most of the trace mixture of carbon has to be in the form of CO_2 rather than CH_4 or CO. Therefore a detection of water vapor features together with a confirmation of nonexistence of methane features are sufficient evidence for a water-dominated atmosphere on an exoplanet having similar temperatures as GJ 1214b. If a water-rich atmosphere continues to lose hydrogen, free oxygen may be left over in the atmosphere to form oxygen-rich atmospheres.

For hydrocarbon-rich atmospheres, I find that it is the scarcity of hydrogen, probably a result of preferred loss of light elements, that drives the formation of unsaturated hydrocarbon. C_2H_2 and C_2H_4 can be the dominant forms of carbon in some cases, and they are the hallmark molecules for oxygen-poor carbon-rich thick atmospheres on terrestrial exoplanets. Therefore they should be considered among "standard" building blocks for atmospheres on terrestrial exoplanets. Also for hydrocarbon-rich atmospheres I find that H_2O should be scarce and most of oxygen should be in the form of CO.

In terms of observational characterization of thick atmospheres on terrestrial exoplanets, my photochemistry-thermochemistry models can eliminate a significant part of molecular composition parameter space. In all, the ranges of molecular compositions presented in this chapter that contain hallmark molecules will allow observational characterization of different atmosphere scenarios on super Earths and mini Neptunes.

Chapter 5

Theoretical Spectra of Airless Terrestrial Exoplanets

5.1 Background

5.1.1 Airless Terrestrial Exoplanets

A few exoplanets have been suggested to have rocky surfaces, because the mass and radius constraints indicate that the planets are predominantly rocky with no extensive atmosphere envelope, i.e., likely rocky surfaces. Corot-7b opens up the possibility of close-in airless rocky exoplanets (Léger et al., 2009; Queloz et al., 2009). Due to the small star-planet distance, Corot-7b may have molten or even vaporized metals on its sub-stellar surface (Léger et al., 2011). Recently observations of transits of 55 Cnc e, a 8-$M_\oplus$ planet around a G8V star, determine the planetary radius to be 2.2 $R_\oplus$, which suggests that it can be a rocky planet (Winn et al., 2011; Demory et al., 2011; Gillon et al., 2012). The Kepler mission, with unprecedented photometric precision, is very powerful in discovering small-size transiting exoplanets. Kepler-10b, a 4.5-$M_\oplus$ planet, is the first rocky exoplanet discovered by Kepler (Batalha et al., 2011). Kepler recently discovered several planets with size in the "super earth" regime, including Kepler-11b (Lissauer et al., 2011), Kepler-18b (Cochran et al., 2011), Kepler-20b (Gautier et al., 2012) and notably Kepler-22b in its host star's habitable zone (Borucki et al., 2012).

Due to uncertainties of the planets' radii and masses, however, the composition of these Kepler super-Earths is ambiguous. They can be predominantly rocky like Earth, or have significant gas envelope like Neptune. Also, Kepler has detected Earth-sized transiting planets, Kepler-20e and Kepler-20f, with no constraints on their masses due to difficulties of followup radial-velocity observations (Fressin et al., 2012). With the progress of the Kepler mission, other transit surveys and followup observations, more and more exoplanets that potentially have rocky surfaces will be discovered and confirmed.

The purpose of this chapter is to identify mineral-specific spectral features that would allow characterization of the surface composition of airless rocky exoplanets. The analogs of airless or nearly airless rocky exoplanets in the Solar System are the Moon, Mars, Mercury and asteroids, whose surface compositions have been studied extensively by spectroscopy of reflected solar radiation and planetary thermal emission (see Pieters and Englert, 1993; de Pater and Lissauer, 2001, and extensive references therein). For investigations of the Solar System in 1970s and 1980s, the rocky bodies were still spatially unresolved or poorly resolved with resolution of a few thousand kilometers, and spectra of reflected solar radiation in the near-infrared (NIR) and spectra of planetary emission in the mid-infrared (MIR) were the only information to infer their surface composition. Thanks to prominent absorption features of specific minerals, notably olivine, pyroxene and ices, infrared spectroscopy provided significant constraints on the surface composition of rocky planets of the Solar System (e.g. Pieters and Englert, 1993).

Using infrared spectroscopy to characterize mineral composition is also applicable to study solid surfaces of exoplanets. Both reflected stellar radiation and planetary thermal emission from an exoplanet are potentially observable by secondary eclipses if the planet is transiting, as well as by direct imaging (e.g. Seager et al., 2000; Seager, 2010). Still, characterization of exoplanetary surfaces is very different from the investigation of the Solar System analog surfaces, due to the fact that an exoplanet cannot be spatially resolved and the spectroscopy of exoplanets is limited to very low spectral resolutions, probably broad-band photometry in the near term. As a result,

it is essential to focus on the most prominent spectral features in the disk-averaged radiation from an exoplanet.

In addition to the photochemistry model intended for terrestrial exoplanet atmospheres, I have also developed a theoretical framework to compute disk-integrated spectra of airless rocky exoplanets. The model self-consistently treats reflection and thermal emission and investigate the spectral features that can be used to interpret the mineral composition on exoplanetary surfaces. So far, the study of spectral features due to exoplanets' surfaces has been limited to features in the reflected light by vegetation (see Seager et al., 2005, for the "red-edge") and a liquid water ocean (e.g. Ford et al., 2001; Cowan et al., 2009). In this chapter I employ a generalized approach to investigate spectral features of solid materials on an exoplanet's surface, with a consistent treatment of reflected stellar irradiation and planetary thermal emission.

I focus on airless rocky exoplanets with solid surfaces, whose surface temperatures are lower than the melting temperature of silicates and other common minerals ($\sim$ 1000 - 2000 K). This surface temperature requirement ensures that the planetary thermal emission and the reflected stellar radiation can be separated in wavelengths. As shown in Figure 5-1, Kepler-22b, Kepler-20f and Kepler-11b can have an unmelted silicate surface. Moreover, a large number of Kepler planetary candidates have the orbital distances that permit unmelted silicate surfaces. For now I do not consider close-in rocky exoplanets that have molten lava surfaces, such as the case of Corot-7b. Once melted, crystal-field features, such as Fe^{2+} electronic transition at 1 μm, will no longer persist in the same manner as in crystalline minerals. *In situ* measurements of active lava flow in Hawaii confirm that NIR spectra of molten lava are dominated by black-body emission (Flynn and Mouginis-Mark, 1992). I will address the spectral features of molten lava on close-in rocky exoplanet in future works.

5.1.2   Spectral Features of Geological Mineral Surfaces

The spectral reflectances of minerals have features specific to their chemical compositions and crystal structures. From the visible to the NIR wavelengths (VNIR; 0.3 - 3 μm), minerals such as pyroxene, olivine and hematite create prominent absorption
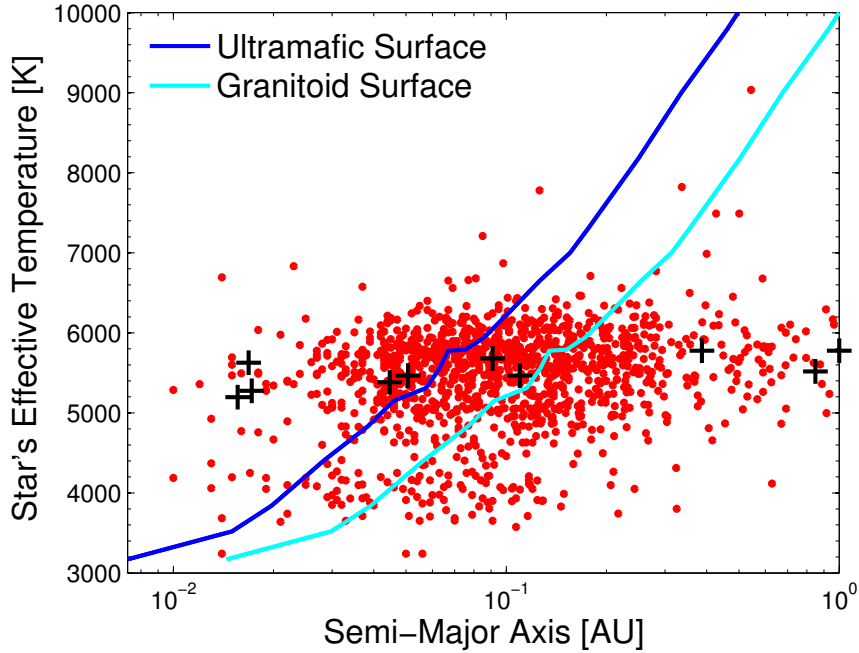
Figure 5-1: Relations between the spectral type of main-sequence stars (represented by effective temperatures) and the innermost orbital distance for a rocky planet to stay unmelted. Red dots are Kepler-released planet candidates as of April 2011 (Borucki et al., 2011). From left to right, the black markers correspond to planets that have or may have rocky surfaces: 55 Cnc e, Kepler-10 b, Corot-7 b, Kepler-18 b, Kepler-20 e, Kepler-11 b, Kepler-20 f, Mercury, Kepler-22 b and Earth. The lines are obtained by comparing sub-stellar (hottest) temperature and the zero-pressure melting temperature of silicates. Stellar luminosity data are taken from Cox (2000), amid significant uncertainties for effective temperature below 4500 K and for different stellar metalicities (e.g. Muirhead et al., 2012). Wavelength-dependent reflectivity and emissivity are considered in the computation of substellar temperature. The two lines correspond to limiting cases of silicates, for which ultramafic is the most refractive with a melting temperature of 1600 K and granitoid is the least refractive with a melting temperature of 1000 K. The melting temperatures assumed are typical, but exact numbers sensitively depend on content of volatiles and detailed mixtures of minerals (Best and Christiansen, 2001). A rocky planet that falls on the left side of the blue line certainly has molten lava on its surface, and a rocky planet that falls on the right side of the cyan line has solid silicates surface, i.e., the focus of this chapter.

features in reflection data, mostly due to electronic transitions of transition element ions (i.e., Fe^{2+}, Fe^{3+}, Ti^{3+}, etc.) in the the crystal structures of minerals (Burns, 1993). For example, Fe^{2+} in the crystal field of olivine absorbs strongly at 1 μm. Position, strength, and number of features of the 1-μm absorption band are diagnostic of the relative proportions of the Mg and Fe cations in olivines (e.g. Sunshine and Pieters, 1998). In the ultraviolet (UV) and visible wavelengths, many minerals, such as hematite (Fe_2O_3), have strong charge-transfer absorption bands, making them very dark (e.g. Clark, 1999). For secondary minerals, typically formed by interactions with water, their volatile components, such as hydroxyl (OH), water (H_2O), and carbonates (CO_3^{2+}), absorb strongly in the NIR due to overtone and combination absorptions from vibrations, i.e. bands and stretches of components in the crystal structure (e.g. Farmer, 1974). See Table 5.1 for a list of common minerals on terrestrial planet surfaces and their key features in the NIR reflectance spectroscopy.

Table 5.1: Common minerals on terrestrial planet surfaces and their key features in the NIR reflectance spectroscopy. Spectra used are from representative samples of average grain diameters less than 200 μm, comparable to lunar soil (Duke et al., 1970).

Mineral	Chemical Formula	Key Features
Olivine (Forsterite, 89Fo)[a]	$(Mg_{0.89},Fe_{0.11})_2SiO_4$	Absorption band at 1 μm
Low-calcium pyroxene (Enstatite)[b]	$(Mg_{0.8},Fe_{0.2})SiO_3$	Absorption bands at 0.9 μm and 1.9 μm
High-calcium pyroxene (Augite)[a]	$(Ca,Na)(Mg,Fe,Al)(Si,Al)_2O_6$	Absorption bands at 1 μm and 2.3 μm
Plagioclase (Anorthite)[a]	$CaAl_2Si_2O_8$	High albedo, flat spectrum, absorption at 1.3 μm
Hydrated silicate (Saponite)[a]	$Ca_{0.25}(Mg,Fe)_3(Si,Al)_4O_{10}OH_2{\cdot}n(H_2O)$	Absorption bands at 1.4 μm, 1.9 μm and 2.3 μm
Hematite[a]	Fe_2O_3	Low albedo, absorptions at 0.53 μm and 0.86 μm
Water ice[c]	H_2O[d]	Absorption bands at 1.5 μm and 2 μm

[a]

Reflectance data are from the USGS Digital Spectral Library (Clark et al., 2007).

[b] Reflectance data are from the RELAB Spectral Database (2010).

[c] Reflectance data are from Calvin and Clark (1991).

[d] H_2O and OH also have strong fundamentals at about 3 μm (H_2O stretch, OH stretch, OH bend) and 6 μm (H_2O bend).

Similar to reflected stellar radiation, planetary thermal emission is encoded with information about the planet's surface composition. Absorption in the mid-infrared (MIR; 3 - 25 μm) is due to vibrational motions in crystal lattices, so that their wavelengths are related to the crystal structure and elemental composition (i.e., min-

eralogy) (Farmer, 1974). Silicates have the most intense (i.e., the greatest absorption coefficient) spectral features between 8 and 12 μm due to the Si-O stretching, and the second most intense features between 15 and 25 μm due to the Si-O bending or deformation (Salisbury, 1993). These vibration bands are so strong that they can manifest as mirror-like reflectance peaks and therefore emittance troughs. The shapes of these bands are complicated by the so-called "transparency feature", features associated with a change from surface to volume scattering, and therefore are sensitive to particle size (Salisbury and Walter, 1989; Salisbury, 1993). At the short-wavelength edge of the Si-O stretching band (7.5 $\sim$ 9.0 μm), there is always a reflectance minimum (emittance maximum) as the refractive index of the mineral approaches that of the medium. This emittance maximum is termed "Christiansen Feature" (CF), unique and ubiquitous for silicates. The wavelength of the CF is indicative of silica content of the material, i.e., more mafic silicates have the CF at longer wavelengths (Salisbury and Walter, 1989; Walter and Salisbury, 1989). For example, Glotch et al. (2010) inferred highly silica-rich compositions on the Moon by determining the CF wavelengths. Iron oxides also show spectral features due to Fe-O fundamentals, but at longer wavelengths than Si-O fundamentals, because iron is more massive than silicon (Clark, 1999). For example, hematite, Fe_2O_3, has 3 strong stretching modes between 16 and 30 μm.

Spectral features of pure particulate minerals discussed above can be wide and deep, and could stand out in low-resolution and low signal-to-noise ratio spectra. In electronic processes, the electron participating in transitions may be shared between individual atoms and energy levels of shared electrons become smeared over wide energy bands, which results in wide spectral features (Burns, 1993; Clark, 1999). In vibrational processes, absorption bands are typically narrower than electronic features but can be broadened if the crystal is poorly ordered or if bands overlap (Farmer, 1974; Clark, 1999).

In reality, the contrast of spectral features may be significantly reduced, especially for thermal emission in MIR. Typical thermal emission band contrasts on planetary surfaces are less than $\sim$0.1 in the Solar System (Sprague, 2000; Christensen et al.,

2000; Clark et al., 2007). The reduction of spectral contrast in the thermal emission is mostly due to multiple scattering between regolith particles, with contributions of surface roughness and volume absorption (Hapke, 1993; Kirkland et al., 2003). Multiple reflection, as a result of surface roughness, increases the emergent emissivity (ϵ_e) towards unity, as illustrated by

$$\epsilon_e = 1 - (1 - \epsilon)^{(n+1)} \, , \tag{5.1}$$

where ϵ is the true emissivity of material and n is the number of reflections (Kirkland et al., 2003). As a result, unique identification of mineral compositions using planetary thermal emission usually requires high signal-to-noise ratio and high resolution spectroscopy.

Finally, mixing of minerals and space weathering may also reduce contrast of the spectral features. There are two levels of mixing, microscopic and macroscopic. Microscopic mixing (or intimate mixing) concerns particulates of different minerals that may be intimately mixed, such that photons are multiply-scattered by interactions with materials of different compositions. This is especially relevant for reflectance in VNIR. Macroscopic mixing (or areal mixing) concerns the planetary surface viewed as a disk average, which may contain discrete patches of different minerals or mineral assemblages. The average of macroscopic mixing can be modeled as a linear combination of reflected flux, whereas the microscopic mixing has to be treated as a multi-component radiative transfer problem. For spatially unresolved exoplanets, both microscopic mixing and macroscopic mixing need to be considered. Space weathering does not change the bulk mineralogic composition of the rocks and soils, but leads to formation of nanophase iron throughout the whole of the mature portion of the regolith, occurring in both vapor-deposited coatings on grain surfaces and in agglutinate particles, which alters the spectral properties of the surface significantly (e.g. Pieters et al., 2000; Hapke, 2001).

5.1.3 Solar System Airless Body Surface Spectra

Infrared spectral features have been used to study surface compositions of Solar System rocky planets. In the early-stage investigations, ground-based or balloon-based telescopic observations have been used to characterize the surfaces, for example the Moon (e.g. Murcray et al., 1970; Pieters, 1978; McCord et al., 1981; Pieters, 1986; Tyler et al., 1988), Mars (e.g. Singer et al., 1979; McCord et al., 1982), and Mercury (e.g. Vilas, 1985; Tyler et al., 1988; Blewett et al., 1997; Sprague et al., 2002). As a benchmark for the exoplanet investigations, I focus here on a description of the most prominent features in the low-spatial-resolution reflectance spectra and their implications. Several representative ground-based spectra of the Moon, Mars, and Mercury and the prominent features therein are shown in Figure 5-2.

Reflectance spectra at NIR have been used to characterize the lunar mare and the lunar highlands. The lunar mare are generally dark and absorb strongly at 1 μm and 2 μm, which indicate they are of basaltic composition (e.g. Pieters, 1978, and see Figure 5-2). The 1-μm absorption is due to iron-bearing glass, pyroxene, and olivine, and the 2-μm absorption is exclusively due to pyroxene (Pieters, 1978). Moreover, the relative strength of the 1-μm absorption and the 2-μm absorption, as well as the band center positions of these absorptions, are used to infer the amount of olivine versus pyroxene and pyroxene composition of the lunar mare (McCord et al., 1981). The basaltic nature of the lunar mare indicates that they formed by volcanic eruptions. In contrast to the lunar mare, the lunar highlands are bright and have nearly flat spectra at NIR with weak 1-μm and 2-μm absorptions, exhibiting a plagioclase composition with minor amounts of pyroxene (e.g. Pieters, 1986, and see Figure 5-2). The nearly pure plagioclase composition of the lunar highlands indicates that they are primary crust formed from solidification of a magma ocean (e.g. Warren, 1985).

Spatially unresolved spectroscopy of Mars has provided essential information to determine the surface composition of the red planet. Mars spectra feature strong Fe^{3+} charge-transfer and crystal field absorptions from the near-UV to about 0.75 μm (McCord and Westphal, 1971; Singer et al., 1979, see Figure 5-2). These spectral
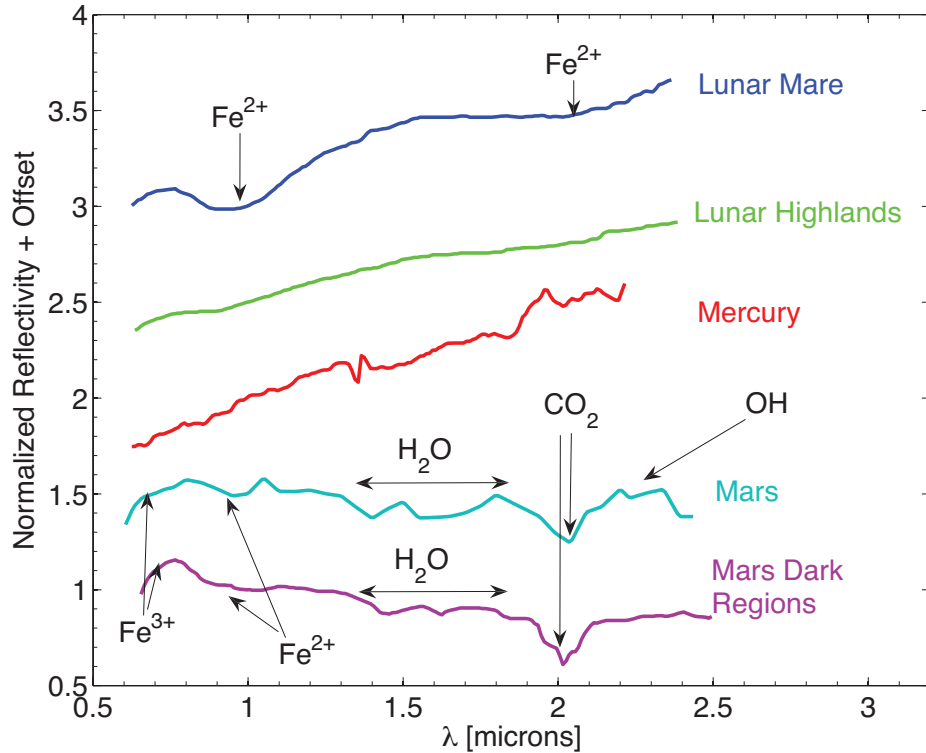
Figure 5-2: Ground-based telescopic reflectance spectra of the Moon, Mars and Mercury. The representative spectra shown on the figure are: (1) Lunar Mare Serenitatis, immature surface revealed by impact cratering, data from Pieters (1986); (2) Lunar Highland Descartes, immature surface revealed by impact cratering, data from Pieters (1986); (3) Mercury, disk average from bright limb to terminator, data from Blewett et al. (1997); (4) Mars, disk average, data from McCord and Westphal (1971); (5) Mars, a dark region near equator of ~ 1000 km in diameter, data from McCord et al. (1982). Reflectivity is normalized to be 1 at 1 μm and offset for clarity. Absorption of olivine and pyroxene (Fe^{2+}) manifests in the lunar mare spectrum at 1 μm and 2 μm, and also shows in the Mars spectra at 1 μm. Mars' atmospheric CO_2 imprints a deep absorption band at 2 μm. Mars spectra also contain strong charge-transfer absorption of Fe^{3+} at wavelengths shorter than 0.75 μm, wide absorption feature from 1.4 to 1.7 μm, attributed to water ice on the surface, and a weak absorption near 2.2 μm, interpreted as hydrated minerals.

features, together with the visual red color and the polarization properties of Mars, established that the major component of the Martian surface is ferric oxides (e.g., hematite). Also, the spectra from dark areas on Mars show features of mixtures of pyroxene and olivine, probably covered by a layer of ferric oxides (McCord et al., 1982, see Figure 5-2). The mineral composition of the Martian surface is interpreted as a result of secondary basaltic volcanism, affected by later oxidative weathering, perhaps in presence of liquid water to form Fe^{3+} oxides (Mustard et al., 2005).

Telescopic spectra of Mercury suggest a surface similar to the lunar highlands. The NIR spectra of Mercury are flat without the signature Fe^{+2} absorptions at 1 and 2 μm (Vilas, 1985, see Figure 5-2). Also, emission features in the mid-infrared (7 – 13 μm) characteristic of silicate materials have been reported for Mercury (e.g. Tyler et al., 1988). The spectroscopic evidence suggested a low-iron plagioclase surface similar to the lunar highlands (Blewett et al., 1997), consistent with the outcome of solidification of magma ocean without mantle overturn (Brown and Elkins-Tanton, 2009). Recent observations from a spacecraft orbiting Mercury have challenged this view by measuring Mg-rich, Fe-poor and Al-poor chemical compositions (ultramafic) and morphologies consistent with flood volcanism (Nittler et al., 2011; Head et al., 2011; Blewett et al., 2011). Research is on-going to explain Mercury data; a potential explanation reconciling all observations is atypically low iron content ($< \sim$ 1 %) in common minerals forming ultramafic crusts (olivine, pyroxene), which usually exhibit Fe^{+2} absorptions.

5.2   Model

5.2.1   Types of Planetary Solid Surface

The assemblage of minerals provides valuable information on the geological history and even the interior structure of the planet. For example, in the Solar System, feldspathic surfaces, such as the lunar highlands, are primitive products of crystallization from a magma ocean, since plagioclase is light in density and floats on top of the

magma ocean (e.g. Warren, 1985). For a relatively large planet with mass similar to that of Earth and Mars, the predicted crust composition after the overturn of the mantle in order to form a stable density stratification is dominated by Mg-rich olivines and pyroxenes, i.e., an ultramafic surface (Elkins-Tanton et al., 2005). Subsequent partial melting of mantle (i.e., volcanism) leads to production of distinctive igneous rocks such as basalts, i.e. the lunar mare. Finally, re-processing, heating and partial melting of these materials leads to the generation of granites, a regime on Earth driven by plate tectonics and incorporation of water in subducted crustal materials to lower the melting point (Taylor, 1989).

I consider multiple geologically plausible planetary surface types as several assemblages of minerals, tabulated in Table 5.2. The types include primary crust, i.e., the crust that forms from solidification of magma ocean; secondary crust, i.e., the crust that forms from volcanic eruptions; and tertiary crust, i.e., the crust that forms from tectonic re-processing. Each type of igneous crust differs from another by assemblages of minerals, which are in turn governed by thermodynamics, planetary composition, and planetary history (e.g. Best and Christiansen, 2001; Hazen et al., 2008). Moreover, various modification processes in the planetary evolution may alter the surface spectral properties significantly. The modification processes include aqueous alteration and oxidative weathering [1]. Additionally I simulate an ice-rich planet and one lacking a silicate crust or mantle. The list in Table 5.2 encompasses the most common surface types; abiotic mechanisms of surface formation and modification are considered, and the list largely covers the diversified solid surfaces on Solar System rocky planets.

As is evident from Table 5.2, a planet's surface is defined as the assemblage of several endmember minerals. Moreover, a planet's surface may be composed of bulk patches of different crusts, as is the case for the lunar mare and highlands. It is therefore essential to consider the macroscopic mixture of different crusts as well as the microscopic (intimate) mixture of different minerals for each crust.

I model the intimate mixture of minerals as follows. For each endmember min-

---

[1]Space weathering is discussed in section 5.4.2

Table 5.2: Potential crustal compositions of rocky exoplanets. NIR spectra were defined for eight notional exoplanet surface types from laboratory measurement of rock powders (sample) or radiative transfer modeling combining endmember mineral samples measured in the laboratory (modeled).

Type	Mineral Composition	Spectrum Source	Indication	Solar System Examples
Metal-rich	Pyrite	Sample[a]	Primary crust with mantle ripped off	N/A
Ultramafic	60% Olivine, 40% Enstatite	Modeled[b]	Primary crust with mantle overturn; or secondary crust from hot lavas	Primary Earth and Mars; and early Earth lavas
Feldspathic	97% Fe-plagioclase, 3% Augite	Sample[c]	Primary crust without mantle overturn	Lunar Highlands
Basaltic	76% Plagioclase, 8% Augite, 6% Enstatite, 5% Glass, 1% Olivine	Sample[d]	Secondary crust	Lunar Mare and locations on current Earth
Granitoid	40% K-feldspar, 35% Quartz 20% Plagioclase, 5% Biotite	Modeled[b]	Tertiary crust	Current Earth
Clay	50% Mg-smectite, 50% Serpentine	Modeled[b]	Aqueously altered crust	Locations on current Earth and Mars
Ice-rich silicate	50% Water ice, 50% Basalt	Modeled[b]	Ice-rich silicate mantle	Locations on current Earth and Mars
Fe-oxidized	50% Nanophase hematite, 50% Basalt	Modeled[b]	Oxidative weathering	Current Mars

[a]
Clark et al. (2007).

[b]Spectra are synthesized from the measured spectra of each endmember minerals in Clark et al. (2007).

[c]Lunar anorthosite, sample 15415, Cheek et al. (2009).

[d]Basalt sample 79-3b from Wyatt et al. (2001).

eral, I use the measured bidirectional reflectance in the USGS Digital Spectral Library (Clark et al., 2007) or the RELAB Spectral Database (2010). I retrieve the wavelength-dependent single scattering albedo (ω) of each type of mineral from the experimental data based on an analytical radiative transfer model of (Hapke, 1981, 2002), which will be detailed in section 5.2.2. I average the mineral composition utilizing single scattering albedo spectra of endmembers, weighted by their mixing ratios. The bidirectional, directional-hemispherical reflectance and directional emissivity of the mixture can thus be computed using the Hapke radiative transfer model in the forward sense (Hapke, 1981, 2002). This method of computing reflectance spectra of mineral mixtures has been proven within 10% error by experiments for binary and ternary mixing among components with moderate albedo contrast (Mustard and Pieters, 1989).

There are some fundamental limitations of this approach to synthesize reflectance spectra of mineral mixtures. First, the Hapke radiative-transfer method is designed for mixture of particulate materials whose grain sizes are small and whose phase dependent scattering behaviors are similar. Although regoliths are widespread on the surfaces of rocky bodies in the Solar System as a result of extensive meteoritic bombardments, it is uncertain whether an exoplanet's surface is made of regolith or bulk rocks [2]. Second, the Hapke radiative-transfer method may induce an error up to 25% for for dark materials (basalts) in mixtures with clay (Ehlmann & Mustard, 2013, in preparation). For these reasons, I choose well-characterized actual materials rather than Hapke modeled spectra as representative of feldspathic and basaltic surface types (see Table 5.2), and results from intimate mixing studies should be considered indicative rather than exact.

---

[2]I focus here on regolith surfaces. Surfaces of an airless planetary body are most likely comprised of particulate regoliths, because impact gardening effectively converts surface rocks to a regolith layer.

5.2.2 Bidirectional Reflectance Spectra of Planetary Surface Material

For computation of planetary surface spectra the most important parameter is bidirectional reflectance of surface solid material, which is usually characterized by the radiance coefficient (r_c). The radiance coefficient is defined as the brightness of a surface relative to the brightness of a Lambert surface identically illuminated, which depends on the direction of both incident and scattered light. The radiance coefficient of a solid material not only depends on its chemical composition, but also depends on its crystal structures. Reflectance spectra of these minerals are shown in Figure 5-3.

Hapke (1981, 2002) presents a straightforward method to compute the approximated radiance coefficient of any particulate material in terms its single scattering albedo. In essence, Hapke (1981, 2002) treats the problem as the radiative transfer of a planar, semi-infinite, particulate medium illuminated by collimated light. The key assumption to achieve a convenient analytical expression is to assume isotropic scatterers for multiple scattering and non-isotropic scatterers for single scattering (Hapke, 1981). The resulting expression has been proved to be correct and handy in the interpretation of surface composition of the Moon and Mars (e.g. Hapke, 2002).

Experimental data of radiance coefficient (r_c) of common minerals and mixtures are typically presented for certain combinations of incidence angle (μ_0), scattering angle (μ) and phase angle (g). For application to exoplanets, I extend the experimentally measured r_c to any combination of (μ_0, μ, g) using the analytical expression of Hapke (2002). Also, I compute the directional-hemispherical reflectance (r_h) for different minerals based on experimental bidirectional reflection using an analytical expression given by Hapke (2002). The analytical form of Hapke (2002) employs a parameter h to describe the opposition effect and a phase function to describe the single particle scattering. For fine grains, $h \sim 0.1 - 0.4$. I assume $h = 0.2$ and the
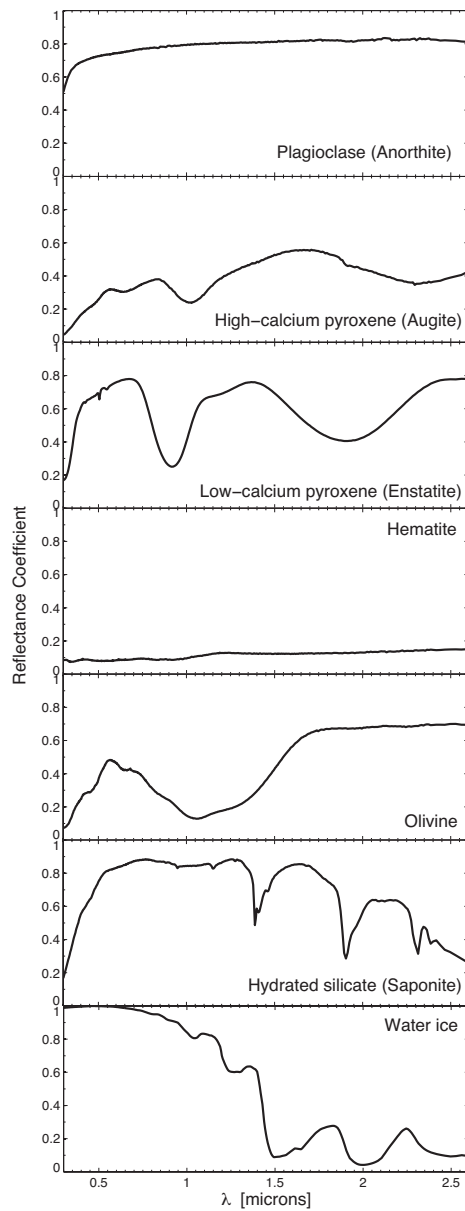
Figure 5-3: Radiance coefficient of common minerals on terrestrial planet surfaces listed in Table 5.1. Bidirectional reflectance spectra measured at incidence angle $i = 30°$, scattering angle $e = 0°$ and phase angle $g = 30°$ (Calvin and Clark, 1991; Clark et al., 2007, RELAB 2010) are used to derive the radiance coefficient. Plagioclase (non-iron-bearing) has a bright and flat NIR spectrum and hematite has a dark and flat NIR spectrum. Mafic minerals, i.e., olivine and pyroxene, have a deep and wide electronic absorption at 1 μm. In addition, pyroxene has an absorption near 2 μm, and the band center location depends on its calcium content. Water ice has deep and wide vibrational absorption bands at 1.5 μm and 2 μm, whereas hydrated minerals have narrow vibrational absorption bands at 1.4, 1.9 and 2.3 μm.

phase function to be the first order Legendre expansion as

$$p(g) = 1 + b\cos(g) , \tag{5.2}$$

where b is the anisotropy parameter in $[-1, 1]$. It is typically assumed that $b = 0$, i.e. isotropic scattering. Numerical experiments show that the retrieval of single scattering albedo and the computation of radiance coefficient do not sensitively depend on the assumptions of h and b.

For consistent treatment of reflection and thermal emission, I use experimentally measured reflectance and derive emissivities of mineral assemblages. In the Hapke framework, the directional emissivity and the directional-hemispherical reflectance obey Kirchhoff's Law (Hapke, 1993). I performed cross-checks between the derived emissivity and the experimentally measured emissivity of pure minerals (Christensen et al., 2000) and demonstrate that they are roughly consistent.

5.2.3 Disk-Averaged Spectral Model

Where this framework differ from the solar-system models is that spectra of exoplanets are always disk integrated. The observable quantity of exoplanet reflection is the occultation depth of the secondary eclipse. Reflected light from an exoplanet is an average over the entire sub-stellar hemisphere. Moreover, the planetary radiation flux combines the reflected stellar radiation and the thermal emission, as these two components may overlap in wavelength ranges. Here I present a detailed formulation of disk-averaged reflection and thermal emission spectra from an airless rocky exoplanet with contribution from thermal emission, in terms of the radiance coefficient (r_c) and the directional-hemispherical reflectance (r_h) of its surface materials.

Radiative flux per unit area per wavelength from an exoplanet for an Earth-based observer F_p (erg s^{-1} cm^{-2} nm^{-1}) is a hemisphere-integral as

$$F_p = \left(\frac{R_p}{D}\right)^2 \int_{-\frac{\pi}{2}}^{\frac{\pi}{2}} \int_{-\frac{\pi}{2}}^{\frac{\pi}{2}} I_p(\theta, \phi) \cos^2\theta \cos\phi \, d\theta d\phi , \tag{5.3}$$

in which R_p is the radius of the planet, D is the distance to the observer, and $I_p(\theta, \phi)$ is the intensity from a location on the hemisphere towards the observer specified by latitude-longitude coordinates (θ, ϕ). The coordinate system is chosen such that the observer is at the direction of $(\theta = 0, \phi = 0)$. The planetary radiance is composed of the reflection of stellar light and the thermal emission from the planet itself,

$$I_p(\theta, \phi) = I_s(\theta, \phi) + I_t(\theta, \phi) .\tag{5.4}$$

The reflected intensity is related to the incident stellar irradiance (F_{inc}) as

$$I_s(\theta, \phi) = F_{inc}\frac{\mu_0}{\pi}r_c(\mu_0, \mu, g) ,\tag{5.5}$$

where r_c is the radiance coefficient as a function of the incidence angle i, the scattering angle e and the phase angle of scattering g. By definition, a Lambertian sphere has $r_c = 1$. Let α be the phase angle of the exoplanet with respect to the Earth, so that the stellar coplanar light comes from the direction of $(\theta = 0, \phi = \alpha)$. For each surface element, there are the following geometric relations:

$$\mu_0 \equiv \cos i = \cos\theta \cos(\alpha - \phi) ,\tag{5.6}$$

$$\mu \equiv \cos e = \cos\theta \cos\phi ,\tag{5.7}$$

$$g = \alpha .\tag{5.8}$$

The thermal emission of the planet depends on its surface temperature, which is controlled by both stellar radiation and planetary surface properties. The irradiance incident on the planet is

$$F_{inc} = \pi B_\lambda[T_*]\left(\frac{R_*}{D_p}\right)^2 ,\tag{5.9}$$

and the stellar irradiance for the observer is

$$F_* = \pi B_\lambda[T_*]\left(\frac{R_*}{D}\right)^2 ,\tag{5.10}$$

in which T_* and R_* are the temperature and the radius of the star, D_p is the semi-

major axis of the planet's orbit, and B_λ is the Planck function for blackbody radiance. The thermal emission intensity is

$$I_t(\theta, \phi) = \epsilon_\lambda(\mu) B_\lambda[T(\theta, \phi)] \ , \tag{5.11}$$

where ϵ_λ is the directional emissivity, and $T(\theta, \phi)$ is the temperature of the planet's surface. According to the Kirchhoff's law of thermal radiation and the framework of Hapke (1993), ϵ_λ is tied to the directional-hemispherical reflectance r_{dh} via

$$\epsilon_\lambda(\mu) = 1 - r_{dh}(\mu) \ . \tag{5.12}$$

An effectively airless rocky exoplanet, without efficient heat transport mechanisms, is likely to have local thermal equilibrium (e.g. Léger et al., 2011, for CoRot-7b). The energy balance equation can therefore be written as

$$\mu_0 \int \epsilon_\lambda(\mu_0) F_{inc} d\lambda = \pi \int \epsilon_\lambda^h B_\lambda[T] d\lambda \ , \tag{5.13}$$

where ϵ_λ^h is the hemispheric emissivity, i.e., the hemispherical average of the directional emissivity. By solving this equation I determine the local surface temperature and then compute the directional thermal emission of each surface element.

Finally, the occultation depth of the secondary eclipse is

$$\frac{F_p}{F_*} = \frac{1}{F_{inc}} \int_{-\frac{\pi}{2}}^{\frac{\pi}{2}} \int_{-\frac{\pi}{2}}^{\frac{\pi}{2}} I_p(\theta, \phi) \cos^2\theta \cos\phi \ d\theta d\phi \ \times \left(\frac{R_p}{D_p}\right)^2 \equiv A_g \left(\frac{R_p}{D_p}\right)^2 \ , \tag{5.14}$$

where A_g is the apparent geometric albedo of the planet, and $I_p(\theta, \phi)$ should be evaluated from Equation (5.4) at $\alpha = 0$. Here I include thermal emission into the definition of geometric albedo, because for close-in exoplanets the reflected stellar light and the thermal emission may not be separated in spectra. In case of negligible thermal emission, for example in the visible and NIR wavelengths for Earth-like planets, the geometric albedo in Equation (5.14) can be simplified to be the conventional

definition as

$$A_{\mathrm{g}} = \frac{1}{\pi} \int_{-\frac{\pi}{2}}^{\frac{\pi}{2}} \int_{-\frac{\pi}{2}}^{\frac{\pi}{2}} r_c(\mu_0, \mu_0, 0) \cos^3 \theta \cos^2 \phi \; d\theta d\phi \; , \qquad (5.15)$$

consistent with Sobolev (1975) and Seager (2010). In addition, I use the apparent brightness temperature (T_{b}) to describe the thermal emissivity of the planet, namely

$$\pi B_\lambda[T_{\mathrm{b}}] \left(\frac{R_{\mathrm{p}}}{D} \right)^2 = F_{\mathrm{p}} \; . \qquad (5.16)$$

The brightness temperature defined as such can be compared with observations directly, and takes into account the disk average of directional emissivities and surface temperatures.

5.3   Results

The main findings are: rocky silicate surfaces lead to unique features in planetary thermal emission at the mid-infrared due to strong Si-O vibrational bands (7 - 13 μm and 15 - 25 μm); the location of the emissivity maxima at the short-wavelength edge of the silicate feature (7 - 9 μm) is indicative of the silica content in the surface silicates; ultramafic surfaces can be uniquely identified in the reflectance spectra via a prominent absorption feature at 1 μm (i.e., the J band); hydrous surfaces induce strong absorption at 2 μm (i.e., the K band); and surface water ice has a unique absorption feature in the reflected stellar light at 1.5 μm (i.e., the H band).

In the following I present disk-average spectra of airless rocky exoplanets and describe the main results. I compute the disk average using Equation (5.14) based on measured or modeled bidirectional reflectance of mineral assemblages as tabulated in Table 5.2. Figure 5-4 shows the VNIR geometric albedos and MIR brightness temperatures of airless exoplanet fully covered by the 8 types of crust; Table 5.3 lists the main spectral features due to surface minerals in the planetary thermal emission; Table 5.4 lists the geometric albedos of the 8 cases averaged in the NIR J (1.1 - 1.4 μm), H (1.5 - 1.8 μm), and K (2 - 2.4 μm) bands; Figure 5-5 is a scatter plot showing the relation between broad-band true geometric albedos for the 8 cases; Figure 5-6

explores the effect of macroscopic mixture of two types of crust; and Figure 5-7 shows the modeled planetary spectra of Kepler-20 f if the planet has a particulate solid surface.

5.3.1 Silicate Features in the Thermal Emission of Rocky Exoplanets

Silicate surfaces possess prominent minima in the thermal emission spectra from 7 - 13 μm and 15 - 25 μm (see Figure 5-4). These Si-O stretching and bending vibrations manifest in the thermal emission spectra as troughs of complicated shapes, due to a strong reststrahlen reflection at the band center and volume scattering near the band edges. Prominent Si-O features, e.g. in the ultramafic and granitoid surfaces, have equivalent width (EW) larger than 1 μm and ΔT_b larger than 20 K (see Table 5.3). For comparison, the atmospheric O_3 absorption line at 9.6 μm has ΔT_b of about 30 K for the Earth (Des Marais et al., 2002; Belu et al., 2011). For close-in rocky exoplanets, ΔT_b of the silicate features can be as large as of 200 K (see Figure 5-4), which corresponds to a variation of secondary transit depth of 2 part-per-million (ppm) for the case of Kepler-20f (see Figure 5-7). In contrast to silicate surfaces, iron-oxidized surfaces do not have thermal emission troughs in 7 - 13 μm, but usually have a clear double-peak Fe-O feature in the 15 - 25 μm band, as shown in Figure 5-4 for the Fe-oxidized surface. Silicates and iron-oxides can therefore be distinguished based on thermal emission spectra. In summary, wide troughs of brightness temperature in both 7 - 13 μm and 15 - 25 μm constitute a unique signature of silicate surfaces of exoplanets.

Furthermore, high-resolution spectra of the silicate bands can allow identification of different kinds of silicate surfaces. As shown in Table 5.3, as silica content in the mineral assemblage increases, the Christiansen feature (CF), defined as the emissivity maxima at the edge of the main Si-O band, shifts to shorter wavelengths. Note that the ultramafic surface is the most silica-poor and the granitoid surface is the most silica-rich. This well-known effect in mineralogy is applicable to spectral
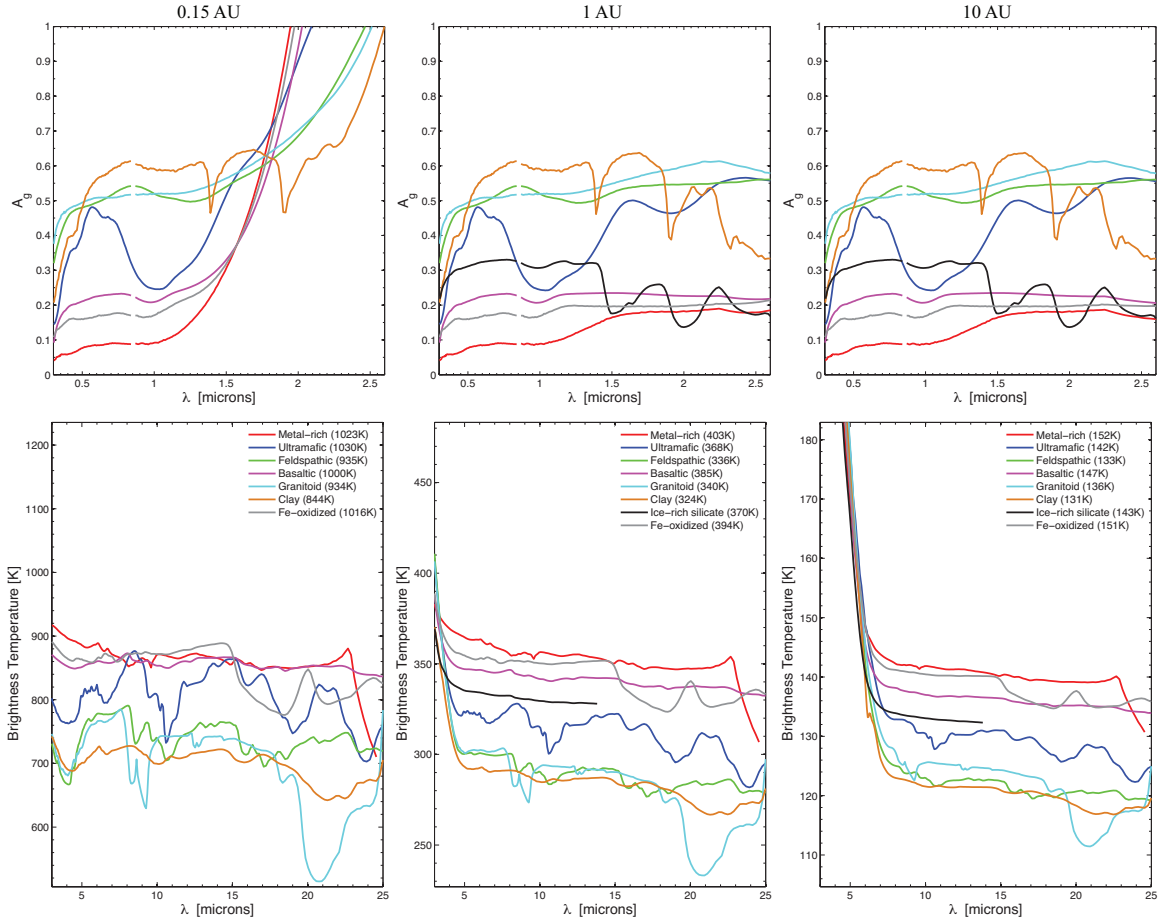
Figure 5-4: Apparent geometric albedo in VNIR and brightness temperature in MIR of an airless exoplanet fully covered by the 8 types of crust listed in Table 5.2. The three planetary scenarios correspond to solar-like host star and semi-major axis $D_{\rm p} = 0.15$ AU, 1 AU and 10 AU. For a semi-major axis of 1 and 10 AU, the planetary flux in VNIR is purely due to reflection and the geometric albedo is the true $A_{\rm g}$ independent of stellar irradiance; for close-in exoplanets (e.g., $D_{\rm p} = 0.15$ AU), thermal emission extends to about 1 μm. In parentheses I list the sub-stellar temperatures on the planet's surface.
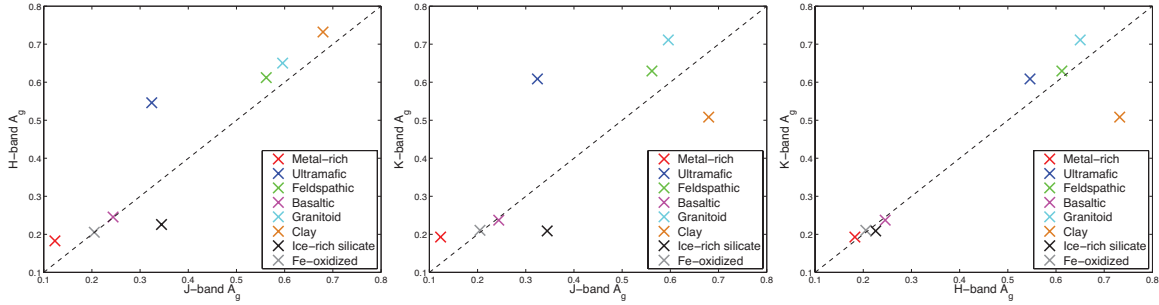
Figure 5-5: Comparison between geometric albedos in J, H, and K bands for airless exoplanets with 8 types of crust listed in Table 5.2. The dashed line indicates a flat spectrum. The thermal emission is not included. Note that ultramafic surfaces have J-band albedo significantly smaller than H-band and K-band albedo, ice-rich silicate surfaces have H-band and K-band albedo significantly smaller than J-band albedo, and clay surfaces have K-band albedo significantly smaller than J-band and H-band albedo.
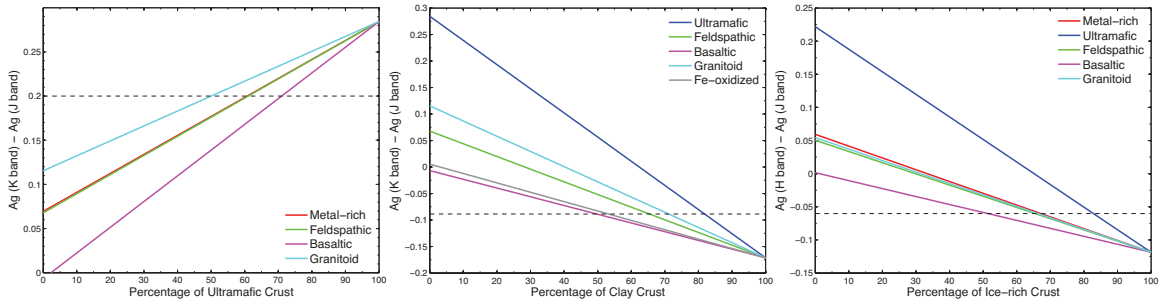
Figure 5-6: Colors of exoplanetary surfaces that contain macroscopic mixture of two types of crusts. The horizontal axis is the percentage of feature-creating constituents. The vertical axis the difference between the planet's geometric albedo in two NIR bands. The color of each line corresponds different companion constituents, tabulated as the legend in the plots. The horizontal lines are the limits of the color differences in order to infer that as least 50% of the planetary surface is ultramafic, clay, and ice-rich, respectively.
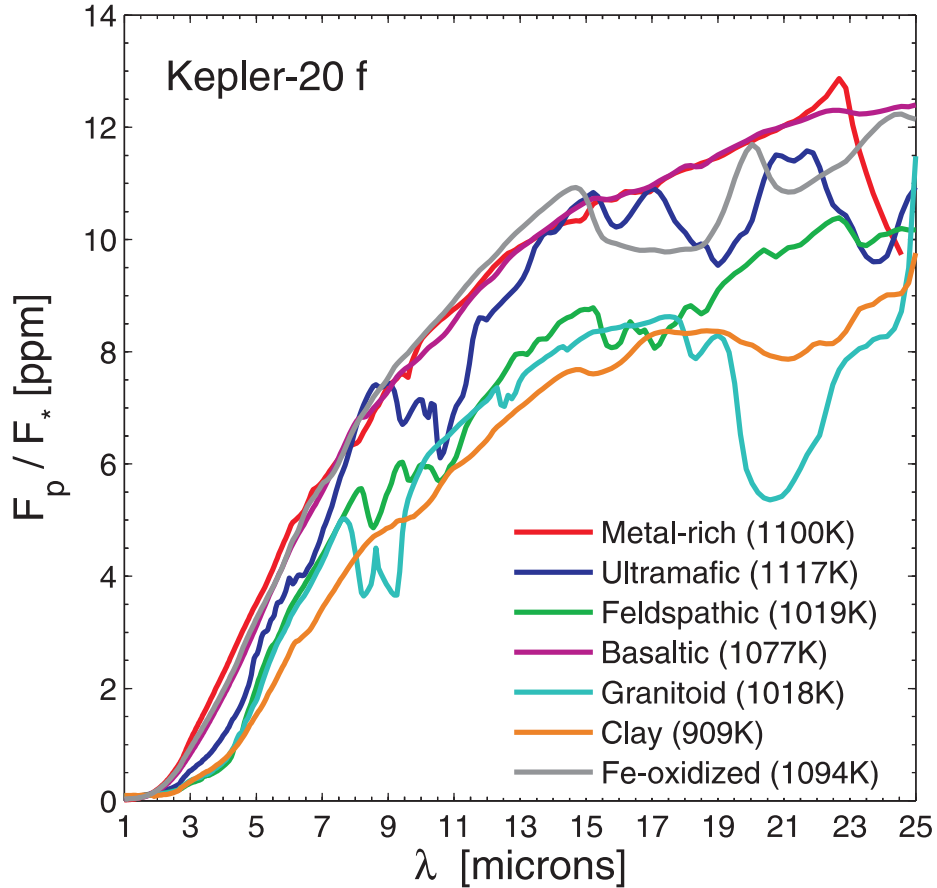
Figure 5-7: Modeled transit depth of the secondary eclipse of Kepler-20f, if the planet's surface is covered by particulate materials as listed in Table 5.2. I use the planetary parameters of Fressin et al. (2012) and find that in the Kepler's bandpass the secondary transit depth is less than 1 part-per-millon (ppm). Sub-stellar temperatures listed in the figure are self-consistently computed in the model, and I verify that except for the granitoid and clay the surfaces are solid anywhere on the planet. Note that the Si-O features lead to variations in secondary transit depth as large as 2 ppm in both the 7 - 13 μm band and the 15 - 25 μm band, for ultramafic and granitoid surfaces. The iron-oxide feature in the 15 - 25 μm band and the pyrite feature at > 22 μm are also evident.

analysis of disk-integrated planetary thermal emission for characterizing rocky surfaces. Determination of the CF wavelength, however, involves tracing the curvature of brightness temperature spectra and therefore requires high-resolution spectra with a high signal-to-noise ratio. At a minimum, the determination of CF location and thus silica content requires three narrow bands in the 7 - 9 μm region (see Greenhagen et al., 2010; Glotch et al., 2010, for an example applicable to the Moon).

Not only the spectral features, but also the thermal emission continuum provide valuable information on the planetary surfaces. Thermal emission of an effectively airless rocky exoplanet probes the planet's surface temperature, which in turn depends on its surface composition. A highly reflective surface at VNIR, for example the feldspathic surface, has much lower equilibrium temperature than a VNIR absorptive surface, for example the basaltic surface (e.g. Figure 5-4). For an airless Earth analog, the brightness temperature continuum from 5 to 25 μm is about 340 K if the surface is basaltic and 290 K if the surface is feldspathic (see Figure 5-4). Solely due to different VNIR reflectivities, the apparent temperature difference of the planet, ΔT_b, can be as large as 50 K. As a result, equilibrium temperature of planetary solid surfaces, derived from the planetary thermal emission, may coarsely constrain the planetary surface composition, for example to the level of feldspathic versus ultramafic. Note in Figure 5-4 that more than one types of crust have overall low VNIR albedos, including metal-rich, basaltic and Fe-oxidized crusts; several crusts have overall high VNIR albedos, including feldsphathic, granitoid and clay crusts; and several crusts have intermediate VNIR albedos, including ultramafic and ice-rich silicate crusts. Moreover, the overall surface reflectivity sensitively depends on the surface roughness and particle size. Intrinsic degeneracy between surface composition and roughness or particle size exists if thermal emission continuum, or equilibrium temperature, is the only piece of information. This highlights the utility of multiple spectral channels in characterizing exoplanet surfaces.

Last but not the least, thermal emission does not cause the reduction of spectral feature contrasts at NIR wavelengths, unless the exoplanet is very hot when in a close-in orbit (i.e., semi-major axis less than $\sim$0.2 AU). For an analog of Earth or

Mars, the thermal emission is negligible at NIR. For close-in exoplanets, the sub-stellar temperature may be very high and their thermal emission may extend to the NIR if the planet's orbit is at 0.15 AU (e.g. Figure 5-4 upper left). In this case, the thermal emission may severely reduce the spectral features at > 2 μm, because the thermal emission compensates for the absorption of stellar radiation. According to Kirchhoff's law, a surface has high emissivity at wavelengths where it absorbs strongly. For example, the strong absorption at 2.3 μm of hydrated silicates is largely compensated by the strong thermal emission at the same wavelengths (see Figure 5-4). For even shorter orbital periods, the sub-solar point may reach the melting temperature of minerals on the surface, which creates molten lava on the surface (see Figure 5-1). For solar-type stars, the transition of solid surface and molten lava happens at about 0.1 AU. To date exoplanets that could be rocky mostly lie in the regime of molten lava. Notably, Kepler-20f is marginally at the melting point for a granitoid surface, and is certainly solid for more refractory surfaces such as ultramafic. Since it is unlikely that Kepler-20f possesses a significant gas envelope (Fressin et al., 2012), Kepler-20f may be a good exoplanetary candidate for solid surface characterization via prominent silicate and iron-oxide features (see Figure 5-7).

5.3.2 General Reflection Spectra of Exoplanets with Solid Surfaces

Planetary surfaces of different compositions can have very different overall reflectivity. As shown in Figure 5-4, a pure feldspathic surface (e.g., the lunar highlands) is very bright, with a geometric albedo $\sim$0.6 and a relatively flat NIR spectrum. In contrast, basaltic, Fe-oxidized or metal-rich surfaces are very dark, with a geometric albedo less than 0.3. As shown in Figure 5-5, when these spectra are downsampled to the resolution of the J, H, and K bands, there is a strong correlation between reflectivity in the three bands for most surface types.

The absorption band near 1 μm is deep and wide for the ultramafic surface. The

Table 5.3: Spectral features in planetary thermal emission that are characteristic of surface compositions.

Crust Type	CF^a (μm)	Feature	$Range^c$ (μm)	Emissivity Minima (μm)	EW^d (μm)	$\Delta T_b{}^e$ (K)
Metal-rich	NA	Pyrite band	> 22.7	-	0.27	> 47.07
Ultramafic	8.5	Si-O stretch	8.5 - 13.7	10.6	0.60	25.0
		Si-O bending^b	> 15.1	16.1, 19.0, 23.9	1.38	8.9, 26.9, 40.6
Feldspathic	8.0	Si-O stretch	8.0 - 12.9	8.6, 10.6	0.47	9.4, 12.9
		Si-O bending^b	> 15.4	15.9, 17.1, 18.5, 23.5	0.67	8.0, 12.7, 10.9, 10.6
Basaltic	8.0	Si-O stretch	8.0 - 12.9	10.8	0.13	3.9
		Si-O bending^b	> 15.0	15.9, 17.1, 18.5	0.35	2.9, 4.6, 5.9
Granitoid	7.6	Si-O stretch	7.6 - 10.2	8.3, 9.3	0.48	18.3, 24.0
		Si-O bending^b	> 14.8	18.3, 20.9, 24.1	2.10	17.0, 57.1, 29.4
Clay	8.0	Si-O stretch	8.0 - 13.0	10.1, 11.5	0.17	4.6, 2.6
		Si-O bending^b	> 14.1	15.8, 21.3, 22.5, 24.6	1.02	4.8, 20.5, 20.3, 14.1
Ice-rich silicate	7.9	Si-O stretch	7.9 - 12.8	10.9	0.05	1.3
Fe-oxidized	8.1	Si-O stretch	8.1 - 11.9	10.8	0.02	1.2
		Fe-O stretch	> 14.3	18.5, 21.3	1.38	28.2, 25.5

a
The wavelengths of the Christiansen Feature are defined as the emission maxima at the short-wavelength edge of Si-O stretch fundamentals.
bThese complex spectral features are mainly due to Si-O bending and deformation, with minor contribution of Si-O-Si stretch.
cFor certain spectral features the wavelength ranges are not well defined, due to the complex nature of these features and limitations of experimental measurements at mid and far infrared wavelengths.
dEquivalent widths of spectral features are defined as EW $= \int (1 - f/f_0) d\lambda$ where f is the observable planetary flux and f_0 is the continuum. The continuum is derived from linear interpolation of brightness temperature between the edges of features. When only one edge can be defined, the continuum is derived from the constant brightness temperature, and the actual equivalent width of the feature might be larger than tabulated.
$e\Delta T_b$ is the decrease of brightness temperature attributed to the spectral features with respect to the continuum, reported for each corresponding emissivity minima.

constituents of this surface are olivine and pyroxene, both of which have Fe^{2+} and absorb strongly near 1.0 μm. Weaker absorptions in this band can also be found in the feldspathic, basaltic, Fe-oxidized, and ice-rich silicate cases because they all contain some olivine or pyroxene in their composition. The absorptions are caused by ferrous iron, commonly present at $> 1\%$ levels in the igneous minerals comprising these surfaces (although see section 5.1.3 discussion on Mercury for the possibility of non-ferrous components). For the feldspathic crust, the absorption peak is shifted to $\sim$1.3 μm, which is distinctive for Fe-anorthite, a feldspar that has been positively identified in the lunar highlands (e.g. Pieters, 1986). The Fe-oxidzed surface, which contains substantial hematite, shows absorptions at wavelengths shorter than 1.0 μm due to charge transfer absorptions for Fe^{3+}.

Signature narrow absorption features at NIR are characteristic of water ice as well as hydrated minerals. As shown in Figures 5-3 and 5-4, water ice and hydrated minerals have high reflectivities at 1 μm and absorb strongly at longer wavelengths. The drop in reflectance at wavelengths longer than $\sim$2 μm is due to the presence of both the very strong OH stretch fundamental and overtone of the H_2O bend near 3 μm. Note that the amount of equivalent water in hydrated minerals is small ($<\sim$15%), but even minor amounts of water (or OH) lead to prominent absorption features in the infrared. Sharp features due to bends and stretches of OH and H_2O occur at 1.4 and 1.9 μm in hydrated minerals and 1.5 and 2.0 μm in ice.

The non-linear effect of intimate mixing of different minerals can serve to subdue the absorptions of present phases. Darker phases are especially effective in hiding other constituents. Even though bright plagioclase is often the most abundant constituent in basalt, basalt is typically dark due to nonlinear mixing between plagioclase and dark constituents present at the few percent level. These nonlinear affects require careful analysis of detectability thresholds. Nevertheless, as discussed below, the absorptions of ultramafic and hydrous surface types can be distinguished in broad-band telescopic data.

Table 5.4: Average geometric albedo and color of an airless exoplanet fully covered by 8 types of crust listed in Table 5.2 in NIR J, H and K bands. The two planet scenarios correspond to one case where reflection dominates the NIR planetary flux and the other case of close-in exoplanets where thermal emission extends to the NIR. Note that in the reflection-dominated case, the ultramafic surface is the only type of crust considered that has significantly higher albedo in the K band than in the J band, hydrous crusts are the only ones with lower albedos in the K band than J band, and ice-rich silicate surface is the only type of crust that has lower albedo in the H band than in the J band.

Planet Scenario	G Star, 1 AU					G Star, 0.15 AU				
Crust Type	J	H	K	K-J	H-J	J	H	K	K-J	H-J
Metal-rich	0.12	0.18	0.19	0.07	0.06	0.17	0.56	2.28	2.12	0.40
Ultramafic	0.32	0.55	0.61	0.29	0.23	0.33	0.59	0.78	0.45	0.25
Feldspathic	0.56	0.61	0.63	0.07	0.05	0.56	0.62	0.68	0.12	0.06
Basaltic	0.24	0.25	0.24	0.00	0.01	0.28	0.56	2.03	1.75	0.28
Granitoid	0.60	0.65	0.71	0.11	0.05	0.60	0.65	0.72	0.13	0.06
Clay	0.68	0.73	0.51	-0.17	0.05	0.68	0.73	0.59	-0.09	0.05
Ice-rich silicate	0.34	0.23	0.21	-0.13	-0.11	0.36	0.43	1.51	1.15	0.07
Fe-oxidized	0.21	0.21	0.21	0.00	0.00	0.25	0.58	2.24	2.00	0.33

Broad-Band Spectral Feature of the Ultramafic Surface

The NIR J band (1.1-1.4 μm) is sensitive to the detection of ultramafic crusts that contain ferrous igneous minerals on an exoplanet's surface. In the J band, surface absorbers include olivine and pyroxene (see Figure 5-3). Made of these two types of minerals, the ultramafic crust leads to a distinctive J-band geometric albedo significantly lower than the H band and the K band (see Figure 5-5 and Table 5.4), unique in my set of representative surfaces. Here I define a key parameter for characterization of surface composition as the difference between the K-band geometric albedo ($A_g(K)$) and the J-band geometric albedo ($A_g(J)$). This parameter basically describes the "color" of exoplanetary surfaces in the NIR wavelengths. Note that thermal emission may contribute to the apparent geometric albedo, as shown by Figure 5-4 and Table 5.4. By saying "color" I refer to the true geometric albedo with component of thermal emission properly removed. For an exoplanet completely covered by ultramafic crust, $A_g(K) - A_g(J) = 0.29$, whereas all other crustal types give value less than 0.1 (see

Table 5.4). It is therefore very likely that an ulframafic surface on exoplanets will stand out in the reflectance spectra.

Macroscopic mixtures between the ultramafic surface and other types of surfaces linearly lowers the spectral contrast of the J-band absorption feature. When mixed with other surfaces that have relatively flat spectra, such as basalt and granite, the J band feature of an ultramafic surface will appear to be shallower. As shown in Figure 5-6, the key parameter $A_g(K) - A_g(J)$ depends linearly on the percentage of ultramafic crust on the planet's surface. A detection of $A_g(K) - A_g(J) > 0.2$ indicates that more than a half of the planetary surface need to be covered by ultramatic materials.

Broad-Band Spectral Feature of the Water and Hydrated Mineral Surfaces

The NIR H band (1.5-1.8 μm) is suitable for the detection of water ice on an exoplanet's surface. At the H band, the most prominent absorber is water ice. In fact, water ice absorption in the H band is so strong that small amount (10%) of water ice on a very reflective surface can significantly reduce the planetary geometric albedo. An ice-rich surface is the only type of surface in my sample that has lower albedo in H band than in J band (Table 5.4). As a result, if one observes a high J-band albedo and a low H-band albedo for an airless exoplanet, it is very likely that water ice exists on the planet's surface. If $A_g(H) - A_g(J) < -0.06$, more than half of the planetary surface is likely to be ice-rich (see Figure 5-6).

The NIR K band (2-2.4 μm) is sensitive to water ice and hydrated minerals on an exoplanet's surface. I find that ice-rich surfaces and aqueously altered surfaces produce strong K-band absorption, which leads to a K-band albedo smaller than the J-band albedo (see Figure 5-5). For example, for a generally reflective surface in K band, e.g., plagioclase- or olivine-rich, a small amount of water ice (10%) can reduce the planetary geometric albedo significantly. As shown in Figure 5-6, the key parameter $A_g(K) - A_g(J)$ depends linearly on the percentage of clay crust on the planet's surface. A detection of $A_g(K) - A_g(J) < -0.09$ indicates that more than a half of the planetary surface need to be covered by hydrated materials.

5.4 Discussion

5.4.1 Effects of Atmospheres

If the exoplanet has a thin atmosphere, molecular NIR absorptions will introduce additional features in its reflection and thermal emission spectra (e.g. Mars reflectance spectra in Figure 5-2). Common molecules that actively absorb at NIR in an rocky exoplanet's atmosphere include H_2O, CO_2, CO, CH_4, NH_3, SO_2, etc (e.g. Seager and Deming, 2010). Based on the HITRAN molecular absorption line database, I estimate that for an atmosphere of Earth-like temperature and pressure, 18 parts-per-million (ppm) of H_2O or 173 ppm of CH_4 can produce an integrated optical depth larger than unity in the J band. Similarly, 32 ppm of CH_4 can produce an integrated optical depth larger than unity in the H band; and 104 ppm of CO_2, or 4 ppm of CH_4, or 5 ppm of NH_3 can produce an integrated optical depth larger than unity in the K band.

For the broad-band infrared photometry, the effect of atmospheres on characterization of surface composition can be very serious. For example, I have demonstrated that water ice on the planet's surface produce H-band absorption, or negative $A_{\mathrm{g}}(\mathrm{H}) - A_{\mathrm{g}}(\mathrm{J})$. However, water vapor in the planet's atmosphere absorbs in J band, which will reduce the apparent contrast of the surface-related H-band feature. For another example, a J-band absorption feature in reflectance spectra can be interpreted as absorption of olivine and pyroxene on the surface, or as the absorption of water vapor in the atmosphere. Without any prior knowledge on the planet's atmosphere, it could be hard to draw conclusive surface compositions from broad-band spectrophotometry observations.

There are two possible ways to break the surface-atmosphere degeneracy in the exoplanet reflection spectra. First, observing the primary transit can determine the atmospheric composition of the exoplanet via transmission spectroscopy (e.g. Seager and Deming, 2010). The surface minerals do not induce any spectral features in the transmission of stellar radiation observable in primary transit. The difficulty of this approach is that the magnitude of atmospheric signal from the primary transit is proportional to the atmospheric scale height (e.g. Miller-Ricci et al., 2009; Seager,

2010), therefore for a terrestrial-like atmosphere the signal may be too low to be detected. Second, high-resolution spectroscopy, rather than spectrophotometry, can distinguish a surface absorption from an atmospheric absorption. For reflection, the iron-related absorption in silicates are typically very wide and smooth in wavelength (see Figure 5-4), but the atmospheric molecular features are typically narrow and only occur at specific wavelengths; for thermal emission, the silicate vibrational features have particular shapes which can hardly be produced by any plausible temperature structures in the planetary atmosphere (see Figure 5-4 and Figure 5-7 for an example of Kepler-20f). As a result, one can break the surface-atmosphere degeneracy in the exoplanet reflection spectra by achieving high spectral resolution.

In the extreme case, the refractory rocks may even be vaporized on the dayside and form a metal vapor atmosphere, as suggested for CoRot-7b by Schaefer and Fegley (2010) and Léger et al. (2011). It has been shown that metal vapor atmospheres create narrow and strong metal transition lines in the visible wavelengths (e.g. Seager and Sasselov, 1998). It is therefore unlikely that metal vapor atmospheres impede spectral characterization of the surface beneath.

5.4.2 Effects of Space Weathering

The surface of an airless planet is subject to space weathering. The processes of space weathering include collision of galactic cosmic rays, sputtering from solar wind particles, bombardment of micrometeorites, etc. Space weathering will produce a thin layer of nanophase iron on mineral grain surfaces and agglutinates in the regolith, altering surface spectral properties significantly. In general, as a surface matures due to space weathering, it becomes darker, redder, and the depth of its diagnostic absorption bands is reduced (Pieters et al., 1993; Hapke, 2001).

The broad-band diagnostic features considered in this paper will be subdue for an exoplanet covered by space-weathered (mature) surfaces. Figure 5-8 presents several reflectance spectra of selected mature lunar and martian surfaces. Fe^{2+} absorption features at 1 μm and 2 μm become very shallow for the mature lunar mare (e.g., Figure 5-8 vs. Figure 5-3). Space weathering is very effective in reducing the diagnostic

features. Nonetheless, various mechanisms can refresh a planet's surface in the course of evolution, which include impact cratering, volcanism, plate tectonics, etc. As a result, the fact that space weathering reduces the 1-μm and 2-μm spectral feature makes this detection indicative of active or recent re-surfacing on the planet.

Finally, for weathered surfaces the slope of reflectance spectra could be broadly diagnostic of the composition of weathering products and the nature of weathering. As shown in Figure 5-8, after space weathering, the reflectance spectrum from the basaltic lunar mare have a steep upward slope, as expected. In contrast, the basaltic martian lowlands become bluer after weathering. The downward slope in the spectra of mature martian lowlands likely indicates silica and nanophase iron oxides coatings caused by chemical reactions in thin films of water on basaltic rocks (Mustard et al., 2005). Although weathering reduces the contrast of spectral features, it causes slopes in reflectance spectra relevant to understanding planetary surface processes.

5.4.3 Detection Potential

The characterization of airless rocky exoplanets' solid surfaces is not inherently more difficult than the characterization of their atmospheres. Via the thermal emission, the silicate, iron-oxide and metal-rich surfaces manifest themselves differently in the planetary spectra, with a spectral contrast comparable to that of atmospheric CO_2 or O_3 features. The secondary transit signal of an exoplanet is larger if the planet is closer to its host star. As shown in Figure 5-1, however, an airless rocky planet cannot be too close to the star in order to keep its surface solid, which limits the potential occultation depth of the planet. For an Earth-sized planet around a G type star, the occultation depth can be larger than 10 ppm in MIR, and the surface characterization by transits requires a photometric precision of 2 ppm in MIR (see Figure 5-7 for an example of Kepler-20f). Such precision and corresponding signal-to-noise ratio may be attainable by the *James Webb Space Telescope* (JWST) if the telescope would observe all transits in its 5-year nominal mission time (Belu et al., 2011). Much higher secondary transit depths may be possible if the rocky exoplanets are discovered to orbit around M dwarfs, because M dwarfs have smaller
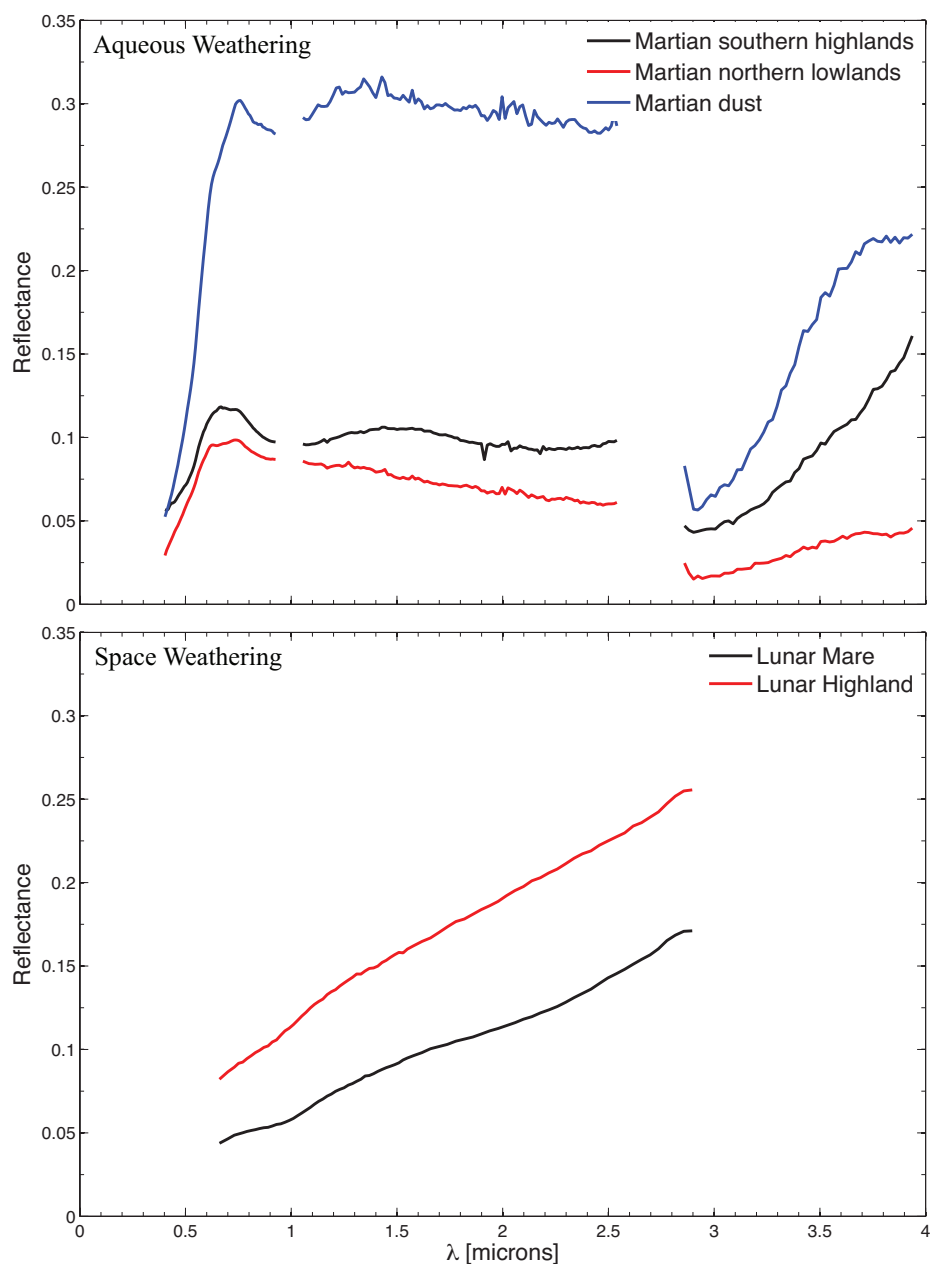
Figure 5-8: Reflectance spectra of weathered surfaces on the Moon and Mars. Mars spectra are measured by the OMEGA Visible and Infrared Mineralogical Mapping Spectrometer onboard the Mars Express orbiter: Skok et al. (2010) for martian lowlands, and Mustard et al. (2005) for martian highlands and martian dust. Gaps in the spectra correspond to detector boundaries. The Moon's spectra are measured by the Moon Mineralogy Mapper (Isaacson, personal communication). The drop in reflectivity at $\sim 2.8\ \mu$m in all the martian spectra is due to strong OH-stretch fundamentals and the presence of water ice.

radius and surface temperature compared to solar-type stars. M dwarfs are the most feasible targets for the characterization of rocky exoplanets' atmospheres (e.g. Seager and Deming, 2010), the same for the characterization of rocky exoplanet's surfaces. For instance, an Earth-sized planet at a 0.02-AU orbit of an M dwarf with effective temperature of 3000 K and size of 0.5 $R_\odot$ can have solid silicate surfaces (Figure 5-1), and the secondary transit depth ranges from 50 to 100 ppm in the mid-infrared. Such planets, if discovered, may be proven to have certain type of silicate surfaces (e.g., ultramafic versus granitoid) or iron-oxide surfaces by MIR spectroscopy.

The possibility of rocky super-Earths should not be neglected. A number of transiting exoplanets with size of about 2 $R_\oplus$ have been detected, and the mass and radius constraints cannot exclude the possibility of a silicate-dominant composition (e.g. Lissauer et al., 2011; Gautier et al., 2012; Borucki et al., 2012). Notably, Kepler-11b and Kepler-22b may have solid silicate surfaces according to their orbital semi-major axis (Figure 5-1). The secondary transit depths are 20 - 40 ppm for Kepler-11b and 5 - 10 ppm for Kepler-22b in the mid-infrared. As an application of my theoretical model, the contrast of the silicate features is computed to be 10 ppm in the 7 - 13 μm band for Kepler-11b and 2 ppm in the 15 - 25 μm band for Kepler-22b. Furthermore, large planets around M dwarfs, although not yet discovered, have the best potential for surface characterization. For example, a 2-$R_\oplus$ planet orbiting at 0.02 AU around a 0.5-$R_\odot$ M star having effective temperature of 3000 K, the secondary transit depth is up to ∼10 parts-per-million (ppm) at VNIR (λ < 3 μm), and up to 300 ppm in MIR. The planet's thermal emission flux at ∼ 10 μm can vary between 200 and 300 ppm for different types of crust. As a comparison, the warm SPITZER has achieved the photometric precision as high as 65 ppm for bright stars such as 55 Cnc (Demory et al., 2011). Characterization of rocky exoplanets' surfaces via the thermal emission is therefore possible with current space-based facilities if suitable targets are discovered.

Surface characterization by VNIR reflectance of rocky exoplanets is beyond the reach of current observation technology. The occultation depth of secondary eclipse at VNIR is fundamentally limited by the melting temperature of silicate rocks. To

maintain a solid surface, the exoplanet's surface temperature should be lower than the melting temperature. Averaging the emissivity over the stellar-radiation wavelengths and the thermal-emission wavelengths, the local energy balance equation for surface temperature (Eq. 5.13) can be solved to give the planet's sub-stellar temperature (T_p) as

$$T_\mathrm{p} = T_* \left(\frac{\epsilon_{VNIR}}{\epsilon_{MIR}} \right)^{1/4} \left(\frac{R_*}{D_\mathrm{p}} \right)^{1/2} , \qquad (5.17)$$

where ϵ_{VNIR} and ϵ_{MIR} are the Planck mean emissivity in the wavelength ranges of stellar and planetary emission, respectively. Algebra from Equation (5.17) and Equation(5.14) gives the following expression of the occultation depth:

$$\frac{F_\mathrm{p}}{F_*} = A_\mathrm{g} \frac{\epsilon_{VNIR}}{\epsilon_{MIR}} \left(\frac{R_\mathrm{p}}{R_*} \right)^2 \left(\frac{T_\mathrm{p}}{T_*} \right)^4 . \qquad (5.18)$$

Without considering the thermal emission, A_g is the true geometric albedo of the planet and is in the order of unity. The occultation depth increases rapidly with the surface temperature and the radius of the planet. For an Earth-like exoplanet around a Sun-like star, having surface temperature of 1000 K, the secondary occultation depth is about 0.1 ppm. Even for close-in rocky planets around M dwarfs (see Figure 5-4), the VNIR reflection only leads to a transit depth in the order of 10 ppm. To characterize surface compositions by measuring secondary transits, the required photometric precision is in the order of 1 ppm. Photometric precision is fundamentally limited by the photon noise and the stellar variability. For Kepler observing a star of V mag of 13, the photometric precision per 6.5-hour transit is about 20 ppm (Koch et al., 2010). Therefore, the required photometric precision for surface characterization by VNIR reflectance is currently not possible. The photometric precision might be significantly improved by accumulating a large number of transits, with space-based broad-band photometry instruments observing certain key objects for long periods, which requires a comprehensive understanding of noises, systematics, and stellar variability.

In the future, direct imaging can be suitable for characterizing solid surfaces of exoplanets. If direct imaging could spatially resolve the exoplanetary system, long-

cadence observations can be carried out to obtain low-resolution spectra of the planet's reflection and thermal emission. Specific absorption features of mafic minerals, water ice and hydrated minerals in the reflection, as well as silicate and iron-oxide features in the thermal emission presented in this paper could stand out with broad-band photometry, and might be detectable by direct imaging.

5.4.4 Connection of Surface Composition to the Planetary Interior and Evolution

Planetary radius and mass inferred from primary transits and radial velocity measurements constrain the density of transiting exoplanets. The assemblage of minerals comprising the surface of a rocky planetary body provides additional valuable constraints on understanding exoplanet interior structure and geologic evolution. Planetary surface composition depends on the bulk composition of the exoplanet, the history and nature of magmatic and thermal processes, and the subsequent interaction of produced solids with atmospheric volatiles and/or the space environment. I list as follows, in the order of detection likelihood, several type of planetary surfaces and their implications on the planet's interior structure and geological history.

A silicate surface, detectable via the prominent silicate features in the MIR thermal emission, will resolve the ambiguity of whether or not the planet has a significant envelope of volatiles. Due to the uncertainties in the measurements of mass and radius, the constraints of planetary interior are always ambiguous with various interpretation acceptable by data (e.g. Rogers and Seager, 2010a). Theoretical studies of the volatile evolution may provide additional but indirect constraints (see Fressin et al., 2012, for an example of Kepler-20e and Kepler-20f). With the detection of planetary thermal emission in MIR and the identification of surface silicate features described in this paper, the possibility of significant volatile envelope can be readily excluded, and the planet can be confirmed to have silicate surface and mantle. The surface characterization enabled by MIR spectroscopy will therefore provide an essential dimension of constraints on the interpretation of mass-radius relationship of

the planet.

A surface bright in VNIR, inferred from low equilibrium temperature, is likely to have felsic composition. Although the overall VNIR reflectivity is largely controlled by unknown factors such as surface roughness and weathering processes, no known surface process can increase the surface reflectivity. In other words, the detection of a bright surface indicates that the surface is intrinsically bright when fresh. As shown in Figure 5-4, a bright surface can be feldspathic, granitoid, and clay; all are silica-rich (termed "felsic"). A felsic surface on a planet of size larger than Mars is probably produced by slow intrusion of molten lava, which indicates plate-tectonics and potential geological setting for the origins of life (Best and Christiansen, 2001; Southam et al., 2007). A caveat here is that high VNIR reflectivity can also be attributed to atmospheric effects, such as bright clouds and hazes. A careful study, probably with transmission spectra, needs to be carried out to distinguish a bright solid surface against a bright cloud deck.

An ultramafic surface indicated by the 1-μm absorption feature in reflectance spectra implies either mantle overturn of the planet or very high temperature lavas. For rocky planets such as Mars and Earth, mantle pressures lead to the retention of Al in garnet, making it unavailable for feldspar formation. Consequently, the predicted primary crust composition, following mantle overturn to form a stable density stratification, is dominated by Mg-rich olivines and pyroxenes (Elkins-Tanton et al., 2005). As the surface matures, the 1-μm absorption feature diminishes. As a result, if strong 1-μm feature is identified from the J-band absorption, one may infer that the lava eruption or mantle overturn was geologically recent. The key indicator mineral is olivine and its strong contrast in the J-band due to the 1-μm absorptions makes detection possible.

A surface with hydrous materials, indicated by signature absorption features of ice or OH, implies substantial volatile inventory and constrains the planetary temperature to less than $\sim$700 K over geologic time to retain these materials on the surface. Hydrous materials, such as clays, would indicate liquid water having interacted with the crust, a parameter relevant to the habitability of the planet.

211

5.5 Summary

I have developed a theoretical framework to investigate reflection and thermal emission spectra of airless rocky exoplanets. I have modeled representative planetary surface types as fully covered by particulate mineral assemblages, whose mineral compositions depend on formation and evolutionary history of the planet. The most prominent spectral features and their geological implications are listed in the order of detectability.

- The silicate surface leads to Si-O vibrational features in both the 7 - 13 μm band and the 15 - 25 μm band. The silicate features are universal for all rocky surfaces, the magnitude of which can be as large as 20 K in terms of brightness temperature for an airless Earth analog. The silicate features allow unambiguous detection of rocky exoplanets via mid-infrared spectroscopy.

- Iron-oxidation leads to Fe-O vibrational features in the 15 - 25 μm band, which indicates an oxidized surface geochemical environment.

- The location of emissivity maxima at the short-wavelength edge (7 - 9 μm) of the main silicate feature uniquely indicates the silica content, which can be used to determine whether the surface is ultramafic, mafic or felsic. The location of the emissivity maxima may be found via photometry using 3 or more narrow-bands in the 7 - 9 μm region.

- The iron crystal-field electron band at 1 μm is indicative of olivine and pyroxene minerals. In terms of NIR broad-band photometry, the difference between the J-band geometric albedo and the K-band geometric albedo ($A_{\mathrm{g}}(\mathrm{K}) - A_{\mathrm{g}}(\mathrm{J})$) may distinguish ultramafic surfaces with these minerals, implying either mantle overturn of the planet or very high temperature lavas.

- The OH vibrational bands beyond 2 μm are indicative of either surface water ice or hydrated minerals, which indicates extant or past water on the planet's surface. A broad vibrational absorption band at 1.5 μm is diagnostic of water ice on the surface.

I propose that observations of rocky exoplanet reflection and thermal emission will provide valuable information on the planet's surface mineral composition. Broadband photometry of secondary eclipses in MIR may be able to identify a planetary surface of silicates or iron oxides (i.e., a rocky surface) via prominent spectral features. The required photometry precision is 2 ppm for planets around G stars and 20 ppm for planets around M stars. Next-generation space infrared facilities, such as the JWST, will likely be able to identify silicate surfaces around Sun-like stars. Reflected stellar light can also be used to uniquely determine the mineral composition of an exoplanet's surface, and is particularly useful for identifying ferrous or hydrated surface compositions. The occultation depth of the secondary eclipse in VNIR, however, is very small and beyond the reach of current technology. The required photometric precision for surface characterization via reflection is less than 0.1 part per million for an Earth-sized exoplanet around a Sun-like star, and 1 part per million for an Earth-sized exoplanet around an M dwarf. Although reflection of Earth-sized rocky planets are difficult to observe, planets as large as 55 Cnc e, if orbiting around M dwarfs, are best targets for long-period spacebased photometric monitoring. Eventually, the unique identification of minerals on exoplanets' surfaces may rely upon direct imaging. There are degeneracies among surface-related absorption features and atmospheric features, which may be broken by achieving high spectral resolution or by observing the primary transit and obtaining the transmission spectra. The surface mineral composition provides important constraints on the composition and the geological history of the exoplanet, which will constitute a new dimension of exoplanet characterization.

Chapter 6

Conclusion

I have developed a comprehensive one-dimensional photochemistry-thermochemistry kinetic-transport model for the study of terrestrial exoplanet atmospheres from the ground up. The model computes steady-state molecular compositions for atmospheres on terrestrial exoplanets. The generic reaction network of the model includes 110 molecules and aerosols made of C, H, O, N, and S elements, and more than 800 photochemical and chemical reactions. The model is applicable for both low pressure regimes in which photochemical processes and vertical transport dominate, and high pressure regimes in which thermochemical equilibrium holds. With modern numerical algorithms, the photochemistry-thermochemistry model has desirable features for exoplanet exploration, including the capacity to treat both reduced and oxidized atmospheres and to find steady-state solutions starting from any reasonable initial conditions. These features make the model the first photochemistry-thermochemistry model for non-H_2-dominated thick atmospheres on terrestrial exoplanets. I have tested my model by reproducing the compositions of current atmospheres of Earth and Mars, and the composition of the deep atmosphere of Jupiter.

Using the photochemistry model, I have explored the compositions of thin atmospheres on terrestrial exoplanets. Terrestrial exoplanets with thin atmospheres are important because they hold the most interest for the search of extraterrestrial life. In the seemingly infinite parameter space that defines thin atmospheres, the atmospheric redox power - the ability to reduce or oxidize a gas in the atmosphere - is

the key to understand the fates and the spectral effects of surface gas emission. I have for the first time systematically simulated both reducing and oxidizing atmospheres on terrestrial exoplanets and revealed the redox controlling effect of both the composition of major gases and the surface source and sink of trace gases. An important example of this redox controlling effect is that the surface emission of reducing gases, H_2 and CH_4, controls whether photochemically produced O_2 can build up in a CO_2-dominated atmosphere. I found that without surface emission of H_2 or CH_4, photochemical O_2 can build up in 1-bar CO_2-dominated atmospheres to levels that have conventionally been accepted as unique signatures of life. My finding implies a risk of false positives in using O_2 as the remote-sensing probe of biotic photosynthesis for terrestrial exoplanets, important for the design of a Terrestrial Planet Finder like mission.

I have also used my photochemistry model to investigate the carbon and sulfur chemistry of thin atmospheres on terrestrial exoplanets in detail. I found that volcanic carbon compounds (CH_4 and CO_2) are likely to be abundant in terrestrial exoplanet atmospheres due to their long chemical lifetimes; but volcanic sulfur compounds (H_2S and SO_2) are chemically short-lived and therefore cannot accumulate in virtually any types of terrestrial exoplanet atmospheres. The emission of sulfur compounds from the surface leads to photochemical formation of elemental sulfur and sulfuric acid in the atmosphere, which would condense to form aerosols if saturated. For a planet in the habitable zone of a Sun-like star or a M star, Earth-like sulfur emission rates would result in optically thick aerosol layers in 1-bar H_2-dominated atmospheres; and a sulfur emission rate 2-orders-of-magnitude higher than the Earth's volcanic sulfur emission rate would result in optically thick aerosol layers in 1-bar N_2- and CO_2-dominated atmospheres. The composition of the photochemically produced aerosols mostly depends on the redox state of the atmosphere: S_8 aerosols are formed in the reducing atmospheres (e.g., H_2 atmospheres), and both S_8 and H_2SO_4 aerosols are formed in the oxidized atmospheres that could be both reducing and oxidizing (e.g., N_2 and CO_2 atmospheres). Based on extensive numerical simulations, I have provided empirical formulae that show the dependency of the aerosol optical depth on

the surface sulfur emission rates, the dry deposition velocities of sulfur compounds, and the aerosol particle sizes.

In addition to thin atmospheres, I have also used my photochemistry-thermochemistry model to investigate terrestrial exoplanets with extensive gas envelopes, a unique category of planets discovered by exoplanet exploration. Thick atmospheres on terrestrial exoplanets are intriguing because they maintain thermochemical equilibrium at depth like atmospheres on gas giants, but some of them will have non-H_2-dominated compositions. Therefore thick atmospheres on terrestrial exoplanets are brand new theoretical subjects to be studied by photochemistry-thermochemistry models.

I have explored the molecular compositions of thick atmospheres on warm and hot terrestrial exoplanets, with GJ 1214b and 55 Cnc e as the prototypes. Using the hydrogen abundance (X_H) and the carbon to oxygen abundance ratio (X_C/X_O) as the primary parameters, I classified thick atmospheres on terrestrial exoplanets into hydrogen-rich atmospheres, water-rich atmospheres, oxygen-rich atmospheres, and hydrocarbon-rich atmospheres. I found that when $X_H > 0.7$, the atmosphere has free hydrogen and chemically behaves like H_2-dominated atmospheres on gas giants. When $0.3 < X_H < 0.7$, the atmosphere is water-rich for small X_C/X_O and hydrocarbon-rich for large X_C/X_O. In the middle of these regimes the molecular composition depends on temperature sensitively. In general, when hydrogen is no longer a dominant element in a thick atmosphere, the dominant molecule in the observable level ($10^{-3} \sim 1$ bar) of the atmosphere can be H_2O, CO_2, CO, H_2, CH_4, unsaturated hydrocarbons (C_2H_2 and C_2H_4), and even O_2.

The main findings pertinent to certain types of thick atmospheres include: (1) water-dominated atmospheres, in which most molecules are water vapor, only exist for carbon to oxygen ratios much lower than the solar ratio, and in a H_2-depleted water-dominated atmosphere, most of the trace mixture of carbon has to be in the form of CO_2 rather than CH_4 or CO; (2) the preferred loss of light elements from a carbon-rich atmosphere leads to formation of unsaturated hydrocarbons, i.e., C_2H_4 and C_2H_2, and they are the hallmark molecules for oxygen-poor and carbon-rich thick atmospheres on terrestrial exoplanets.

217

Applying my results to observations of super Earths and mini Neptunes, I found for warm super Earths and mini Neptunes having temperatures as GJ 1214b that (1) the C_2H_2 features at 1.0 and 1.5 μm in transmission spectra are diagnostic for hydrocarbon-rich atmospheres; (2) a constraint on the thermal emission at 4.5 μm could differentiate water-rich atmospheres versus hydrocarbon-rich atmospheres; (3) a detection of water-vapor features and a confirmation of nonexistence of methane features provide sufficient evidence for a water-dominated atmosphere. For a hot super Earth like 55 Cnc e, the diagnostic features of water-rich atmospheres (H_2O) and the diagnostic features of hydrocarbon-rich atmospheres (CO and C_2H_2) are well separated in transmission spectra in 0.6-5 μm, which would enable straightforward characterization if the planet has an thick atmosphere. In general, my results imply that chemical stability has to be taken into account when interpreting the spectrum of a super Earth/mini Neptune like GJ 1214b and 55 Cnc e, and that hydrocarbons (C_2H_4 and C_2H_2) should be considered among "standard" building blocks for thick atmospheres on terrestrial exoplanets.

Some terrestrial exoplanets will not have an atmosphere. To complete the study of terrestrial exoplanets, I have developed a framework to compute disk-integrated reflection-and-thermal-emission spectrum from a bare-rock exoplanet. Based on common mineral assemblages on the surfaces of Solar-System planets and moons, I found that a silicate surface on an exoplanet is spectroscopically detectable via prominent Si-O features in the thermal emission bands of 7-13 μm. The surface characterization thus provides a method to unambiguously identify a rocky exoplanet. In the distant future, near-infrared broadband photometry using direct imaging may pinpoint ultramafic surfaces (implying primary crust from a magma ocean or high-temperature lavas), hydrated surfaces, and water ice (implying extant or past water on the surface).

As a whole, I have outlined a roadmap to characterize terrestrial exoplanets in this thesis. Current and near-future observations of terrestrial exoplanets will focus on super Earths with think atmospheres. My findings imply that the carbon to oxygen elemental abundance ratio is the key parameter that defines thick atmospheres on super Earths, and this parameter can be constrained by detecting spectral features

of hallmark molecules that indicate the atmospheric scenarios presented in this thesis. For the future when terrestrial exoplanet characterization focuses on habitable planets with thin atmospheres, the photochemistry model presented here will be pivotal because it is the interface between the fundamental unknowns (e.g., geological sources, biological sources, mixing rates, and escape rates) and the observables (e.g., abundances of trace gases and their spectral signatures). The benchmark atmosphere scenarios presented in this thesis are useful for quickly assessing the lifetime of trace gases in both reducing and oxidizing thin atmospheres on terrestrial exoplanets for the exploration of possible biosignature gases. Finally, for some terrestrial exoplanets that do not have an atmosphere, I outlined how to characterize their surfaces by detecting spectral features of surface minerals.

The current thesis has presented a forward photochemistry-thermochemistry model for exploring plausible components in terrestrial exoplanet atmospheres. Looking forward, a theoretical framework to retrieve the fundamental unknowns from observations and to obtain a profound understanding of the evolution of terrestrial exoplanet atmospheres is still to be achieved. I will continue to study the chemical evolution of terrestrial exoplanet atmospheres. First, I plan to develop a Bayesian photochemistry framework to constrain the key physical parameters that control the compositions of terrestrial exoplanet atmospheres. The Bayesian photochemistry framework will be useful for gaining physical insight from *Hubble*, *Spitzer*, and ground-based observations of super Earths with thick atmospheres. Next, I plan to develop an evolutionary atmosphere model to reveal the planetary parameter regimes for build-up and stability of common volatiles (including water) on terrestrial exoplanets. The evolutionary atmosphere model will elucidate the origins and evolution of atmospheres on terrestrial exoplanets and help identify the most favorable terrestrial exoplanets that will continue to be discovered for follow-up observations. Eventually, my research will result in a collection of hallmarks of active geological and even biological inputs to the atmospheres on terrestrial exoplanets, and guide the planning of future observations and missions to characterize terrestrial exoplanets.

Appendix A

Reaction Rates in the Photochemistry Model

Table A.1: Reaction rates of bimolecular reactions, termolecular reactions, and thermodissociation reactions in the photochemistry model

No.	Reactants	Products	Reaction Rate[a]	Reference	Temperature[b]	Note
R1	$C + CH_2$	$\longrightarrow CH + CH$	$2.69 \times 10^{-12} \exp(-23573.0/T)$	NIST	1000-4000	
R2	$C + CN$	$\longrightarrow C_2 + N$	$4.98 \times 10^{-10} \exp(-18041.0/T)$	NIST	5000-8000	
R3	$C + H_2$	$\longrightarrow CH + H$	$6.64 \times 10^{-10} \exp(-11700.0/T)$	NIST	1520-2540	
R4	$C + H_2S$	$\longrightarrow CH + HS$	2.1×10^{-10}	NIST	298	
R5	$C + N_2$	$\longrightarrow CN + N$	$8.7 \times 10^{-11} \exp(-22611.0/T)$	NIST	2000-5000	
R6	$C + O_2$	$\longrightarrow CO + O$	$5.1 \times 10^{-11}(T/298.0)^{-0.3}$	NIST	15-295	Low Temperature
R7	$C + OCS$	$\longrightarrow CO + CS$	1.01×10^{-10}	NIST	298	
R8	$C + SO_2$	$\longrightarrow CO + SO$	6.91×10^{-11}	NIST	298	
R9	$C_2H + C_2H_3$	$\longrightarrow C_2H_2 + C_2H_2$	1.6×10^{-12}	NIST	300-2500	
R10	$H_2 + C_2H_4$	$\longrightarrow C_2H_5 + H$	$1.69 \times 10^{-11} \exp(-34277.6/T)$	NIST	300-2500	
R11	$C_2H + C_2H_5$	$\longrightarrow C_2H_4 + C_2H_2$	3.0×10^{-12}	NIST	300-2500	
R12	$C_2H + C_2H_6$	$\longrightarrow C_2H_2 + C_2H_5$	6.0×10^{-12}	NIST	300-2500	
R13	$C_2H + CH_3O_2$	$\longrightarrow CH_3O + C_2HO$	4.0×10^{-11}	NIST	300-2500	
R14	$C_2H + CH_4O$	$\longrightarrow C_2H_2 + CH_3O$	2.0×10^{-12}	NIST	300-2500	
R15	$C_2H_2 + C_2H_5$	$\longrightarrow C_2H_6 + C_2H$	$4.5 \times 10^{-13} \exp(-11800.0/T)$	NIST	300-2500	
R16	$C_2H_2 + C_2H_6$	$\longrightarrow C_2H_5 + C_2H_3$	$1.6 \times 10^{-12} \exp(-2300.0/T)$	NIST	300-2500	
R17	$C_2H_2 + CN$	$\longrightarrow HCN + C_2H$	2.2×10^{-10}	NIST	294	
R18	$C_2H_3 + C_2H_4O$	$\longrightarrow C_2H_4 + C_2H_3O$	$1.35 \times 10^{-13} \exp(-1850.0/T)$	NIST	480-520	Low Temperature
R19	$C_2H_4 + C_2H_5$	$\longrightarrow C_2H_3 + C_2H_6$	$5.83 \times 10^{-14}(T/298.0)^{3.13} \exp(-9060.0/T)$	NIST	300-2500	Low Temperature
R20	$C_2H_4 + CN$	$\longrightarrow HCN + C_2H_3$	2.1×10^{-10}	NIST	294	
R21	$C_2H_5 + C_2H_3$	$\longrightarrow C_2H_4 + C_2H_4$	4.4×10^{-11}	NIST	298	
R22	$C_2H_5 + C_2H_3$	$\longrightarrow C_2H_6 + C_2H_2$	2.4×10^{-11}	NIST	298	
R23	$C_2H_5 + C_2H_4O$	$\longrightarrow C_2H_6 + C_2H_3O$	$2.1 \times 10^{-12} \exp(-4280.0/T)$	NIST	357-676	Low Temperature
R24	$C_2H_5 + CNO$	$\longrightarrow HCN + C_2H_4O$	8.7×10^{-13}	NIST	293	
R25	$C_2H_5 + CNO$	$\longrightarrow HCNO + C_2H_4$	1.1×10^{-10}	NIST	293	

Continued on next page …

222

No.	Reactants	Products	Reaction Rate[a]	Reference	Temperature[b]	Note
R26	$C_2H_5O + O_2$	$\longrightarrow C_2H_4O + HO_2$	$6.3 \times 10^{-14} \exp(-550.0/T)$	JPL	200-300	Low Temperature
R27	$C_2H_6 + C_2H_3$	$\longrightarrow C_2H_5 + C_2H_4$	$1.46 \times 10^{-13}(T/298.0)^{3.3} \exp(-5280.0/T)$	NIST	300-2500	
R28	$C_2H_6 + C_2H_3O$	$\longrightarrow C_2H_4O + C_2H_5$	$1.91 \times 10^{-13}(T/298.0)^{2.75} \exp(-8820.0/T)$	NIST	300-2500	
R29	$C_2H_6 + CN$	$\longrightarrow HCN + C_2H_5$	$1.36 \times 10^{-11}(T/298.0)^{1.26} \exp(208.0/T)$	NIST	300-2500	
R30	$CH + C_2H_6$	$\longrightarrow C_2H_4 + CH_3$	1.3×10^{-10}	NIST	298	
R31	$CH + CH$	$\longrightarrow C_2H_2$	2.0×10^{-10}	NIST	298	
R32	$CH + CH_2O$	$\longrightarrow C_2H_3O$	$1.57 \times 10^{-10} \exp(260.0/T)$	NIST	297-670	Low Temperature
R33	$CH + CH_4$	$\longrightarrow C_2H_4 + H$	1.7×10^{-11}	NIST	298	
R34	$CH_2 + C_2H$	$\longrightarrow C_2H_2 + CH$	3.0×10^{-11}	NIST	300-2500	
R35	$CH_2 + C_2H_2O$	$\longrightarrow C_2H_4 + CO$	2.1×10^{-10}	NIST	298	
R36	$CH_2 + C_2H_3$	$\longrightarrow C_2H_2 + CH_3$	3.0×10^{-11}	NIST	300-2500	
R37	$CH_2 + C_2H_3O$	$\longrightarrow C_2H_2O + CH_3$	3.0×10^{-11}	NIST	300-2500	
R38	$CH_2 + C_2H_5$	$\longrightarrow C_2H_4 + CH_3$	3.0×10^{-11}	NIST	300-2500	
R39	$CH_2 + C_2H_6$	$\longrightarrow C_2H_5 + CH_3$	$1.07 \times 10^{-11} \exp(-3980.0/T)$	NIST	296-707	Low Temperature
R40	$NH + OH$	$\longrightarrow NH_2 + O$	$2.94 \times 10^{-12}(T/298.0)^{0.1} \exp(5800.0/T)$	NIST	298-3000	
R41	$H_2 + C_2H_2$	$\longrightarrow C_2H_3 + H$	$4.0 \times 10^{-12} \exp(-32714.0/T)$	NIST	300-2500	
R42	$CH_2 + CH_2$	$\longrightarrow C_2H_2 + H_2$	$2.62 \times 10^{-9} \exp(-6010.0/T)$	NIST	1100-2700	High Temperature
R43	$CH_2 + CH_2$	$\longrightarrow C_2H_2 + H + H$	$3.32 \times 10^{-10} \exp(-5530.0/T)$	NIST	1100-2700	High Temperature
R44	$CH_2 + CH_3$	$\longrightarrow C_2H_4 + H$	7.0×10^{-11}	NIST	300-2500	
R45	$CH_2 + CH_3O$	$\longrightarrow C_2H_4 + OH$	4.0×10^{-11}	NIST	300-2500	
R46	$CH_2 + CH_3O$	$\longrightarrow CH_2O + CH_3$	2.0×10^{-12}	NIST	300-2500	
R47	$CH_2 + CH_3O_2$	$\longrightarrow CH_2O + CH_3O$	3.0×10^{-11}	NIST	300-2500	
R48	$CH_2 + CH_4$	$\longrightarrow CH_3 + CH_3$	$7.12 \times 10^{-12} \exp(-5050.0/T)$	NIST	296-707	Low Temperature
R49	$CH_2 + CH_4O$	$\longrightarrow CH_3 + CH_3O$	$1.12 \times 10^{-15}(T/298.0)^{3.1} \exp(-3490.0/T)$	NIST	300-2500	
R50	$CH_2 + CHO$	$\longrightarrow CO + CH_3$	3.0×10^{-11}	NIST	300-2500	
R51	$CH_2O + C_2H_3$	$\longrightarrow C_2H_4 + CHO$	$8.07 \times 10^{-14}(T/298.0)^{2.81} \exp(-2950.0/T)$	NIST	300-2500	
R52	$CH_2O + C_2H_3O$	$\longrightarrow C_2H_4O + CHO$	$3.0 \times 10^{-13} \exp(-6500.0/T)$	NIST	300-2500	
R53	$CH_2O + C_2H_5$	$\longrightarrow C_2H_6 + CHO$	$8.19 \times 10^{-14}(T/298.0)^{2.81} \exp(-2950.0/T)$	NIST	300-2500	

Continued on next page …

223

No.	Reactants	Products	Reaction Rate[a]	Reference	Temperature[b]	Note
R54	$CH_2O + CH_3O_2$	$\longrightarrow CHO + CH_4O_2$	$3.3 \times 10^{-12} \exp(-5870.0/T)$	NIST	300-2500	
R55	$CH_2O + CN$	$\longrightarrow HCN + CHO$	7.0×10^{-11}	NIST	500-2500	
R56	$CH_2O + CNO$	$\longrightarrow HCNO + CHO$	1.0×10^{-11}	NIST	500-2500	
R57	$CH_3 + C_2H_2$	$\longrightarrow CH_4 + C_2H$	$3.0 \times 10^{-13} \exp(-8700.0/T)$	NIST	300-2500	
R58	$CH_3 + C_2H_2O$	$\longrightarrow CO + C_2H_5$	8.3×10^{-12}	NIST	1640-1950	High Temperature
R59	$CH_3 + C_2H_3$	$\longrightarrow CH_4 + C_2H_2$	$1.5 \times 10^{-11} \exp(385.0/T)$	NIST	300-900	
R60	$CH_3 + C_2H_3O$	$\longrightarrow C_2H_6 + CO$	5.4×10^{-11}	NIST	298	
R61	$CH_3 + C_2H_3O$	$\longrightarrow CH_4 + C_2H_2O$	$3.52 \times 10^{-12}(T/298.0)^{-0.8}$	NIST	300-2500	
R62	$CH_3 + C_2H_4$	$\longrightarrow CH_4 + C_2H_3$	$1.57 \times 10^{-14}(T/298.0)^{3.7} \exp(-4780.0/T)$	NIST	300-2500	
R63	$CH_3 + C_2H_4O$	$\longrightarrow CH_4 + C_2H_3O$	$2.97 \times 10^{-16}(T/298.0)^{5.64} \exp(-1240.0/T)$	NIST	300-1250	
R64	$CH_3 + C_2H_5$	$\longrightarrow CH_4 + C_2H_4$	$1.88 \times 10^{-12}(T/298.0)^{-0.5}$	NIST	300-2500	
R65	$CH_3 + C_2H_6$	$\longrightarrow CH_4 + C_2H_5$	$1.74 \times 10^{-16}(T/298.0)^{6} \exp(-3040.0/T)$	NIST	300-1500	
R66	$CH_3 + CH_2O$	$\longrightarrow CH_4 + CHO$	$1.6 \times 10^{-16}(T/298.0)^{6.1} \exp(-990.0/T)$	NIST	300-2000	
R67	$CH_3 + CH_3O$	$\longrightarrow CH_2O + CH_4$	4.0×10^{-11}	NIST	300-2500	
R68	$CH_3 + CH_3O_2$	$\longrightarrow CH_3O + CH_3O$	4.0×10^{-11}	NIST	300-2500	
R69	$CH_3 + CH_4O$	$\longrightarrow CH_4 + CH_3O$	$1.12 \times 10^{-15}(T/298.0)^{3.1} \exp(-3490.0/T)$	NIST	300-2500	
R70	$CH_3 + CHO$	$\longrightarrow C_2H_4O$	3.0×10^{-11}	NIST	300-2500	
R71	$CH_3 + CHO$	$\longrightarrow CH_4 + CO$	2.0×10^{-10}	NIST	300-2500	
R72	$CH_3 + CNO$	$\longrightarrow CH_2O + HCN$	4.2×10^{-13}	NIST	293	
R73	$CH_3O + C_2H$	$\longrightarrow CH_2O + C_2H_2$	6.0×10^{-11}	NIST	300-2500	
R74	$CH_3O + C_2H_2$	$\longrightarrow C_2H_3 + CH_2O$	$1.2 \times 10^{-12} \exp(-4529.0/T)$	NIST	300-2500	
R75	$CH_3O + C_2H_3$	$\longrightarrow C_2H_4 + CH_2O$	4.0×10^{-11}	NIST	300-2500	
R76	$CH_3O + C_2H_5$	$\longrightarrow C_2H_4 + CH_4O$	4.0×10^{-12}	NIST	300-2500	
R77	$CH_3O + C_2H_5$	$\longrightarrow C_2H_6 + CH_2O$	4.0×10^{-11}	NIST	300-2500	
R78	$CH_3O + C_2H_6$	$\longrightarrow C_2H_5 + CH_4O$	$4.0 \times 10^{-13} \exp(-3570.0/T)$	NIST	300-2500	
R79	$CH_3O + CH_2O$	$\longrightarrow CH_4O + CHO$	$1.7 \times 10^{-13} \exp(-1500.0/T)$	NIST	300-2500	
R80	$CH_3O + CH_3O_2$	$\longrightarrow CH_2O + CH_4O_2$	5.0×10^{-13}	NIST	300-2500	
R81	$CH_3O + O_2$	$\longrightarrow CH_2O + HO_2$	9.1×10^{-12}	JPL	200-300	Low Temperature

Continued on next page ...

224

No.	Reactants	Products	Reaction Rate[a]	Reference	Temperature[b]	Note
R82	$CH_3O_2 + C_2H_3$	$\longrightarrow CH_3O + C_2H_3O$	4.0×10^{-11}	NIST	300-2500	
R83	$CH_3O_2 + C_2H_5$	$\longrightarrow C_2H_5O + CH_3O$	4.0×10^{-11}	NIST	300-2500	
R84	$CH_3O_2 + C_2H_6$	$\longrightarrow C_2H_5 + CH_4O_2$	4.9×10^{-13}	NIST	300-2500	
R85	$CH_3O_2 + CH_3O_2$	$\longrightarrow CH_3O + CH_3O + O_2$	$5.9 \times 10^{-14} \exp(390.0/T)$	JPL	200-300	Low Temperature
R86	$CH_3O_2 + CH_3O_2$	$\longrightarrow CH_4O + CH_2O + O_2$	$3.6 \times 10^{-14} \exp(390.0/T)$	JPL	200-300	Low Temperature
R87	$CH_3O_2 + CH_4O$	$\longrightarrow CH_4O_2 + CH_3O$	$3.0 \times 10^{-12} \exp(-6900.0/T)$	NIST	300-2500	
R88	$CH_3S + CO$	$\longrightarrow OCS + CH_3$	$8.43 \times 10^{-13}(T/298.0)^{1.57} \exp(-3359.0/T)$	NIST	200-3000	
R89	$CH_3S + O_2$	$\longrightarrow CH_3 + SO_2$	$6.23 \times 10^{-8}(T/298.0)^{-3.8} \exp(-6189.2/T)$	NIST	200-2000	
R90	$CH_3S + O_3$	$\longrightarrow CH_3O + SO_2$	$1.5 \times 10^{-12} \exp(360.0/T)$	JPL	200-300	Low Temperature
R91	$CH_4 + C_2H$	$\longrightarrow C_2H_2 + CH_3$	$3.0 \times 10^{-12} \exp(-250.0/T)$	NIST	300-2500	
R92	$CH_4 + C_2H_2$	$\longrightarrow C_2H_3 + CH_3$	$5.0 \times 10^{-13} \exp(-2479.0/T)$	NIST	290-310	Low Temperature
R93	$CH_4 + C_2H_3$	$\longrightarrow C_2H_4 + CH_3$	$2.13 \times 10^{-14}(T/298.0)^{4.02} \exp(-2479.0/T)$	NIST	300-2500	
R94	$CH_4 + C_2H_5$	$\longrightarrow C_2H_6 + CH_3$	$2.51 \times 10^{-15}(T/298.0)^{4.14} \exp(-6320.0/T)$	NIST	300-2500	
R95	$CH_4 + CH_3$	$\longrightarrow H_2 + C_2H_5$	$1.66 \times 10^{-11} \exp(-11600.0/T)$	NIST	1950-2770	
R96	$CH_4 + CH_3O$	$\longrightarrow CH_4O + CH_3$	$2.61 \times 10^{-13} \exp(-4450.0/T)$	NIST	300-2500	
R97	$CH_4 + CH_3O_2$	$\longrightarrow CH_3 + CH_4O_2$	$3.0 \times 10^{-13} \exp(-9299.5/T)$	NIST	300-2500	
R98	$CH_4 + CHO$	$\longrightarrow CH_2O + CH_3$	$1.36 \times 10^{-13}(T/298.0)^{2.85} \exp(-11300.0/T)$	NIST	300-2500	
R99	$CH_4 + CN$	$\longrightarrow HCN + CH_3$	$5.11 \times 10^{-13}(T/298.0)^{2.64} \exp(150.3/T)$	NIST	290-1500	
R100	$CH_4 + CNO$	$\longrightarrow CH_3 + HCNO$	$1.62 \times 10^{-11} \exp(-4090.5/T)$	NIST	512-1100	
R101	$CH_4O + CN$	$\longrightarrow HCN + CH_3O$	1.2×10^{-10}	NIST	294	
R102	$CH_4S + CN$	$\longrightarrow HCN + CH_3S$	2.19×10^{-10}	NIST	293	
R103	$CH_4S + H$	$\longrightarrow CH_3 + H_2S$	$1.15 \times 10^{-11} \exp(-840.0/T)$	NIST	313-454	Low Temperature
R104	$CH_4S + H$	$\longrightarrow H_2 + CH_3S$	$4.82 \times 10^{-11} \exp(-1309.8/T)$	NIST	313-454	Low Temperature
R105	$CH_4S + NO_3$	$\longrightarrow CH_3S + HNO_3$	$4.4 \times 10^{-13} \exp(210.0/T)$	JPL	200-300	Low Temperature
R106	$CH_4S + O$	$\longrightarrow CH_3 + HSO$	$3.45 \times 10^{-14}(T/298.0)^{4.7} \exp(1210.0/T)$	NIST	254-495	Low Temperature
R107	$CH_4S + OH$	$\longrightarrow H_2O + CH_3S$	$9.9 \times 10^{-12} \exp(360.0/T)$	JPL	200-300	Low Temperature
R108	$CHO + C_2H$	$\longrightarrow C_2H_2 + CO$	1.0×10^{-10}	NIST	300-2500	
R109	$CHO + C_2H_3$	$\longrightarrow C_2H_4 + CO$	1.5×10^{-10}	NIST	300-2500	

Continued on next page ...

225

No.	Reactants	Products	Reaction Rate[a]	Reference	Temperature[b]	Note
R110	$CHO + C_2H_3O$	$\longrightarrow C_2H_4O + CO$	1.5×10^{-11}	NIST	300-2500	
R111	$CHO + C_2H_4O$	$\longrightarrow CH_4 + CO + CHO$	$1.33 \times 10^{-11} \exp(-523.0/T)$	NIST	415-670	Low Temperature
R112	$CHO + C_2H_5$	$\longrightarrow C_2H_6 + CO$	2.0×10^{-10}	NIST	300-2500	
R113	$CHO + CH_3O$	$\longrightarrow CH_4O + CO$	1.5×10^{-10}	NIST	300-2500	
R114	$CHO + CH_3O$	$\longrightarrow CH_2O + CH_2O$	3.0×10^{-10}	NIST	300-2500	
R115	$CHO + CH_4O$	$\longrightarrow CH_2O + CH_3O$	$2.41 \times 10^{-13}(T/298.0)^{2.9} \exp(-6600.0/T)$	NIST	300-2500	
R116	$CHO + CN$	$\longrightarrow HCN + CO$	1.0×10^{-10}	NIST	500-2500	
R117	$CHO + CNO$	$\longrightarrow HCNO + CO$	6.0×10^{-11}	NIST	500-2500	
R118	$CHO + O_2$	$\longrightarrow CO + HO_2$	5.2×10^{-12}	JPL	200-400	Low Temperature
R119	$CN + HCNO$	$\longrightarrow HCN + CNO$	1.1×10^{-10}	NIST	298	
R120	$CO + C_2H_2$	$\longrightarrow C_2H + CHO$	$8.0 \times 10^{-10} \exp(-53641.4/T)$	NIST	300-2500	
R121	$CO + C_2H_4$	$\longrightarrow C_2H_3 + CHO$	$2.5 \times 10^{-10} \exp(-45583.2/T)$	NIST	300-2500	
R122	$CO + CH_3$	$\longrightarrow C_2H_2 + OH$	$6.3 \times 10^{-11} \exp(-30428.9/T)$	NIST	1500-1900	
R123	$CO_2 + CH_2$	$\longrightarrow CH_2O + CO$	3.9×10^{-14}	NIST	300-2500	
R124	$CO_2 + CN$	$\longrightarrow CNO + CO$	$1.35 \times 10^{-12}(T/298.0)^{2.16} \exp(-13470.5/T)$	NIST	300-3000	
R125	$CS + O$	$\longrightarrow CO + S$	$2.7 \times 10^{-10} \exp(-760.0/T)$	JPL	200-300	Low Temperature
R126	$CS + O_3$	$\longrightarrow O_2 + OCS$	3.0×10^{-16}	NIST	298	
R127	$H + C_2H$	$\longrightarrow C_2H_2$	3.0×10^{-10}	NIST	300-2500	
R128	$H + C_2H$	$\longrightarrow H_2 + C_2$	$6.0 \times 10^{-11} \exp(-14192.0/T)$	NIST	300-2500	
R129	$H + C_2H_2$	$\longrightarrow C_2H + H_2$	$1.0 \times 10^{-10} \exp(-11200.0/T)$	NIST	300-2500	
R130	$H + C_2H_2O$	$\longrightarrow CO + CH_3$	$5.0 \times 10^{-12}(T/298.0)^{1.45} \exp(-1398.8/T)$	NIST	200-2500	
R131	$H + C_2H_3$	$\longrightarrow C_2H_4$	$2.02 \times 10^{-10}(T/298.0)^{0.2}$	NIST	200-2000	
R132	$H + C_2H_3$	$\longrightarrow C_2H_2 + H_2$	2.0×10^{-11}	NIST	300-2500	
R133	$H + C_2H_3O$	$\longrightarrow CHO + CH_3$	2.2×10^{-11}	NIST	298	
R134	$H + C_2H_3O$	$\longrightarrow C_2H_2O + H_2$	1.2×10^{-11}	NIST	298	
R135	$H + C_2H_4$	$\longrightarrow C_2H_3 + H_2$	$4.0 \times 10^{-12}(T/298.0)^{2.53} \exp(-6160.0/T)$	NIST	300-2500	
R136	$H + C_2H_4O$	$\longrightarrow C_2H_5O$	$1.33 \times 10^{-11} \exp(-3221.0/T)$	NIST	298-2000	
R137	$H + C_2H_4O$	$\longrightarrow C_2H_3O + H_2$	$6.64 \times 10^{-11} \exp(-2120.4/T)$	NIST	300-2000	

Continued on next page ...

226

No.	Reactants	Products	Reaction Rate^a	Reference	Temperature^b	Note
R138	$H + C_2H_4O$	$\longrightarrow CH_4 + CHO$	$1.08 \times 10^{-10} \exp(-2120.4/T)$	NIST	300-2000	
R139	$H + N_2O$	$\longrightarrow N_2 + OH$	$1.60 \times 10^{-10} \exp(-7600.0/T)$	NIST	700-2500	High Temperature
R140	$H + C_2H_5$	$\longrightarrow CH_3 + CH_3$	6.0×10^{-11}	NIST	300-2000	
R141	$H + C_2H_5$	$\longrightarrow C_2H_4 + H_2$	3.0×10^{-12}	NIST	300-2500	
R142	$H + C_2H_5O$	$\longrightarrow C_2H_4O + H_2$	3.32×10^{-11}	NIST	295	
R143	$H + C_2H_6$	$\longrightarrow C_2H_5 + H_2$	$1.23 \times 10^{-11}(T/298.0)^{1.5} \exp(-3729.6/T)$	NIST	300-2000	
R144	$H + C_2HO$	$\longrightarrow CO + CH_2$	4.98×10^{-11}	NIST	1000-2500	High Temperature
R145	$H + CH$	$\longrightarrow C + H_2$	$1.31 \times 10^{-10} \exp(-85.6/T)$	NIST	300-2000	
R146	$H + CH_2$	$\longrightarrow CH + H_2$	$1.0 \times 10^{-11} \exp(900.0/T)$	NIST	300-3000	
R147	$H + CH_2O$	$\longrightarrow CH_3O$	$4.0 \times 10^{-11} \exp(-2068.7/T)$	NIST	290-2000	
R148	$H + CH_2O$	$\longrightarrow H_2 + CHO$	$4.78 \times 10^{-12}(T/298.0)^{1.9} \exp(-1380.0/T)$	NIST	250-5000	
R149	$H + CH_3$	$\longrightarrow CH_2 + H_2$	$1.0 \times 10^{-10} \exp(-7600.0/T)$	NIST	300-2500	
R150	$H + CH_3NO_2$	$\longrightarrow CH_4O + NO$	$2.0 \times 10^{-13} \exp(-956.2/T)$	NIST	223-398	Low Temperature
R151	$H + CH_3NO_2$	$\longrightarrow CH_3 + HNO_2$	$5.28 \times 10^{-9} \exp(-7920.0/T)$	NIST	1000-1100	High Temperature
R152	$H + CH_3O$	$\longrightarrow CH_4O$	$2.89 \times 10^{-10}(T/298.0)^{0.04}$	NIST	300-2500	
R153	$H + CH_3O$	$\longrightarrow CH_3 + OH$	0;	NIST	300-2500	
R154	$H + CH_3O$	$\longrightarrow CH_2O + H_2$	1.0×10^{-11}	NIST	300-2500	
R155	$H + CH_3O_2$	$\longrightarrow CH_3O + OH$	1.6×10^{-10}	NIST	300-2500	
R156	$H + CH_3O_2$	$\longrightarrow CH_4 + O_2$	$1.17 \times 10^{-11}(T/298.0)^{1.02} \exp(-8352.9/T)$	NIST	273-2000	
R157	$H + CH_4$	$\longrightarrow CH_3 + H_2$	$5.83 \times 10^{-13}(T/298.0)^{3.0} \exp(-4040.0/T)$	NIST	300-2500	
R158	$H + CH_4O$	$\longrightarrow CH_3 + H_2O$	$3.32 \times 10^{-10} \exp(-2670.0/T)$	NIST	1370-1840	High Temperature
R159	$H + CH_4O$	$\longrightarrow CH_3O + H_2$	$2.93 \times 10^{-14}(T/298.0)^{3.4} \exp(-3640.0/T)$	NIST	300-2500	
R160	$H + CH_4O_2$	$\longrightarrow CH_3O + H_2O$	$1.21 \times 10^{-13} \exp(-936.0/T)$	NIST	250-358	Low Temperature
R161	$H + CH_4O_2$	$\longrightarrow H_2 + CH_3O_2$	$1.46 \times 10^{-13} \exp(-936.0/T)$	NIST	250-358	Low Temperature
R162	$H + CHO$	$\longrightarrow CO + H_2$	1.50×10^{-10}	NIST	300-2500	
R163	$H + CNO$	$\longrightarrow CO + NH$	8.9×10^{-11}	NIST	500-2500	
R164	$H + CNO$	$\longrightarrow HCN + O$	$1.86 \times 10^{-11}(T/298.0)^{0.9} \exp(-2920.2/T)$	NIST	500-2500	
R165	$H + CO_2$	$\longrightarrow CO + OH$	$2.51 \times 10^{-10} \exp(-13350.0/T)$	NIST	300-2500	

Continued on next page ...

227

No.	Reactants	Products	Reaction Rate[a]	Reference	Temperature[b]	Note
R166	$H + H_2O$	$\longrightarrow H_2 + OH$	$6.82 \times 10^{-12}(T/298.0)^{1.6}\exp(-9720.0/T)$	NIST	300-2500	
R167	$H + H_2O_2$	$\longrightarrow OH + H_2O$	$1.69 \times 10^{-11}\exp(-1800.0/T)$	NIST	300-1000	
R168	$H + H_2O_2$	$\longrightarrow H_2 + HO_2$	$2.81 \times 10^{-12}\exp(-1890.0/T)$	NIST	300-1000	
R169	$H + HCNO$	$\longrightarrow H_2 + CNO$	$1.91 \times 10^{-12}(T/298.0)^{1.66}\exp(-7000.0/T)$	NIST	500-2500	
R170	$H + HCNO$	$\longrightarrow CN + H_2O$	1.66×10^{-12}	NIST	1800-2600	High Temperature
R171	$H + HCNO$	$\longrightarrow CO + NH_2$	$5.0 \times 10^{-11}\exp(-2300.0/T)$	NIST	500-2500	
R172	$H + HNO$	$\longrightarrow H_2 + NO$	$3.0 \times 10^{-11}\exp(-500.0/T)$	NIST	298-2000	
R173	$H + HNO$	$\longrightarrow OH + NH$	$2.41 \times 10^{-9}(T/298.0)^{-0.5}\exp(-9010.0/T)$	NIST	350-3000	
R174	$H + HNO$	$\longrightarrow NH_2 + O$	$1.05 \times 10^{-9}(T/298.0)^{-0.3}\exp(-14673.2/T)$	NIST	550-3000	
R175	$H + HNO_2$	$\longrightarrow OH + HNO$	$1.26 \times 10^{-11}(T/298.0)^{0.86}\exp(-2500.0/T)$	NIST	300-2500	
R176	$H + HNO_2$	$\longrightarrow H_2 + NO_2$	$2.0 \times 10^{-11}\exp(-3700.0/T)$	NIST	300-2500	
R177	$H + HNO_2$	$\longrightarrow H_2O + NO$	$6.39 \times 10^{-13}(T/298.0)^{1.89}\exp(-1940.0/T)$	NIST	300-2500	
R178	$H + HNO_3$	$\longrightarrow H_2O + NO_2$	$1.39 \times 10^{-14}(T/298.0)^{3.29}\exp(-3160.0/T)$	NIST	300-3000	
R179	$H + HNO_3$	$\longrightarrow H_2 + NO_3$	$5.65 \times 10^{-12}(T/298.0)^{1.53}\exp(-8250.0/T)$	NIST	300-3000	
R180	$H + HO_2$	$\longrightarrow OH + OH$	7.2×10^{-11}	JPL	298	
R181	$H + HO_2$	$\longrightarrow O + H_2O$	1.6×10^{-12}	JPL	298	
R182	$H + HO_2$	$\longrightarrow H_2 + O_2$	6.9×10^{-12}	JPL	298	
R183	$H + N_2O$	$\longrightarrow NO + NH$	$5.03 \times 10^{-7}(T/298.0)^{-2.16}\exp(-18642.2/T)$	NIST	300-4000	
R184	$H + NH$	$\longrightarrow H_2 + N$	1.69×10^{-11}	NIST	1500-2500	High Temperature
R185	$H + NH_2$	$\longrightarrow H_2 + NH$	$1.05 \times 10^{-10}\exp(-4450.1/T)$	NIST	1100-1800	High Temperature
R186	$H + NH_3$	$\longrightarrow H_2 + NH_2$	$7.80 \times 10^{-13}(T/298.0)^{2.4}\exp(-4990.1/T)$	NIST	490-1780	
R187	$H + NO$	$\longrightarrow NH + O$	$9.3 \times 10^{-10}(T/298.0)^{-0.1}\exp(-35240.0/T)$	NIST	1300-3000	
R188	$H + NO$	$\longrightarrow OH + N$	$3.6 \times 10^{-10}\exp(-24896.0/T)$	NIST	1500-4500	
R189	$H + NO_2$	$\longrightarrow OH + NO$	$4.0 \times 10^{-10}\exp(-340.0/T)$	JPL	200-300	Low Temperature
R190	$H + NO_3$	$\longrightarrow OH + NO_2$	9.4×10^{-11}	NIST	298	
R191	$H + O_2$	$\longrightarrow O + OH$	$6.73 \times 10^{-10}(T/298.0)^{-0.59}\exp(-8152.0/T)$	NIST	800-3500	High Temperature
R192	$H + O_3$	$\longrightarrow OH + O_2$	$1.4 \times 10^{-10}\exp(-470.0/T)$	JPL	200-300	Low Temperature
R193	$H_2 + C$	$\longrightarrow CH + H$	$6.64 \times 10^{-10}\exp(-11700.0/T)$	NIST	1520-2540	

Continued on next page ...

228

No.	Reactants	Products	Reaction Rate[a]	Reference	Temperature[b]	Note
R194	$H_2 + C_2$	$\longrightarrow C_2H + H$	$1.1 \times 10^{-10} \exp(-4000.0/T)$	NIST	2580-4650	High Temperature
R195	$H_2 + C_2H$	$\longrightarrow C_2H_2 + H$	$8.95 \times 10^{-13}(T/298.0)^{2.57} \exp(-130.0/T)$	NIST	200-2000	
R196	$H_2 + C_2H_2$	$\longrightarrow C_2H_4$	$5.0 \times 10^{-13} \exp(-19604.4/T)$	NIST	300-2500	
R197	$H_2 + C_2H_3$	$\longrightarrow C_2H_4 + H$	$1.61 \times 10^{-13}(T/298.0)^{2.63} \exp(-4300.0/T)$	NIST	300-2500	
R198	$H_2 + C_2H_5$	$\longrightarrow C_2H_6 + H$	$4.12 \times 10^{-15}(T/298.0)^{3.6} \exp(-4250.0/T)$	NIST	300-2500	
R199	$H_2 + C_2HO$	$\longrightarrow C_2H_3O$	$1.0 \times 10^{-11} \exp(-2000.0/T)$	NIST	438-761	
R200	$H_2 + C_2HO$	$\longrightarrow CH_3 + CO$	$1.2 \times 10^{-11} \exp(-2000.0/T)$	NIST	438-761	
R201	$NH + NO$	$\longrightarrow OH + N_2$	$5.86 \times 10^{-12}(T/298.0)^{-0.5} \exp(-60.0/T)$	NIST	300-4000	
R202	$H_2 + CH$	$\longrightarrow CH_2 + H$	$3.75 \times 10^{-10} \exp(-1660.0/T)$	NIST	327-397	Low Temperature
R203	$H_2 + CH_3$	$\longrightarrow CH_4 + H$	$6.86 \times 10^{-14}(T/298.0)^{2.74} \exp(-4740.0/T)$	NIST	300-2500	
R204	$H_2 + CH_3O$	$\longrightarrow CH_4O + H$	$9.96 \times 10^{-14}(T/298.0)^{2} \exp(-6720.0/T)$	NIST	300-2500	
R205	$H_2 + CH_3O_2$	$\longrightarrow CH_4O_2 + H$	$5.0 \times 10^{-11} \exp(-13110.0/T)$	NIST	300-2500	
R206	$H_2 + CHO$	$\longrightarrow CH_2O + H$	$2.66 \times 10^{-13}(T/298.0)^{2.0} \exp(-8970.0/T)$	NIST	300-2500	
R207	$H_2 + CN$	$\longrightarrow HCN + H$	$5.65 \times 10^{-13}(T/298.0)^{2.45} \exp(-1131.0/T)$	NIST	300-2500	
R208	$H_2 + HNO$	$\longrightarrow NH + H_2O$	$1.66 \times 10^{-10} \exp(-8059.4/T)$	NIST	1300-1900	High Temperature
R209	$H_2 + HO_2$	$\longrightarrow H_2O_2 + H$	$5.0 \times 10^{-11} \exp(-13110.0/T)$	NIST	300-2500	
R210	$H_2 + N_2O$	$\longrightarrow H_2O + N_2$	$5.73 \times 10^{-12}(T/298.0)^{0.5}$	NIST	1700-3000	High Temperature
R211	$H_2 + NH$	$\longrightarrow NH_2 + H$	$3.5 \times 10^{-11} \exp(-7758.0/T)$	NIST	833-1432	High Temperature
R212	$H_2 + NH_2$	$\longrightarrow NH_3 + H$	$6.75 \times 10^{-14}(T/298.0)^{2.6} \exp(-3006.8/T)$	NIST	400-2200	
R213	$H_2 + NO_2$	$\longrightarrow H + HNO_2$	$4.0 \times 10^{-11} \exp(-14553.0/T)$	NIST	760-1000	
R214	$H_2O + C$	$\longrightarrow CH + OH$	$1.3 \times 10^{-12} \exp(-19845.0/T)$	NIST	1000-4000	
R215	$H_2O + C_2H$	$\longrightarrow C_2H_2 + OH$	$7.74 \times 10^{-14}(T/298.0)^{3.05} \exp(-376.0/T)$	NIST	300-2000	
R216	$HSO + O_3$	$\longrightarrow HSO_2 + O_2$	3.0×10^{-14}	JPL	298	
R217	$H_2O + C_2H_5$	$\longrightarrow C_2H_6 + OH$	$2.06 \times 10^{-14}(T/298.0)^{1.44} \exp(-10200.0/T)$	NIST	300-2500	
R218	$H_2O + CH$	$\longrightarrow CH_3O$	$9.48 \times 10^{-12} \exp(380.0/T)$	NIST	298-669	Low Temperature
R219	$H_2O + CN$	$\longrightarrow HCN + OH$	$1.3 \times 10^{-11} \exp(-3760.0/T)$	NIST	500-2500	
R220	$H_2O + CNO$	$\longrightarrow HCNO + OH$	$9.13 \times 10^{-14}(T/298.0)^{2.17} \exp(-3050.0/T)$	NIST	500-2500	
R221	$H_2O_2 + C_2H_3$	$\longrightarrow C_2H_4 + HO_2$	$2.0 \times 10^{-14} \exp(300.0/T)$	NIST	300-2500	

Continued on next page ...

229

No.	Reactants	Products	Reaction Rate^a	Reference	Temperature^b	Note
R222	$H_2O_2 + C_2H_3O$	$\longrightarrow C_2H_4O + HO_2$	$3.0 \times 10^{-13} \exp(-4140.0/T)$	NIST	300–2500	
R223	$H_2O_2 + C_2H_5$	$\longrightarrow C_2H_6 + HO_2$	$1.45 \times 10^{-14} \exp(-490.0/T)$	NIST	300–2500	
R224	$H_2O_2 + CH_3$	$\longrightarrow CH_4 + HO_2$	$2.0 \times 10^{-14} \exp(300.0/T)$	NIST	300–2500	
R225	$H_2O_2 + CH_3O$	$\longrightarrow CH_4O + HO_2$	$5.0 \times 10^{-15} \exp(-1300.0/T)$	NIST	300–2500	
R226	$H_2O_2 + CH_3O_2$	$\longrightarrow CH_4O_2 + HO_2$	$4.0 \times 10^{-12} \exp(-5000.0/T)$	NIST	300–2500	
R227	$H_2O_2 + CHO$	$\longrightarrow CH_2O + HO_2$	$1.69 \times 10^{-13} \exp(-3490.0/T)$	NIST	300–2500	
R228	$H_2S + CH$	$\longrightarrow HS + CH_2$	2.8×10^{-10}	NIST	330	
R229	$H_2S + CH_2$	$\longrightarrow HS + CH_3$	2.0×10^{-12}	NIST	295	
R230	$H_2S + H$	$\longrightarrow H_2 + HS$	$3.66 \times 10^{-12}(T/298.0)^{1.94} \exp(-454.6/T)$	NIST	190–2237	
R231	$H_2S + O$	$\longrightarrow OH + HS$	$9.2 \times 10^{-12} \exp(-1800.0/T)$	JPL	200–300	Low Temperature
R232	$H_2S + OH$	$\longrightarrow H_2O + HS$	$6.1 \times 10^{-12} \exp(-75.0/T)$	JPL	200–300	Low Temperature
R233	$HCN + CNO$	$\longrightarrow HCNO + CN$	$2.0 \times 10^{-11} \exp(-4460.0/T)$	NIST	500–2500	
R234	$HNO + C_2H_5$	$\longrightarrow C_2H_6 + NO$	1.66×10^{-12}	NIST	883–953	High Temperature
R235	$HNO + CH_3$	$\longrightarrow CH_4 + NO$	$1.85 \times 10^{-11}(T/298.0)^{0.76} \exp(-175.6/T)$	NIST	298–2500	
R236	$HNO + CH_3O$	$\longrightarrow CH_4O + NO$	5.0×10^{-11}	NIST	298	
R237	$HNO + CHO$	$\longrightarrow CH_2O + NO$	$1.0 \times 10^{-12} \exp(-1000.0/T)$	NIST	300–2500	
R238	$HNO + CN$	$\longrightarrow HCN + NO$	3.0×10^{-11}	NIST	500–2500	
R239	$HNO + CNO$	$\longrightarrow HCNO + NO$	3.0×10^{-11}	NIST	500–2500	
R240	$HNO + CO$	$\longrightarrow CO_2 + NH$	$3.3 \times 10^{-12} \exp(-6190.0/T)$	NIST	1200–1900	High Temperature
R241	$HNO_2 + CH_3$	$\longrightarrow CH_4 + NO_2$	$3.55 \times 10^{-7} \exp(-10100.0/T)$	NIST	1000–1100	High Temperature
R242	$HNO_2 + CN$	$\longrightarrow HCN + NO_2$	2.0×10^{-11}	NIST	500–2500	
R243	$HNO_2 + CNO$	$\longrightarrow HCNO + NO_2$	6.0×10^{-12}	NIST	500–2500	
R244	$HO_2 + C_2H_2$	$\longrightarrow C_2H_3 + O_2$	$5.0 \times 10^{-14}(T/298.0)^{1.61} \exp(-7129.7/T)$	NIST	300–2500	
R245	$HO_2 + C_2H_2$	$\longrightarrow C_2H_2O + OH$	$1.0 \times 10^{-14} \exp(-4000.3/T)$	NIST	300–2500	
R246	$HO_2 + C_2H_3$	$\longrightarrow OH + CH_3 + CO$	5.0×10^{-11}	NIST	300–2500	
R247	$HO_2 + C_2H_3O$	$\longrightarrow OH + CH_3 + CO_2$	5.0×10^{-11}	NIST	300–2500	
R248	$HO_2 + C_2H_4$	$\longrightarrow C_2H_4O + OH$	$1.0 \times 10^{-14} \exp(-4000.3/T)$	NIST	300–2500	
R249	$HO_2 + C_2H_4O$	$\longrightarrow C_2H_3O + H_2O_2$	$5.0 \times 10^{-12} \exp(-6000.4/T)$	NIST	900–1200	High Temperature

Continued on next page …

230

No.	Reactants	Products	Reaction Rate[a]	Temperature[b]	Reference	Note
R250	$HO_2 + C_2H_5$	$\longrightarrow C_2H_4 + H_2O_2$	5.0×10^{-13}	300-2500	NIST	
R251	$HO_2 + C_2H_5$	$\longrightarrow C_2H_6 + O_2$	5.0×10^{-13}	300-2500	NIST	
R252	$HO_2 + CH_2O$	$\longrightarrow CHO + H_2O_2$	$3.3 \times 10^{-12} \exp(-5870.5/T)$	300-2500	NIST	
R253	$HO_2 + CH_2O$	$\longrightarrow CH_3O + O_2$	$5.63 \times 10^{-12} \exp(-9620.6/T)$	1200-1800	NIST	High Temperature
R254	$HO_2 + CH_3O_2$	$\longrightarrow CH_4O_2 + O_2$	$4.1 \times 10^{-13} \exp(750.0/T)$	200-300	JPL	Low Temperature
R255	$HO_2 + CH_4O$	$\longrightarrow CH_3O + H_2O_2$	$1.6 \times 10^{-13} \exp(-6330.0/T)$	300-2500	NIST	High Temperature
R256	$HO_2 + CNO$	$\longrightarrow HCNO + O_2$	3.32×10^{-11}	623-773	NIST	High Temperature
R257	$HO_2 + HO_2$	$\longrightarrow H_2O_2 + O_2$	$3.5 \times 10^{-13} \exp(430.0/T)$	200-300	JPL	Low Temperature
R258	$HO_2 + NH_2$	$\longrightarrow NH_3 + O_2$	3.4×10^{-11}	298	JPL	
R259	$HO_2 + NO$	$\longrightarrow OH + NO_2$	$3.5 \times 10^{-12} \exp(250.0/T)$	200-300	JPL	Low Temperature
R260	$HO_2 + NO_3$	$\longrightarrow OH + NO_2 + O_2$	3.5×10^{-12}	298	JPL	
R261	$HO_2 + O_3$	$\longrightarrow OH + O_2 + O_2$	$1.0 \times 10^{-14} \exp(-490.0/T)$	200-300	JPL	Low Temperature
R262	$HS + CH_3$	$\longrightarrow CH_4S$	1.66×10^{-11}	681-723	NIST	High Temperature
R263	$HS + HO_2$	$\longrightarrow OH + HSO$	1.0×10^{-11}	298	NIST	
R264	$HS + HS$	$\longrightarrow S + H_2S$	1.5×10^{-11}	298	NIST	
R265	$HS + NO_2$	$\longrightarrow NO + HSO$	$2.9 \times 10^{-11} \exp(240.0/T)$	220-420	JPL	Low Temperature
R266	$HS + O$	$\longrightarrow H + SO$	1.6×10^{-10}	298	NIST	
R267	$HS + CHO$	$\longrightarrow H_2S + CO$	5.0×10^{-11}	298	Kasting (1990)	
R268	$HS + O_2$	$\longrightarrow SO + OH$	4.0×10^{-19}	298	NIST	
R269	$HS + O_3$	$\longrightarrow O_2 + HSO$	$9.0 \times 10^{-12} \exp(-280.0/T)$	200-300	JPL	Low Temperature
R270	$HSO + NO_2$	$\longrightarrow HSO_2 + NO$	9.6×10^{-12}	298	JPL	
R271	$HSO + O_3$	$\longrightarrow HS + O_2 + O_2$	7.0×10^{-14}	298	JPL	
R272	$HS + CH_2O$	$\longrightarrow H_2S + CHO$	$1.7 \times 10^{-11} \exp(-800.0/T)$	200-300	JPL	Low Temperature
R273	$HSO_2 + O_2$	$\longrightarrow HO_2 + SO_2$	3.0×10^{-13}	298	JPL	
R274	$HSO_3 + O$	$\longrightarrow OH + SO_3$	1.0×10^{-11}	298	Kasting (1990)	
R275	$HSO_3 + O_2$	$\longrightarrow HO_2 + SO_3$	$1.3 \times 10^{-12} \exp(-330.0/T)$	200-300	JPL	Low Temperature
R276	$N + C_2$	$\longrightarrow CN + C$	2.8×10^{-11}	298	NIST	
R277	$N + C_2H_3$	$\longrightarrow C_2H_2N + H$	6.2×10^{-11}	298	NIST	

Continued on next page ...

231

No.	Reactants	Products	Reaction Rate^a	Reference	Temperature^b	Note
R278	$N + C_2H_3$	$\longrightarrow C_2H_2 + NH$	1.2×10^{-11}	NIST	298	
R279	$N + C_2H_4$	$\longrightarrow HCN + CH_3$	4.2×10^{-14}	NIST	298	
R280	$N + CH$	$\longrightarrow C + NH$	$3.0 \times 10^{-11}(T/298.0)^{0.65} \exp(-1203.0/T)$	NIST	990-1010	High Temperature
R281	$N + CH$	$\longrightarrow CN + H$	$1.66 \times 10^{-10}(T/298.0)^{-0.09}$	NIST	216-584	Low Temperature
R282	$N + CH_3$	$\longrightarrow H_2 + HCN$	$4.3 \times 10^{-10} \exp(-420.0/T)$	NIST	200-423	Low Temperature
R283	$N + CH_4O$	$\longrightarrow CH_3 + HNO$	$4.0 \times 10^{-10} \exp(-4330.0/T)$	NIST	309-409	Low Temperature
R284	$N + CN$	$\longrightarrow C + N_2$	3.0×10^{-10}	NIST	300-2500	
R285	$N + CNO$	$\longrightarrow CO + N_2$	3.3×10^{-11}	NIST	1100-1400	High Temperature
R286	$N + CNO$	$\longrightarrow CN + NO$	1.66×10^{-12}	NIST	1400-2000	High Temperature
R287	$N + H_2O$	$\longrightarrow OH + NH$	$6.03 \times 10^{-11}(T/298.0)^{1.2} \exp(-19243.6/T)$	NIST	800-3000	
R288	$N + HCNO$	$\longrightarrow NH + CNO$	$3.85 \times 10^{-5} \exp(-26460.0/T)$	NIST	1000-3000	
R289	$N + NH$	$\longrightarrow N_2 + H$	$1.95 \times 10^{-11}(T/298.0)^{0.51} \exp(-9.6/T)$	NIST	300-2500	
R290	$N + NH_2$	$\longrightarrow NH + NH$	$3.0 \times 10^{-13} \exp(-7600.0/T)$	NIST	1000-4000	High Temperature
R291	$N + NO$	$\longrightarrow O + N_2$	$2.1 \times 10^{-11} \exp(100.0/T)$	JPL	200-300	Low Temperature
R292	$N + NO_2$	$\longrightarrow N_2O + O$	$5.8 \times 10^{-12} \exp(220.0/T)$	JPL	200-300	Low Temperature
R293	$N + O_2$	$\longrightarrow NO + O$	$1.5 \times 10^{-11} \exp(-3600.0/T)$	JPL	200-300	Low Temperature
R294	$N + O_3$	$\longrightarrow NO + O_2$	2.0×10^{-16}	JPL	298	
R295	$N + OH$	$\longrightarrow NO + H$	4.7×10^{-11}	NIST	300-2500	
R296	$N_2O + C$	$\longrightarrow CO + N_2$	8.0×10^{-12}	NIST	298	
R297	$N_2O + CH$	$\longrightarrow HCN + NO$	$3.1 \times 10^{-11} \exp(257.4/T)$	NIST	200-1250	
R298	$N_2O + CN$	$\longrightarrow N_2 + CNO$	2.0×10^{-12}	NIST	297	
R299	$N_2O + HCN$	$\longrightarrow HCNO + N_2$	2.0×10^{-11}	NIST	1400-1800	High Temperature
R300	$NH + NH_3$	$\longrightarrow NH_2 + NH_2$	$5.25 \times 10^{-10} \exp(-13470.0/T)$	NIST	1300-1700	
R301	$NH + NO$	$\longrightarrow N_2O + H$	$1.17 \times 10^{-10}(T/298.0)^{-1.03} \exp(-420.0/T)$	NIST	300-4000	
R302	$NH + NO_2$	$\longrightarrow NO + HNO$	$2.1 \times 10^{-13} \exp(1140.2/T)$	NIST	200-300	
R303	$NH + NO_2$	$\longrightarrow OH + N_2O$	$1.4 \times 10^{-13} \exp(1140.2/T)$	NIST	200-300	Low Temperature
R304	$NH + O$	$\longrightarrow NO + H$	1.16×10^{-10}	NIST	250-3000	
R305	$NH + O$	$\longrightarrow OH + N$	1.16×10^{-11}	NIST	250-3000	

Continued on next page ...

No.	Reactants	Products	Reaction Rate^a	Reference	Temperature^b	Note
R306	$NH + O_2$	$\longrightarrow OH + NO$	$6.74 \times 10^{-14}(T/298.0)^{0.79} \exp(-601.4/T)$	NIST	298-2200	
R307	$NH + O_2$	$\longrightarrow O + HNO$	$6.79 \times 10^{-14}(T/298.0)^{2.0} \exp(-3270.2/T)$	NIST	300-3300	
R308	$NH + OH$	$\longrightarrow H + HNO$	3.32×10^{-11}	NIST	298-3000	
R309	$NH + OH$	$\longrightarrow H_2O + N$	$3.1 \times 10^{-12}(T/298.0)^{1.2}$	NIST	298-3000	
R310	$NH_2 + C$	$\longrightarrow CH + NH$	$9.61 \times 10^{-13} \exp(-10500.0/T)$	NIST	1000-4000	
R311	$NH_2 + C_2H_2$	$\longrightarrow C_2H + NH_3$	$8.2 \times 10^{-13} \exp(-2780.0/T)$	NIST	340-510	Low Temperature
R312	$NH_2 + C_2H_4$	$\longrightarrow C_2H_3 + NH_3$	$3.42 \times 10^{-14} \exp(-1320.6/T)$	NIST	250-465	Low Temperature
R313	$NH_2 + C_2H_4O$	$\longrightarrow C_2H_3O + NH_3$	$3.5 \times 10^{-13} \exp(-1250.0/T)$	NIST	297-453	Low Temperature
R314	$NH_2 + C_2H_5$	$\longrightarrow C_2H_6 + NH$	$5.1 \times 10^{-12} \exp(-4678.6/T)$	NIST	300-2000	
R315	$NH_2 + C_2H_6$	$\longrightarrow C_2H_5 + NH_3$	$2.74 \times 10^{-14}(T/298.0)^{3.46} \exp(-2820.0/T)$	NIST	300-2000	
R316	$NH_2 + CH_3$	$\longrightarrow CH_4 + NH$	$8.4 \times 10^{-10} \exp(-4834.9/T)$	NIST	300-2000	
R317	$NH_2 + CH_4$	$\longrightarrow CH_3 + NH_3$	$8.77 \times 10^{-15}(T/298.0)^{3} \exp(-2130.0/T)$	NIST	300-2000	
R318	$NH_2 + CNO$	$\longrightarrow HCNO + NH$	$1.71 \times 10^{-11}(T/298.0)^{1.91} \exp(1039.0/T)$	NIST	1000-3000	High Temperature
R319	$NH_2 + H_2O$	$\longrightarrow OH + NH_3$	$2.1 \times 10^{-13}(T/298.0)^{1.9} \exp(-5725.0/T)$	NIST	300-3000	
R320	$NH_2 + NO$	$\longrightarrow H_2O + N_2$	$4.0 \times 10^{-12} \exp(450.0/T)$	JPL	200-300	Low Temperature
R321	$NH_2 + NO_2$	$\longrightarrow H_2O + N_2O$	$2.1 \times 10^{-12} \exp(650.0/T)$	JPL	200-300	Low Temperature
R322	$NH_2 + O$	$\longrightarrow H + HNO$	7.47×10^{-11}	NIST	298-3000	
R323	$NH_2 + O$	$\longrightarrow OH + NH$	1.16×10^{-11}	NIST	298-3000	
R324	$NH_2 + O$	$\longrightarrow H_2 + NO$	8.3×10^{-12}	NIST	298-3000	
R325	$NH_2 + O_3$	$\longrightarrow H_2O + NO_2$	$4.3 \times 10^{-12} \exp(-930.0/T)$	JPL	200-300	
R326	$NH_2 + OH$	$\longrightarrow H_2O + NH$	$7.69 \times 10^{-13}(T/298.0)^{1.5} \exp(-230.0/T)$	NIST	250-3000	
R327	$NH_3 + CH$	$\longrightarrow HCN + H_2 + H$	$7.24 \times 10^{-11} \exp(317.0/T)$	NIST	300-1300	
R328	$NH_3 + CH_3$	$\longrightarrow CH_4 + NH_2$	$9.55 \times 10^{-14} \exp(-4895.0/T)$	NIST	350-600	Low Temperature
R329	$NH_3 + CN$	$\longrightarrow HCN + NH_2$	1.66×10^{-11}	NIST	300-700	Low Temperature
R330	$NH_3 + CNO$	$\longrightarrow CO + N_2H_3$	$6.29 \times 10^{-14}(T/298.0)^{2.48} \exp(-493.0/T)$	NIST	295-882	
R331	$NO + C$	$\longrightarrow CO + N$	$3.49 \times 10^{-11}(T/298.0)^{-0.02}$	NIST	200-5000	
R332	$NO + C$	$\longrightarrow CN + O$	$5.57 \times 10^{-11}(T/298.0)^{-0.32}$	NIST	200-5000	
R333	$NO + C_2H$	$\longrightarrow HCN + CO$	3.6×10^{-11}	NIST	298	

Continued on next page ...

233

No.	Reactants	Products	Reaction Rate^a	Reference	Temperature^b	Note
R334	$NO + C_2H_3$	$\longrightarrow CH_2O + HCN$	$5.0 \times 10^{-11}(T/298.0)^{-3.38} \exp(-516.0/T)$	NIST	200-2000	
R335	$NO + C_2H_5O$	$\longrightarrow C_2H_4O + HNO$	1.3×10^{-11}	NIST	298	
R336	$NO + C_2HO$	$\longrightarrow CO + HCNO$	$1.4 \times 10^{-11} \exp(320.0/T)$	NIST	296-2000	
R337	$NO + C_2HO$	$\longrightarrow HCN + CO_2$	$6.12 \times 10^{-12}(T/298.0)^{-0.72} \exp(200.0/T)$	NIST	296-2000	
R338	$NO + CH$	$\longrightarrow N + CHO$	1.33×10^{-11}	NIST	298	
R339	$NO + CH$	$\longrightarrow H + CNO$	4.0×10^{-11}	NIST	298	
R340	$NO + CH$	$\longrightarrow CO + NH$	2.5×10^{-10}	NIST	298	
R341	$NO + CH$	$\longrightarrow O + HCN$	1.37×10^{-10}	NIST	298	
R342	$NO + CH$	$\longrightarrow CN + OH$	1.4×10^{-10}	NIST	289	
R343	$NO + CH_2$	$\longrightarrow HCNO + H$	$4.17 \times 10^{-12} \exp(-3007.0/T)$	NIST	1100-2600	High Temperature
R344	$NO + CH_2$	$\longrightarrow HCN + OH$	$8.32 \times 10^{-13} \exp(-1443.0/T)$	NIST	1100-2600	High Temperature
R345	$NO + CH_3$	$\longrightarrow HCN + H_2O$	$4.0 \times 10^{-12} \exp(-7900.0/T)$	NIST	1300-2080	High Temperature
R346	$NO + CH_3O$	$\longrightarrow CH_2O + HNO$	$4.0 \times 10^{-12}(T/298.0)^{-0.7}$	NIST	200-400	Low Temperature
R347	$NO + CH_3O_2$	$\longrightarrow CH_3O + NO_2$	$2.8 \times 10^{-12} \exp(300.0/T)$	JPL	200-300	Low Temperature
R348	$NO + CHO$	$\longrightarrow CO + HNO$	1.2×10^{-11}	NIST	295-2500	
R349	$NO + CN$	$\longrightarrow CO + N_2$	$1.79 \times 10^{-10} \exp(-4040.0/T)$	NIST	687-1500	High Temperature
R350	$NO + CNO$	$\longrightarrow CO + N_2O$	$5.15 \times 10^{-11}(T/298.0)^{-1.34} \exp(-360.0/T)$	NIST	300-3000	
R351	$NO + CNO$	$\longrightarrow CO_2 + N_2$	$1.29 \times 10^{-10}(T/298.0)^{-1.97} \exp(-560.0/T)$	NIST	300-3000	
R352	$NO + CNO$	$\longrightarrow CO + N_2 + O$	$2.78 \times 10^{-11}(T/298.0)^{-1.73} \exp(-380.0/T)$	NIST	300-3000	
R353	$NO + NO_3$	$\longrightarrow NO_2 + NO_2$	$1.5 \times 10^{-11} \exp(170.0/T)$	JPL	200-300	Low Temperature
R354	$NO + O_3$	$\longrightarrow NO_2 + O_2$	$3.0 \times 10^{-12} \exp(-1500.0/T)$	JPL	200-300	Low Temperature
R355	$NO_2 + C$	$\longrightarrow CO + NO$	1.1×10^{-10}	NIST	300	
R356	$NO_2 + C_2H$	$\longrightarrow C_2HO + NO$	$7.6 \times 10^{-11} \exp(130.0/T)$	NIST	288-800	Low Temperature
R357	$NO_2 + C_2H_3$	$\longrightarrow C_2H_3O + NO$	$4.21 \times 10^{-11}(T/298.0)^{-0.6}$	NIST	220-336	Low Temperature
R358	$NO_2 + C_2H_3O$	$\longrightarrow CO_2 + CH_3 + NO$	$7.3 \times 10^{-11} \exp(80.6/T)$	NIST	298-328	Low Temperature
R359	$NO_2 + C_2H_5O$	$\longrightarrow C_2H_4O + HNO_2$	$1.3 \times 10^{-11}(T/298.0)^{-1.0}$	NIST	200-300	Low Temperature
R360	$NO_2 + C_2HO$	$\longrightarrow CO_2 + HCNO$	$9.72 \times 10^{-12} \exp(171.0/T)$	NIST	298-423	Low Temperature
R361	$NO_2 + C_2HO$	$\longrightarrow CO + CHO + NO$	$1.46 \times 10^{-11} \exp(171.0/T)$	NIST	298-423	Low Temperature

Continued on next page ...

234

No.	Reactants	Products	Reaction Rate[a]	Reference	Temperature[b]	Note
R362	$NO_2 + CH$	$\longrightarrow CHO + NO$	1.45×10^{-10}	NIST	298	
R363	$NO_2 + CH_2$	$\longrightarrow CH_2O + NO$	6.91×10^{-11}	NIST	295	
R364	$NO_2 + CH_3$	$\longrightarrow CH_3O + NO$	2.26×10^{-11}	NIST	233-1700	
R365	$NO_2 + CH_3$	$\longrightarrow CH_2O + HNO$	5.4×10^{-12}	NIST	298	
R366	$NO_2 + CH_3O$	$\longrightarrow CH_2O + HNO_2$	$1.1 \times 10^{-11} \exp\left(-1200.0/T\right)$	JPL	200-300	Low Temperature
R367	$NO_2 + CH_4$	$\longrightarrow HNO_2 + CH_3$	$1.58 \times 10^{-9} \exp\left(-19364.0/T\right)$	NIST	600-1100	
R368	$NO_2 + CHO$	$\longrightarrow NO + CHO_2$	2.71×10^{-11}	NIST	296	
R369	$NO_2 + CHO$	$\longrightarrow NO + CO + OH$	4.0×10^{-11}	NIST	298	
R370	$NO_2 + CHO$	$\longrightarrow NO + CO_2 + H$	$1.94 \times 10^{-10}(T/298.0)^{-0.75} \exp\left(-970.0/T\right)$	NIST	294-1650	
R371	$NO_2 + CN$	$\longrightarrow NO + CNO$	$4.0 \times 10^{-11} \exp\left(186.0/T\right)$	NIST	500-2500	
R372	$NO_2 + CN$	$\longrightarrow CO + N_2O$	7.11×10^{-12}	NIST	298	
R373	$NO_2 + CN$	$\longrightarrow CO_2 + N_2$	5.2×10^{-12}	NIST	298	
R374	$NO_2 + CNO$	$\longrightarrow CO_2 + N_2O$	1.64×10^{-11}	NIST	296	
R375	$NO_2 + CNO$	$\longrightarrow CO + NO + NO$	1.3×10^{-12}	NIST	296	
R376	$NO_2 + NO_3$	$\longrightarrow NO + NO_2 + O_2$	$4.5 \times 10^{-14} \exp\left(-1260.0/T\right)$	JPL	200-300	Low Temperature
R377	$NO_2 + O_3$	$\longrightarrow NO_3 + O_2$	$1.2 \times 10^{-13} \exp\left(-2450.0/T\right)$	JPL	200-300	Low Temperature
R378	$NO_3 + C_2H_3O$	$\longrightarrow C_2H_2O + HNO_3$	2.5×10^{-11}	NIST	298	
R379	$NO_3 + C_2H_4O$	$\longrightarrow C_2H_3O + HNO_3$	$1.4 \times 10^{-12} \exp\left(-1900.0/T\right)$	JPL	200-300	Low Temperature
R380	$NO_3 + C_2H_5$	$\longrightarrow C_2H_5O + NO_2$	4.0×10^{-11}	NIST	298	
R381	$NO_3 + CH_3$	$\longrightarrow CH_3O + NO_2$	3.5×10^{-11}	NIST	298	
R382	$NO_3 + CH_3O$	$\longrightarrow CH_3O_2 + NO_2$	1.8×10^{-12}	NIST	298	
R383	$NO_3 + CH_3O$	$\longrightarrow CH_2O + HNO_3$	1.5×10^{-12}	NIST	298	
R384	$NO_3 + CH_3O_2$	$\longrightarrow CH_3O + NO_2 + O_2$	1.3×10^{-12}	NIST	298	
R385	$NO_3 + CH_4O$	$\longrightarrow CH_3O + HNO_3$	$9.4 \times 10^{-13} \exp\left(-2646.0/T\right)$	NIST	258-367	Low Temperature
R386	$NO_3 + HCNO$	$\longrightarrow CO_2 + NO + HNO$	$1.66 \times 10^{-12} \exp\left(-5027.0/T\right)$	NIST	623-773	High Temperature
R387	$NO_3 + NO_3$	$\longrightarrow NO_2 + NO_2 + O_2$	$8.5 \times 10^{-13} \exp\left(-2450.0/T\right)$	JPL	200-300	Low Temperature
R388	$O + C_2$	$\longrightarrow CO + C$	6.0×10^{-10}	NIST	8000	High Temperature
R389	$O + C_2H$	$\longrightarrow CO + CH$	1.7×10^{-11}	NIST	300-2500	

Continued on next page ...

235

No.	Reactants	Products	Reaction Rate[a]	Reference	Temperature[b]	Note
R390	$O + C_2H_2$	$\longrightarrow H + C_2HO$	$1.5 \times 10^{-11} \exp(-2280.0/T)$	NIST	300–2500	
R391	$O + C_2H_2$	$\longrightarrow CO + CH_2$	$3.49 \times 10^{-12}(T/298.0)^{1.5} \exp(-850.0/T)$	NIST	300–2500	
R392	$O + C_2H_2N$	$\longrightarrow CH_2O + CN$	$8.49 \times 10^{-11}(T/298.0)^{0.64}$	NIST	253–353	Low Temperature
R393	$O + C_2H_3$	$\longrightarrow C_2H_3O$	$5.5 \times 10^{-11}(T/298.0)^{0.2} \exp(215.0/T)$	NIST	200–2500	
R394	$O + C_2H_3$	$\longrightarrow C_2H_2 + OH$	$5.5 \times 10^{-11}(T/298.0)^{0.2} \exp(215.0/T)$	NIST	200–2500	
R395	$O + C_2H_3$	$\longrightarrow C_2H_2O + H$	1.6×10^{-10}	NIST	300–2500	
R396	$O + C_2H_4$	$\longrightarrow C_2H_3O + H$	$3.85 \times 10^{-13}(T/298.0)^{1.88} \exp(-91.4/T)$	NIST	300–2000	
R397	$O + C_2H_4$	$\longrightarrow C_2H_3 + OH$	$1.33 \times 10^{-12}(T/298.0)^{1.91} \exp(-1880.0/T)$	NIST	290–1510	
R398	$O + C_2H_4$	$\longrightarrow CH_3 + CHO$	$1.5 \times 10^{-12}(T/298.0)^{1.55} \exp(-215.0/T)$	NIST	300–2500	
R399	$O + C_2H_4$	$\longrightarrow C_2H_2O + H_2$	$5.5 \times 10^{-14}(T/298.0)^{1.88} \exp(-91.4/T)$	NIST	300–2000	
R400	$O + C_2H_4$	$\longrightarrow CH_2O + CH_2$	$8.3 \times 10^{-12} \exp(-754.0/T)$	NIST	226–380	Low Temperature
R401	$O + C_2H_4O$	$\longrightarrow C_2H_3O + OH$	$1.8 \times 10^{-11} \exp(-1100.0/T)$	JPL	200–300	Low Temperature
R402	$O + C_2H_5$	$\longrightarrow C_2H_5O$	$6.3 \times 10^{-11}(T/298.0)^{0.03} \exp(198.45/T)$	NIST	200–2500	
R403	$O + C_2H_5$	$\longrightarrow C_2H_4O + H$	1.33×10^{-10}	NIST	300–2500	
R404	$O + C_2H_5$	$\longrightarrow C_2H_4 + OH$	$6.3 \times 10^{-12}(T/298.0)^{0.03} \exp(198.45/T)$	NIST	200–2500	
R405	$O + C_2H_5$	$\longrightarrow CH_2O + CH_3$	2.67×10^{-11}	NIST	300–2500	
R406	$O + C_2H_6$	$\longrightarrow C_2H_5 + OH$	$8.54 \times 10^{-12}(T/298.0)^{1.5} \exp(-2920.0/T)$	NIST	300–1200	
R407	$O + CH$	$\longrightarrow OH + C$	$2.52 \times 10^{-11} \exp(-2380.0/T)$	NIST	10–6000	
R408	$O + CH$	$\longrightarrow CO + H$	6.6×10^{-11}	NIST	300–2000	
R409	$O + CH_2$	$\longrightarrow CH + OH$	7.2×10^{-12}	NIST	300–2500	
R410	$O + CH_2$	$\longrightarrow CHO + H$	5.0×10^{-11}	NIST	1200–1800	High Temperature
R411	$O + CH_2$	$\longrightarrow CO + H + H$	1.2×10^{-10}	NIST	300–2500	
R412	$O + CH_2$	$\longrightarrow CO + H_2$	7.3×10^{-11}	NIST	300–2500	
R413	$O + CH_2O$	$\longrightarrow CHO + OH$	$1.78 \times 10^{-11}(tl[i]/298.0, 0.57) \exp(-1390.0/T)$	NIST	250–2200	
R414	$O + CH_3$	$\longrightarrow CH_3O$	$7.51 \times 10^{-14}(T/298.0)^{-2.12} \exp(-314.0/T)$	NIST	300–2500	
R415	$O + CH_3$	$\longrightarrow CH_2O + H$	1.4×10^{-10}	NIST	300–2500	
R416	$O + CH_3$	$\longrightarrow CO + H_2 + H$	5.72×10^{-11}	NIST	290–900	
R417	$O + CH_3NO_2$	$\longrightarrow OH + CH_2O + NO$	$2.32 \times 10^{-11} \exp(-2620.0/T)$	NIST	300–410	Low Temperature

Continued on next page ...

236

No.	Reactants	Products	Reaction Rate[a]	Reference	Temperature[b]	Note
R418	$O + CH_3NO_3$	$\longrightarrow OH + CH_2O + NO_2$	$2.49 \times 10^{-11} \exp(-2650.0/T)$	NIST	294-473	Low Temperature
R419	$O + CH_3O$	$\longrightarrow CH_2O + OH$	7.0×10^{-11}	NIST	300-2500	
R420	$O + CH_3O$	$\longrightarrow CH_3 + O_2$	2.5×10^{-11}	NIST	298	
R421	$O_3 + C_2H_2$	$\longrightarrow CO + CH_2O_2$	$1.0 \times 10^{-14} \exp(-4100/T)$	JPL	200-300	Low Temperature
R422	$O + CH_3O_2$	$\longrightarrow CH_3O + O_2$	8.3×10^{-11}	NIST	300-2000	
R423	$O + CH_4$	$\longrightarrow CH_3 + OH$	$2.26 \times 10^{-12}(T/298.0)^{2.2} \exp(-3820.0/T)$	NIST	420-1520	
R424	$O + CH_4O$	$\longrightarrow CH_3O + OH$	$1.66 \times 10^{-11} \exp(-2360.0/T)$	NIST	300-1000	
R425	$O + CH_4O_2$	$\longrightarrow CH_3O_2 + OH$	$3.3 \times 10^{-11} \exp(-2390.0/T)$	NIST	300-1000	
R426	$O + CHO$	$\longrightarrow CO + OH$	5.0×10^{-11}	NIST	300-2500	
R427	$O + CHO$	$\longrightarrow CO_2 + H$	5.0×10^{-11}	NIST	300-2500	
R428	$O + CHO_2$	$\longrightarrow CO_2 + OH$	1.44×10^{-11}	JPL	298	
R429	$O + CN$	$\longrightarrow C + NO$	$5.37 \times 10^{-11} \exp(-13711.0/T)$	NIST	200-5000	
R430	$O + CN$	$\longrightarrow CO + N$	$3.4 \times 10^{-11} \exp(-210.0/T)$	NIST	500-2500	
R431	$O + CNO$	$\longrightarrow CO + NO$	7.5×10^{-11}	NIST	500-2500	
R432	$O + CNO$	$\longrightarrow CN + O_2$	$4.05 \times 10^{-10}(T/298.0)^{-1.43} \exp(-3500.0/T)$	NIST	500-2500	
R433	$O + H_2$	$\longrightarrow H + OH$	$3.44 \times 10^{-13}(T/298.0)^{2.67} \exp(-3160.0/T)$	NIST	300-2500	
R434	$O + H_2O_2$	$\longrightarrow OH + HO_2$	$1.4 \times 10^{-12} \exp(-2000.0/T)$	JPL	200-300	Low Temperature
R435	$O + HCN$	$\longrightarrow H + CNO$	$7.0 \times 10^{-12} \exp(-4000.0/T)$	JPL	470-900	
R436	$O + HCN$	$\longrightarrow CO + NH$	$3.0 \times 10^{-12} \exp(-4000.0/T)$	JPL	470-900	
R437	$O + HCNO$	$\longrightarrow CNO + OH$	$6.16 \times 10^{-13}(T/298.0)^{2.11} \exp(-5750.0/T)$	NIST	500-2500	
R438	$O + HCNO$	$\longrightarrow CO_2 + NH$	$4.93 \times 10^{-13}(T/298.0)^{1.41} \exp(-4290.0/T)$	NIST	500-2500	
R439	$O + HNO$	$\longrightarrow OH + NO$	6.0×10^{-11}	NIST	300-2500	
R440	$O + HNO_4$	$\longrightarrow HNO_3 + O_2$	$7.8 \times 10^{-11} \exp(-3400.0/T)$	JPL	200-300	Low Temperature
R441	$O + HO_2$	$\longrightarrow OH + O_2$	$3.0 \times 10^{-11} \exp(200.0/T)$	JPL	200-300	Low Temperature
R442	$O + NO_2$	$\longrightarrow NO + O_2$	$5.1 \times 10^{-12} \exp(210.0/T)$	JPL	200-300	Low Temperature
R443	$O + NO_3$	$\longrightarrow NO_2 + O_2$	1.0×10^{-11}	JPL	200-300	Low Temperature
R444	$O + O_3$	$\longrightarrow O_2 + O_2$	$8.0 \times 10^{-12} \exp(-2060.0/T)$	JPL	200-300	Low Temperature
R445	$O + OH$	$\longrightarrow O_2 + H$	$2.2 \times 10^{-11} \exp(120.0/T)$	JPL	200-300	Low Temperature

Continued on next page ...

No.	Reactants	Products	Reaction Rate[a]	Reference	Temperature[b]	Note
R446	$O + S_2$	$\longrightarrow S + SO$	1.66×10^{-11}	NIST	298	
R447	$O(^1D) + C_2H_4$	$\longrightarrow C_2H_3 + OH$	2.19×10^{-10}	NIST	298	
R448	$O(^1D) + C_2H_6$	$\longrightarrow C_2H_5 + OH$	6.29×10^{-10}	NIST	300	
R449	$O(^1D) + CH_4$	$\longrightarrow CH_3O + H$	3.5×10^{-11}	JPL	200-300	Low Temperature
R450	$O(^1D) + CH_4$	$\longrightarrow CH_3 + OH$	1.31×10^{-10}	JPL	200-300	Low Temperature
R451	$O(^1D) + CH_4$	$\longrightarrow CH_2O + H_2$	9.0×10^{-12}	JPL	200-300	Low Temperature
R452	$O(^1D) + CH_4O$	$\longrightarrow CH_3O_2 + H$	9.0×10^{-11}	NIST	300	
R453	$O(^1D) + CH_4O$	$\longrightarrow CH_3O + OH$	4.2×10^{-10}	NIST	300	
R454	$O(^1D) + CO_2$	$\longrightarrow CO_2 + O$	$7.5 \times 10^{-11} \exp(115.0/T)$	JPL	200-300	Low Temperature
R455	$O(^1D) + H_2$	$\longrightarrow H + OH$	1.2×10^{-10}	JPL	200-300	Low Temperature
R456	$O(^1D) + H_2O$	$\longrightarrow OH + OH$	$1.63 \times 10^{-10} \exp(60.0/T)$	JPL	200-300	Low Temperature
R457	$O(^1D) + HCNO$	$\longrightarrow CO_2 + NH$	4.6×10^{-11}	NIST	298	
R458	$O(^1D) + N_2$	$\longrightarrow O + N_2$	$2.15 \times 10^{-11} \exp(110.0/T)$	JPL	200-300	Low Temperature
R459	$O(^1D) + N_2O$	$\longrightarrow O_2 + N_2$	$4.63 \times 10^{-11} \exp(20.0/T)$	JPL	200-300	Low Temperature
R460	$O(^1D) + N_2O$	$\longrightarrow NO + NO$	$7.25 \times 10^{-11} \exp(20.0/T)$	JPL	200-300	Low Temperature
R461	$O(^1D) + NH_3$	$\longrightarrow OH + NH_2$	2.5×10^{-10}	JPL	200-300	Low Temperature
R462	$O(^1D) + NO$	$\longrightarrow O_2 + N$	8.5×10^{-11}	NIST	300	
R463	$O(^1D) + NO_2$	$\longrightarrow O_2 + NO$	3.0×10^{-10}	NIST	300	
R464	$O(^1D) + O_2$	$\longrightarrow O + O_2$	$3.3 \times 10^{-11} \exp(55.0/T)$	JPL	200-300	Low Temperature
R465	$O(^1D) + O_3$	$\longrightarrow O_2 + O_2$	1.2×10^{-10}	JPL	200-300	Low Temperature
R466	$O(^1D) + O_3$	$\longrightarrow O_2 + O + O$	1.2×10^{-10}	JPL	200-300	Low Temperature
R467	$O(^1D) + OCS$	$\longrightarrow CO + SO$	3.0×10^{-10}	NIST	300	
R468	$O_3 + C_2H_4$	$\longrightarrow CH_2O + CH_2O_2$	$1.2 \times 10^{-14} \exp(-2630.0/T)$	JPL	178-360	Low Temperature
R469	$O_3 + C_2H_5$	$\longrightarrow C_2H_5O + O_2$	3.32×10^{-14}	NIST	298	
R470	$O_3 + CH_3$	$\longrightarrow CH_3O + O_2$	$5.4 \times 10^{-12} \exp(-220.0/T)$	JPL	200-300	Low Temperature
R471	$O_3 + CH_3O$	$\longrightarrow CH_3O_2 + O_2$	2.53×10^{-14}	NIST	298	
R472	$O_3 + CH_3O_2$	$\longrightarrow CH_3O + O_2 + O_2$	$2.9 \times 10^{-16} \exp(-1000.0/T)$	JPL	200-300	Low Temperature
R473	$OCS + OH$	$\longrightarrow CO_2 + HS$	$1.1 \times 10^{-13} \exp(-1200.0/T)$	JPL	200-300	Low Temperature

Continued on next page ...

238

No.	Reactants	Products	Reaction Rate[a]	Reference	Temperature[b]	Note
R474	$OCS + CH$	$\longrightarrow CHO + CS$	$2.0 \times 10^{-10} \exp(190.0/T)$	NIST	297-667	Low Temperature
R475	$OCS + O$	$\longrightarrow CO + SO$	$2.1 \times 10^{-11} \exp(-2200.0/T)$	JPL	200-300	Low Temperature
R476	$OH + C_2$	$\longrightarrow CO + CH$	8.3×10^{-12}	NIST	2200	High Temperature
R477	$OH + C_2H$	$\longrightarrow CO + CH_2$	3.0×10^{-11}	NIST	300-2500	
R478	$OH + C_2H$	$\longrightarrow C_2H_2 + O$	3.0×10^{-11}	NIST	300-2500	
R479	$OH + C_2H_2$	$\longrightarrow C_2H_2O + H$	$4.12 \times 10^{-13}(T/298.0)^{2.3} \exp(-6790.0/T)$	NIST	500-2500	
R480	$OH + C_2H_2$	$\longrightarrow C_2H + H_2O$	$1.03 \times 10^{-13}(T/298.0)^{2.68} \exp(-6060.0/T)$	NIST	300-2500	
R481	$OH + C_2H_2$	$\longrightarrow C_2HO + H_2$	1.91×10^{-13}	NIST	295	
R482	$OH + C_2H_2$	$\longrightarrow CO + CH_3$	$6.34 \times 10^{-18}(T/298.0)^{4.0} \exp(1010.0/T)$	NIST	500-2500	
R483	$OH + C_2H_2O$	$\longrightarrow CO + CH_3O$	1.0×10^{-11}	NIST	298	
R484	$OH + C_2H_2O$	$\longrightarrow CO_2 + CH_3$	4.98×10^{-12}	NIST	800-1200	High Temperature
R485	$OH + C_2H_3$	$\longrightarrow C_2H_4O$	5.0×10^{-11}	NIST	300-2500	
R486	$OH + C_2H_3$	$\longrightarrow C_2H_2 + H_2O$	5.0×10^{-11}	NIST	300-2500	
R487	$OH + C_2H_3O$	$\longrightarrow C_2H_2O + H_2O$	2.0×10^{-11}	NIST	300-2500	
R488	$OH + C_2H_4$	$\longrightarrow C_2H_3 + H_2O$	$1.66 \times 10^{-13}(T/298.0)^{2.75} \exp(-2100.0/T)$	NIST	300-2500	
R489	$OH + C_2H_4O$	$\longrightarrow C_2H_3O + H_2O$	$4.4 \times 10^{-12} \exp(364.0/T)$	NIST	200-350	Low Temperature
R490	$OH + C_2H_5$	$\longrightarrow C_2H_4 + H_2O$	4.0×10^{-11}	NIST	300-2500	
R491	$OH + C_2H_6$	$\longrightarrow C_2H_5 + H_2O$	$8.7 \times 10^{-12} \exp(-1070.0/T)$	JPL	200-300	Low Temperature
R492	$OH + CH_2$	$\longrightarrow CH_2O + H$	3.0×10^{-11}	NIST	300-2500	
R493	$OH + CH_2O$	$\longrightarrow CHO + H_2O$	$5.5 \times 10^{-12} \exp(125.0/T)$	JPL	200-300	Low Temperature
R494	$OH + CH_2O_2$	$\longrightarrow CHO_2 + H_2O$	4.0×10^{-13}	JPL	200-300	Low Temperature
R495	$OH + CH_3$	$\longrightarrow CH_3O + H$	$6.45 \times 10^{-13}(T/298.0)^{1.0} \exp(-6012.0/T)$	NIST	300-3000	High Temperature
R496	$OH + CH_3$	$\longrightarrow CH_2 + H_2O$	$7.13 \times 10^{-20}(T)^{2.568} \exp(-2012.0/T)$	NIST	300-1000	
R497	$OH + CH_3$	$\longrightarrow CH_2O + H_2$	$0;$	NIST	600-2500	High Temperature
R498	$OH + CH_3NO_3$	$\longrightarrow CH_2O + NO_2 + H_2O$	$8.0 \times 10^{-13} \exp(-1000.0/T)$	JPL	200-300	Low Temperature
R499	$OH + CH_3O$	$\longrightarrow CH_2O + H_2O$	3.0×10^{-11}	NIST	300-2500	
R500	$OH + CH_3O_2$	$\longrightarrow CH_4O + O_2$	1.0×10^{-10}	NIST	300-2500	
R501	$OH + CH_4$	$\longrightarrow CH_3 + H_2O$	$2.45 \times 10^{-12} \exp(-1775.0/T)$	JPL	200-300	Low Temperature

Continued on next page ...

No.	Reactants	Products	Reaction Rate[a]	Reference	Temperature[b]	Note
R502	$OH + CH_4O$	$\longrightarrow CH_3O + H_2O$	$2.9 \times 10^{-12} \exp(-345.0/T)$	JPL	200-300	Low Temperature
R503	$OH + CH_4O_2$	$\longrightarrow CH_3O_2 + H_2O$	$3.8 \times 10^{-12} \exp(200.0/T)$	JPL	200-300	Low Temperature
R504	$OH + CHO$	$\longrightarrow CO + H_2O$	1.69×10^{-10}	NIST	300-2500	
R505	$OH + CHO_2$	$\longrightarrow CO_2 + H_2O$	1.0×10^{-10}	NIST	300	
R506	$OH + CN$	$\longrightarrow H + CNO$	7.0×10^{-11}	NIST	500-2500	
R507	$OH + CN$	$\longrightarrow O + HCN$	$1.0 \times 10^{-11} \exp(-1000.0/T)$	NIST	500-2500	
R508	$OH + CNO$	$\longrightarrow CHO + NO$	4.0×10^{-13}	NIST	1500	High Temperature
R509	$OH + CNO$	$\longrightarrow HCNO + O$	$5.38 \times 10^{-14}(T/298.0)^{2.27} \exp(-497.0/T)$	NIST	500-2500	
R510	$OH + CNO$	$\longrightarrow CO + NO + H$	9.3×10^{-15}	NIST	1000	High Temperature
R511	$OH + CO$	$\longrightarrow CO_2 + H$	$5.4 \times 10^{-14}(T/298.0)^{1.5} \exp(250.0/T)$	NIST	300-2000	
R512	$OH + H_2$	$\longrightarrow H_2O + H$	$2.8 \times 10^{-12} \exp(-1800.0/T)$	JPL	200-300	Low Temperature
R513	$OH + H_2O_2$	$\longrightarrow H_2O + HO_2$	$2.9 \times 10^{-12} \exp(-160.0/T)$	JPL	200-300	Low Temperature
R514	$OH + HCN$	$\longrightarrow HCNO + H$	$4.65 \times 10^{-11} \exp(-1860.0/T)$	NIST	1500-2400	High Temperature
R515	$OH + HCN$	$\longrightarrow CO + NH_2$	$1.1 \times 10^{-13} \exp(-5890.0/T)$	NIST	500-2500	
R516	$OH + HCN$	$\longrightarrow CN + H_2O$	$1.84 \times 10^{-13}(T/298.0)^{1.5} \exp(-3890.0/T)$	NIST	298-2840	
R517	$OH + HCNO$	$\longrightarrow CNO + H_2O$	$9.43 \times 10^{-14}(T/298.0)^2 \exp(-1290.0/T)$	NIST	500-2500	
R518	$OH + HCNO$	$\longrightarrow CO_2 + NH_2$	$1.54 \times 10^{-14}(T/298.0)^{1.5} \exp(-1810.0/T)$	NIST	1250-1860	High Temperature
R519	$OH + HNO$	$\longrightarrow H_2O + NO$	$8.0 \times 10^{-11} \exp(-500.0/T)$	NIST	300-2000	
R520	$OH + HNO_2$	$\longrightarrow H_2O + NO_2$	$1.8 \times 10^{-11} \exp(-390.0/T)$	JPL	200-300	Low Temperature
R521	$OH + HNO_4$	$\longrightarrow H_2O + NO_2 + O_2$	$1.3 \times 10^{-12} \exp(380.0/T)$	JPL	200-300	Low Temperature
R522	$OH + HO_2$	$\longrightarrow H_2O + O_2$	$4.8 \times 10^{-11} \exp(250.0/T)$	JPL	200-300	Low Temperature
R523	$OH + NH_3$	$\longrightarrow H_2O + NH_2$	$1.7 \times 10^{-12} \exp(-710.0/T)$	JPL	200-300	Low Temperature
R524	$OH + NO_3$	$\longrightarrow HO_2 + NO_2$	2.0×10^{-11}	NIST	298	
R525	$OH + O_3$	$\longrightarrow HO_2 + O_2$	$1.7 \times 10^{-12} \exp(-940.0/T)$	JPL	200-300	Low Temperature
R526	$OH + OH$	$\longrightarrow H_2O + O$	1.8×10^{-12}	JPL	200-300	Low Temperature
R527	$OH + S$	$\longrightarrow H + SO$	6.6×10^{-11}	JPL	298	
R528	$OH + SO$	$\longrightarrow SO_2 + H$	$2.7 \times 10^{-11} \exp(355.0/T)$	JPL	200-300	Low Temperature
R529	$S + C_2H_6$	$\longrightarrow C_2H_5 + HS$	$2.04 \times 10^{-10} \exp(-7420.0/T)$	NIST	880-1150	High Temperature

Continued on next page ...

No.	Reactants	Products	Reaction Rate[a]	Reference	Temperature[b]	Note
R530	$S + CH_4$	$\longrightarrow CH_3 + HS$	$3.4 \times 10^{-10} \exp(-10000.0/T)$	NIST	1140-1480	High Temperature
R531	$S + H_2$	$\longrightarrow H + HS$	$2.24 \times 10^{-10} \exp(-9710.0/T)$	NIST	910-1660	High Temperature
R532	$S + H_2S$	$\longrightarrow HS + HS$	$1.38 \times 10^{-10} \exp(-3720.0/T)$	NIST	1050-1540	High Temperature
R533	$S + HS$	$\longrightarrow H + S_2$	4.0×10^{-11}	NIST	295	
R534	$S + NO$	$\longrightarrow SO + N$	$1.75 \times 10^{-10} \exp(-20206.0/T)$	NIST	2420-3870	
R535	$S + NO_2$	$\longrightarrow NO + SO$	$4.9 \times 10^{-11} \exp(84.2/T)$	NIST	296-410	Low Temperature
R536	$S + O_2$	$\longrightarrow SO + O$	2.3×10^{-12}	JPL	200-300	Low Temperature
R537	$S + O_3$	$\longrightarrow O_2 + SO$	1.2×10^{-11}	JPL	298	
R538	$S + OCS$	$\longrightarrow CO + S_2$	$1.5 \times 10^{-12} \exp(-1260.0/T)$	NIST	300-2570	
R539	$S + SO_2$	$\longrightarrow SO + SO$	$9.77 \times 10^{-12} \exp(-4546.0/T)$	NIST	1120-1540	High Temperature
R540	$CS + O_2$	$\longrightarrow OCS + O$	2.9×10^{-19}	JPL	298	
R541	$SO + NO_2$	$\longrightarrow SO_2 + NO$	1.4×10^{-11}	JPL	200-300	Low Temperature
R542	$CS + NO_2$	$\longrightarrow OCS + NO$	7.6×10^{-17}	JPL	298	
R543	$SO + CHO$	$\longrightarrow HSO + CO$	$5.5 \times 10^{-11}(T)^{-0.4}$	Kasting (1990)		Low Temperature
R544	$SO + O_2$	$\longrightarrow SO_2 + O$	$1.25 \times 10^{-13} \exp(-2190.0/T)$	JPL	200-300	Low Temperature
R545	$SO + O_3$	$\longrightarrow SO_2 + O_2$	$3.4 \times 10^{-12} \exp(-1100.0/T)$	JPL	200-300	Low Temperature
R546	$SO_2 + C_2H$	$\longrightarrow CO + OCS + H$	1.1×10^{-11}	NIST	298	
R547	$SO_2 + CH$	$\longrightarrow CHO + SO$	$1.32 \times 10^{-10} \exp(250.0/T)$	NIST	295-665	Low Temperature
R548	$SO_2 + CH_2$	$\longrightarrow CH_2O + SO$	4.9×10^{-12}	NIST	295	
R549	$SO_2 + CN$	$\longrightarrow CNO + SO$	4.4×10^{-12}	NIST	298	
R550	$SO_2 + H$	$\longrightarrow OH + SO$	$4.58 \times 10^{-8}(T/298.0)^{-2.3} \exp(-15635.0/T)$	NIST	900-1800	High Temperature
R551	$SO_2 + HO_2$	$\longrightarrow HSO_2 + O_2$	$8.6 \times 10^{-10} \exp(-5230.0/T)$	NIST	400-2000	
R552	$SO_2 + NO_2$	$\longrightarrow SO_3 + NO$	$1.05 \times 10^{-11} \exp(-13591.0/T)$	NIST	703-1850	
R553	$SO_2 + O$	$\longrightarrow SO + O_2$	$8.3 \times 10^{-12} \exp(-9800.0/T)$	NIST	440-3000	
R554	$SO_3 + H$	$\longrightarrow OH + SO_2$	$1.46 \times 10^{-11}(T/298.0)^{1.22} \exp(-1672.0/T)$	NIST	700-2000	
R555	$SO_3 + O$	$\longrightarrow SO_2 + O_2$	$1.06 \times 10^{-13}(T/298.0)^{2.57} \exp(-14673.0/T)$	NIST	1000-2000	
R556	$SO_3 + OH$	$\longrightarrow HO_2 + SO_2$	$9.73 \times 10^{-14}(T/298.0)^{2.46} \exp(-13711.0/T)$	NIST	800-2000	
R557	$SO_3 + SO$	$\longrightarrow SO_2 + SO_2$	2.0×10^{-15}	NIST	298	

Continued on next page ...

No.	Reactants	Products	Reaction Rate[a]	Reference	Temperature[b]	Note
R558	$HSO + O_2$	$\longrightarrow OH + SO_2$	1.69×10^{-15}	NIST	298	
R559	$SO + SO$	$\longrightarrow SO_2 + S$	3.5×10^{-15}	NIST	298	
R560	$HS + H$	$\longrightarrow H_2 + S$	2.16×10^{-11}	NIST	295	
R561	$CHO + CHO$	$\longrightarrow CH_2O + CO$	3.0×10^{-11}	NIST	300-2500	
R562	$^1SO_2 + O_2$	$\longrightarrow O + SO_3$	1.0×10^{-16}	Turco et al. (1982)		Low Temperature
R563	$^1SO_2 + SO_2$	$\longrightarrow SO + SO_3$	4.0×10^{-12}	Turco et al. (1982)		Low Temperature
R564	$^3SO_2 + SO_2$	$\longrightarrow SO + SO_3$	7.0×10^{-14}	Turco et al. (1982)		Low Temperature
R565	$SO_3 + H_2O$	$\longrightarrow H_2SO_4$	1.2×10^{-15}	NIST	298	
R566	$HSO_3 + OH$	$\longrightarrow H_2O + SO_3$	1.0×10^{-11}	Kasting (1990)		Low Temperature
R567	$HSO_3 + H$	$\longrightarrow H_2 + SO_3$	1.0×10^{-11}	Kasting (1990)		Low Temperature
R568	$NO_2 + CHO$	$\longrightarrow CO + HNO_2$	$3.49 \times 10^{-24}(T/298.0)^{3.29} \exp(-1180.0/T)$	NIST	294-1650	
R569	$S + CHO$	$\longrightarrow HS + CO$	5.0×10^{-11}	Kasting (1990)		Low Temperature
R570	$S + HO_2$	$\longrightarrow HS + O_2$	1.5×10^{-11}	Kasting (1990)		Low Temperature
R571	$S + HO_2$	$\longrightarrow SO + OH$	1.5×10^{-11}	Kasting (1990)		Low Temperature
R572	$S + CO_2$	$\longrightarrow SO + CO$	1.0×10^{-20}	Yung & Demore (1999)		Low Temperature
R573	$HSO + NO$	$\longrightarrow HNO + SO$	$3.7 \times 10^{-12} \exp(250.0/T)$	Kasting (1990)		Low Temperature
R574	$HSO + OH$	$\longrightarrow H_2O + SO$	$4.8 \times 10^{-11} \exp(250.0/T)$	Kasting (1990)		Low Temperature
R575	$HSO + H$	$\longrightarrow HS + OH$	7.29×10^{-11}	Kasting (1990)		Low Temperature
R576	$HSO + H$	$\longrightarrow H_2 + SO$	6.48×10^{-12}	Kasting (1990)		Low Temperature
R577	$HSO + HS$	$\longrightarrow H_2S + SO$	1.0×10^{-12}	Kasting (1990)		Low Temperature
R578	$HSO + O$	$\longrightarrow OH + SO$	$3.0 \times 10^{-11} \exp(200.0/T)$	Kasting (1990)		Low Temperature
R579	$HSO + S$	$\longrightarrow HS + SO$	1.0×10^{-11}	Kasting (1990)		Low Temperature
R580	$H + C_3H_4^2$	$\longrightarrow H + C_3H_4^1$	$1.0 \times 10^{-11} \exp(-1000.0/T)$	Yung & Demore (1999)		Low Temperature
R581	$H + C_3H_5$	$\longrightarrow C_3H_4^1 + H_2$	6.0×10^{-12}	Yung & Demore (1999)		Low Temperature
R582	$H + C_3H_5$	$\longrightarrow C_3H_4^2 + H_2$	6.0×10^{-12}	Yung & Demore (1999)		Low Temperature
R583	$H + C_3H_5$	$\longrightarrow CH_4 + C_2H_2$	6.0×10^{-12}	Yung & Demore (1999)		Low Temperature
R584	$H + C_3H_6$	$\longrightarrow C_3H_5 + H_2$	$4.4 \times 10^{-13}(T/298.0)^{2.5} \exp(-1250.0/T)$	NIST	300-2500	
R585	$H + C_3H_7$	$\longrightarrow C_3H_6 + H_2$	5.0×10^{-11}	Yung & Demore (1999)		Low Temperature

Continued on next page ...

242

No.	Reactants	Products	Reaction Rate[a]	Reference	Temperature[b]	Note
R586	$H + C_3H_7$	$\longrightarrow C_2H_5 + CH_3$	6.0×10^{-11}	Yung & Demore (1999)		Low Temperature
R587	$H + C_4H_3$	$\longrightarrow C_2H_2 + C_2H_2$	3.3×10^{-12}	Yung & Demore (1999)		Low Temperature
R588	$H + C_4H_3$	$\longrightarrow C_4H_2 + H_2$	6.0×10^{-12}	Yung & Demore (1999)		Low Temperature
R589	$H + C_4H_5$	$\longrightarrow C_4H_4 + H_2$	6.0×10^{-12}	Yung & Demore (1999)		Low Temperature
R590	$H + C_4H_9$	$\longrightarrow C_4H_8 + H_2$	1.5×10^{-12}	NIST	300-2500	
R591	$H + C_6H_3$	$\longrightarrow C_2H_2 + C_4H_2$	3.3×10^{-12}	Yung & Demore (1999)		Low Temperature
R592	$H + C_6H_3$	$\longrightarrow C_6H_2 + H_2$	6.0×10^{-12}	Yung & Demore (1999)		Low Temperature
R593	$CH + C_2H_2$	$\longrightarrow C_3H_2 + H$	$3.5 \times 10^{-10} \exp(61.0/T)$	Yung & Demore (1999)		Low Temperature
R594	$CH + C_2H_4$	$\longrightarrow C_3H_4^2 + H$	$2.23 \times 10^{-10} \exp(173.0/T)$	Yung & Demore (1999)		Low Temperature
R595	$CH + C_2H_6$	$\longrightarrow C_3H_6 + H$	$1.8 \times 10^{-10} \exp(132.0/T)$	Yung & Demore (1999)		Low Temperature
R596	$CH_2^1 + H_2$	$\longrightarrow CH_2 + H_2$	1.26×10^{-11}	Yung & Demore (1999)		Low Temperature
R597	$CH_2^1 + H_2$	$\longrightarrow CH_3 + H$	9.24×10^{-11}	Yung & Demore (1999)		Low Temperature
R598	$CH_2^1 + CH_4$	$\longrightarrow CH_2 + CH_4$	1.2×10^{-11}	Yung & Demore (1999)		Low Temperature
R599	$CH_2^1 + CH_4$	$\longrightarrow CH_3 + CH_3$	5.9×10^{-11}	Yung & Demore (1999)		Low Temperature
R600	$CH_2 + C_2H_2$	$\longrightarrow C_3H_2 + H_2$	$1.0 \times 10^{-10} \exp(-3332.0/T)$	Yung & Demore (1999)		Low Temperature
R601	$CH_2 + C_2H_2$	$\longrightarrow C_3H_3 + H$	$1.0 \times 10^{-10} \exp(-3332.0/T)$	Yung & Demore (1999)		Low Temperature
R602	$CH_3 + C_2H_3$	$\longrightarrow C_3H_5 + H$	6.5×10^{-13}	Yung & Demore (1999)		Low Temperature
R603	$CH_3 + C_3H_5$	$\longrightarrow CH_4 + C_3H_4^1$	6.5×10^{-13}	Yung & Demore (1999)		Low Temperature
R604	$CH_3 + C_3H_5$	$\longrightarrow CH_4 + C_3H_4^2$	6.5×10^{-13}	Yung & Demore (1999)		Low Temperature
R605	$CH_3 + C_3H_7$	$\longrightarrow CH_4 + C_3H_6$	$1.85 \times 10^{-12} \exp(339.0/T)$	Yung & Demore (1999)		Low Temperature
R606	$CH_3 + C_3H_8$	$\longrightarrow CH_4 + C_3H_7$	$1.3 \times 10^{-24}(T)^{4.0} \exp(-4175.0/T)$	Yung & Demore (1999)		Low Temperature
R607	$CH_3 + C_4H_5$	$\longrightarrow CH_4 + C_4H_4$	6.5×10^{-13}	Yung & Demore (1999)		Low Temperature
R608	$C_2 + CH_4$	$\longrightarrow C_2H + CH_3$	$5.5 \times 10^{-11} \exp(-297.0/T)$	Yung & Demore (1999)		Low Temperature
R609	$C_2H + C_2H_2$	$\longrightarrow C_4H_2 + H$	$1.25 \times 10^{-10}(T/298.0)^{0.24} \exp(37.3/T)$	NIST	200-2000	
R610	$C_2H + C_2H_4$	$\longrightarrow C_4H_4 + H$	2.0×10^{-11}	NIST	300-2500	
R611	$NO + CN$	$\longrightarrow CNO + N$	$1.6 \times 10^{-10} \exp(-21168.0/T)$	NIST	500-2500	
R612	$C_2H + C_3H_8$	$\longrightarrow C_2H_2 + C_3H_7$	6.0×10^{-12}	NIST	300-2500	
R613	$C_2H + C_4H_2$	$\longrightarrow C_6H_2 + H$	1.5×10^{-10}	Yung & Demore (1999)		Low Temperature

Continued on next page ...

243

No.	Reactants	Products	Reaction Rate[a]	Reference	Temperature[b]	Note
R614	$C_2H + C_4H_{10}$	$\longrightarrow C_2H_2 + C_4H_9$	1.0×10^{-11}	NIST	300-2500	
R615	$C_2H + C_6H_2$	$\longrightarrow C_8H_2 + H$	3.75×10^{-12}	Yung & Demore (1999)		Low Temperature
R616	$C_2H + C_8H_2$	$\longrightarrow$ Haze	3.75×10^{-12}	Yung & Demore (1999)		Low Temperature
R617	$C_2H_3 + C_2H_3$	$\longrightarrow C_2H_4 + C_2H_2$	1.8×10^{-11}	Yung & Demore (1999)		Low Temperature
R618	$C_2H_5 + C_2H_5$	$\longrightarrow C_2H_6 + C_2H_4$	$1.2 \times 10^{-11} \exp(-540.0/T)$	Yung & Demore (1999)		Low Temperature
R619	$C_3H_2 + C_2H_2$	$\longrightarrow C_4H_2 + CH_2$	5.0×10^{-13}	Yung & Demore (1999)		Low Temperature
R620	$C_3H_3 + C_2H_2$	$\longrightarrow C_4H_2 + CH_3$	2.0×10^{-13}	Yung & Demore (1999)		Low Temperature
R621	$C_3H_5 + H_2$	$\longrightarrow C_3H_6 + H$	$1.39 \times 10^{-13}(T/298.0)^{2.38} \exp(-9560.0/T)$	NIST	300-2500	
R622	$C_3H_7 + H_2$	$\longrightarrow C_3H_8 + H$	$3.19 \times 10^{-14}(T/298.0)^{2.84} \exp(-4600.0/T)$	NIST	300-2500	
R623	$C_4H + H_2$	$\longrightarrow C_4H_2 + H$	$6.3 \times 10^{-12} \exp(-1450.0/T)$	Yung & Demore (1999)		Low Temperature
R624	$C_4H + CH_4$	$\longrightarrow C_4H_2 + CH_3$	$9.0 \times 10^{-12} \exp(-250.0/T)$	Yung & Demore (1999)		Low Temperature
R625	$C_4H + C_2H_2$	$\longrightarrow C_6H_2 + H$	1.5×10^{-10}	Yung & Demore (1999)		Low Temperature
R626	$C_4H + C_2H_6$	$\longrightarrow C_4H_2 + C_2H_5$	2.1×10^{-11}	Yung & Demore (1999)		Low Temperature
R627	$C_4H + C_4H_2$	$\longrightarrow C_8H_2 + H$	3.75×10^{-12}	Yung & Demore (1999)		Low Temperature
R628	$C_4H + C_6H_2$	$\longrightarrow$ Haze	3.75×10^{-12}	Yung & Demore (1999)		Low Temperature
R629	$C_4H + C_8H_2$	$\longrightarrow$ Haze	3.75×10^{-12}	Yung & Demore (1999)		Low Temperature
R630	$C_4H_5 + H_2$	$\longrightarrow C_4H_6^1 + H$	$1.8 \times 10^{-11} \exp(-1699/T)$	Yung & Demore (1999)		Low Temperature
R631	$C_4H_5 + C_2H_2$	$\longrightarrow C_6H_6 + H$	$3.0 \times 10^{-12} \exp(-1861/T)$	Yung & Demore (1999)		Low Temperature
R632	$C_6H + H_2$	$\longrightarrow C_6H_2 + H$	$6.3 \times 10^{-12} \exp(-1450.0/T)$	Yung & Demore (1999)		Low Temperature
R633	$C_6H + CH_4$	$\longrightarrow C_6H_2 + CH_3$	$9.0 \times 10^{-12} \exp(-250.0/T)$	Yung & Demore (1999)		Low Temperature
R634	$C_6H + C_2H_2$	$\longrightarrow C_8H_2 + H$	3.75×10^{-12}	Yung & Demore (1999)		Low Temperature
R635	$C_6H + C_2H_6$	$\longrightarrow C_6H_2 + C_2H_5$	2.1×10^{-11}	Yung & Demore (1999)		Low Temperature
R636	$C_6H + C_4H_2$	$\longrightarrow$ Haze	3.75×10^{-12}	Yung & Demore (1999)		Low Temperature
R637	$C_6H + C_6H_2$	$\longrightarrow$ Haze	3.75×10^{-12}	Yung & Demore (1999)		Low Temperature
R638	$C_6H + C_8H_2$	$\longrightarrow$ Haze	3.75×10^{-12}	Yung & Demore (1999)		Low Temperature
R639	$N_2H_4 + H$	$\longrightarrow N_2H_3 + H_2$	$1.17 \times 10^{-11} \exp(-1260.0/T)$	NIST	222-657	Low Temperature
R640	$NO_2 + CH_3$	$\longrightarrow CH_3NO_2$	$3.44 \times 10^{-11}(T/298.0)^{-0.6}$	NIST	300-1400	
R641	$N_2H_3 + H$	$\longrightarrow NH_2 + NH_2$	2.66×10^{-12}	NIST	300	

Continued on next page …

244

No.	Reactants	Products	Reaction Rate[a]	Reference	Temperature[b]	Note
R642	$N_2H_3 + N_2H_3$	$\longrightarrow N_2H_4 + N_2H_2$	1.9×10^{-11}	NIST	298	
R643	$N_2H_3 + N_2H_3$	$\longrightarrow NH_3 + NH_3 + N_2$	5.0×10^{-12}	NIST	423	
R644	$NH_2 + OH$	$\longrightarrow NH_3 + O$	$3.32 \times 10^{-13}(T/298.0)^{0.4}\exp(-250.2/T)$	NIST	250-3000	
R645	$O_2 + CHO_2$	$\longrightarrow HO_2 + CO_2$	2.0×10^{-12}	NIST	220-430	Low Temperature
M1	$C + C$	$\longrightarrow C_2$	$5.46 \times 10^{-31}(T/298.0)^{-1.6} \times N$	NIST	5000-6000	High Temperature
M2	$C + H_2$	$\longrightarrow CH_2$	$k_0 = 7.0 \times 10^{-32}$ $k_\infty = 2.06 \times 10^{-11}\exp(-57.0/T)$	NIST	300	
M3	$CH_3 + CH_3$	$\longrightarrow C_2H_6$	$k_0 = 1.68 \times 10^{-24}(T/298.0)^{-7.0}\exp(-1390.0/T)$ $k_\infty = 1.12 \times 10^{-9}T^{-0.5}\exp(-25.0/T)$ $F_c = 0.62\exp(-T/1180.0) + 0.38\exp(-T/73.0)$	Moses et al. (2012)	300-2000	
M4	$CH_3 + O_2$	$\longrightarrow CH_3O_2$	$k_0 = 4.0 \times 10^{-31}(T/300.0)^{-3.6}$ $k_\infty = 1.2 \times 10^{-12}(T/300.0)^{1.1}$	JPL	200-300	Low Temperature
M5	$CO + CH$	$\longrightarrow C_2HO$	$k_0 = 4.1 \times 10^{-30}(T/298.0)^{-2.1}$ $k_\infty = 3.0 \times 10^{-11}(T/298.0)^{-0.9}$	NIST	53-584	Low Temperature
M6	$CO + CH_3$	$\longrightarrow C_2H_3O$	$k_0 = 3.0 \times 10^{-34}\exp(-1910.0/T)$ $K_\infty = 8.4 \times 10^{-13}\exp(-3460.0/T)$	NIST	300-1700	
M7	$H + C_2H_2$	$\longrightarrow C_2H_3$	$k_0 = 3.3 \times 10^{-30}\exp(-740.0/T)$ $k_\infty = 1.4 \times 10^{-11}\exp(-1300.0/T)$ $k_0 = 3.8 \times 10^{-8}T^{-7.3}\exp(-3633.0/T)$ $k_\infty = 7.5 \times 10^{-15}T^{-1.5}\exp(-1300.0/T)$ $F_c = 0.44$	NIST	$T < 400$ K $T < 400$ K $T > 400$ K $T > 400$ K	
M8	$H + C_2H_2O$	$\longrightarrow C_2H_3O$	$k_0 = 1.38 \times 10^{-30}$ $k_\infty = 2.66 \times 10^{-11}\exp(-755.3/T)$	NIST	1000-1700	High Temperature
M9	$H + C_2H_4$	$\longrightarrow C_2H_5$	$k_0 = 7.69 \times 10^{-30}\exp(-380.0/T)$ $k_\infty = 9.68 \times 10^{-12}(T/298.0)^{1.28}\exp(-650.0/T)$ $F_c = 0.24\exp(-T/4.0) + 0.76\exp(-T/1025.0)$	Moses et al. (2012)	300-800	
M10	$H + CHO$	$\longrightarrow CH_2O$	$3.21 \times 10^{-30}(T/298.0)^{-2.57}\exp(-215.0/T) \times N$	NIST	1560-2270	
M11	$H + CN$	$\longrightarrow HCN$	$9.35 \times 10^{-30}(T/298.0)^{-2.0}\exp(-521.0/T)$			

Continued on next page ...

245

No.	Reactants	Products	Reaction Rate[a]	Reference	Temperature[b]	Note
M12	$H + CO$	$\longrightarrow CHO$	$k_\infty = 1.73 \times 10^{-10}(T/298.0)^{-0.5}$; $k_0 = 5.29 \times 10^{-34} \exp(-370.0/T)$	NIST	500-2500	
M13	$H + H$	$\longrightarrow H_2$	$k_\infty = 1.96 \times 10^{-13} \exp(-1370.0/T)$; $6.04 \times 10^{-33}(T/298.0)^{-1.0} \times N$	NIST	300-2500	
M14	$H + NH_2$	$\longrightarrow NH_3$	$k_0 = 5.33 \times 10^{-25} T^{-2.0}$; $k_\infty = 2.66 \times 10^{-11}$	NIST	300-2500	
M15	$H + NO$	$\longrightarrow HNO$	$k_0 = 2.44 \times 10^{-10}(T/298.0)^{-0.41}$; $k_\infty = 1.34 \times 10^{-31}(T/298.0)^{-1.32} \exp(-370.5/T)$	NIST	298	
M16	$H + O$	$\longrightarrow OH$	$K_0 = 4.36 \times 10^{-32}(T/298.0)^{-1.0}$; $k_\infty = 1.0 \times 10^{-11}$	NIST	230-4200	
M17	$H + O_2$	$\longrightarrow HO_2$	$k_0 = 4.4 \times 10^{-32}(T/300.0)^{-1.3}$; $k_\infty = 7.5 \times 10^{-11}(T/300.0)^{0.2}$	NIST	300-2500	
M18	$H + OH$	$\longrightarrow H_2O$	$k_0 = 6.87 \times 10^{-31}(T/298.0)^{-2.0}$; $k_\infty = 1.58 \times 10^{-10}(T/298.0)^{0.23} \exp(57.7/T)$	JPL	200-300	Low Temperature
M19	$HO_2 + HO_2$	$\longrightarrow H_2O_2 + O_2$	$k_0 = 1.7 \times 10^{-33} \exp(1000.0/T)$; $k_\infty = 2.3 \times 10^{-13} \exp(600.0/T)$	NIST	300-3000	
M20	$HO_2 + NO_2$	$\longrightarrow HNO_4$	$k_0 = 2.0 \times 10^{-31}(T/300.0)^{-3.4}$; $k_\infty = 2.9 \times 10^{-12}(T/300.0)^{-1.1}$	JPL	200-300	Low Temperature
M21	$HS + O_2$	$\longrightarrow HSO_2$	$k_0 = 9.18 \times 10^{-34}(T/298.0)^{-1.69}$; $k_\infty = 2.01 \times 10^{-10}(T/298.0)^{0.31}$	JPL	200-300	Low Temperature
M22	$N + C$	$\longrightarrow CN$	$9.4 \times 10^{-33} \times N$	NIST	200-400	Low Temperature
M23	$N + H$	$\longrightarrow NH$	$5.0 \times 10^{-32} \times N$	NIST	298	
M24	$N + H_2$	$\longrightarrow NH_2$	$k_0 = 8.3 \times 10^{-38}$; $k_\infty = 1.94 \times 10^{-20}$	NIST	298	
M25	$N + N$	$\longrightarrow N_2$	$1.38 \times 10^{-33} \exp(502.7/T) \times N$	JPL	298	
M26	$N + O$	$\longrightarrow NO$	$5.46 \times 10^{-33}(T/298.0)^{-1.29} \times N$	NIST	90-6400	Low Temperature
M27	$NO + CH_3O$	$\longrightarrow CH_3NO_2$	$k_0 = 2.3 \times 10^{-29}(T/300.0)^{-2.8}$; $k_\infty = 3.8 \times 10^{-11}(T/300.0)^{-0.6}$	JPL	196-297 / 200-300	Low Temperature

Continued on next page ...

246

No.	Reactants	Products	Reaction Rate[a]	Reference	Temperature[b]	Note
M28	$NO_2 + CH_3O$	$\longrightarrow CH_3NO_3$	$k_0 = 5.3 \times 10^{-29}(T/300.0)^{-4.4}$ $k_\infty = 1.9 \times 10^{-11}(T/300.0)^{-1.8}$	JPL	200-300	Low Temperature
M29	$NO_2 + NO_3$	$\longrightarrow N_2O_5$	$k_0 = 2.0 \times 10^{-30}(T/300.0)^{-4.4}$ $k_\infty = 1.4 \times 10^{-12}(T/300.0)^{-0.7}$	JPL	200-300	Low Temperature
M30	$O + C$	$\longrightarrow CO$	$2.0 \times 10^{-34} \times N$	NIST	8000	High Temperature
M31	$O + CO$	$\longrightarrow CO_2$	$k_0 = 1.7 \times 10^{-33} \exp(-1509.0/T)$ $k_\infty = 2.7 \times 10^{-14} \exp(-1459.0/T)$	NIST	300-2500	
M32	$O + NO$	$\longrightarrow NO_2$	$k_0 = 9.0 \times 10^{-32}(T/300)^{-1.5}$ $k_\infty = 3.0 \times 10^{-11}$	JPL	200-300	Low Temperature
M33	$O + NO_2$	$\longrightarrow NO_3$	$k_0 = 2.5 \times 10^{-31}(T/300.0)^{-1.8}$ $k_\infty = 2.2 \times 10^{-11}(T/300.0)^{-0.7}$	JPL	200-300	Low Temperature
M34	$O + O$	$\longrightarrow O_2$	$5.21 \times 10^{-35} \exp(900.0/T) \times N$	NIST	200-4000	Low Temperature
M35	$O + O_2$	$\longrightarrow O_3$	$6.0 \times 10^{-34}(T/300.0)^{-2.4} \times N$	JPL	200-300	Low Temperature
M36	$O(^1D) + N_2$	$\longrightarrow N_2O$	$2.8 \times 10^{-36}(T/300.0)^{-0.9} \times N$	JPL	200-300	Low Temperature
M37	$OH + C_2H_2$	$\longrightarrow C_2H_3O$	$k_0 = 5.5 \times 10^{-30}$ $k_\infty = 8.3 \times 10^{-13}(T/300.0)^{2.0}$	JPL	200-300	Low Temperature
M38	$OH + C_2H_4$	$\longrightarrow C_2H_5O$	$k_0 = 1.0 \times 10^{-28}(T/300.0)^{-4.5}$ $k_\infty = 7.5 \times 10^{-12}(T/300.0)^{-0.85}$	JPL	200-300	Low Temperature
M39	$NH_2 + C_2H_3$	$\longrightarrow C_2H_5N$	$1.8 \times 10^{-27}(T/298.0)^{-3.85} \times N$		200-400	Low Temperature
M40	$OH + HNO_3$	$\longrightarrow H_2O + NO_3$	$k_0 = 2.4 \times 10^{-14} \exp(460.0/T)$ $k_2 = 2.7 \times 10^{-17} \exp(2199.0/T)$ $k_3 = 6.5 \times 10^{-34} \exp(1355.0/T)$ $k = k_0 + k_3 \times N/(1.0 + K_3 \times N/k_2)$	JPL	200-300	Low Temperature
M41	$OH + NO$	$\longrightarrow HNO_2$	$k_0 = 7.0 \times 10^{-31}(T/300.0)^{-2.6}$ $k_\infty = 3.6 \times 10^{-11}(T/300.0)^{-0.1}$	JPL	200-300	Low Temperature
M42	$OH + NO_2$	$\longrightarrow HNO_3$	$k_0 = 1.8 \times 10^{-30}(T/300.0)^{-3.0}$ $k_\infty = 2.8 \times 10^{-11}$	JPL	200-300	Low Temperature
M43	$OH + OH$	$\longrightarrow H_2O_2$	$k_0 = 6.9 \times 10^{-31}(T/300.0)^{-1.0}$	JPL	200-300	Low Temperature

Continued on next page ...

247

No.	Reactants	Products	Reaction Rate[a]	Reference	Temperature[b]	Note
M44	$S + S$	$\longrightarrow S_2$	$k_\infty = 2.6 \times 10^{-11}$; $k_0 = 2.0 \times 10^{-33} \exp(206.0/T)$	JPL	200-300	Low Temperature
M45	$SO + O$	$\longrightarrow SO_2$	$k_\infty = 2.3 \times 10^{-14} \exp(415.0/T)$	Moses et al. (2002)	100-500	Low Temperature
M46	$SO + OH$	$\longrightarrow HSO_2$	$k_0 = 4.82 \times 10^{-31}(T/298.0)^{-2.17}$; $k_\infty = 5.31 \times 10^{-11}$	NIST	298-3000	
M47	$SO_2 + H$	$\longrightarrow HSO_2$	$k_0 = 6.45 \times 10^{-29}(T/298.0)^{-3.48} \exp(-490.0/T)$; $k_0 = 4.47 \times 10^{-11}(T/298.0)^{0.5} \exp(200.0/T)$	NIST	200-2000	
M48	$SO_2 + O$	$\longrightarrow SO_3$	$k_0 = 5.61 \times 10^{-30}(T/298.0)^{-5.19} \exp(-2271.0/T)$; $k_\infty = 7.58 \times 10^{-12}(T/298.0)^{1.59} \exp(1244.0/T)$	NIST	200-1000	
M49	$SO_2 + OH$	$\longrightarrow HSO_3$	$k_0 = 1.8 \times 10^{-33}(T/300.0)^{2.0}$; $k_0 = 4.2 \times 10^{-14}(T/300.0)^{1.8}$; $k_0 = 3.3 \times 10^{-31}(T/300.0)^{-4.3}$; $k_\infty = 1.6 \times 10^{-12}$	JPL	200-300	Low Temperature
M50	$H + SO$	$\longrightarrow HSO$	$k_0 = 5.7 \times 10^{-32}(T/300.0)^{-1.6}$; $k_\infty = 7.5 \times 10^{-11}$	Kasting (1990)	200-300	Low Temperature
M51	$S + S_2$	$\longrightarrow S_3$	$1.1 \times 10^{-30}(T/300.0)^{-2.0} \times N$	Moses et al. (2002)		Low Temperature
M52	$S + S_3$	$\longrightarrow S_4$	$1.1 \times 10^{-30}(T/300.0)^{-2.0} \times N$	Moses et al. (2002)		Low Temperature
M53	$S_2 + S_2$	$\longrightarrow S_4$	$4.0 \times 10^{-31} \exp(900.0/T) \times N$	Moses et al. (2002)		Low Temperature
M54	$S_4 + S_4$	$\longrightarrow S_8(A)$	$4.0 \times 10^{-31} \exp(900.0/T) \times N$	Moses et al. (2002)		Low Temperature
M55	$H + CH_2$	$\longrightarrow CH_3$	$k_0 = 5.8 \times 10^{-30} \exp(355.0/T)$; $k_\infty = 2.37 \times 10^{-12} \exp(523.0/T)$	Yung & Demore (1999)		Low Temperature
M56	$H + CH_3$	$\longrightarrow CH_4$	$k_0 = 6.2 \times 10^{-29}(T/298.0)^{-1.8}$; $k_\infty = 3.5 \times 10^{-10}$	NIST	300-1000	
M57	$H + C_2H_5$	$\longrightarrow C_2H_6$	$k_0 = 5.5 \times 10^{-23}(T)^{-2.0} \exp(-1040/T)$; $k_\infty = 1.5 \times 10^{-10}$	Yung & Demore (1999)		Low Temperature
M58	$H + C_3H_2$	$\longrightarrow C_3H_3$	$4.42 \times 10^{-10}(T/298.0)^{0.22} \exp(43.0/T)$	NIST	200-2000	
M59	$H + C_3H_3$	$\longrightarrow C_3H_4^1$	$1.9 \times 10^{-10}(T/298.0)^{0.1} \exp(16.0/T)$	NIST	200-2000	
M60	$H + C_3H_3$	$\longrightarrow C_3H_4^2$	$1.1 \times 10^{-10}(T/298.0)^{0.21} \exp(86.6/T)$	NIST	200-2000	

Continued on next page ...

248

No.	Reactants	Products	Reaction Rate[a]	Reference	Temperature[b]	Note
M61	$H + C_3H_4^1$	$\longrightarrow CH_3 + C_2H_2$	$9.49 \times 10^{-12}(T/298.0)^{1.74}\exp(3872.8/T)$	NIST	200-3000	
M62	$H + C_3H_4^1$	$\longrightarrow C_3H_5$	$9.61 \times 10^{-12}\exp(-1560.0/T)$	NIST	195-503	Low Temperature
M63	$H + C_3H_4^2$	$\longrightarrow CH_3 + C_2H_2$	$9.49 \times 10^{-12}(T/298.0)^{1.74}\exp(3872.8/T)$	NIST	200-3000	
M64	$H + C_3H_4^2$	$\longrightarrow C_3H_5$	$1.01 \times 10^{-11}(T/298.0)^{0.69}\exp(1509.0/T)$	NIST	350-1200	
M65	$H + C_3H_5$	$\longrightarrow C_3H_6$	$2.64 \times 10^{-10}(T/298.0)^{0.18}\exp(62.5/T)$	NIST	200-2000	
M66	$H + C_3H_6$	$\longrightarrow C_3H_7$	$7.59 \times 10^{-12}(T/298.0)^{0.51}\exp(-1318.2/T)$	NIST	298-2000	
M67	$H + C_3H_7$	$\longrightarrow C_3H_8$	3.32×10^{-11}	NIST	300-2000	
M68	$H + C_3H_8$	$\longrightarrow C_3H_7 + H_2$	$4.23 \times 10^{-12}(T/298.0)^{2.54}\exp(-3400/T)$	NIST	298-2500	
M69	$H + C_4H_2$	$\longrightarrow C_4H_3$	$k_0 = 1.0 \times 10^{-28}$ $k_\infty = 1.39 \times 10^{-10}\exp(-1184/T)$	Yung & Demore (1999)		Low Temperature
M70	$H + C_4H_5$	$\longrightarrow C_4H_6^1$	$6.68 \times 10^{-11}(T/298.0)^{0.31}\exp(93.8/T)$	NIST	200-2000	
M71	$H + C_6H_2$	$\longrightarrow C_6H_3$	$k_0 = 1.0 \times 10^{-28}$ $k_\infty = 1.39 \times 10^{-10}\exp(-1184/T)$	Yung & Demore (1999)		Low Temperature
M72	$CH + H_2$	$\longrightarrow CH_3$	$k_0 = 9.0 \times 10^{-31}\exp(550.0/T)$ $k_\infty = 2.0 \times 10^{-10}(T/298.0)^{0.15}$	Yung & Demore (1999)		Low Temperature
M73	$CH_3 + C_2H_3$	$\longrightarrow C_3H_6$	1.2×10^{-10}	NIST	298	
M74	$CH_3 + C_2H_5$	$\longrightarrow C_3H_8$	5.6×10^{-11}	NIST	300-2000	
M75	$CH_3 + C_3H_3$	$\longrightarrow C_4H_6^1$	8.3×10^{-12}	NIST	1200-1500	High Temperature
M76	$CH_3 + C_3H_3$	$\longrightarrow C_4H_6^2$	8.3×10^{-12}	NIST	1200-1500	High Temperature
M77	$CH_3 + C_3H_5$	$\longrightarrow C_4H_8$	$2.72 \times 10^{-11}(T/298.0)^{-0.32}\exp(66.1/T)$	NIST	300-2500	
M78	$CH_3 + C_3H_6$	$\longrightarrow C_4H_9$	$1.27 \times 10^{-14}(T/298.0)^{2.67}\exp(-3447.0/T)$	NIST	298-2000	
M79	$CH_3 + C_3H_7$	$\longrightarrow C_4H_{10}$	$5.16 \times 10^{-11}(T/298.0)^{-0.32}$	NIST	300-2500	
M80	$C_2H_3 + C_2H_2$	$\longrightarrow C_4H_5$	$2.09 \times 10^{-14}(T/298.0)^{1.9}\exp(-1060/T)$	NIST	300-1500	
M81	$C_2H_3 + C_2H_3$	$\longrightarrow C_4H_6^3$	$k_0 = 8.76 \times 10^{-6}(T)^{-7.03}\exp(-1390/T)$ $k_\infty = 8.2 \times 10^{-11}$	Yung & Demore (1999)		Low Temperature
M82	$C_2H_3 + C_2H_5$	$\longrightarrow C_4H_8$	6.5×10^{-11}	NIST	298	
M83	$C_2H_5 + C_2H_5$	$\longrightarrow C_4H_{10}$	1.9×10^{-11}	NIST	300-1200	
M84	$NH_2 + NH_2$	$\longrightarrow N_2H_4$	$k_0 = 4.48 \times 10^{-14}T^{-5.49}\exp(-1000.0/T)$	NIST		

Continued on next page ...

No.	Reactants	Products	Reaction Rate[a]	Reference	Temperature[b]	Note
M85	$NH_2 + CH_3$	$\longrightarrow CH_5N$	$k_\infty = 9.33 \times 10^{-10} T^{-0.414} \exp(-33.0/T)$ $F_c = 0.31$	Klippenstein et al. (2009)	200-400	Low Temperature
M86	$CH_3 + OH$	$\longrightarrow CH_4O$	$k_0 = 2.0 \times 10^{-18} T^{-3.85}$ $k_\infty = 4.0 \times 10^{-12} T^{0.42}$	Moses et al. (2012)	200-400	Low Temperature
M87	$CH_3 + OH$	$\longrightarrow {}^1CH_2 + H_2O$	$k_0 = 1.932 \times 10^3 T^{-9.88} \exp(-7544.0/T)$ $+5.109 \times 10^{-11} T^{-6.25} \exp(-1433.0/T)$ $k_\infty = 1.031 \times 10^{-10} T^{-0.018} \exp(-16.74/T)$ $F_c = 0.1855 \exp(-T/155.8) + 0.8145 \exp(-T/1675.0)$ $+ \exp(-4531.0/T)$	Jasper et al. (2007)	300-2000	
M88	$CH_3 + OH$	$\longrightarrow CH_3O + H$	$k_0 = 3.714 \times 10^{-8} T^{-1.172} \exp(-132.0/T)$ $+1.535 \times 10^{-19} T^{2.127} \exp(-547.8/T)$ $k_\infty = 7.976 \times 10^{-4} T^{4.096} \exp(625/T)$ $F_c = 0.4863 \exp(-T/321.4) + 0.5137 \exp(-T/30000.0)$ $+ \exp(-2804.0/T)$	Jasper et al. (2007)	300-3000	
			$k_0 = 1.092 \times 10^{-14} T^{0.996} \exp(-1606.0/T)$ $k_\infty = 5.864 \times 10^{-6} T^{5.009} \exp(-949.4/T)$ $F_c = 0.8622 \exp(-T/9321.0) + 0.1378 \exp(-T/361.8)$ $+ \exp(-3125.0/T)$	Jasper et al. (2007)	300-3000	
M89	$CH_3 + OH$	$\longrightarrow CH_2O + H_2$	$k_0 = 2.359 \times 10^{-10} T^{-1.234} \exp(19.57/T)$ $+3.141 \times 10^3 T^{-4.484} \exp(-9188.0/T)$ $k_\infty = 5.876 \times 10^{-14} T^{6.721} \exp(1521/T)$ $F_c = 0.5 \exp(-T/22122.0) + 0.5 \exp(-T/174.9)$ $+ \exp(-3047.0/T)$	Jasper et al. (2007)	300-3000	
T1	O_3	$\longrightarrow O_2 + O$	$7.16 \times 10^{-10} \exp(-11200.0/T) \times N$	NIST	300-3000	
T2	HO_2	$\longrightarrow O_2 + H$	$2.41 \times 10^{-8} (T/298.0)^{-1.18} \exp(-24415.0/T) \times N$	NIST	200-2000	
T3	H_2O_2	$\longrightarrow OH + OH$	$2.01 \times 10^{-7} \exp(-22852.0/T) \times N$	NIST	700-1500	
T4	N_2O	$\longrightarrow N_2 + O$	$k_0 = 5.88 \times 10^{-10} \exp(-28265.0/T)$ $k_\infty = 1.30 \times 10^{11} \exp(-30000.0/T)$	NIST	900-2000	

No.	Reactants	Products	Reaction Rate[a]	Reference	Temperature[b]	Note
T5	NO_2	$\longrightarrow NO + O$	$1.88 \times 10^{-4}(T/298.0)^{-3.37}\exp(-37645.0/T) \times N$	NIST	1400-2500	
T6	NO_3	$\longrightarrow NO + O_2$	$k_0 = 2.5 \times 10^{-14}\exp(-1230.0/T)$ $k_\infty = 2.5 \times 10^6\exp(-6100.0/T)$	NIST	298-934	Low Temperature
T7	N_2O_5	$\longrightarrow NO_2 + NO_3$	$k_0 = 1.0 \times 10^{-3}(T/298.0)^{-3.5}\exp(-11000.0/T) \times N$ $k_\infty = 5.48 \times 10^{-7}(T/298.0)^{-1.24}\exp(-25312.0/T) \times N$	NIST	200-400	
T8	HNO	$\longrightarrow H + NO$	$k_0 = 1.98 \times 10^{-3}(T/298.0)^{-3.8}\exp(-25257.0/T)$ $k_\infty = 1.09 \times 10^{16}(T/298.0)^{-1.23}\exp(-25016.0/T)$	NIST	300-2500	
T9	HNO_2	$\longrightarrow OH + NO$	$k_0 = 1.15 \times 10^{-6}\exp(-23092.0/T)$ $k_\infty = 9.33 \times 10^{15}\exp(-24656.0/T)$	NIST	300-2500	
T10	HNO_3	$\longrightarrow OH + NO_2$	$k_0 = 8.0 \times 10^{-2}(T/298.0)^{-6.55}\exp(-26099.0/T)$ $k_\infty = 5.56 \times 10^{17}(T/298.0)^{-2.27}\exp(-26340.0/T)$	NIST	300-2000	
T11	HNO_3	$\longrightarrow HO_2 + NO$	$6.31 \times 10^{17}\exp(-13110.0/T)$	NIST	295-1200	
T12	HNO_4	$\longrightarrow O_2 + HNO_2$	$k_0 = 4.10 \times 10^{-5}\exp(-10600.0/T) \times N$	NIST	245-328	Low Temperature
T13	HNO_4	$\longrightarrow HO_2 + NO_2$	$k_0 = 7.7 \times 10^{-9}\exp(-33075.0/T)$	NIST	260-300	Low Temperature
T14	CH_2O	$\longrightarrow CO + H_2$	$k_\infty = 3.7 \times 10^{13}\exp(-36202.0/T)$	NIST	1400-3200	
T15	CH_2O_2	$\longrightarrow CO_2 + H_2$	$k_0 = 2.81 \times 10^{-9}\exp(-25738.0/T)$ $k_\infty = 4.46 \times 10^{13}\exp(-34398.0/T)$	NIST	1280-2030	
T16	CH_2O_2	$\longrightarrow CO + H_2O$	$k_0 = 6.73 \times 10^{-9}\exp(-26700.0/T)$ $k_\infty = 7.49 \times 10^{14}\exp(-34518.0/T)$	NIST	1370-2000	
T17	CH_3O_2	$\longrightarrow CH_2O + OH$	5.0×10^4	NIST	249	Low Temperature
T18	CH_3O_2	$\longrightarrow CH_2O_2 + H$	$1.0 \times 10^{14}\exp(-7500.0/T)$	NIST	298-343	Low Temperature
T19	CH_4O	$\longrightarrow CH_3O + H$	$2.16 \times 10^{-8}\exp(-33556.0/T) \times N$	NIST	1400-2500	
T20	CH_4O	$\longrightarrow CH_3 + OH$	$1.1 \times 10^{-7}\exp(-33075.0/T) \times N$	NIST	1000-2000	
T21	CH_4O	$\longrightarrow CH_2O + H_2$	$2.12 \times 10^{13}(T/298.0)^{1.22}\exp(-43539.0/T)$	NIST	300-2500	
T22	CH_4O	$\longrightarrow CH_{21} + H_2O$	$k_0 = 1.484 \times 10^{30}T^{-10.2}\exp(-52454.0/T)$ $+1.223 \times 10^{17}T^{-6.577}\exp(-48007.0/T)$ $k_\infty = 3.121 \times 10^{18}T^{-1.017}\exp(-46156.0/T)$ $F_c = 0.9922\exp(-T/943.0) + 0.0078\exp(-T/47310.0)$			

No.	Reactants	Products	Reaction Rate[a]	Reference	Temperature[b]	Note
T23	CH_4O_2	$\longrightarrow CH_3O + OH$	$+ \exp(-47110.0/T)$	Jasper et al. (2009)	300–3000	
T24	CH_4O_2	$\longrightarrow CH_2O + H_2O$	$6.0 \times 10^{14} \exp(-21288.0/T)$	NIST	500–800	
T25	C_2H_3	$\longrightarrow C_2H_2 + H$	$4.15 \times 10^{13} \exp(-22731.0/T)$	NIST	300–1000	
T26	C_2H_4	$\longrightarrow C_2H_2 + H_2$	$0.19 \times (T/298.0)^{-7.5} \exp(-22852.0/T) \times N$	NIST	500–2500	
T27	C_2H_5	$\longrightarrow C_2H_4 + H$	$5.8 \times 10^{-8} \exp(-35961.0/T) \times N$	NIST	1500–3200	
T28	C_2H_6	$\longrightarrow C_2H_5 + H$	$1.69 \times 10^{-6} \exp(-16838.0/T) \times N$	NIST	700–900	
T29	C_2HO	$\longrightarrow CO + CH$	$8.11 \times 10^{17}(T/298.0)^{-1.23} \exp(-51356.0/T)$	NIST	200–2500	
T30	C_2H_2O	$\longrightarrow CO + CH_2$	$1.08 \times 10^{-8} \exp(-29828.0/T) \times N$	NIST	1500–2500	
T31	C_2H_3O	$\longrightarrow C_2H_2 + OH$	$k_0 = 5.98 \times 10^{-9} \exp(-29828.0/T)$; $k_\infty = 3.00 \times 10^{14} \exp(-35720.0/T)$	NIST	1000–2000	
T32	C_2H_3O	$\longrightarrow CO + CH_3$	$2.2 \times 10^{12} \exp(-15154.0/T)$	NIST	627–713	
T33	C_2H_4O	$\longrightarrow CHO + CH_3$	$6.82 \times 10^{-3}(T/298.0)^{-8.62} \exp(-11300.0/T) \times N$	NIST	500–2500	
T34	C_2H_4O	$\longrightarrow C_2H_2O + H_2$	$2.0 \times 10^{15} \exp(-39810.0/T)$	NIST	500–2000	
T35	C_2H_4O	$\longrightarrow CH_4 + CO$	$3.0 \times 10^{14} \exp(-42216.0/T)$	NIST	1000–1700	
T36	C_2H_5O	$\longrightarrow CH_2O + CH_3$	$1.0 \times 10^{15} \exp(-42817.0/T)$	NIST	1000–1700	
T37	C_2H_5O	$\longrightarrow C_2H_4 + OH$	$1.33 \times 10^{15}(T/298.0)^{-2.02} \exp(-12749.0/T)$	NIST	298–2000	
T38	C_2H_5O	$\longrightarrow C_2H_4O + H$	$6.19 \times 10^{11} \exp(-11900.0/T)$; $1.07 \times 10^{14}(T/298.0)^{-0.69} \exp(-11187.0/T)$	NIST	544–673	
T39	$HCNO$	$\longrightarrow CO + NH$	$k_0 = 7.69 \times 10^{-4}(T/298.0)^{-3.10} \exp(-51356.0/T)$; $k_\infty = 6.00 \times 10^{13} \exp(-50154.0/T)$	NIST	298–2000	
T40	CNO	$\longrightarrow CO + N$	$1.69 \times 10^{-9} \exp(-23453.0/T) \times N$	NIST	1420–1750	High Temperature
T41	SO_3	$\longrightarrow SO_2 + O$	$9.47 \times 10^{-7} \exp(-40051.0/T) \times N$	NIST	1450–2600	
T42	HSO	$\longrightarrow SO + H$	$1.4 \times 10^{-8} \exp(-29467.0/T) \times N$	NIST	1273–1348	
T43	HSO_2	$\longrightarrow SO_2 + H$	$k_0 = 4.16 \times 10^{-7}(T/298.0)^{-3.29} \exp(-9610.0/T)$; $k_\infty = 3.42 \times 10^{13}(T/298.0)^{0.90} \exp(-9240.0/T)$	NIST	1100–2000	
T44	HSO_2	$\longrightarrow O + HSO$	$k_0 = 4.61 \times 10^{-4}(T/298.0)^{-5.87} \exp(-15635.0/T)$; $k_\infty = 4.53 \times 10^{16}(T/298.0)^{-1.07} \exp(-14312.0/T)$	NIST	200–2000	
T45	HSO_2	$\longrightarrow O_2 + HS$	$k_0 = 2.73 \times 10^{-8}(T/298.0)^{-2.82} \exp(3750.0/T)$	NIST	200–2000	

No.	Reactants	Products	Reaction Rate[a]	Reference	Temperature[b]	Note
T46	CHO	$\longrightarrow CO + H$	$k_\infty = 9.93 \times 10^{15}(T/298.0)^{-1.07}\exp(-3900.0/T)$	NIST	200–2000	
T47	CH_3O	$\longrightarrow CH_2O + H$	$6.0 \times 10^{-11}\exp(-7721.0/T) \times N$	NIST	298–1229	
T48	CHO_2	$\longrightarrow CO + OH$	$k_0 = 9.0 \times 10^{-11}(T/298.0)^{0.00}\exp(-6790.0/T)$; $k_\infty = 1.69 \times 10^{14}(T/298.0)^{-0.39}\exp(-13230.0/T)$	NIST	298–2000	
T49	CHO_2	$\longrightarrow CO_2 + H$	$k_0 = 4.92 \times 10^{-29}(T/298.0)^{-2.40}\exp(-18882.0/T)$; $k_\infty = 29.85 \times (T/298.0)^{0.13}\exp(-18401.0/T)$	NIST	200–2200	
T50	CH_3NO_2	$\longrightarrow CH_3O + NO$	$k_0 = 7.23 \times 10^{-31}(T/298.0)^{-3.15}\exp(-18642.0/T)$; $k_\infty = 125.0 \times (T/298.0)^{0.41}\exp(-17800.0/T)$	NIST	200–2200	
T51	CH_3NO_2	$\longrightarrow CH_2O + HNO$	$1.32 \times 10^{-6}\exp(-17199.0/T) \times N$	NIST	680–955	
T52	CH_3NO_3	$\longrightarrow CH_3O + NO_2$	$3.98 \times 10^{13}\exp(-19364.0/T)$	NIST	440–473	
T53	HSO_3	$\longrightarrow OH + SO_2$	$1.0 \times 10^{13}\exp(-16838.0/T)$; $k_0 = 3.16 \times 10^{-4}(T/298.0)^{-4.72}\exp(-13590.0/T)$; $k_\infty = 4.34 \times 10^{14}(T/298.0)^{0.0}\exp(-12989.0/T)$	NIST	700–1200; 150–1500	
T54	SO_2^1	$\longrightarrow SO_2^3$	$1.0 \times 10^{-12} \times N + 1.5 \times 10^3$	Turco et al. (1982)		Low Temperature
T55	SO_2^1	$\longrightarrow SO_2$	$1.0 \times 10^{-11} \times N + 2.2 \times 10^4$	Turco et al. (1982)		Low Temperature
T56	SO_2^3	$\longrightarrow SO_2$	$1.5 \times 10^{-13} \times N + 1.13 \times 10^3$	Turco et al. (1982)		Low Temperature
T57	HCN	$\longrightarrow H + CN$	$1.93 \times 10^{-4}(T/298.0)^{-2.44}\exp(-62782.1/T) \times N$	NIST	1800–5000	
T58	H_2S	$\longrightarrow H_2 + S$	$3.16 \times 10^{-10}\exp(-32954.6/T) \times N$	NIST	1890–2890	
T59	H_2S	$\longrightarrow HS + H$	$2.92 \times 10^{-8}\exp(-33315.4/T) \times N$	NIST	873–1470	
T60	OCS	$\longrightarrow CO + S$	$4.07 \times 10^{-10}\exp(-30910.0/T) \times N$	NIST	1900–3230	
T61	C_3H_5	$\longrightarrow C_3H_4^1 + H$	$3.98 \times 10^{12}\exp(-18402.0/T)$	NIST	300–2500	
T62	C_3H_5	$\longrightarrow C_3H_4^2 + H$	$1.40 \times 10^{13}\exp(-30188.3/T)$	NIST	300–2500	
T63	C_3H_5	$\longrightarrow C_2H_2 + CH_3$	$1.26 \times 10^{13}\exp(-16838.0/T)$	NIST	300–2500	
T64	C_3H_6	$\longrightarrow C_2H_3 + CH_3$	$1.18 \times 10^{18}(T/298.0)^{-1.2}\exp(-49191.0/T)$	NIST	300–2500	
T65	C_3H_6	$\longrightarrow C_3H_5 + H$	$2.50 \times 10^{15}\exp(-43659.0/T)$	NIST	300–2500	
T66	C_3H_6	$\longrightarrow C_3H_4^2 + H_2$	$4.00 \times 10^{13}\exp(-40291.0/T)$	NIST	1200–1800	
T67	C_3H_7	$\longrightarrow C_3H_6 + H$	$1.09 \times 10^{13}(T/298.0)^{0.17}\exp(-17921.6/T)$	NIST	298–2000	
T68	C_3H_7	$\longrightarrow C_2H_4 + CH_3$	$1.31 \times 10^{13}(T/298.0)^{0.87}\exp(-15274.6/T)$	NIST	298–1000	

Continued on next page ...

253

No.	Reactants	Products	Reaction Rate[a]	Reference	Temperature[b]	Note
T69	C_3H_8	$\longrightarrow C_3H_7 + H$	$1.58 \times 10^{16} \exp(-49071.0/T)$	NIST	300-2500	
T70	C_3H_8	$\longrightarrow C_2H_5 + CH_3$	$1.07 \times 10^{12}(T/298.0)^{-15.74} \exp(-49672.0/T) \times N$	NIST	600-1653	
T71	C_3H_8	$\longrightarrow C_3H_6 + H_2$	3.38×10^{10}	NIST	3392	High Temperature
T72	C_4H_3	$\longrightarrow C_4H_2 + H$	$1.66 \times 10^{-8} \exp(-29707.0/T) \times N$	NIST	1900-2500	
T73	C_4H_4	$\longrightarrow C_4H_3 + H$	$6.3 \times 10^{13} \exp(-43779.0/T)$	NIST	1170-1690	
T74	C_4H_4	$\longrightarrow C_2H_2 + C_2H_2$	$1.15 \times 10^{15} \exp(-43539.0/T)$	NIST	1700-2400	
T75	C_4H_5	$\longrightarrow C_4H_4 + H$	$1.6 \times 10^{14} \exp(-20807.0/T)$	NIST	900-1100	
T76	C_4H_5	$\longrightarrow C_2H_2 + C_2H_3$	$3.57 \times 10^{-8}(T/298.0)^{0.7} \exp(-21288.0/T) \times N$	NIST	300-1500	
T77	$C_4H_6^1$	$\longrightarrow C_4H_5 + H$	$7.7 \times 10^{14} \exp(-44260.0/T)$	NIST	1100-1600	
T78	$C_4H_6^1$	$\longrightarrow C_3H_3 + CH_3$	$5.0 \times 10^{15} \exp(-38126.0/T)$	NIST	300-2500	
T79	$C_4H_6^2$	$\longrightarrow C_4H_5 + H$	$2.0 \times 10^{15} \exp(-43178.0/T)$	NIST	300-2500	
T80	$C_4H_6^2$	$\longrightarrow C_3H_3 + CH_3$	$2.0 \times 10^{15} \exp(-37645.0/T)$	NIST	1100-1600	
T81	$C_4H_6^3$	$\longrightarrow C_4H_5 + H$	$1.58 \times 10^{16} \exp(-55445.0/T)$	NIST	300-2500	
T82	$C_4H_6^3$	$\longrightarrow C_2H_3 + C_2H_3$	$1.8 \times 10^{13} \exp(-42817.0/T)$	NIST	1560-2210	
T83	$C_4H_6^3$	$\longrightarrow C_2H_2 + C_2H_4$	$1.0 \times 10^{14} \exp(-37645.0/T)$	NIST	1100-1600	
T84	C_4H_8	$\longrightarrow CH_3 + C_3H_5$	$1.0 \times 10^{16} \exp(-36683.0/T)$	NIST	300-2500	
T85	C_4H_9	$\longrightarrow H + C_4H_8$	$1.1 \times 10^{13}(T/298.0)^{0.25} \exp(-17921.6/T)$	NIST	298-2000	
T86	C_4H_9	$\longrightarrow CH_3 + C_3H_6$	$7.7 \times 10^{13}(T/298.0)^{0.77} \exp(-15394.8/T)$	NIST	298-2000	
T87	C_4H_{10}	$\longrightarrow H + C_4H_9$	$1.58 \times 10^{16} \exp(-49312.0/T)$	NIST	300-2500	
T88	C_4H_{10}	$\longrightarrow CH_3 + C_3H_7$	$1.0 \times 10^{17} \exp(-42576.0/T)$	NIST	300-2500	
T89	C_4H_{10}	$\longrightarrow C_2H_5 + C_2H_5$	$7.94 \times 10^{16} \exp(-40411.0/T)$	NIST	300-2500	
T90	C_6H_6	$\longrightarrow C_3H_3 + C_3H_3$	$6.31 \times 10^{14} \exp(-31151.0/T)$	NIST	300-2500	
T91	N_2H_4	$\longrightarrow NH_2 + NH_2$	$6.61 \times 10^{-9} \exp(-20567.0/T) \times N$	NIST	1280-1580	
T92	CH_5N	$\longrightarrow CH_4 + NH$	$2.66 \times 10^{-11} \exp(-24295.0/T) \times N$	NIST	1750-2450	
T93	CH_5N	$\longrightarrow CH_3 + NH_2$	$1.36 \times 10^{-7} \exp(-30669.0/T) \times N$	NIST	1530-1980	

a The unit of the reaction rate is cm^3 s^{-1} for bimolecular reactions, cm^6 s^{-1} for termolecular reactions, and s^{-1} for thermodissociation reactions. The unit of the temperature T is K and the unit of the total number density N is cm^{-3}.

b In the column "Temperature" I note the temperature range for which each reaction rate is valid. I annotate "Low Temperature" and "High Temperature" to the reaction

rates only valid at temperatures lower than 300 K and higher than 1000 K, respectively. For low-temperature applications, including explorations of Earth, Mars, and habitable exoplanets, I exclude those reactions marked as "High Temperature".

Table A.2: Photolysis reactions in the photochemistry model

No.	Reactants	Products	Rate 295 K[a]	Rate 200 K[a]	Cross Sections[b]	T[c]	Quantum Yields	T[c]	Note
1	O_2	$O + O$	2.67E-7	2.68E-7	4-108 nm: Brion et al. (1979)	N	< 139 nm: 0.5	N	
					108-129 nm: Ogawa and Ogawa (1975)	N	139-175 nm: 0	N	
					129-173 nm: Yoshino et al. (2005)	N	175-242 nm: 1.0	N	
					176-203 nm: Yoshino et al. (1992)	Y			
					205-245 nm: Sander et al. (2011)				
2	O_2	$O + O(^1D)$	1.31E-6	1.31E-6			< 139 nm: 0.5	N	
							139-175 nm: 1.0	N	
							175-242 nm: 0	N	
3	O_3	$O_2 + O$	6.33E-4	6.28E-4	110-172 nm: Mason et al. (1996)	N	< 186 nm: 0.71	N	
					186-230 nm: Sander et al. (2011)	N	186-220 nm: Sander et al. (2011)	N	
					230-1070 nm: Bogumil et al. (2003)	Y	220-340 nm: Matsumi et al. (2002)	Y	
							340-411 nm: 0.92	N	
							> 411 nm: 1.0	N	
4	O_3	$O_2 + O(^1D)$	3.66E-3	3.63E-3			< 186 nm: 0.29	N	
							186-220 nm: Sander et al. (2011)	N	
							220-340 nm: Matsumi et al. (2002)	Y	
							340-411 nm: 0.08	N	
							> 411 nm: 0	N	
5	HO_2	$O + OH$	2.78E-4	2.78E-4	190-260 nm: Sander et al. (2011)	N	190-260 nm: 1.0	N	
6	H_2O	$H + OH$	4.79E-6	4.79E-6	6-120 nm: Chan (1993)	N	6-240 nm: 1.0	N	
					121-198 nm: Sander et al. (2011)	N			
					199-240 nm: Extrapolation	N			
7	H_2O_2	$OH + OH$	4.79E-5	4.59E-5	190-350 nm: Sander et al. (2011)	Y	190-350 nm: 1.0	N	
8	NO_2	$NO + O$	4.49E-3	4.13E-3	16-200 nm: Au (1997)	N	< 398 nm: 1.0	N	
					205-235 nm: Atkinson et al. (2004)	Y	398-428 nm: Sander et al. (2011)	Y	
					238-667 nm: Vandaele et al. (1998)	Y	> 428 nm: 0	N	
					667-910 nm: Bogumil et al. (2003)	Y			
9	NO_3	$NO + O_2$	1.05E-2	1.43E-2	403-691 nm: Sander et al. (2011)	Y	403-691 nm: Sander et al. (2011)	Y	
10	NO_3	$NO_2 + O$	8.32E-2	1.02E-1	403-691 nm: Sander et al. (2011)	Y	403-691 nm: Sander et al. (2011)	Y	
11	N_2O	$N_2 + O(^1D)$	6.93E-7	5.52E-7	130-160 nm: Nicolet and Peetermans (1972)	N	130-140 nm: 0	N	
					160-240 nm: Sander et al. (2011)	Y	140-230 nm: 1.0	N	
							230-240 nm: 0	N	
12	N_2O_5	$NO_3 + NO_2$	8.54E-5	4.82E-5	200-410 nm: Sander et al. (2011)	Y	< 248 nm: 1.0	N	
							248-300 nm: Linear interpolation	N	
							> 300 nm: 0	N	
13	N_2O_5	$NO_3 + NO + O$	1.51E-4	1.46E-4			< 248 nm: 0	N	

Continued on next page …

No.	Reactants	Products	Rate 295 K[a]	Rate 200 K[a]	Cross Sections[b]	T[c]	Quantum Yields	T[c]	Note
							248-300 nm: Linear interpolation > 300 nm: 0.7	N N	
14	HNO_2	$NO + OH$	8.41E-4	8.41E-4	184-396 nm: Sander et al. (2011)	N	184-396 nm: 1.0	N	
15	HNO_3	$NO_2 + OH$	6.19E-5	5.45E-5	105-191 nm: Suto and Lee (1984) 192-350 nm: Sander et al. (2011)	N Y	< 193 nm: 0.33 193-200 nm: Linear interpolation 200-350 nm: 1.0	N N N	
16	HNO_3	$HNO_2 + O$	1.93E-5	1.90E-5	192-350 nm: Sander et al. (2011)	N	< 193 nm: 0.39 193-200 nm: Linear interpolation 200-350 nm: 0.0	N N N	
17	HNO_3	$HNO_2 + O(^1D)$	1.39E-5	1.38E-5			< 193 nm: 0.28 193-200 nm: Linear interpolation 200-350 nm: 0.0	N N N	
18	HNO_4	$NO_2 + HO_2$	1.81E-4	1.81E-4	190-350 nm: Sander et al. (2011)	N	190-350 nm: Sander et al. (2011)	N	
19	HNO_4	$NO_3 + OH$	4.84E-5	4.84E-5	190-350 nm: Sander et al. (2011)	N	190-350 nm: Sander et al. (2011)	N	
20	CH_2O	$CHO + H$	4.15E-5	4.15E-5	226-375 nm: Sander et al. (2011)	Y	226-250 nm: 0.31 250-375 nm: Sander et al. (2011)	N N	
21	CH_2O	$H_2 + CO$	3.54E-5	3.30E-5			226-250 nm: 0.49 250-375 nm: Sander et al. (2011)	N Y	P dependence omitted
22	C_2H_4O	$CH_3 + CHO$	2.60E-5	2.60E-5	202-360 nm: Sander et al. (2011)	N	< 256 nm: 0.29 256-332 nm: Sander et al. (2011) > 332 nm: 0	N N N	
23	C_2H_4O	$CH_4 + CO$	3.18E-6	3.18E-6			< 256 nm: 0.48 256-332 nm: Sander et al. (2011) > 332 nm: 0	N N N	
24	CH_4O_2	$CH_3O + OH$	2.56E-5	2.56E-5	210-405 nm: Sander et al. (2011)	N	210-405 nm: 1.0	N	
25	CH_3NO_2	$CH_3O + NO$	1.58E-3	1.58E-3	190-440 nm: Sander et al. (2011)	N	190-440 nm: 1.0	N	
26	CH_3NO_3	$CH_3O + NO_2$	1.38E-4	1.33E-4	190-344 nm: Sander et al. (2011)	Y	190-344 nm: 1.0	N	
27	CH_2O_2	$CHO + OH$	6.20E-6	6.20E-6	195-250 nm: Sander et al. (2011)	N	195-250 nm: 0.7	N	
28	CH_2O_2	$CHO_2 + H$	1.33E-6	1.33E-6			195-250 nm: 0.15	N	
29	CH_2O_2	$H_2O + CO$	1.33E-6	1.33E-6			195-250 nm: 0.15	N	
30	SO_3	$SO_2 + O$	2.33E-5	2.33E-5	140-180 nm: Hintze et al. (2003) 180-330 nm: Sander et al. (2011)	N N	140-330 nm: 1.0	N	
31	OCS	$CO + S$	1.99E-5	1.68E-5	186-296 nm: Sander et al. (2011)	Y	186-296 nm: 1.0	N	
32	CH_4	$CH_3 + H$	1.79E-6	1.79E-6	52-125 nm: Kameta et al. (2002) 125-142 nm: Chen and Wu (2004) 142-152 nm: Lee et al. (2001)	N N N	0.41 (Smith and Raulin, 1999)	N	
33	CH_4	$^1CH_2 + H_2$	2.31E-6	2.31E-6			0.53 (Smith and Raulin, 1999)	N	
34	CH_4	$CH + H_2 + H$	2.62E-7	2.62E-7			0.06 (Smith and Raulin, 1999)	N	

No.	Reactants	Products	Rate 295 K[a]	Rate 200 K[a]	Cross Sections[b]	T[c]	Quantum Yields	T[c]	Note
35	CO	$C + O$	2.32E-8	2.32E-8	6-177 nm: Chan (1993)	N	< 111 nm: 1.0 > 111 nm: 0	N N	
36	CO_2	$CO + O$	5.62E-9	3.67E-9	35-197 nm: Huestis and Berkowitz (2010) 197-270 nm: Ityaksov et al. (2008) For 195 K: 108-118 nm: Stark et al. (2007) 118-163 nm: Yoshino et al. (1996) 163-193 nm: Parkinson (2003)	Y N	< 167 nm: 0 167-205 nm: 1.0 > 205 nm: 0	N N N	
37	CO_2	$CO + O(^1D)$	1.43E-7	1.34E-7			< 167 nm: 1.0 167-205 nm: 0 > 205 nm: 0	N N N	
38	H_2	$H + H$	1.68E-8	1.68E-8	18-70 nm: Lee et al. (1976) 70-87 nm: Cook and Metzger (1964) 87-124 nm: Backx et al. (1976)	N N N	< 80 nm: 0.1 (Mentall and Gentieu, 1970) 80-85 nm: 1.0 > 85 nm: 0	N N N	
39	N_2	$N + N$	5.61E-7	5.61E-7	6-108 nm: Chan (1993)	N	6-108 nm: 1.0	N	
40	CH_4O	$CH_3O + H$	5.45E-6	5.45E-6	16-106 nm: Burton (1992) 106-165 nm: Nee (1985) 165-220 nm: Cheng et al. (2002)	N N N	16-220 nm: 1.0	N	
41	HCN	$H + CN$	3.13E-7	3.13E-7	133-145 nm: Macpherson and Simons (1978)	N	133-145 nm: 1.0	N	Incomplete wavelength coverage
42	NH_3	$NH_2 + H$	6.91E-5	6.91E-5	8-106 nm: Samson et al. (1987) 106-140 nm: Wu et al. (2007) 140-230 nm: Cheng et al. (2006)	N N N	< 106 nm: 0.3 (Lilly et al., 1973) 106-165 nm: Linear interpolation > 165 nm: 1.0	N N N	
43	NH_3	$NH + H_2$	1.43E-6	1.43E-6			< 106 nm: 0.7 10-165 nm: Linear interpolation > 165 nm: 0	N N N	
44	NO	$N + O$	4.07E-6	4.07E-6	7-177 nm: Iida (1986) 186-227 nm: Thompson et al. (1963)	N N	< 191 nm: 1.0 > 191 nm: 0	N N	
45	H_2S	$HS + H$	1.27E-4	1.30E-4	5-160 nm: Feng (1999a) 160-260 nm: Wu and Chen (1998)	N Y	5-260 nm: 1.0	N	
46	SO_2	$SO + O$	1.05E-4	8.54E-5	5-106 nm: Feng (1999b) 106-171 nm: Manatt and Lane (1993) 171-239 nm: Wu et al. (2000) 239-395 nm: Bogumil et al. (2003)	N N Y N	< 220 nm: 1.0 220-340 nm: 0 > 340 nm: 0	N N N	
47	SO_2	$^1SO_2$	8.27E-4	8.17E-4			< 220 nm: 0 220-340 nm: 1.0 > 340 nm: 0	N N N	
48	SO_2	$^3SO_2$	7.52E-7	1.66E-6			< 340 nm: 0 > 340 nm: 1.0	N N	

Continued on next page ...

258

No.	Reactants	Products	Rate 295 K[a]	Rate 200 K[a]	Cross Sections[b]	T[c]	Quantum Yields	T[c]	Note
49	HSO	$HS + O$	2.78E-4	2.78E-4	190-260 nm: Sander et al. (2011)	N	190-260 nm: 1.0	N	Assumed as HO_2
50	H_2SO_4	$SO_3 + H_2O$	1.36E-5	1.36E-5	118-180 nm: Mills et al. (2005)	N	118-180 nm: 1.0	N	
					510-735 nm: Lane and Kjaergaard (2008)	N	510-735 nm: 1.0	N	
51	SO	$S + O$	3.66E-4	3.66E-4	100-190 nm: Linear interpolation	N	100235 nm: 1.0	N	
					190-235 nm: Phillips (1981)	N			
52	S_2	$S + S$	4.00E-3	4.00E-3	Photolysis around 280 nm, value estimated by de Almeida and Singh (1986)				
53	S_3	$S_2 + S$	5.74E-1	5.74E-1	350-475 nm: Billmers and Smith (1991)	N	350-475 nm: 1.0	N	
54	S_4	$S_2 + S_2$	1.10E-1	1.10E-1	425-575 nm: Billmers and Smith (1991)	N	425-575 nm: 1.0	N	
55	C_2H_2	$C_2H + H$	1.27E-6	1.22E-5	6-137 nm: Cooper et al. (1995)	N	6-217 nm: 1.0 (Lauter et al. 2002)	N	
					137-185 nm: Smith et al. (1991)	Y	> 217 nm: 0	N	
					185-236 nm: Bénilan et al. (2000)	Y			
56	C_2H_3	$C_2H_2 + H$	9.97E-3	9.97E-3	225-238 nm: Fahr et al. (1998)	N	225-446 nm: 1.0	N	Incomplete Wavelength Coverage
					400-446 nm: Hunziker et al. (1983)	N			
57	C_2H_4	$C_2H_2 + H_2$	6.35E-6	6.35E-6	50-105 nm: Holland (1997)	N	50-209 nm: 0.4	N	
					105-175 nm: Lu et al. (2004)	N			
					175-209 nm: Orkin et al. (1997)	N			
58	C_2H_4	$C_2H_2 + 2\,H$	7.93E-6	7.93E-6			50-209 nm: 0.5	N	
59	C_2H_4	$C_2H_3 + H$	1.59E-6	1.59E-6			50-209 nm: 0.1	N	
60	C_2H_5	$CH_3 + {}^1CH_2$	4.28E-4	4.28E-4	200-260 nm: Fagerström et al. (1993)	N	200-260 nm: 1.0	N	
61	C_2H_6	$C_2H_4 + H_2$	7.98E-7	7.98E-7	13-120 nm: Kameta et al. (1996)	N	13-160 nm: 0.14 (Akimoto et al. 1965)	N	
					120-150 nm: Chen and Wu (2004)	N			
					150-160 nm: Lee et al. (2001)	N			
62	C_2H_6	$C_2H_4 + 2\,H$	1.77E-6	1.77E-6			13-160 nm: 0.31	N	
63	C_2H_6	$C_2H_2 + 2\,H_2$	1.54E-6	1.54E-6			13-160 nm: 0.27	N	
64	C_2H_6	$CH_4 + {}^1CH_2$	1.25E-6	1.25E-6			13-160 nm: 0.22	N	
65	C_2H_6	$CH_3 + CH_3$	3.42E-7	3.42E-7			13-160 nm: 0.06	N	
66	N_2H_2	$N_2 + H_2$	1.13E-4	1.13E-4	191-291 nm: Vaghjiani (1993)	N	191-291 nm: 1.0	N	Assumed as N_2H_4
67	N_2H_4	$N_2H_3 + H$	1.13E-4	1.13E-4	191-291 nm: Vaghjiani (1993)	N	191-291 nm: 1.0	N	
68	CH_5N	$HCN + 2\,H_2$	1.21E-5	1.21E-5	5-83 nm: Burton et al. (1994)	N	5-247 nm: 0.08	N	
					83-247 nm: Hubin-Franskin et al. (2002)	N			
69	C_2H_5N	$HCN + CH_3 + H$	2.75E-5	2.75E-5	111-213 nm: Basch et al. (1969)	N	111-213 nm: 0.1	N	
70	HNO	$NO + H$	8.41E-4	8.41E-4	184-396 nm: Sander et al. (2011)	N	184-396nm: 1.0	N	Assumed as HNO_2

a   The rates (s^{-1}) are computed with the unattenuated solar spectrum from 100 nm (down to 67 nm for H_2 and N_2) to 1000 nm at 1 AU with cross sections and quantum yields at 295 K and 200 K, and divided by 2 for diurnal average.

b   The sources of data for cross sections are listed for each molecule in the row of its first photodissociation branch. The photolysis reaction rates for other branches are computed using the same cross sections but different quantum yields.

c Temperature dependence of cross sections and quantum yields: Y indicates temperature dependence has available measurements and is taken into account for the respective wavelength range.

Appendix B

Additional Information on the Photochemistry Model

B.1   Formulation of Vertical Diffusion Flux

The vertical diffusion flux can be derived rigorously from the general diffusion equation for a minor constituent in a heterogenous atmosphere that

$$\Phi = -K\left[\frac{\partial n}{\partial z} + n\left(\frac{1}{H_0} + \frac{1}{T}\frac{dT}{dz}\right)\right] - D\left[\frac{\partial n}{\partial z} + n\left(\frac{1}{H} + \frac{1+\alpha_{\mathrm{T}}}{T}\frac{dT}{dz}\right)\right], \qquad \text{(B.1)}$$

in which the first term is the eddy diffusion flux (Φ_K) and the second term is the molecular diffusion flux (Φ_D). Note that $n = Nf$, and then the eddy diffusion flux can be simplified as

$$
\begin{aligned}
\Phi_K &= -K\left[\frac{\partial n}{\partial z} + n\left(\frac{1}{H_0} + \frac{1}{T}\frac{dT}{dz}\right)\right], \\
&= -K\left[N\frac{\partial f}{\partial z} + fN\left(\frac{1}{N}\frac{\partial N}{\partial z} + \frac{1}{H_0} + \frac{1}{T}\frac{dT}{dz}\right)\right], \\
&= -K\left[N\frac{\partial f}{\partial z} + fN\left(\frac{1}{N}\frac{\partial N}{\partial z} - \frac{1}{P}\frac{\partial P}{\partial z} + \frac{1}{T}\frac{dT}{dz}\right)\right], \\
&= -KN\frac{\partial f}{\partial z}, \qquad\qquad\qquad\qquad\qquad\qquad\qquad\qquad\qquad \text{(B.2)}
\end{aligned}
$$

in which I have used the definition of atmospheric scale height and the ideal gas law.

The fundamental difference between the molecular diffusion and the eddy diffusion is in the scale height term. The molecular diffusion depends on the specific scale height for the molecule, whereas the total atmospheric pressure falls according to the mean scale height. The molecular diffusion term can be similarly simplified as

$$
\begin{aligned}
\Phi_D &= -D\left[\frac{\partial n}{\partial z} + n\left(\frac{1}{H} + \frac{1+\alpha_T}{T}\frac{dT}{dz}\right)\right], \\
&= -D\left[\frac{\partial n}{\partial z} + n\left(\frac{1}{H_0} + \frac{1}{T}\frac{dT}{dz}\right) - n\left(\frac{1}{H_0} - \frac{1}{H} - \frac{\alpha_T}{T}\frac{dT}{dz}\right)\right], \\
&= -DN\frac{\partial f}{\partial z} + Dn\left(\frac{1}{H_0} - \frac{1}{H} - \frac{\alpha_T}{T}\frac{dT}{dz}\right),
\end{aligned}
\tag{B.3}
$$

which yields equation (2.2).

B.2   Mean Stellar Zenith Angle for One-Dimensional Photochemistry Model

All 1-dimensional photochemistry models need to assume a zenith angle (θ_0) for the incoming stellar radiation as a global average. Various values have been adopted in previous photochemistry models, for example $\theta_0 = 50°$ (Zahnle et al., 2006), $\theta_0 = 57.3°$ (Zahnle et al., 2008), and $\theta_0 = 48°$ (Moses et al., 2011). We find that all these assumptions are plausible and provide justification as follows.

At different location of star-facing hemisphere of the planet, the local stellar zenith angle is $\mu \equiv \cos\theta = \cos\psi\cos\phi$ where ψ and ϕ are the local latitude and longitude, respectively. A dayside disk average should be weighted by the radiation intensity at certain optical depth τ, viz.

$$
\exp(-\tau/\mu_0) = \frac{1}{\pi}\int_{-\pi/2}^{\pi/2}\int_{-\pi/2}^{\pi/2}\exp(-\tau/\cos\psi\cos\phi)\cos^2\psi\cos\phi\,d\psi\,d\phi.
\tag{B.4}
$$

Equation (B.4) is well-defined for any particular level of optical depth, and can be solved numerically. The relationship between the average zenith angle and the optical depth of concern is illustrated in Figure B-1.
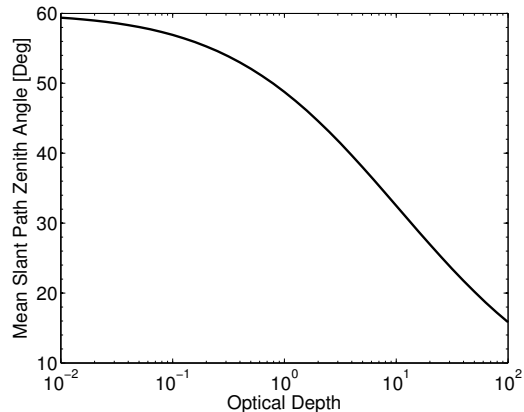
Figure B-1: Mean zenith angle of stellar radiation for photochemistry models as a function of optical depth.

Figure B-1 shows that the appropriate mean zenith angle depends on the optical depth of concern. I find that optical depth between 0.1 and 1.0 corresponds to a mean zenith angle between 57° and 48°. In the extreme of zero optical depth, the appropriate mean zenith angle is 60°. In general, it is appropriate to assume the mean zenith angle to be 48° ∼ 60° for the application of 1-dimensional photochemistry model.

B.3   Deposition Velocities

In the photochemical model I calculate the number density in the bottom layer of the atmosphere. The interaction between the bottom layer and the surface consists of two steps: first, the molecular transport across a thin stagnant layer of air adjacent to the surface, called the *quasi-laminar sublayer*; second, the uptake at the surface. Each step provides a resistance to the overall dry deposition, viz.

$$V_{\text{DEP}}^{-1} = r_b + r_c, \tag{B.5}$$

in which r_b is the quasi-laminar resistance and r_c is the surface resistance. The quasi-laminar resistance is

$$r_b = \frac{5 \, \mathrm{Sc}^{2/3}}{u_*},$$

(B.6)

in which Sc is the dimensionless Schmidt number defined as the ratio between the kinetic viscosity of air and the molecular diffusivity of the molecule considered, and u_* is the friction velocity (Seinfeld and Pandis, 2006). The friction velocity depends on the wind speed adjacent to the surface and the roughness of the surface. In the current model, the friction velocity u_* should be treated as a free parameter varying from 0.1 to 1 m s^{-1}.

The surface resistance is more complicated and largely depends on the property of the surface and the solubility of the molecule. For example, I consider two general types of surfaces, ocean and land. For the land I envisage desert-like surface and do not consider the complications of foliage.

For the deposition to the ocean, the surface resistance is

$$r_c = \frac{1}{k_G} + \frac{1}{k_L H},$$

(B.7)

in which k_G is the gas phase mass transfer coefficient, k_L is the liquid phase mass transfer coefficient and H is the dimensionless Henry's law constant (Seinfeld and Pandis, 2006). These parameters depend on the wind speed (or the friction velocity), and the Schmidt number of the molecule in sea water.

The surface resistance to the land is even more complicated and depends on the properties of land, for example, surface morphology, roughness, vegetation, canopy, etc. There have been tremendous efforts to measure and parameterize the surface resistance of different molecules on different types of land on Earth. For example, the surface resistance to a featureless desert can be expressed as

$$r_c = \left(\frac{10^{-5} H}{r_S} + \frac{f_0}{r_O} \right)^{-1},$$

(B.8)

in which H is in the unit of M atm^{-1}, f_0 is a normalized (0 to 1) reactivity factor,

264
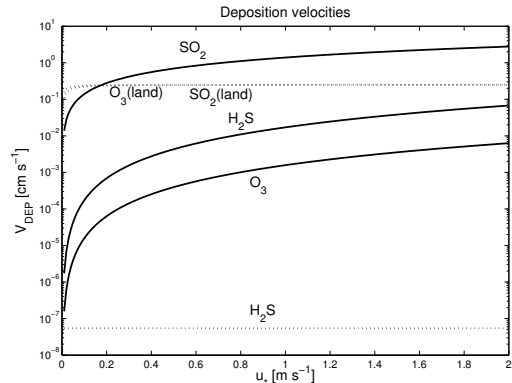
Figure B-2: Deposition velocities to the ocean (solid lines) and the land (dotted lines) as a function of the friction velocity u_*. The calculation is for the terrestrial atmosphere at $T = 273.15$ K, $P = 1$ atm. The ocean is assumed to have a pH of about 6.5. The land is assumed to be featureless desert.

$r_S = 1000$ s m^{-1} and $r_O = 400$ s m^{-1} (Seinfeld and Pandis, 2006).

I present the deposition velocities of slightly soluble gases (such as H$_2$S), highly soluble gases (such as SO$_2$), not soluble but reactive gases (such as O$_3$) to the ocean and the land in Figure B-2. The deposition velocity to the ocean critically depends on the solubility of the gas. For poorly soluble gas, the deposition velocity to the ocean is negligible. For the highly soluble gas, the deposition velocity is limited by the friction velocity, or the wind speed. For the reactive gas, the deposition velocity can be also very high. In particular, the deposition velocity of H$_2$S to the land the negligible, and in most cases, the deposition velocity of H$_2$S to the ocean is smaller than 0.1 cm s^{-1}. The estimate of dry deposition velocity here only considers the surface uptake, but not the eventual loss of a gas at or beneath the surface. The effective dry deposition velocity might be smaller than what we estimate if no effective loss mechanism is available at the surface and the surface is saturated (e.g. Kharecha et al., 2005).

B.4 Photochemical Stability of Atmospheric Trace Gases

I here present an analytical treatment of the photochemical stability of radiative trace gases. The goal of the analytical treatment is to obtain a useful formula that computes the critical pressure level of any radiative trace gas above which the photodissociation of the gas is important. The key idea is that the photolysis rate at any certain altitude (denoted as z^*) is proportional to the radiation flux in the dissociating wavelengths at this altitude, which is attenuated by absorptions above z^*. The problem can be significantly simplified, if the absorption is mainly due to the gas itself. This is an analog to the concept of the Chapman layer in the ionosphere (e.g. Banks and Kockarts, 1973).

In the following I first derive the analytical formula for the case of self-shielding and then extend the formula to the generic situation.

I intend to relate the ultraviolet optical depth to the pressure level. The ultraviolet optical depth in the dissociating wavelength range of a specified gas is

$$\tau_{\mathrm{UV}} = \frac{\sigma_{\mathrm{UV}}}{\mu_0} \int_{z^*}^{\infty} n(z) \ dz, \tag{B.9}$$

where σ_{UV} is the characteristic cross section in the wavelengths that lead to photolysis. Under hydrostatic conditions,

$$P_{\mathrm{atm}} = M_{\mathrm{atm}} g \int_{z^*}^{\infty} N(z) \ dz, \tag{B.10}$$

where P_{atm} is the atmospheric pressure at the altitude of z^* and M_{atm} is the mean molecular mass. One can define the column averaged mixing ratio as

$$F = \frac{\int_{z^*}^{\infty} n(z) \ dz}{\int_{z^*}^{\infty} N(z) \ dz}, \tag{B.11}$$

and then the UV optical depth at z^* can be related to the atmospheric pressure as

$$\tau_{\mathrm{UV}} = \frac{\sigma_{\mathrm{UV}} F P_{\mathrm{atm}}}{\mu_0 g M_{\mathrm{atm}}}.$$ (B.12)

The molecule is subject to rapid photodissociation if the UV optical depth is smaller than unity, or $\tau_{\mathrm{UV}} < 1$, so that the critical pressure level above which photolysis is important is

$$P^* = \frac{\mu_0 g M_{\mathrm{atm}}}{\sigma_{\mathrm{UV}} F}.$$ (B.13)

The equation (B.13) can be readily extended to include other gases in the atmosphere may provide additional shielding, viz.,

$$P^* = \frac{\mu_0 g M_{\mathrm{atm}}}{\sigma_{\mathrm{UV}} F + \sigma'_{\mathrm{UV}} F'},$$ (B.14)

where σ'_{UV} and F' is the cross section and the mixing ratio of the interfering species.

Equations (B.13, B.14) define a critical pressure level (or altitude) for each radiative trace gas subject to photolysis. Above the critical altitude, the gas is readily photodissociated and its mixing ratio decreases with altitude rapidly if no efficient reformation pathway exists; below the critical altitude, photolysis is not important and the gas is likely to be well-mixed. The critical pressure (altitude) is also defined for a certain mixing ratio. If the mixing ratio is larger, the critical pressure is smaller, and the gas is photochemically stable up to a higher altitude. Mean cross sections in dissociating wavelengths and the critical pressure level corresponding to 1 ppm mixing ratio of common spectrally active gases are tabulated in Table B.1.

Despite simplicity, equations (B.13, B.14) predict the behavior of trace gases in the upper part of terrestrial exoplanet atmospheres, in agreement with results from the full photochemistry code. For example, 10-ppm methane in the N_2 atmosphere is photodissociated above an altitude of ~ 10 Pa pressure level, in agreement with Table B.1. Using equation (B.14) I estimate the 10-ppm critical pressure for methane in the CO_2 atmosphere to be about 0.1 Pa, consistent with results from the full photochemistry code as shown in Figure 3-1. For another example, for H_2S in the H_2

Table B.1: Mean cross sections in dissociating wavelengths of common atmospheric trace gases and the critical pressures for photochemical stability. The mean cross sections are weighted by the Solar spectrum and quantum yields in the dissociation wavelengths. The critical pressure is evaluated according to equation (B.13) with the conditions of $\mu_0 = 0.5$, $g = 9.8$ m s^{-1}, $M_{\mathrm{atm}} = 4.65 \times 10^{-26}$ kg (N$_2$-dominated atmosphere), and $F = 10^{-6}$ (1 ppm). The additional shielding from other gases and reforming reactions are omitted in the estimate of critical pressures.

Name	Dissociation Wavelength (nm)	Mean Cross Section (cm^2)	1-ppm Critical Pressure (Pa)
H$_2$	$18 - 85$	1.10E-17	2.07E+02
O$_2$	$4 - 245$	7.18E-21	3.17E+05
H$_2$O	$6 - 198$	1.72E-18	1.33E+03
NH$_3$	$8 - 230$	1.31E-18	1.73E+03
N$_2$O	$130 - 240$	1.38E-20	1.65E+05
CH$_4$	$52 - 152$	1.81E-17	1.26E+02
CO$_2$	$35 - 205$	7.44E-22	3.06E+06
H$_2$S	$5 - 259$	1.11E-18	2.05E+03
OCS	$186 - 296$	2.74E-20	8.33E+04
SO$_2$	$5 - 395$	3.74E-18	6.09E+02

atmosphere, the near-surface mixing ratio is about 10^{-9}, and according to Table B.1, I find the critical pressure is in the order of 10^5 Pa, i.e., H$_2$S is photodissociated at all altitudes of the H$_2$ atmosphere. This is again consistent with the full photochemistry model (see the upper panel of Figure 3-1).

Equations (B.13, B.14) provide an order-of-magnitude assessment on whether or not a vertically well mixed distribution of gas is a good assumption when investigating spectra of super Earths. When the critical pressure defined by equations (B.13, B.14) is smaller than the pressure level that generates the spectral feature, it is plausible to assume the gas is vertically well-mixed. However, if the critical pressure is larger than the pressure level that generates the spectral feature, cautions should be taken because the gas could be photochemically depleted. If data suggests an abundance of a certain gas above its critical altitude, an additional mechanism, such as ultraviolet shielding by other gases, or efficient reformation, must be at play. In summary, equations (B.13, B.14) provide a simplified approach to take into account the effects of photochemistry for the interpretation of spectral features and for observation planning.

Bibliography

Allard, F., Hauschildt, P. H., Alexander, D. R., and Starrfield, S. (1997). Model Atmospheres of Very Low Mass Stars and Brown Dwarfs. *Annual Review of Astronomy & Astrophysics*, 35:137–177.

Allen, M., Yung, Y. L., and Pinto, J. P. (1980). Titan - Aerosol photochemistry and variations related to the sunspot cycle. *Astrophysical Journal Letters*, 242:L125–L128.

Anbar, A. D., Allen, M., and Nair, H. A. (1993). Photodissociation in the atmosphere of Mars - Impact of high resolution, temperature-dependent CO2 cross-section measurements. *Journal of Geophysical Research*, 98:10925.

Angel, J. R. P., Cheng, A. Y. S., and Woolf, N. J. (1986). A space telescope for infrared spectroscopy of earth-like planets. *Nature*, 322:341–343.

Archer, D. (2010). *The Long Thaw: How Humans Are Changing the Next 100,000 Years of Earth's Climate*.

Atkinson, R., Baulch, D. L., Cox, R. A., Crowley, J. N., Hampson, R. F., Hynes, R. G., Jenkin, M. E., Rossi, M. J., and Troe, J. (2004). Evaluated kinetic and photochemical data for atmospheric chemistry: Volume I - gas phase reactions of O_x, HO_x, NO_x and SO_x species. *Atmospheric Chemistry & Physics*, 4:1461–1738.

Atreya, S. K., Adams, E. Y., Niemann, H. B., Demick-Montelara, J. E., Owen, T. C., Fulchignoni, M., Ferri, F., and Wilson, E. H. (2006). Titan's methane cycle. *Planetary and Space Science*, 54:1177–1187.

Au, J. (1997). Absolute oscillator strenghts for the valence-shell photoabsorption (2 200 eV) and the molecular and dissociative photoionization (11 80 eV) of nitrogen dioxide. *Chemical Physics*, 218:109–126.

Backx, C., Wight, G. R., and Van der Wiel, M. J. (1976). Oscillator strengths (10-70 eV) for absorption, ionization and dissociation in H_2, HD and D_2, obtained by an electron-ion coincidence method. *Journal of Physics B Atomic Molecular Physics*, 9:315–331.

Banks, P. M. and Kockarts, G. (1973). *Aeronomy*.

Barclay, T., Rowe, J. F., Lissauer, J. J., Huber, D., Fressin, F., Howell, S. B., Bryson, S. T., Chaplin, W. J., Désert, J.-M., Lopez, E. D., Marcy, G. W., Mullally, F., Ragozzine, D., Torres, G., Adams, E. R., Agol, E., Barrado, D., Basu, S., Bedding, T. R., Buchhave, L. A., Charbonneau, D., Christiansen, J. L., Christensen-Dalsgaard, J., Ciardi, D., Cochran, W. D., Dupree, A. K., Elsworth, Y., Everett, M., Fischer, D. A., Ford, E. B., Fortney, J. J., Geary, J. C., Haas, M. R., Handberg, R., Hekker, S., Henze, C. E., Horch, E., Howard, A. W., Hunter, R. C., Isaacson, H., Jenkins, J. M., Karoff, C., Kawaler, S. D., Kjeldsen, H., Klaus, T. C., Latham, D. W., Li, J., Lillo-Box, J., Lund, M. N., Lundkvist, M., Metcalfe, T. S., Miglio, A., Morris, R. L., Quintana, E. V., Stello, D., Smith, J. C., Still, M., and Thompson, S. E. (2013). A sub-Mercury-sized exoplanet. *Nature*, 494:452–454.

Barstow, J. K., Aigrain, S., Irwin, P. G. J., Bowles, N., Fletcher, L. N., and Lee, J.-M. (2013). On the potential of the EChO mission to characterize gas giant atmospheres. *Monthly Notices of the Royal Astronomical Society*, 430:1188–1207.

Basch, H., Robin, M. B., Kuebler, N. A., Baker, C., and Turner, D. W. (1969). Optical and Photoelectron Spectra of Small Rings. III. The Saturated Three-Membered Rings. *Journal of Chemical Physics*, 51:52–66.

Batalha, N. M., Borucki, W. J., Bryson, S. T., Buchhave, L. A., Caldwell, D. A., Christensen-Dalsgaard, J., Ciardi, D., Dunham, E. W., Fressin, F., Gautier, III, T. N., Gilliland, R. L., Haas, M. R., Howell, S. B., Jenkins, J. M., Kjeldsen, H., Koch, D. G., Latham, D. W., Lissauer, J. J., Marcy, G. W., Rowe, J. F., Sasselov, D. D., Seager, S., Steffen, J. H., Torres, G., Basri, G. S., Brown, T. M., Charbonneau, D., Christiansen, J., Clarke, B., Cochran, W. D., Dupree, A., Fabrycky, D. C., Fischer, D., Ford, E. B., Fortney, J., Girouard, F. R., Holman, M. J., Johnson, J., Isaacson, H., Klaus, T. C., Machalek, P., Moorehead, A. V., Morehead, R. C., Ragozzine, D., Tenenbaum, P., Twicken, J., Quinn, S., VanCleve, J., Walkowicz, L. M., Welsh, W. F., Devore, E., and Gould, A. (2011). Kepler's First Rocky Planet: Kepler-10b. *Astrophysical Journal*, 729:27.

Batalha, N. M., Borucki, W. J., Koch, D. G., Bryson, S. T., Haas, M. R., Brown, T. M., Caldwell, D. A., Hall, J. R., Gilliland, R. L., Latham, D. W., Meibom, S., and Monet, D. G. (2010). Selection, Prioritization, and Characteristics of Kepler Target Stars. *Astrophysical Journal Letters*, 713:L109–L114.

Batalha, N. M., Rowe, J. F., Bryson, S. T., Barclay, T., Burke, C. J., Caldwell, D. A., Christiansen, J. L., Mullally, F., Thompson, S. E., Brown, T. M., Dupree, A. K., Fabrycky, D. C., Ford, E. B., Fortney, J. J., Gilliland, R. L., Isaacson, H., Latham, D. W., Marcy, G. W., Quinn, S. N., Ragozzine, D., Shporer, A., Borucki, W. J., Ciardi, D. R., Gautier, III, T. N., Haas, M. R., Jenkins, J. M., Koch, D. G., Lissauer, J. J., Rapin, W., Basri, G. S., Boss, A. P., Buchhave, L. A., Carter, J. A., Charbonneau, D., Christensen-Dalsgaard, J., Clarke, B. D., Cochran, W. D., Demory, B.-O., Desert, J.-M., Devore, E., Doyle, L. R., Esquerdo, G. A., Everett, M., Fressin, F., Geary, J. C., Girouard, F. R., Gould, A., Hall, J. R., Holman, M. J.,

Howard, A. W., Howell, S. B., Ibrahim, K. A., Kinemuchi, K., Kjeldsen, H., Klaus, T. C., Li, J., Lucas, P. W., Meibom, S., Morris, R. L., Prša, A., Quintana, E., Sanderfer, D. T., Sasselov, D., Seader, S. E., Smith, J. C., Steffen, J. H., Still, M., Stumpe, M. C., Tarter, J. C., Tenenbaum, P., Torres, G., Twicken, J. D., Uddin, K., Van Cleve, J., Walkowicz, L., and Welsh, W. F. (2013). Planetary Candidates Observed by Kepler. III. Analysis of the First 16 Months of Data. *Astrophysical Journal Supplement Series*, 204:24.

Bauer, S. J. and Lammer, H. (2004). *Planetary aeronomy : atmosphere environments in planetary systems.*

Baulch, D. L., Bowman, C. T., Cobos, C. J., Cox, R. A., Just, T., Kerr, J. A., Pilling, M. J., Stocker, D., Troe, J., Tsang, W., Walker, R. W., and Warnatz, J. (2005). Evaluated kinetic data for combustion modeling: Supplement ii. *Journal of Physical and Chemical Reference Data*, 34(3):757–1397.

Baulch, D. L., Cobos, C. J., Cox, R. A., Frank, P., Hayman, G., Just, T., Kerr, J. A., Murrells, T., Pilling, M. J., Troe, J., Walker, R. W., and Warnatz, J. (1994). Evaluated kinetic data for combustion modeling. supplement i. *Journal of Physical and Chemical Reference Data*, 23(6):847–848.

Bean, J. L., Désert, J.-M., Kabath, P., Stalder, B., Seager, S., Miller-Ricci Kempton, E., Berta, Z. K., Homeier, D., Walsh, S., and Seifahrt, A. (2011). The Optical and Near-infrared Transmission Spectrum of the Super-Earth GJ 1214b: Further Evidence for a Metal-rich Atmosphere. *Astrophysical Journal*, 743:92.

Bean, J. L., Miller-Ricci Kempton, E., and Homeier, D. (2010). A ground-based transmission spectrum of the super-Earth exoplanet GJ 1214b. *Nature*, 468:669–672.

Beichman, C., Lawson, P., Lay, O., Ahmed, A., Unwin, S., and Johnston, K. (2006). Status of the terrestrial planet finder interferometer (TPF-I). In *Society of Photo-Optical Instrumentation Engineers (SPIE) Conference Series*, volume 6268 of *Society of Photo-Optical Instrumentation Engineers (SPIE) Conference Series*.

Beichman, C. A., Woolf, N. J., and Lindensmith, C. A. (1999). *The Terrestrial Planet Finder (TPF) : a NASA Origins Program to search for habitable planets.*

Belu, A. R., Selsis, F., Morales, J.-C., Ribas, I., Cossou, C., and Rauer, H. (2011). Primary and secondary eclipse spectroscopy with JWST: exploring the exoplanet parameter space. *Astronomy & Astrophysics*, 525:A83.

Bénilan, Y., Smith, N., Jolly, A., and Raulin, F. (2000). The long wavelength range temperature variations of the mid-UV acetylene absorption coefficient. *Planetary and Space Science*, 48:463–471.

Benneke, B. and Seager, S. (2012). Atmospheric Retrieval for Super-Earths: Uniquely Constraining the Atmospheric Composition with Transmission Spectroscopy. *Astrophysical Journal*, 753:100.

Berta, Z. K., Charbonneau, D., Désert, J.-M., Miller-Ricci Kempton, E., McCullough, P. R., Burke, C. J., Fortney, J. J., Irwin, J., Nutzman, P., and Homeier, D. (2012). The Flat Transmission Spectrum of the Super-Earth GJ1214b from Wide Field Camera 3 on the Hubble Space Telescope. *Astrophysical Journal*, 747:35.

Best, M. G. and Christiansen, E. H. (2001). *Igneous Petrology*.

Bézard, B., Lellouch, E., Strobel, D., Maillard, J.-P., and Drossart, P. (2002). Carbon Monoxide on Jupiter: Evidence for Both Internal and External Sources. *Icarus*, 159:95–111.

Billmers, R. I. and Smith, A. L. (1991). Ultraviolet-visible absorption spectra of equilibrium sulfur vapor: molar absorptivity spectra of s3 and s4. *The Journal of Physical Chemistry*, 95(11):4242–4245.

Blewett, D. T., Chabot, N. L., Denevi, B. W., Ernst, C. M., Head, J. W., Izenberg, N. R., Murchie, S. L., Solomon, S. C., Nittler, L. R., McCoy, T. J., Xiao, Z., Baker, D. M. H., Fassett, C. I., Braden, S. E., Oberst, J., Scholten, F., Preusker, F., and Hurwitz, D. M. (2011). Hollows on Mercury: MESSENGER Evidence for Geologically Recent Volatile-Related Activity. *Science*, 333:1856–.

Blewett, D. T., Lucey, P. G., Hawke, B. R., Ling, G. G., and Robinson, M. S. (1997). A Comparison of Mercurian Reflectance and Spectral Quantities with Those of the Moon. *Icarus*, 129:217–231.

Bogumil, K., Orphal, J., Homann, T., Voigt, S., Spietz, P., Fleischmann, O., Vogel, A., Hartmann, M., Kromminga, H., Bovensmann, H., Frerick, J., and Burrows, J. (2003). Measurements of molecular absorption spectra with the sciamachy pre-flight model: instrument characterization and reference data for atmospheric remote-sensing in the 230-2380 nm region. *Journal of Photochemistry and Photobiology A: Chemistry*, 157(2-3):167 – 184.

Bond, J. C., O'Brien, D. P., and Lauretta, D. S. (2010). The Compositional Diversity of Extrasolar Terrestrial Planets. I. In Situ Simulations. *Astrophysical Journal*, 715:1050–1070.

Bonfils, X., Gillon, M., Forveille, T., Delfosse, X., Deming, D., Demory, B.-O., Lovis, C., Mayor, M., Neves, V., Perrier, C., Santos, N. C., Seager, S., Udry, S., Boisse, I., and Bonnefoy, M. (2011). A short-period super-Earth orbiting the M2.5 dwarf GJ 3634. Detection with HARPS velocimetry and transit search with Spitzer photometry. *Astronomy & Astrophysics*, 528:A111.

Borucki, W. J., Agol, E., Fressin, F., Kaltenegger, L., Rowe, J., Isaacson, H., Fischer, D., Batalha, N., Lissauer, J. J., Marcy, G. W., Fabrycky, D., Dsert, J.-M., Bryson, S. T., Barclay, T., Bastien, F., Boss, A., Brugamyer, E., Buchhave, L. A., Burke, C., Caldwell, D. A., Carter, J., Charbonneau, D., Crepp, J. R., Christensen-Dalsgaard, J., Christiansen, J. L., Ciardi, D., Cochran, W. D., DeVore, E., Doyle, L., Dupree, A. K., Endl, M., Everett, M. E., Ford, E. B., Fortney, J., Gautier,

T. N., Geary, J. C., Gould, A., Haas, M., Henze, C., Howard, A. W., Howell, S. B., Huber, D., Jenkins, J. M., Kjeldsen, H., Kolbl, R., Kolodziejczak, J., Latham, D. W., Lee, B. L., Lopez, E., Mullally, F., Orosz, J. A., Prsa, A., Quintana, E. V., Sanchis-Ojeda, R., Sasselov, D., Seader, S., Shporer, A., Steffen, J. H., Still, M., Tenenbaum, P., Thompson, S. E., Torres, G., Twicken, J. D., Welsh, W. F., and Winn, J. N. (2013). Kepler-62: A five-planet system with planets of 1.4 and 1.6 earth radii in the habitable zone. *Science*, 340(6132):587–590.

Borucki, W. J., Koch, D. G., Basri, G., Batalha, N., Brown, T. M., Bryson, S. T., Caldwell, D., Christensen-Dalsgaard, J., Cochran, W. D., DeVore, E., Dunham, E. W., Gautier, III, T. N., Geary, J. C., Gilliland, R., Gould, A., Howell, S. B., Jenkins, J. M., Latham, D. W., Lissauer, J. J., Marcy, G. W., Rowe, J., Sasselov, D., Boss, A., Charbonneau, D., Ciardi, D., Doyle, L., Dupree, A. K., Ford, E. B., Fortney, J., Holman, M. J., Seager, S., Steffen, J. H., Tarter, J., Welsh, W. F., Allen, C., Buchhave, L. A., Christiansen, J. L., Clarke, B. D., Das, S., Désert, J.-M., Endl, M., Fabrycky, D., Fressin, F., Haas, M., Horch, E., Howard, A., Isaacson, H., Kjeldsen, H., Kolodziejczak, J., Kulesa, C., Li, J., Lucas, P. W., Machalek, P., McCarthy, D., MacQueen, P., Meibom, S., Miquel, T., Prsa, A., Quinn, S. N., Quintana, E. V., Ragozzine, D., Sherry, W., Shporer, A., Tenenbaum, P., Torres, G., Twicken, J. D., Van Cleve, J., Walkowicz, L., Witteborn, F. C., and Still, M. (2011). Characteristics of Planetary Candidates Observed by Kepler. II. Analysis of the First Four Months of Data. *Astrophysical Journal*, 736:19.

Borucki, W. J., Koch, D. G., Batalha, N., Bryson, S. T., Rowe, J., Fressin, F., Torres, G., Caldwell, D. A., Christensen-Dalsgaard, J., Cochran, W. D., DeVore, E., Gautier, T. N., Geary, J. C., Gilliland, R., Gould, A., Howell, S. B., Jenkins, J. M., Latham, D. W., Lissauer, J. J., Marcy, G. W., Sasselov, D., Boss, A., Charbonneau, D., Ciardi, D., Kaltenegger, L., Doyle, L., Dupree, A. K., Ford, E. B., Fortney, J., Holman, M. J., Steffen, J. H., Mullally, F., Still, M., Tarter, J., Ballard, S., Buchhave, L. A., Carter, J., Christiansen, J. L., Demory, B.-O., Désert, J.-M., Dressing, C., Endl, M., Fabrycky, D., Fischer, D., Haas, M. R., Henze, C., Horch, E., Howard, A. W., Isaacson, H., Kjeldsen, H., Johnson, J. A., Klaus, T., Kolodziejczak, J., Barclay, T., Li, J., Meibom, S., Prsa, A., Quinn, S. N., Quintana, E. V., Robertson, P., Sherry, W., Shporer, A., Tenenbaum, P., Thompson, S. E., Twicken, J. D., Van Cleve, J., Welsh, W. F., Basu, S., Chaplin, W., Miglio, A., Kawaler, S. D., Arentoft, T., Stello, D., Metcalfe, T. S., Verner, G. A., Karoff, C., Lundkvist, M., Lund, M. N., Handberg, R., Elsworth, Y., Hekker, S., Huber, D., Bedding, T. R., and Rapin, W. (2012). Kepler-22b: A 2.4 Earth-radius Planet in the Habitable Zone of a Sun-like Star. *Astrophysical Journal*, 745:120.

Borysow, A. (2002). Collision-induced absorption coefficients of H_2 pairs at temperatures from 60 K to 1000 K. *Astronomy & Astrophysics*, 390:779–782.

Brasseur, G. P. and Solomon, S. (2005). *Aeronomy of the Middle Atmosphere*.

Brion, C., Tan, K., van der Wiel, M., and van der Leeuw, P. (1979). Dipole oscillator

strengths for the photoabsorption, photoionization and fragmentation of molecular oxygen. *Journal of Electron Spectroscopy and Related Phenomena*, 17(2):101 – 119.

Broeg, C., Fortier, A., Ehrenreich, D., Alibert, Y., Baumjohann, W., Benz, W., Deleuil, M., Gillon, M., Ivanov, A., Liseau, R., Meyer, M., Oloffson, G., Pagano, I., Piotto, G., Pollacco, D., Queloz, D., Ragazzoni, R., Renotte, E., Steller, M., and Thomas, N. (2013). CHEOPS: A transit photometry mission for ESA's small mission programme. In *European Physical Journal Web of Conferences*, volume 47 of *European Physical Journal Web of Conferences*, page 3005.

Brogi, M., Snellen, I. A. G., de Kok, R. J., Albrecht, S., Birkby, J., and de Mooij, E. J. W. (2012). The signature of orbital motion from the dayside of the planet τ Boötis b. *Nature*, 486:502–504.

Brown, S. M. and Elkins-Tanton, L. T. (2009). Compositions of Mercury's earliest crust from magma ocean models. *Earth and Planetary Science Letters*, 286:446–455.

Burcat, A. and Ruscic, B. (2005). *Third Millennium Ideal Gas and Condensed Phase Thermochemical Database for Combustion with Updates from Active Thermochemical Tables.*

Burgisser, A. and Scaillet, B. (2007). Redox evolution of a degassing magma rising to the surface. *Nature*, 445:194–197.

Burns, R. G. (1993). *Mineralogical Applications of Crystal Field Theory.*

Burton, G. (1992). Absolute oscillator strengths for photoabsorption (6 360 eV) and ionic photofragmentation (10 80 eV) of methanol. *Chemical Physics*, 167:349–367.

Burton, G. R., Chan, W. F., Cooper, G., Brion, C., Kumar, A., and Meath, W. J. (1994). Valence shell absolute photoabsorption oscillator strengths, constrained dipole oscillator strength distributions, and dipole properties for ch3nh2, (ch3)2nh, and (ch3)3n. *Canadian Journal of Chemistry*, 72(3):529–546.

Calvin, W. M. and Clark, R. N. (1991). Modeling the reflectance spectrum of Callisto 0.25 to 4.1 microns. *Icarus*, 89:305–317.

Carlson, R. W., Kamp, L. W., Baines, K. H., Pollack, J. B., Grinspoon, D. H., Encrenaz, T., Drossart, P., and Taylor, F. W. (1993). Variations in Venus cloud particle properties: A new view of Venus's cloud morphology as observed by Galileo Near-Infrared Mapping Spectrometer. *Planetary and Space Science*, 41:477–485.

Cecchi-Pestellini, C., Ciaravella, A., Micela, G., and Penz, T. (2009). The relative role of EUV radiation and X-rays in the heating of hydrogen-rich exoplanet atmospheres. *Astronomy & Astrophysics*, 496:863–868.

Chan, W. (1993). The electronic spectrum of water in the discrete and continuum regions. Absolute optical oscillator strengths for photoabsorption (6 200 eV). *Chemical Physics*, 178:387–400.

Charbonneau, D., Allen, L. E., Megeath, S. T., Torres, G., Alonso, R., Brown, T. M., Gilliland, R. L., Latham, D. W., Mandushev, G., O'Donovan, F. T., and Sozzetti, A. (2005). Detection of Thermal Emission from an Extrasolar Planet. *Astrophysical Journal*, 626:523–529.

Charbonneau, D., Berta, Z. K., Irwin, J., Burke, C. J., Nutzman, P., Buchhave, L. A., Lovis, C., Bonfils, X., Latham, D. W., Udry, S., Murray-Clay, R. A., Holman, M. J., Falco, E. E., Winn, J. N., Queloz, D., Pepe, F., Mayor, M., Delfosse, X., and Forveille, T. (2009). A super-Earth transiting a nearby low-mass star. *Nature*, 462:891–894.

Charbonneau, D., Brown, T. M., Noyes, R. W., and Gilliland, R. L. (2002). Detection of an Extrasolar Planet Atmosphere. *Astrophysical Journal*, 568:377–384.

Chase, M. (1998). *NIST-JANAF Thermochemical Tables, 4th Edition*.

Cheek, L. C., Pieters, C. M., Dyar, M. D., and Milam, K. A. (2009). Revisiting Plagioclase Optical Properties for Lunar Exploration. In *Lunar and Planetary Institute Science Conference Abstracts*, volume 40 of *Lunar and Planetary Inst. Technical Report*, page 1928.

Chen, F. Z. and Wu, C. Y. R. (2004). Temperature-dependent photoabsorption cross sections in the VUV-UV region. I. Methane and ethane. *J. Quant. Spectrosc. Radiat. Transfer.*, 85:195–209.

Cheng, B.-M., Bahou, M., Lee, Y.-P., and Lee, L. C. (2002). Absorption cross sections and solar photodissociation rates of deuterated isotopomers of methanol. *Journal of Geophysical Research (Space Physics)*, 107:1161.

Cheng, B.-M., Lu, H.-C., Chen, H.-K., Bahou, M., Lee, Y.-P., Mebel, A. M., Lee, L. C., Liang, M.-C., and Yung, Y. L. (2006). Absorption Cross Sections of NH_3, NH_2D, NHD_2, and ND_3 in the Spectral Range 140-220 nm and Implications for Planetary Isotopic Fractionation. *Astrophysical Journal*, 647:1535–1542.

Chilcote, J. K., Larkin, J. E., Maire, J., Perrin, M. D., Fitzgerald, M. P., Doyon, R., Thibault, S., Bauman, B., Macintosh, B. A., Graham, J. R., and Saddlemyer, L. (2012). Performance of the integral field spectrograph for the Gemini Planet Imager. In *Society of Photo-Optical Instrumentation Engineers (SPIE) Conference Series*, volume 8446 of *Society of Photo-Optical Instrumentation Engineers (SPIE) Conference Series*.

Christensen, P. R., Bandfield, J. L., Hamilton, V. E., Howard, D. A., Lane, M. D., Piatek, J. L., Ruff, S. W., and Stefanov, W. L. (2000). A thermal emission spectral library of rock-forming minerals. *Journal of Geophysical Research*, 105:9735–9740.

Clark, R. N. (1999). *Manual of Remote Sensing, Vol. 3, Remote Sensing for the Earth Sciences, Spectroscopy of Rocks and Minerals, and Principles of Spectroscopy.*

Clark, R. N., Swayze, G. A., Wise, R., and et al. (2007). *USGS Digital Spectral Library splib06a: U.S. Geological Survey, Digital Data Series 231.*

Cochran, W. D., Fabrycky, D. C., Torres, G., Fressin, F., Désert, J.-M., Ragozzine, D., Sasselov, D., Fortney, J. J., Rowe, J. F., Brugamyer, E. J., Bryson, S. T., Carter, J. A., Ciardi, D. R., Howell, S. B., Steffen, J. H., Borucki, W. J., Koch, D. G., Winn, J. N., Welsh, W. F., Uddin, K., Tenenbaum, P., Still, M., Seager, S., Quinn, S. N., Mullally, F., Miller, N., Marcy, G. W., MacQueen, P. J., Lucas, P., Lissauer, J. J., Latham, D. W., Knutson, H., Kinemuchi, K., Johnson, J. A., Jenkins, J. M., Isaacson, H., Howard, A., Horch, E., Holman, M. J., Henze, C. E., Haas, M. R., Gilliland, R. L., Gautier, III, T. N., Ford, E. B., Fischer, D. A., Everett, M., Endl, M., Demory, B.-O., Deming, D., Charbonneau, D., Caldwell, D., Buchhave, L., Brown, T. M., and Batalha, N. (2011). Kepler-18b, c, and d: A System of Three Planets Confirmed by Transit Timing Variations, Light Curve Validation, Warm-Spitzer Photometry, and Radial Velocity Measurements. *Astrophysical Journal Supplement Series*, 197:7.

Conte, S. D. and deBoor, C. (1972). *Elementary Numerical Analysis.*

Cook, G. R. and Metzger, P. H. (1964). Photoionization and Absorption Cross Sections of H2 and D2 in the Vacuum Ultraviolet Region. *Journal of the Optical Society of America (1917-1983)*, 54:968.

Cooper, C. S. and Showman, A. P. (2006). Dynamics and Disequilibrium Carbon Chemistry in Hot Jupiter Atmospheres, with Application to HD 209458b. *Astrophysical Journal*, 649:1048–1063.

Cooper, G., Burton, G. R., and Brion, C. (1995). Absolute uv and soft x-ray photoabsorption of acetylene by high resolution dipole (e,e) spectroscopy. *Journal of Electron Spectroscopy and Related Phenomena*, 73(2):139 – 148.

Coustenis, A. (2005). Formation and Evolution of Titan's Atmosphere. *Space Science Reviews*, 116:171–184.

Cowan, N. B., Agol, E., Meadows, V. S., Robinson, T., Livengood, T. A., Deming, D., Lisse, C. M., A'Hearn, M. F., Wellnitz, D. D., Seager, S., Charbonneau, D., and EPOXI Team (2009). Alien Maps of an Ocean-bearing World. *Astrophysical Journal*, 700:915–923.

Cox, A. N. (2000). *Allen's astrophysical quantities.*

Crampton, D. and Simard, L. (2006). Instrument concepts and scientific opportunities for TMT. In *Society of Photo-Optical Instrumentation Engineers (SPIE) Conference Series*, volume 6269 of *Society of Photo-Optical Instrumentation Engineers (SPIE) Conference Series.*

Croll, B., Albert, L., Jayawardhana, R., Miller-Ricci Kempton, E., Fortney, J. J., Murray, N., and Neilson, H. (2011). Broadband Transmission Spectroscopy of the Super-Earth GJ 1214b Suggests a Low Mean Molecular Weight Atmosphere. *Astrophysical Journal*, 736:78.

Curdt, W., Landi, E., and Feldman, U. (2004). The SUMER spectral atlas of solar coronal features. *Astronomy & Astrophysics*, 427:1045–1054.

Curran, H. J. (2006). Rate constant estimation for c1 to c4 alkyl and alkoxyl radical decomposition. *International Journal of Chemical Kinetics*, 38(4):250–275.

Dalgarno, A. and Williams, D. A. (1962). Rayleigh Scattering by Molecular Hydrogen. *Astrophysical Journal*, 136:690–692.

Dawson, R. I. and Fabrycky, D. C. (2010). Radial Velocity Planets De-aliased: A New, Short Period for Super-Earth 55 Cnc e. *Astrophysical Journal*, 722:937–953.

de Almeida, A. A. and Singh, P. D. (1986). Photodissociation lifetime of (S-32)2 molecule in comets. *Earth Moon and Planets*, 36:117–125.

de Mooij, E. J. W., Brogi, M., de Kok, R. J., Koppenhoefer, J., Nefs, S. V., Snellen, I. A. G., Greiner, J., Hanse, J., Heinsbroek, R. C., Lee, C. H., and van der Werf, P. P. (2012). Optical to near-infrared transit observations of super-Earth GJ 1214b: water-world or mini-Neptune? *Astronomy & Astrophysics*, 538:A46.

de Pater, I. and Lissauer, J. J. (2001). *Planetary Sciences*.

Delgado Mena, E., Israelian, G., González Hernández, J. I., Bond, J. C., Santos, N. C., Udry, S., and Mayor, M. (2010). Chemical Clues on the Formation of Planetary Systems: C/O Versus Mg/Si for HARPS GTO Sample. *Astrophysical Journal*, 725:2349–2358.

Deming, D., Seager, S., Richardson, L. J., and Harrington, J. (2005). Infrared radiation from an extrasolar planet. *Nature*, 434:740–743.

Deming, D., Seager, S., Winn, J., Miller-Ricci, E., Clampin, M., Lindler, D., Greene, T., Charbonneau, D., Laughlin, G., Ricker, G., Latham, D., and Ennico, K. (2009). Discovery and Characterization of Transiting Super Earths Using an All-Sky Transit Survey and Follow-up by the James Webb Space Telescope. *Publications of the Astronomical Society of the Pacific*, 121:952–967.

Deming, D., Wilkins, A., McCullough, P., Burrows, A., Fortney, J. J., Agol, E., Dobbs-Dixon, I., Madhusudhan, N., Crouzet, N., Desert, J.-M., Gilliland, R. L., Haynes, K., Knutson, H. A., Line, M., Magic, Z., Mandell, A. M., Ranjan, S., Charbonneau, D., Clampin, M., Seager, S., and Showman, A. P. (2013). Infrared Transmission Spectroscopy of the Exoplanets HD209458b and XO-1b Using the Wide Field Camera-3 on the Hubble Space Telescope. *ArXiv e-prints*.

Demory, B.-O., Gillon, M., Deming, D., Valencia, D., Seager, S., Benneke, B., Lovis, C., Cubillos, P., Harrington, J., Stevenson, K. B., Mayor, M., Pepe, F., Queloz, D., Ségransan, D., and Udry, S. (2011). Detection of a transit of the super-Earth 55 Cancri e with warm Spitzer. *Astronomy & Astrophysics*, 533:A114.

Demory, B.-O., Gillon, M., Seager, S., Benneke, B., Deming, D., and Jackson, B. (2012a). Detection of Thermal Emission from a Super-Earth. *Astrophysical Journal Letters*, 751:L28.

Demory, B.-O., Gillon, M., Seager, S., Hu, R., Benneke, B., Stamenkovic, V., de Wit, J., Deming, D., Kane, S., and Krick, J. (2012b). The First Orbital Phase Curve of a Rocky Exoplanet. *Spitzer Proposal*, page 90208.

Des Marais, D. J., Harwit, M. O., Jucks, K. W., Kasting, J. F., Lin, D. N. C., Lunine, J. I., Schneider, J., Seager, S., Traub, W. A., and Woolf, N. J. (2002). Remote Sensing of Planetary Properties and Biosignatures on Extrasolar Terrestrial Planets. *Astrobiology*, 2:153–181.

Désert, J.-M., Bean, J., Miller-Ricci Kempton, E., Berta, Z. K., Charbonneau, D., Irwin, J., Fortney, J., Burke, C. J., and Nutzman, P. (2011). Observational Evidence for a Metal-rich Atmosphere on the Super-Earth GJ1214b. *Astrophysical Journal Letters*, 731:L40.

Domagal-Goldman, S. D., Meadows, V. S., Claire, M. W., and Kasting, J. F. (2011). Using Biogenic Sulfur Gases as Remotely Detectable Biosignatures on Anoxic Planets. *Astrobiology*, 11:419–441.

Donahue, T. M., Hoffman, J. H., Hodges, R. R., and Watson, A. J. (1982). Venus was wet - A measurement of the ratio of deuterium to hydrogen. *Science*, 216:630–633.

Dressing, C. D. and Charbonneau, D. (2013). The Occurrence Rate of Small Planets around Small Stars. *ArXiv e-prints*.

Duke, M. B., Woo, C. C., Bird, M. L., Sellers, G. A., and Finkelman, R. B. (1970). Lunar Soil: Size Distribution and Mineralogical Constituents. *Science*, 167:648–650.

Dumusque, X., Pepe, F., Lovis, C., Ségransan, D., Sahlmann, J., Benz, W., Bouchy, F., Mayor, M., Queloz, D., Santos, N., and Udry, S. (2012). An Earth-mass planet orbiting α Centauri B. *Nature*, 491:207–211.

Ehrenreich, D., Bourrier, V., Bonfils, X., Lecavelier des Etangs, A., Hébrard, G., Sing, D. K., Wheatley, P. J., Vidal-Madjar, A., Delfosse, X., Udry, S., Forveille, T., and Moutou, C. (2012). Hint of a transiting extended atmosphere on 55 Cancri b. *Astronomy & Astrophysics*, 547:A18.

Elkins-Tanton, L. T., Hess, P. C., and Parmentier, E. M. (2005). Possible formation of ancient crust on Mars through magma ocean processes. *Journal of Geophysical Research (Planets)*, 110:12.

Elkins-Tanton, L. T. and Seager, S. (2008). Ranges of Atmospheric Mass and Composition of Super-Earth Exoplanets. *Astrophysical Journal*, 685:1237–1246.

Fagerström, K., Lund, A., Mahmoud, G., Jodkowski, J. T., and Ratajczak, E. (1993). Kinetics of the gas-phase reaction between ethyl and hydroxyl radicals. *Chemical Physics Letters*, 208:321–327.

Fahr, A., Hassanzadeh, P., and Atkinson, D. (1998). Ultraviolet absorption spectrum and cross-sections of vinyl (CH) radical in the 225 238 nm region. *Chemical Physics*, 236:43–51.

Farmer, V. C. (1974). *The Infra-Red Spectra of Minerals*.

Farquhar, J., Bao, H., and Thiemens, M. (2000). Atmospheric Influence of Earth's Earliest Sulfur Cycle. *Science*, 289:756–759.

Fegley, B. (2008). *Atmospheric Evolution on Venus*.

Fegley, Jr., B. and Lodders, K. (1994). Chemical models of the deep atmospheres of Jupiter and Saturn. *Icarus*, 110:117–154.

Fegley, Jr., B. and Lodders, K. (1996). Atmospheric Chemistry of the Brown Dwarf Gliese 229B: Thermochemical Equilibrium Predictions. *Astrophysical Journal Letters*, 472:L37.

Fegley, Jr., B. and Prinn, R. G. (1985). Equilibrium and nonequilibrium chemistry of Saturn's atmosphere - Implications for the observability of PH3, N2, CO, and GeH4. *Astrophysical Journal*, 299:1067–1078.

Feng, R. (1999a). Absolute oscillator strengths for hydrogen sulphide: I. Photoabsorption in the valence-shell and the S 2p and 2s inner-shell regions (4 260 eV). *Chemical Physics*, 244:127–142.

Feng, R. (1999b). Absolute photoabsorption oscillator strengths by electron energy loss methods: the valence and S 2p and 2s inner shells of sulphur dioxide in the discrete and continuum regions (3.5 260 eV). *Chemical Physics*, 240:371–386.

Figueira, P., Marmier, M., Boué, G., Lovis, C., Santos, N. C., Montalto, M., Udry, S., Pepe, F., and Mayor, M. (2012). Comparing HARPS and Kepler surveys. The alignment of multiple-planet systems. *Astronomy & Astrophysics*, 541:A139.

Finster, K. (2008). Microbiological disproportionation of inorganic sulfur compounds. *Journal of Sulfur Chemistry*, 29(3-4):281–292.

Flynn, L. P. and Mouginis-Mark, P. J. (1992). Cooling rate of an active Hawaiian lava flow from nighttime spectroradiometer measurements. *Geophysical Research Letters*, 19:1783–1786.

Ford, E. B., Seager, S., and Turner, E. L. (2001). Characterization of extrasolar terrestrial planets from diurnal photometric variability. *Nature*, 412:885–887.

Fortney, J. J. (2012). On the Carbon-to-oxygen Ratio Measurement in nearby Sunlike Stars: Implications for Planet Formation and the Determination of Stellar Abundances. *Astrophysical Journal Letters*, 747:L27.

Forveille, T., Bonfils, X., Delfosse, X., Gillon, M., Udry, S., Bouchy, F., Lovis, C., Mayor, M., Pepe, F., Perrier, C., Queloz, D., Santos, N., and Bertaux, J.-L. (2009). The HARPS search for southern extra-solar planets. XIV. Gl 176b, a super-Earth rather than a Neptune, and at a different period. *Astronomy & Astrophysics*, 493:645–650.

France, K., Froning, C. S., Linsky, J. L., Roberge, A., Stocke, J. T., Tian, F., Bushinsky, R., Désert, J.-M., Mauas, P., Vieytes, M., and Walkowicz, L. M. (2013). The Ultraviolet Radiation Environment around M dwarf Exoplanet Host Stars. *Astrophysical Journal*, 763:149.

Fressin, F., Torres, G., Charbonneau, D., Bryson, S. T., Christiansen, J., Dressing, C. D., Jenkins, J. M., Walkowicz, L. M., and Batalha, N. M. (2013). The false positive rate of Kepler and the occurrence of planets. *ArXiv e-prints*.

Fressin, F., Torres, G., Rowe, J. F., Charbonneau, D., Rogers, L. A., Ballard, S., Batalha, N. M., Borucki, W. J., Bryson, S. T., Buchhave, L. A., Ciardi, D. R., Désert, J.-M., Dressing, C. D., Fabrycky, D. C., Ford, E. B., Gautier, III, T. N., Henze, C. E., Holman, M. J., Howard, A., Howell, S. B., Jenkins, J. M., Koch, D. G., Latham, D. W., Lissauer, J. J., Marcy, G. W., Quinn, S. N., Ragozzine, D., Sasselov, D. D., Seager, S., Barclay, T., Mullally, F., Seader, S. E., Still, M., Twicken, J. D., Thompson, S. E., and Uddin, K. (2012). Two Earth-sized planets orbiting Kepler-20. *Nature*, 482:195–198.

García Muñoz, A. and Pallé, E. (2011). Lunar eclipse theory revisited: Scattered sunlight in both the quiescent and the volcanically perturbed atmosphere. *Journal of Quantitative Spectroscopy & Radiative Transfer*, 112:1609–1621.

García Muñoz, A., Zapatero Osorio, M. R., Barrena, R., Montañés-Rodríguez, P., Martín, E. L., and Pallé, E. (2012). Glancing Views of the Earth: From a Lunar Eclipse to an Exoplanetary Transit. *Astrophysical Journal*, 755:103.

Gardner, J. P., Mather, J. C., Clampin, M., Doyon, R., Greenhouse, M. A., Hammel, H. B., Hutchings, J. B., Jakobsen, P., Lilly, S. J., Long, K. S., Lunine, J. I., McCaughrean, M. J., Mountain, M., Nella, J., Rieke, G. H., Rieke, M. J., Rix, H.-W., Smith, E. P., Sonneborn, G., Stiavelli, M., Stockman, H. S., Windhorst, R. A., and Wright, G. S. (2006). The James Webb Space Telescope. *Space Science Review*, 123:485–606.

Gautier, III, T. N., Charbonneau, D., Rowe, J. F., Marcy, G. W., Isaacson, H., Torres, G., Fressin, F., Rogers, L. A., Désert, J.-M., Buchhave, L. A., Latham, D. W., Quinn, S. N., Ciardi, D. R., Fabrycky, D. C., Ford, E. B., Gilliland, R. L., Walkowicz, L. M., Bryson, S. T., Cochran, W. D., Endl, M., Fischer, D. A., Howell,

S. B., Horch, E. P., Barclay, T., Batalha, N., Borucki, W. J., Christiansen, J. L., Geary, J. C., Henze, C. E., Holman, M. J., Ibrahim, K., Jenkins, J. M., Kinemuchi, K., Koch, D. G., Lissauer, J. J., Sanderfer, D. T., Sasselov, D. D., Seager, S., Silverio, K., Smith, J. C., Still, M., Stumpe, M. C., Tenenbaum, P., and Van Cleve, J. (2012). Kepler-20: A Sun-like Star with Three Sub-Neptune Exoplanets and Two Earth-size Candidates. *Astrophysical Journal*, 749:15.

Gierasch, P. J. and Conrath, B. J. (1985). *Energy Conversion Porcesses in the Outer Planets.*

Gilliland, R. L., Marcy, G. W., Rowe, J. F., Rogers, L., Torres, G., Fressin, F., Lopez, E. D., Buchhave, L. A., Christensen-Dalsgaard, J., Désert, J.-M., Henze, C. E., Isaacson, H., Jenkins, J. M., Lissauer, J. J., Chaplin, W. J., Basu, S., Metcalfe, T. S., Elsworth, Y., Handberg, R., Hekker, S., Huber, D., Karoff, C., Kjeldsen, H., Lund, M. N., Lundkvist, M., Miglio, A., Charbonneau, D., Ford, E. B., Fortney, J. J., Haas, M. R., Howard, A. W., Howell, S. B., Ragozzine, D., and Thompson, S. E. (2013). Kepler-68: Three Planets, One with a Density between that of Earth and Ice Giants. *Astrophysical Journal*, 766:40.

Gillon, M., Demory, B.-O., Benneke, B., Valencia, D., Deming, D., Seager, S., Lovis, C., Mayor, M., Pepe, F., Queloz, D., Ségransan, D., and Udry, S. (2012). Improved precision on the radius of the nearby super-Earth 55 Cnc e. *Astronomy & Astrophysics*, 539:A28.

Gilmozzi, R. and Spyromilio, J. (2008). The 42m European ELT: status. In *Society of Photo-Optical Instrumentation Engineers (SPIE) Conference Series*, volume 7012 of *Society of Photo-Optical Instrumentation Engineers (SPIE) Conference Series*.

Giorgi, F. and Chameides, W. L. (1985). The rainout parameterization in a photo-chemical model. *Journal of Geophysical Research*, 90:7872–7880.

Gladstone, G. R., Allen, M., and Yung, Y. L. (1996). Hydrocarbon Photochemistry in the Upper Atmosphere of Jupiter. *Icarus*, 119:1–52.

Glotch, T. D., Lucey, P. G., Bandfield, J. L., Greenhagen, B. T., Thomas, I. R., Elphic, R. C., Bowles, N., Wyatt, M. B., Allen, C. C., Hanna, K. D., and Paige, D. A. (2010). Highly Silicic Compositions on the Moon. *Science*, 329:1510–.

Greenhagen, B. T., Lucey, P. G., Wyatt, M. B., Glotch, T. D., Allen, C. C., Arnold, J. A., Bandfield, J. L., Bowles, N. E., Hanna, K. L. D., Hayne, P. O., Song, E., Thomas, I. R., and Paige, D. A. (2010). Global Silicate Mineralogy of the Moon from the Diviner Lunar Radiometer. *Science*, 329:1507–.

Griffith, C. A. and Yelle, R. V. (1999). Disequilibrium Chemistry in a Brown Dwarf's Atmosphere: Carbon Monoxide in Gliese 229B. *Astrophysical Journal Letters*, 519:L85–L88.

Guillot, T. (2010). On the radiative equilibrium of irradiated planetary atmospheres. *Astronomy & Astrophysics*, 520:A27.

Guyon, O., Pluzhnik, E. A., Kuchner, M. J., Collins, B., and Ridgway, S. T. (2006). Theoretical Limits on Extrasolar Terrestrial Planet Detection with Coronagraphs. *Astrophysical Journal Supplement Series*, 167:81–99.

Halevy, I., Zuber, M. T., and Schrag, D. P. (2007). A Sulfur Dioxide Climate Feedback on Early Mars. *Science*, 318:1903–.

Hamill, P., Toon, O. B., and Kiang, C. S. (1977). Microphysical processes affecting stratospheric aerosol particles. *Journal of Atmospheric Sciences*, 34:1104–1119.

Hansen, J. E. and Hovenier, J. W. (1974). Interpretation of the polarization of Venus. *Journal of Atmospheric Sciences*, 31:1137–1160.

Hapke, B. (1981). Bidirectional reflectance spectroscopy. I - Theory. *Journal of Geophysical Research*, 86:3039–3054.

Hapke, B. (1993). *Theory of reflectance and emittance spectroscopy.*

Hapke, B. (2001). Space weathering from Mercury to the asteroid belt. *Journal of Geophysical Research*, 106:10039–10074.

Hapke, B. (2002). Bidirectional Reflectance Spectroscopy5. The Coherent Backscatter Opposition Effect and Anisotropic Scattering. *Icarus*, 157:523–534.

Hartogh, P., Błecka, M. I., Jarchow, C., Sagawa, H., Lellouch, E., de Val-Borro, M., Rengel, M., Medvedev, A. S., Swinyard, B. M., Moreno, R., Cavalié, T., Lis, D. C., Banaszkiewicz, M., Bockelée-Morvan, D., Crovisier, J., Encrenaz, T., Küppers, M., Lara, L.-M., Szutowicz, S., Vandenbussche, B., Bensch, F., Bergin, E. A., Billebaud, F., Biver, N., Blake, G. A., Blommaert, J. A. D. L., Cernicharo, J., Decin, L., Encrenaz, P., Feuchtgruber, H., Fulton, T., de Graauw, T., Jehin, E., Kidger, M., Lorente, R., Naylor, D. A., Portyankina, G., Sánchez-Portal, M., Schieder, R., Sidher, S., Thomas, N., Verdugo, E., Waelkens, C., Lorenzani, A., Tofani, G., Natale, E., Pearson, J., Klein, T., Leinz, C., Güsten, R., and Kramer, C. (2010a). First results on Martian carbon monoxide from Herschel/HIFI observations. *Astronomy & Astrophysics*, 521:L48.

Hartogh, P., Jarchow, C., Lellouch, E., de Val-Borro, M., Rengel, M., Moreno, R., Medvedev, A. S., Sagawa, H., Swinyard, B. M., Cavalié, T., Lis, D. C., Błęcka, M. I., Banaszkiewicz, M., Bockelée-Morvan, D., Crovisier, J., Encrenaz, T., Küppers, M., Lara, L.-M., Szutowicz, S., Vandenbussche, B., Bensch, F., Bergin, E. A., Billebaud, F., Biver, N., Blake, G. A., Blommaert, J. A. D. L., Cernicharo, J., Decin, L., Encrenaz, P., Feuchtgruber, H., Fulton, T., de Graauw, T., Jehin, E., Kidger, M., Lorente, R., Naylor, D. A., Portyankina, G., Sánchez-Portal, M., Schieder, R., Sidher, S., Thomas, N., Verdugo, E., Waelkens, C., Whyborn, N., Teyssier, D., Helmich, F., Roelfsema, P., Stutzki, J., Leduc, H. G., and Stern, J. A. (2010b).

Herschel/HIFI observations of Mars: First detection of O_2 at submillimetre wavelengths and upper limits on HCl and H_2O_2. *Astronomy & Astrophysics*, 521:L49.

Hauglustaine, D. A., Grainer, C., Brasseur, G. P., and Mégie, A. (1994). The importance of atmospheric chemistry in the calculation of radiative forcing on the climate system. *Journal of Geophysical Research*, 99:1173–1186.

Hazen, R. M., Papineau, D., Bleeker, W., Downs, R. T., Ferry, J. M., McCoy, T. J., Sverjensky, D. A., and Yang, H. (2008). Mineral evolution. *American Mineralogist*, 93(11-12):1693–1720.

Head, J. W., Chapman, C. R., Strom, R. G., Fassett, C. I., Denevi, B. W., Blewett, D. T., Ernst, C. M., Watters, T. R., Solomon, S. C., Murchie, S. L., Prockter, L. M., Chabot, N. L., Gillis-Davis, J. J., Whitten, J. L., Goudge, T. A., Baker, D. M. H., Hurwitz, D. M., Ostrach, L. R., Xiao, Z., Merline, W. J., Kerber, L., Dickson, J. L., Oberst, J., Byrne, P. K., Klimczak, C., and Nittler, L. R. (2011). Flood Volcanism in the Northern High Latitudes of Mercury Revealed by MESSENGER. *Science*, 333:1853–.

Hintze, P. E., Kjaergaard, H. G., Vaida, V., and Burkholder, J. B. (2003). Vibrational and electronic spectroscopy of sulfuric acid vapor. *The Journal of Physical Chemistry A*, 107(8):1112–1118.

Holland, D. (1997). A photoabsorption, photodissociation and photoelectron spectroscopy study of C2H4 and C2D4. *Chemical Physics*, 219:91–116.

Holland, H. D. (1984). *The chemical evolution of the atmosphere and oceans.*

Holland, H. D. (2002). Volcanic gases, black smokers, and the great oxidation event. *Geochimica et Cosmochimica Acta*, 66:3811–3826.

Holman, M. J., Fabrycky, D. C., Ragozzine, D., Ford, E. B., Steffen, J. H., Welsh, W. F., Lissauer, J. J., Latham, D. W., Marcy, G. W., Walkowicz, L. M., Batalha, N. M., Jenkins, J. M., Rowe, J. F., Cochran, W. D., Fressin, F., Torres, G., Buchhave, L. A., Sasselov, D. D., Borucki, W. J., Koch, D. G., Basri, G., Brown, T. M., Caldwell, D. A., Charbonneau, D., Dunham, E. W., Gautier, T. N., Geary, J. C., Gilliland, R. L., Haas, M. R., Howell, S. B., Ciardi, D. R., Endl, M., Fischer, D., Fürész, G., Hartman, J. D., Isaacson, H., Johnson, J. A., MacQueen, P. J., Moorhead, A. V., Morehead, R. C., and Orosz, J. A. (2010). Kepler-9: A System of Multiple Planets Transiting a Sun-Like Star, Confirmed by Timing Variations. *Science*, 330:51–.

Howard, A. W., Johnson, J. A., Marcy, G. W., Fischer, D. A., Wright, J. T., Henry, G. W., Isaacson, H., Valenti, J. A., Anderson, J., and Piskunov, N. E. (2011). The NASA-UC Eta-Earth Program. III. A Super-Earth Orbiting HD 97658 and a Neptune-mass Planet Orbiting Gl 785. *Astrophysical Journal*, 730:10.

Howard, A. W., Marcy, G. W., Bryson, S. T., Jenkins, J. M., Rowe, J. F., Batalha, N. M., Borucki, W. J., Koch, D. G., Dunham, E. W., Gautier, III, T. N., Van Cleve, J., Cochran, W. D., Latham, D. W., Lissauer, J. J., Torres, G., Brown, T. M., Gilliland, R. L., Buchhave, L. A., Caldwell, D. A., Christensen-Dalsgaard, J., Ciardi, D., Fressin, F., Haas, M. R., Howell, S. B., Kjeldsen, H., Seager, S., Rogers, L., Sasselov, D. D., Steffen, J. H., Basri, G. S., Charbonneau, D., Christiansen, J., Clarke, B., Dupree, A., Fabrycky, D. C., Fischer, D. A., Ford, E. B., Fortney, J. J., Tarter, J., Girouard, F. R., Holman, M. J., Johnson, J. A., Klaus, T. C., Machalek, P., Moorhead, A. V., Morehead, R. C., Ragozzine, D., Tenenbaum, P., Twicken, J. D., Quinn, S. N., Isaacson, H., Shporer, A., Lucas, P. W., Walkowicz, L. M., Welsh, W. F., Boss, A., Devore, E., Gould, A., Smith, J. C., Morris, R. L., Prsa, A., Morton, T. D., Still, M., Thompson, S. E., Mullally, F., Endl, M., and MacQueen, P. J. (2012). Planet Occurrence within 0.25 AU of Solar-type Stars from Kepler. *Astrophysical Journal Supplement Series*, 201:15.

Hubin-Franskin, M.-J., Delwiche, J., Giuliani, A., Ska, M.-P., Motte-Tollet, F., Walker, I. C., Mason, N. J., Gingell, J. M., and Jones, N. C. (2002). Electronic excitation and optical cross sections of methylamine and ethylamine in the UV-VUV spectral region. *Journal of Chemical Physics*, 116:9261–9268.

Huestis, D. L. and Berkowitz, J. (2010). Critical Evaluation of the Photoabsorption Cross Section of CO_2 from 0.125 to 201.6 nm at Room Temperature. In *AAS/Division for Planetary Sciences Meeting Abstracts #42*, volume 42 of *Bulletin of the American Astronomical Society*, page 972.

Hunten, D. M. (1974). The escape of light gases from planetary atmospheres. *Journal of Atmospheric Sciences*, 30:1481–1494.

Hunziker, H. E., Kneppe, H., McLean, A. D., Siegbahn, P., and Wendt, H. R. (1983). Visible electronic absorption spectrum of vinyl radical. *Canadian Journal of Chemistry*, 61(5):993–995.

Iida, Y. (1986). Absolute oscillator strengths for photoabsorption and the molecular and dissociative photoionization of nitric oxide. *Chemical Physics*, 105:211–225.

Ityaksov, D., Linnartz, H., and Ubachs, W. (2008). Deep-UV absorption and Rayleigh scattering of carbon dioxide. *Chemical Physics Letters*, 462:31–34.

Jasper, A. W., Klippenstein, S. J., Harding, L. B., and Ruscic, B. (2007). Kinetics of the reaction of methyl radical with hydroxyl radical and methanol decomposition. *The Journal of Physical Chemistry A*, 111(19):3932–3950. PMID: 17388366.

Johns, M., McCarthy, P., Raybould, K., Bouchez, A., Farahani, A., Filgueira, J., Jacoby, G., Shectman, S., and Sheehan, M. (2012). Giant Magellan Telescope: overview. In *Society of Photo-Optical Instrumentation Engineers (SPIE) Conference Series*, volume 8444 of *Society of Photo-Optical Instrumentation Engineers (SPIE) Conference Series*.

Johnson, T. V., Mousis, O., Lunine, J. I., and Madhusudhan, N. (2012). Planetesimal Compositions in Exoplanet Systems. *Astrophysical Journal*, 757:192.

Jones, A. D. (1976). Optical constants of sulphuric acid in the far infrared. *J. Quant. Spectrosc. Radiat. Transfer.*, 16:1017–1019.

Jucks, K. W., Johnson, D. G., Chance, K. V., Traub, W. A., Margitan, J. J., Osterman, G. B., Salawitch, R. J., and Sasano, Y. (1998). Observations of OH, HO_2, H_2O, and O_3 in the upper stratosphere: Implications for HO_x photochemistry. *Geophysical Research Letters*, 25:3935–3938.

Kaltenegger, L. and Sasselov, D. (2010). Detecting Planetary Geochemical Cycles on Exoplanets: Atmospheric Signatures and the Case of SO_2. *Astrophysical Journal*, 708:1162–1167.

Kaltenegger, L. and Traub, W. A. (2009). Transits of Earth-like Planets. *Astrophysical Journal*, 698:519–527.

Kameta, K., Kouchi, N., Ukai, M., and Hatano, Y. (2002). Photoabsorption, photoionization, and neutral-dissociation cross sections of simple hydrocarbons in the vacuum ultraviolet range. *Journal of Electron Spectroscopy and Related Phenomena*, 123(2-3):225 – 238.

Kameta, K., Machida, S., Kitajima, M., Ukai, M., Kouchi, N., Hatano, Y., and Ito, K. (1996). Photoabsorption, photoionization, and neutral-dissociation cross sections of c2h6 and c3h8 in the extreme-uv region. *Journal of Electron Spectroscopy and Related Phenomena*, 79(0):391 – 393.

Kasting, J. F. (1990). Bolide impacts and the oxidation state of carbon in the earth's early atmosphere. *Origins of Life and Evolution of the Biosphere*, 20:199–231.

Kasting, J. F. (1997). Habitable Zones around Low Mass Stars and the Search For Extraterrestrial Life. *Origins of Life and Evolution of the Biosphere*, 27:291–3107.

Kasting, J. F. and Brown, L. L. (1998). *Setting the Stage: the Early Atmosphere as a Source of Biogenic Compounds, the Molecular Origins of Life: Assembling the Pieces of the Puzzle.*

Kasting, J. F. and Catling, D. (2003). Evolution of a Habitable Planet. *Annual Review of Astronomy & Astrophysics*, 41:429–463.

Kasting, J. F., Holland, H. D., and Pinto, J. P. (1985). Oxidant abundances in rainwater and the evolution of atmospheric oxygen. *Journal of Geophysical Research*, 90:10497.

Kasting, J. F., Liu, S. C., and Donahue, T. M. (1979). Oxygen levels in the prebiological atmosphere. *Journal of Geophysical Research*, 84:3097–3107.

Kasting, J. F. and Walker, J. C. G. (1981). Limits on oxygen concentration in the prebiological atmosphere and the rate of abiotic fixation of nitrogen. *Journal of Geophysical Research*, 86:1147–1158.

Kasting, J. F., Whitmire, D. P., and Reynolds, R. T. (1993). Habitable Zones around Main Sequence Stars. *Icarus*, 101:108–128.

Kasting, J. F., Zahnle, K. J., Pinto, J. P., and Young, A. T. (1989). Sulfur, ultraviolet radiation, and the early evolution of life. *Origins of Life and Evolution of the Biosphere*, 19:95–108.

Kharecha, P., Kasting, J., and Siefert, J. (2005). A coupled atmosphereecosystem model of the early archean earth. *Geobiology*, 3(2):53–76.

Kirkland, L. E., Herr, K. C., and Adams, P. M. (2003). Infrared stealthy surfaces: Why TES and THEMIS may miss some substantial mineral deposits on Mars and implications for remote sensing of planetary surfaces. *Journal of Geophysical Research (Planets)*, 108:5137.

Knutson, H. A., Charbonneau, D., Allen, L. E., Fortney, J. J., Agol, E., Cowan, N. B., Showman, A. P., Cooper, C. S., and Megeath, S. T. (2007). A map of the day-night contrast of the extrasolar planet HD 189733b. *Nature*, 447:183–186.

Koch, D. G., Borucki, W. J., Basri, G., Batalha, N. M., Brown, T. M., Caldwell, D., Christensen-Dalsgaard, J., Cochran, W. D., DeVore, E., Dunham, E. W., Gautier, III, T. N., Geary, J. C., Gilliland, R. L., Gould, A., Jenkins, J., Kondo, Y., Latham, D. W., Lissauer, J. J., Marcy, G., Monet, D., Sasselov, D., Boss, A., Brownlee, D., Caldwell, J., Dupree, A. K., Howell, S. B., Kjeldsen, H., Meibom, S., Morrison, D., Owen, T., Reitsema, H., Tarter, J., Bryson, S. T., Dotson, J. L., Gazis, P., Haas, M. R., Kolodziejczak, J., Rowe, J. F., Van Cleve, J. E., Allen, C., Chandrasekaran, H., Clarke, B. D., Li, J., Quintana, E. V., Tenenbaum, P., Twicken, J. D., and Wu, H. (2010). Kepler Mission Design, Realized Photometric Performance, and Early Science. *Astrophysical Journal Letters*, 713:L79–L86.

Konopacky, Q. M., Barman, T. S., Macintosh, B. A., and Marois, C. (2013). Detection of carbon monoxide and water absorption lines in an exoplanet atmosphere. *Science*, 339(6126):1398–1401.

Kopparapu, R. k., Kasting, J. F., and Zahnle, K. J. (2012). A Photochemical Model for the Carbon-rich Planet WASP-12b. *Astrophysical Journal*, 745:77.

Kopparapu, R. K., Ramirez, R., Kasting, J. F., Eymet, V., Robinson, T. D., Mahadevan, S., Terrien, R. C., Domagal-Goldman, S., Meadows, V., and Deshpande, R. (2013). Habitable Zones around Main-sequence Stars: New Estimates. *Astrophysical Journal*, 765:131.

Kramer, M. and Cypionka, H. (1989). Sulfate formation via atp sulfurylase in thiosulfate- and sulfite-disproportionating bacteria. *Archives of Microbiology*, 151:232–237.

Krasnopolsky, V. A. (1993). Photochemistry of the Martian atmosphere (mean conditions). *Icarus*, 101:313–332.

Krasnopolsky, V. A. (2006). Photochemistry of the martian atmosphere: Seasonal, latitudinal, and diurnal variations. *Icarus*, 185:153–170.

Krasnopolsky, V. A. (2007). Long-term spectroscopic observations of Mars using IRTF/CSHELL: Mapping of O_2 dayglow, CO, and search for CH_4. *Icarus*, 190:93–102.

Krasnopolsky, V. A. (2012). A photochemical model for the Venus atmosphere at 47-112 km. *Icarus*, 218:230–246.

Krasnopolsky, V. A. and Feldman, P. D. (2001). Detection of Molecular Hydrogen in theAtmosphere of Mars. *Science*, 294:1914–1917.

Krasnopolsky, V. A. and Pollack, J. B. (1994). H2O-H2SO4 system in Venus' clouds and OCS, CO, and H2SO4 profiles in Venus' troposphere. *Icarus*, 109:58–78.

Kuchner, M. J. and Seager, S. (2005). Extrasolar Carbon Planets. *ArXiv Astrophysics e-prints*.

Kuchner, M. J. and Traub, W. A. (2002). A Coronagraph with a Band-limited Mask for Finding Terrestrial Planets. *Astrophysical Journal*, 570:900–908.

Lammer, H., Erkaev, N. V., Odert, P., Kislyakova, K. G., Leitzinger, M., and Khodachenko, M. L. (2013). Probing the blow-off criteria of hydrogen-rich 'super-Earths'. *Monthly Notices of the Royal Astronomical Society*, 430:1247–1256.

Lammer, H., Kasting, J. F., Chassefière, E., Johnson, R. E., Kulikov, Y. N., and Tian, F. (2008). Atmospheric Escape and Evolution of Terrestrial Planets and Satellites. *Space Science Review*, 139:399–436.

Lane, J. R. and Kjaergaard, H. G. (2008). Calculated electronic transitions in sulfuric acid and implications for its photodissociation in the atmosphere. *The Journal of Physical Chemistry A*, 112(22):4958–4964.

Lavvas, P. P., Coustenis, A., and Vardavas, I. M. (2008a). Coupling photochemistry with haze formation in Titan's atmosphere, Part I: Model description. *Planetary and Space Science*, 56:27–66.

Lavvas, P. P., Coustenis, A., and Vardavas, I. M. (2008b). Coupling photochemistry with haze formation in Titan's atmosphere, Part II: Results and validation with Cassini/Huygens data. *Planetary and Space Science*, 56:67–99.

Lawson, P. R. and Dooley, J. A. (2005). Technology Plan for the Terrestrial Planet Finder Interferometer. *NASA STI/Recon Technical Report N*, 6:15630.

Lee, A. Y. T., Yung, Y. L., Cheng, B.-M., Bahou, M., Chung, C.-Y., and Lee, Y.-P. (2001). Enhancement of Deuterated Ethane on Jupiter. *Astrophysical Journal Letters*, 551:L93–L96.

Lee, L. C., Carlson, R. W., and Judge, D. L. (1976). The absorption cross sections of H_2 and D_2 from 180 to 780 Å. *J. Quant. Spectrosc. Radiat. Transfer.*, 16:873–877.

Lefèvre, F. and Forget, F. (2009). Observed variations of methane on Mars unexplained by known atmospheric chemistry and physics. *Nature*, 460:720–723.

Léger, A., Grasset, O., Fegley, B., Codron, F., Albarede, A. F., Barge, P., Barnes, R., Cance, P., Carpy, S., Catalano, F., Cavarroc, C., Demangeon, O., Ferraz-Mello, S., Gabor, P., Grießmeier, J.-M., Leibacher, J., Libourel, G., Maurin, A.-S., Raymond, S. N., Rouan, D., Samuel, B., Schaefer, L., Schneider, J., Schuller, P. A., Selsis, F., and Sotin, C. (2011). The extreme physical properties of the CoRoT-7b super-Earth. *Icarus*, 213:1–11.

Leger, A., Mariotti, J. M., Mennesson, B., Ollivier, M., Puget, J. L., Rouan, D., and Schneider, J. (1996). Could We Search for Primitive Life on Extrasolar Planets in the Near Future? *Icarus*, 123:249–255.

Leger, A., Pirre, M., and Marceau, F. J. (1993). Search for primitive life on a distant planet: relevance of 02 and 03 detections. *Astronomy & Astrophysics*, 277:309.

Léger, A., Rouan, D., Schneider, J., Barge, P., Fridlund, M., Samuel, B., Ollivier, M., Guenther, E., Deleuil, M., Deeg, H. J., Auvergne, M., Alonso, R., Aigrain, S., Alapini, A., Almenara, J. M., Baglin, A., Barbieri, M., Bruntt, H., Bordé, P., Bouchy, F., Cabrera, J., Catala, C., Carone, L., Carpano, S., Csizmadia, S., Dvorak, R., Erikson, A., Ferraz-Mello, S., Foing, B., Fressin, F., Gandolfi, D., Gillon, M., Gondoin, P., Grasset, O., Guillot, T., Hatzes, A., Hébrard, G., Jorda, L., Lammer, H., Llebaria, A., Loeillet, B., Mayor, M., Mazeh, T., Moutou, C., Pätzold, M., Pont, F., Queloz, D., Rauer, H., Renner, S., Samadi, R., Shporer, A., Sotin, C., Tingley, B., Wuchterl, G., Adda, M., Agogu, P., Appourchaux, T., Ballans, H., Baron, P., Beaufort, T., Bellenger, R., Berlin, R., Bernardi, P., Blouin, D., Baudin, F., Bodin, P., Boisnard, L., Boit, L., Bonneau, F., Borzeix, S., Briet, R., Buey, J.-T., Butler, B., Cailleau, D., Cautain, R., Chabaud, P.-Y., Chaintreuil, S., Chiavassa, F., Costes, V., Cuna Parrho, V., de Oliveira Fialho, F., Decaudin, M., Defise, J.-M., Djalal, S., Epstein, G., Exil, G.-E., Fauré, C., Fenouillet, T., Gaboriaud, A., Gallic, A., Gamet, P., Gavalda, P., Grolleau, E., Gruneisen, R., Gueguen, L., Guis, V., Guivarc'h, V., Guterman, P., Hallouard, D., Hasiba, J., Heuripeau, F., Huntzinger, G., Hustaix, H., Imad, C., Imbert, C., Johlander, B., Jouret, M., Journoud, P., Karioty, F., Kerjean, L., Lafaille, V., Lafond, L., Lam-Trong, T., Landiech, P., Lapeyrere, V., Larqué, T., Laudet, P., Lautier, N., Lecann, H., Lefevre, L., Leruyet, B., Levacher, P., Magnan, A., Mazy, E., Mertens, F., Mesnager, J.-M., Meunier, J.-C., Michel, J.-P., Monjoin, W., Naudet, D., Nguyen-Kim, K., Orcesi, J.-L., Ottacher, H., Perez, R., Peter, G., Plasson, P., Plesseria, J.-Y., Pontet, B., Pradines, A., Quentin, C., Reynaud, J.-L., Rolland, G., Rollenhagen,

F., Romagnan, R., Russ, N., Schmidt, R., Schwartz, N., Sebbag, I., Sedes, G., Smit, H., Steller, M. B., Sunter, W., Surace, C., Tello, M., Tiphène, D., Toulouse, P., Ulmer, B., Vandermarcq, O., Vergnault, E., Vuillemin, A., and Zanatta, P. (2009). Transiting exoplanets from the CoRoT space mission. VIII. CoRoT-7b: the first super-Earth with measured radius. *Astronomy & Astrophysics*, 506:287–302.

Lelieveld, J., Roelofs, G.-J., Ganzeveld, L., Feichter, J., and Rodhe, H. (1997). Terrestrial Sources and Distribution of Atmospheric Sulphur. *Royal Society of London Philosophical Transactions Series B*, 352:149–157.

Levine, J. S., editor (1985). *The photochemistry of atmospheres. Earth, the other planets, and comets.*

Levine, M., Lisman, D., Shaklan, S., Kasting, J., Traub, W., Alexander, J., Angel, R., Blaurock, C., Brown, M., Brown, R., Burrows, C., Clampin, M., Cohen, E., Content, D., Dewell, L., Dumont, P., Egerman, R., Ferguson, H., Ford, V., Greene, J., Guyon, O., Hammel, H., Heap, S., Ho, T., Horner, S., Hunyadi, S., Irish, S., Jackson, C., Kasdin, J., Kissil, A., Krim, M., Kuchner, M., Kwack, E., Lillie, C., Lin, D., Liu, A., Marchen, L., Marley, M., Meadows, V., Mosier, G., Mouroulis, P., Noecker, M., Ohl, R., Oppenheimer, B., Pitman, J., Ridgway, S., Sabatke, E., Seager, S., Shao, M., Smith, A., Soummer, R., Stapelfeldt, K., Tenerell, D., Trauger, J., and Vanderbei, R. (2009). Terrestrial Planet Finder Coronagraph (TPF-C) Flight Baseline Concept. *ArXiv e-prints.*

Liang, M.-C., Parkinson, C. D., Lee, A. Y.-T., Yung, Y. L., and Seager, S. (2003). Source of Atomic Hydrogen in the Atmosphere of HD 209458b. *Astrophysical Journal Letters*, 596:L247–L250.

Lilly, R., Rebbert, R., and Ausloos, P. (1973). Far ultra-violet photolysis of ammonia quantum yield determination for the primary process: Nh3 (nd3) + hv [rightward arrow] nh (nd) + h2 (d2). *Journal of Photochemistry*, 2(1):49 – 61.

Lindzen, R. A. (1990). *Dynamics in Atmospheric Physics.*

Line, M. R., Liang, M. C., and Yung, Y. L. (2010). High-temperature Photochemistry in the Atmosphere of HD 189733b. *Astrophysical Journal*, 717:496–502.

Liou, K. N. (2002). *An Introduction to Atmospheric Radiation.*

Lissauer, J. J., Fabrycky, D. C., Ford, E. B., Borucki, W. J., Fressin, F., Marcy, G. W., Orosz, J. A., Rowe, J. F., Torres, G., Welsh, W. F., Batalha, N. M., Bryson, S. T., Buchhave, L. A., Caldwell, D. A., Carter, J. A., Charbonneau, D., Christiansen, J. L., Cochran, W. D., Desert, J.-M., Dunham, E. W., Fanelli, M. N., Fortney, J. J., Gautier, III, T. N., Geary, J. C., Gilliland, R. L., Haas, M. R., Hall, J. R., Holman, M. J., Koch, D. G., Latham, D. W., Lopez, E., McCauliff, S., Miller, N., Morehead, R. C., Quintana, E. V., Ragozzine, D., Sasselov, D., Short, D. R., and Steffen, J. H. (2011). A closely packed system of low-mass, low-density planets transiting Kepler-11. *Nature*, 470:53–58.

Lodders, K. (2003). Solar System Abundances and Condensation Temperatures of the Elements. *Astrophysical Journal*, 591:1220–1247.

Lodders, K. (2004). Jupiter Formed with More Tar than Ice. *Astrophysical Journal*, 611:587–597.

Lu, H.-C., Chen, H.-K., and Cheng, B.-M. (2004). Analysis of c2h4 in c2h6 and c2h5d with vuv absorption spectroscopy and a method to remove c2h4 from c2h6 and c2h5d. *Analytical Chemistry*, 76(19):5965–5967.

Lyons, J. R. (2008). An estimate of the equilibrium speciation of sulfur vapor over solid sulfur and implications for planetary atmospheres. *Journal of Sulfur Chemistry*, 29(3-4):269–279.

Macpherson, M. T. and Simons, J. P. (1978). Spectroscopic study of the predissociation h(d)cn(c1a[prime or minute])[rightward arrow] h(d)+ cn(b2[capital sigma]+). *J. Chem. Soc., Faraday Trans. 2*, 74:1965–1977.

Madhusudhan, N. (2012). C/O Ratio as a Dimension for Characterizing Exoplanetary Atmospheres. *Astrophysical Journal*, 758:36.

Madhusudhan, N., Harrington, J., Stevenson, K. B., Nymeyer, S., Campo, C. J., Wheatley, P. J., Deming, D., Blecic, J., Hardy, R. A., Lust, N. B., Anderson, D. R., Collier-Cameron, A., Britt, C. B. T., Bowman, W. C., Hebb, L., Hellier, C., Maxted, P. F. L., Pollacco, D., and West, R. G. (2011a). A high C/O ratio and weak thermal inversion in the atmosphere of exoplanet WASP-12b. *Nature*, 469:64–67.

Madhusudhan, N., Knutson, H., and Desert, J.-M. (2010). Atmospheric composition and thermal structure of super-Earth GJ 1214b. *Spitzer Proposal*, page 70148.

Madhusudhan, N., Mousis, O., Johnson, T. V., and Lunine, J. I. (2011b). Carbon-rich Giant Planets: Atmospheric Chemistry, Thermal Inversions, Spectra, and Formation Conditions. *Astrophysical Journal*, 743:191.

Madhusudhan, N. and Seager, S. (2009). A Temperature and Abundance Retrieval Method for Exoplanet Atmospheres. *Astrophysical Journal*, 707:24–39.

Madhusudhan, N. and Seager, S. (2011). High Metallicity and Non-equilibrium Chemistry in the Dayside Atmosphere of hot-Neptune GJ 436b. *Astrophysical Journal*, 729:41.

Maltagliati, L., Montmessin, F., Fedorova, A., Korablev, O., Forget, F., and Bertaux, J.-L. (2011). Evidence of Water Vapor in Excess of Saturation in the Atmosphere of Mars. *Science*, 333:1868–.

Manabe, S. and Wetherald, R. T. (1967). Thermal Equilibrium of the Atmosphere with a Given Distribution of Relative Humidity. *Journal of Atmospheric Sciences*, 24:241–259.

Manatt, S. L. and Lane, A. L. (1993). A compilation of the absorption cross-sections of SO_2 from 106 to 403 nm. *J. Quant. Spectrosc. Radiat. Transfer.*, 50:267–276.

Marboeuf, U., Mousis, O., Ehrenreich, D., Alibert, Y., Cassan, A., Wakelam, V., and Beaulieu, J.-P. (2008). Composition of Ices in Low-Mass Extrasolar Planets. *Astrophysical Journal*, 681:1624–1630.

Marrero, T. R. and Mason, E. A. (1972). Gaseous Diffusion Coefficients. *Journal of Physical and Chemical Reference Data*, 1:3–118.

Mason, N. J., Gingell, J. M., Davies, J. A., Zhao, H., Walker, I. C., and Siggel, M. R. F. (1996). VUV optical absorption and electron energy-loss spectroscopy of ozone. *Journal of Physics B Atomic Molecular Physics*, 29:3075–3089.

Massie, S. T. and Hunten, D. M. (1981). Stratospheric eddy diffusion coefficients from tracer data. *Journal of Geophysical Research*, 86:9859–9868.

Matsumi, Y., Comes, F. J., Hancock, G., Hofzumahaus, A., Hynes, A. J., Kawasaki, M., and Ravishankara, A. R. (2002). Quantum yields for production of o(1d) in the ultraviolet photolysis of ozone: Recommendation based on evaluation of laboratory data. *Journal of Geophysical Research: Atmospheres*, 107(D3):ACH 1–1–ACH 1–12.

Mayor, M., Marmier, M., Lovis, C., Udry, S., Ségransan, D., Pepe, F., Benz, W., Bertaux, J. ., Bouchy, F., Dumusque, X., Lo Curto, G., Mordasini, C., Queloz, D., and Santos, N. C. (2011). The HARPS search for southern extra-solar planets XXXIV. Occurrence, mass distribution and orbital properties of super-Earths and Neptune-mass planets. *ArXiv e-prints*.

Mayor, M., Udry, S., Lovis, C., Pepe, F., Queloz, D., Benz, W., Bertaux, J.-L., Bouchy, F., Mordasini, C., and Segransan, D. (2009). The HARPS search for southern extra-solar planets. XIII. A planetary system with 3 super-Earths (4.2, 6.9, and 9.2 $M_?$). *Astronomy & Astrophysics*, 493:639–644.

McCord, T. B., Clark, R. N., Hawke, B. R., McFadden, L. A., Owensby, P. D., Pieters, C. M., and Adams, J. B. (1981). Moon - Near-infrared spectral reflectance, a first good look. *Journal of Geophysical Research*, 86:10883–10892.

McCord, T. B., Clark, R. N., and Singer, R. B. (1982). Mars - Near-infrared spectral reflectance of surface regions and compositional implications. *Journal of Geophysical Research*, 87:3021–3032.

McCord, T. B. and Westphal, J. A. (1971). Mars: Narrow-Band Photometry, from 0.3 to 2.5 Microns, of Surface Regions during the 1969 Apparition. *Astrophysical Journal*, 168:141.

McElroy, M. B. and Donahue, T. M. (1972). Stability of the martian atmosphere. *Science*, 177(4053):986–988.

Mentall, J. E. and Gentieu, E. P. (1970). Lyman-α Fluorescence from the Photodissociation of H_2. *Journal of Chemical Physics*, 52:5641–5645.

Meyer, B. (1976). Elemental sulfur. *Chemical Reviews*, 76(3):367–388.

Miller-Ricci, E., Seager, S., and Sasselov, D. (2009). The Atmospheric Signatures of Super-Earths: How to Distinguish Between Hydrogen-Rich and Hydrogen-Poor Atmospheres. *Astrophysical Journal*, 690:1056–1067.

Miller-Ricci Kempton, E., Zahnle, K., and Fortney, J. J. (2012). The Atmospheric Chemistry of GJ 1214b: Photochemistry and Clouds. *Astrophysical Journal*, 745:3.

Mills, M. J., Toon, O. B., Vaida, V., Hintze, P. E., Kjaergaard, H. G., Schofield, D. P., and Robinson, T. W. (2005). Photolysis of sulfuric acid vapor by visible light as a source of the polar stratospheric CN layer. *Journal of Geophysical Research (Atmospheres)*, 110:8201.

Mordasini, C., Alibert, Y., Georgy, C., Dittkrist, K.-M., Klahr, H., and Henning, T. (2012). Characterization of exoplanets from their formation. II. The planetary mass-radius relationship. *Astronomy & Astrophysics*, 547:A112.

Moses, J. I., Madhusudhan, N., Visscher, C., and Freedman, R. S. (2013). Chemical Consequences of the C/O Ratio on Hot Jupiters: Examples from WASP-12b, CoRoT-2b, XO-1b, and HD 189733b. *The Astrophysicsl Journal*, 763:25.

Moses, J. I., Visscher, C., Fortney, J. J., Showman, A. P., Lewis, N. K., Griffith, C. A., Klippenstein, S. J., Shabram, M., Friedson, A. J., Marley, M. S., and Freedman, R. S. (2011). Disequilibrium Carbon, Oxygen, and Nitrogen Chemistry in the Atmospheres of HD 189733b and HD 209458b. *Astrophysical Journal*, 737:15.

Moses, J. I., Zolotov, M. Y., and Fegley, B. (2002). Photochemistry of a Volcanically Driven Atmosphere on Io: Sulfur and Oxygen Species from a Pele-Type Eruption. *Icarus*, 156:76–106.

Muirhead, P. S., Hamren, K., Schlawin, E., Rojas-Ayala, B., Covey, K. R., and Lloyd, J. P. (2012). Characterizing the Cool Kepler Objects of Interests. New Effective Temperatures, Metallicities, Masses, and Radii of Low-mass Kepler Planet-candidate Host Stars. *Astrophysical Journal Letters*, 750:L37.

Mumma, M. J., Villanueva, G. L., Novak, R. E., Hewagama, T., Bonev, B. P., DiSanti, M. A., Mandell, A. M., and Smith, M. D. (2009). Strong Release of Methane on Mars in Northern Summer 2003. *Science*, 323:1041–.

Murcray, F. H., Murcray, D. G., and Williams, W. J. (1970). Infrared emissivity of lunar surface features. 1. Balloon-borne observations. *Journal of Geophysical Research*, 75:2662–2669.

Murphy, D. M. and Koop, T. (2005). Review of the vapour pressures of ice and supercooled water for atmospheric applications. *Quarterly Journal of the Royal Meteorological Society*, 131(608):1539–1565.

Mustard, J. F. and Pieters, C. M. (1989). Photometric phase functions of common geologic minerals and applications to quantitative analysis of mineral mixture reflectance spectra. *Journal of Geophysical Research*, 94:13619–13634.

Mustard, J. F., Poulet, F., Gendrin, A., Bibring, J.-P., Langevin, Y., Gondet, B., Mangold, N., Bellucci, G., and Altieri, F. (2005). Olivine and Pyroxene Diversity in the Crust of Mars. *Science*, 307:1594–1597.

Nair, H., Allen, M., Anbar, A. D., Yung, Y. L., and Clancy, R. T. (1994). A photochemical model of the martian atmosphere. *Icarus*, 111:124–150.

Nee, J. (1985). Photoexcitation processes of CH3OH: Rydberg states and photofragment fluorescence. *Chemical Physics*, 98:147–155.

Nicolet, M. and Peetermans, W. (1972). The production of nitric oxide in the stratosphere by oxidation of nitrous oxide. *Annales Geophysicae*, 28:751–762.

Nittler, L. R., Starr, R. D., Weider, S. Z., McCoy, T. J., Boynton, W. V., Ebel, D. S., Ernst, C. M., Evans, L. G., Goldsten, J. O., Hamara, D. K., Lawrence, D. J., McNutt, R. L., Schlemm, C. E., Solomon, S. C., and Sprague, A. L. (2011). The Major-Element Composition of Mercury's Surface from MESSENGER X-ray Spectrometry. *Science*, 333:1847–.

Nutzman, P. and Charbonneau, D. (2008). Design considerations for a ground-based transit search for habitable planets orbiting m dwarfs. *Publications of the Astronomical Society of the Pacific*, 120(865):pp. 317–327.

Ogawa, S. and Ogawa, M. (1975). Absorption cross sections of $O_2(a^1\Delta_g)$ and $O_2(X^3\Sigma_g{}^-$ in the region from 1087 to 1700 Å. *Canadian Journal of Physics*, 53:1845.

Old, J. G., Gentili, K. L., and Peck, E. R. (1971). Dispersion of Carbon Dioxide. *Journal of the Optical Society of America (1917-1983)*, 61:89.

Oppenheimer, B. R. and Hinkley, S. (2009). High-Contrast Observations in Optical and Infrared Astronomy. *Annual Review of Astronomy & Astrophysics*, 47:253–289.

Orkin, V. L., Huie, R. E., and Kurylo, M. J. (1997). Rate constants for the reactions of oh with hfc-245cb (ch3cf2cf3) and some fluoroalkenes (ch2chcf3, ch2cfcf3, cf2cfcf3, and cf2cf2). *The Journal of Physical Chemistry A*, 101(48):9118–9124.

Owen, T. (1980). The Search for Early Forms of Life in Other Planetary Systems - Future Possibilities Afforded by Spectroscopic Techniques. In Papagiannis, M. D., editor, *Strategies for the Search for Life in the Universe*, volume 83 of *Astrophysics and Space Science Library*, page 177.

Pallé, E., Zapatero Osorio, M. R., Barrena, R., Montañés-Rodríguez, P., and Martín, E. L. (2009). Earth's transmission spectrum from lunar eclipse observations. *Nature*, 459:814–816.

Palmer, K. F. and Williams, D. (1975). Optical constants of sulfuric acid - Application to the clouds of Venus. *Applied Optics*, 14:208–219.

Parkinson, W. (2003). Absolute absorption cross section measurements of CO2 in the wavelength region 163 200 nm and the temperature dependence. *Chemical Physics*, 290:251–256.

Pavlov, A. A., Brown, L. L., and Kasting, J. F. (2001). UV shielding of NH_3 and O_2 by organic hazes in the Archean atmosphere. *Journal of Geophysical Research*, 106:23267–23288.

Pavlov, A. A. and Kasting, J. F. (2002). Mass-Independent Fractionation of Sulfur Isotopes in Archean Sediments: Strong Evidence for an Anoxic Archean Atmosphere. *Astrobiology*, 2:27–41.

Pavlov, A. A., Kasting, J. F., Brown, L. L., Rages, K. A., and Freedman, R. (2000). Greenhouse warming by CH_4 in the atmosphere of early Earth. *Journal of Geophysical Research*, 105:11981–11990.

Pepe, F., Lovis, C., Ségransan, D., Benz, W., Bouchy, F., Dumusque, X., Mayor, M., Queloz, D., Santos, N. C., and Udry, S. (2011). The HARPS search for Earth-like planets in the habitable zone. I. Very low-mass planets around ¡ASTROBJ¿HD 20794¡/ASTROBJ¿, ¡ASTROBJ¿HD 85512¡/ASTROBJ¿, and ¡ASTROBJ¿HD 192310¡/ASTROBJ¿. *Astronomy & Astrophysics*, 534:A58.

Petigura, E. A. and Marcy, G. W. (2011). Carbon and Oxygen in Nearby Stars: Keys to Protoplanetary Disk Chemistry. *Astrophysical Journal*, 735:41.

Petigura, E. A., Marcy, G. W., and Howard, A. W. (2013). A Plateau in the Planet Population Below Twice the Size of Earth. *ArXiv e-prints*.

Phillips, L. F. (1981). Absolute absorption cross sections for SO between 190 and 235 nm. *Journal of Physical Chemistry*, 85:3994–4000.

Pierrehumbert, R. and Gaidos, E. (2011). Hydrogen Greenhouse Planets Beyond the Habitable Zone. *Astrophysical Journal Letters*, 734:L13.

Pieters, C. M. (1978). Mare basalt types on the front side of the moon - A summary of spectral reflectance data. In *Lunar and Planetary Science Conference Proceedings*, volume 9 of *Lunar and Planetary Science Conference Proceedings*, pages 2825–2849.

Pieters, C. M. (1986). Composition of the lunar highland crust from near-infrared spectroscopy. *Reviews of Geophysics*, 24:557–578.

Pieters, C. M. and Englert, P. A. J. (1993). *Remote Geochemical Analysis, Elemental and Mineralogical Composition.*

Pieters, C. M., Fischer, E. M., Rode, O., and Basu, A. (1993). Optical effects of space weathering: The role of the finest fraction. *Journal of Geophysical Research*, 98:20817.

Pieters, C. M., Taylor, L. A., Noble, S. K., Keller, L. P., Hapke, B., Morris, R. V., Allen, C. C., McKay, D. S., and Wentworth, S. (2000). Space weathering on airless bodies: Resolving a mystery with lunar samples. *Meteoritics and Planetary Science*, 35:1101–1107.

Pilcher, C. B. (2003). Biosignatures of Early Earths. *Astrobiology*, 3:471–486.

Press, W. H., Teukolsky, S. A., Vetterling, W. T., and Flannery, B. P. (1992). *Numerical recipes in FORTRAN. The art of scientific computing.*

Prinn, R. G. and Barshay, S. S. (1977). Carbon monoxide on Jupiter and implications for atmospheric convection. *Science*, 198:1031–1034.

Prinn, R. G. and Olaguer, E. P. (1981). Nitrogen on Jupiter - A deep atmospheric source. *Journal of Geophysical Research*, 86:9895–9899.

Queloz, D., Bouchy, F., Moutou, C., Hatzes, A., Hébrard, G., Alonso, R., Auvergne, M., Baglin, A., Barbieri, M., Barge, P., Benz, W., Bordé, P., Deeg, H. J., Deleuil, M., Dvorak, R., Erikson, A., Ferraz Mello, S., Fridlund, M., Gandolfi, D., Gillon, M., Guenther, E., Guillot, T., Jorda, L., Hartmann, M., Lammer, H., Léger, A., Llebaria, A., Lovis, C., Magain, P., Mayor, M., Mazeh, T., Ollivier, M., Pätzold, M., Pepe, F., Rauer, H., Rouan, D., Schneider, J., Segransan, D., Udry, S., and Wuchterl, G. (2009). The CoRoT-7 planetary system: two orbiting super-Earths. *Astronomy & Astrophysics*, 506:303–319.

Rages, K., Pollack, J. B., and Smith, P. H. (1983). Size estimates of Titan's aerosols based on Voyager high-phase-angle images. *Journal of Geophysical Research*, 88:8721–8728.

Ricker, G. R., Latham, D. W., Vanderspek, R. K., Ennico, K. A., Bakos, G., Brown, T. M., Burgasser, A. J., Charbonneau, D., Clampin, M., Deming, L. D., Doty, J. P., Dunham, E. W., Elliot, J. L., Holman, M. J., Ida, S., Jenkins, J. M., Jernigan, J. G., Kawai, N., Laughlin, G. P., Lissauer, J. J., Martel, F., Sasselov, D. D., Schingler, R. H., Seager, S., Torres, G., Udry, S., Villasenor, J. N., Winn, J. N., and Worden, S. P. (2010). Transiting Exoplanet Survey Satellite (TESS). In *American Astronomical Society Meeting Abstracts #215*, volume 42 of *Bulletin of the American Astronomical Society*, page 450.06.

Rivera, E. J., Butler, R. P., Vogt, S. S., Laughlin, G., Henry, G. W., and Meschiari, S. (2010). A Super-Earth Orbiting the Nearby Sun-like Star HD 1461. *Astrophysical Journal*, 708:1492–1499.

Rivera, E. J., Lissauer, J. J., Butler, R. P., Marcy, G. W., Vogt, S. S., Fischer, D. A., Brown, T. M., Laughlin, G., and Henry, G. W. (2005). A ˜7.5 M$_?$ Planet Orbiting the Nearby Star, GJ 876. *Astrophysical Journal*, 634:625–640.

Rodler, F., Lopez-Morales, M., and Ribas, I. (2012). Weighing the Non-transiting Hot Jupiter τ Boo b. *Astrophysical Journal Letters*, 753:L25.

Rogers, L. A. and Seager, S. (2010a). A Framework for Quantifying the Degeneracies of Exoplanet Interior Compositions. *Astrophysical Journal*, 712:974–991.

Rogers, L. A. and Seager, S. (2010b). Three Possible Origins for the Gas Layer on GJ 1214b. *Astrophysical Journal*, 716:1208–1216.

Rothman, L. S., Gordon, I. E., Barbe, A., Benner, D. C., Bernath, P. F., Birk, M., Boudon, V., Brown, L. R., Campargue, A., Champion, J.-P., Chance, K., Coudert, L. H., Dana, V., Devi, V. M., Fally, S., Flaud, J.-M., Gamache, R. R., Goldman, A., Jacquemart, D., Kleiner, I., Lacome, N., Lafferty, W. J., Mandin, J.-Y., Massie, S. T., Mikhailenko, S. N., Miller, C. E., Moazzen-Ahmadi, N., Naumenko, O. V., Nikitin, A. V., Orphal, J., Perevalov, V. I., Perrin, A., Predoi-Cross, A., Rinsland, C. P., Rotger, M., Šimečková, M., Smith, M. A. H., Sung, K., Tashkun, S. A., Tennyson, J., Toth, R. A., Vandaele, A. C., and Vander Auwera, J. (2009). The HITRAN 2008 molecular spectroscopic database. *Journal of Quantitative Spectroscopy and Radiative Transfer*, 110:533–572.

Rugheimer, S., Kaltenegger, L., Zsom, A., Segura, A., and Sasselov, D. (2013). Spectral Fingerprints of Earth-like Planets Around FGK Stars. *Astrobiology*, 13:251–269.

Russell, J. M., Gordley, L. L., Park, J. H., Drayson, S. R., Hesketh, W. D., Cicerone, R. J., Tuck, A. F., Frederick, J. E., Harries, J. E., and Crutzen, P. J. (1993). The halogen occultation experiment. *Journal of Geophysical Research: Atmospheres*, 98(D6):10777–10797.

Salisbury, J. W. (1993). *Mid-Infrared Spectroscopy: Laboratory Data, in Remote Geochemical Analysis: Elemental and Mineralogical Composition.*

Salisbury, J. W. and Walter, L. S. (1989). Thermal Infrared (2.5-13.5 Um) Spectroscopic Remote Sensing of Igneous Rock Types on Particulate Planetary Surfaces. *Journal of Geophysical Research*, 94:9192–9202.

Salpeter, E. E. (1955). The Luminosity Function and Stellar Evolution. *Astrophysical Journal*, 121:161.

Samson, J. A. R., Haddad, G. N., and Kilcoyne, L. D. (1987). Absorption and dissociative photoionization cross sections of NH3 from 80 to 1120 A. *Journal of Chemical Physics*, 87:6416–6422.

Sander, S. P., Friedl, R. R., Abbatt, J. P. D., Barker, J. R., Burkholder, J. B., Golden, D. M., Kolb, C. E., Kurylo, M. J., Moorgat, G. K., and et al. (2011). *Chemical Kinetics and Photochemical Data for Use in Atmospheric Studies, Evaluation Number 17.*

Sasson, R., Wright, R., Arakawa, E. T., Khare, B. N., and Sagan, C. (1985). Optical properties of solid and liquid sulfur at visible and infrared wavelengths. *Icarus*, 64:368–374.

Schaefer, L. and Fegley, B. (2010). Chemistry of atmospheres formed during accretion of the Earth and other terrestrial planets. *Icarus*, 208:438–448.

Seager, S. (2010). *Exoplanet Atmospheres: Physical Processes.*

Seager, S. and Deming, D. (2010). Exoplanet Atmospheres. *Annual Review of Astronomy & Astrophysics*, 48:631–672.

Seager, S. and Sasselov, D. D. (1998). Extrasolar Giant Planets under Strong Stellar Irradiation. *Astrophysical Journal Letters*, 502:L157.

Seager, S. and Sasselov, D. D. (2000). Theoretical Transmission Spectra during Extrasolar Giant Planet Transits. *Astrophysical Journal*, 537:916–921.

Seager, S., Schrenk, M., and Bains, W. (2012). An Astrophysical View of Earth-Based Metabolic Biosignature Gases. *Astrobiology*, 12:61–82.

Seager, S., Turner, E. L., Schafer, J., and Ford, E. B. (2005). Vegetation's Red Edge: A Possible Spectroscopic Biosignature of Extraterrestrial Plants. *Astrobiology*, 5:372–390.

Seager, S., Whitney, B. A., and Sasselov, D. D. (2000). Photometric Light Curves and Polarization of Close-in Extrasolar Giant Planets. *Astrophysical Journal*, 540:504–520.

Segura, A., Kasting, J. F., Meadows, V., Cohen, M., Scalo, J., Crisp, D., Butler, R. A. H., and Tinetti, G. (2005). Biosignatures from Earth-Like Planets Around M Dwarfs. *Astrobiology*, 5:706–725.

Segura, A., Meadows, V. S., Kasting, J. F., Crisp, D., and Cohen, M. (2007). Abiotic formation of O_2 and O_3 in high-CO_2 terrestrial atmospheres. *Astronomy & Astrophysics*, 472:665–679.

Sehmel, G. A. (1980). Particle and gas dry deposition: A review. *Atmospheric Environment (1967)*, 14(9):983 – 1011.

Seiff, A., Kirk, D. B., Knight, T. C. D., Young, R. E., Mihalov, J. D., Young, L. A., Milos, F. S., Schubert, G., Blanchard, R. C., and Atkinson, D. (1998). Thermal structure of Jupiter's atmosphere near the edge of a 5-μm hot spot in the north equatorial belt. *Journal of Geophysical Research*, 103:22857–22890.

Seinfeld, J. H. and Pandis, S. N. (2006). *Atmospheric Chemistry and Physics.*

Selsis, F., Despois, D., and Parisot, J.-P. (2002). Signature of life on exoplanets: Can Darwin produce false positive detections? *Astronomy & Astrophysics*, 388:985–1003.

Sen, B., Toon, G. C., Osterman, G. B., Blavier, J.-F., Margitan, J. J., Salawitch, R. J., and Yue, G. K. (1998). Measurements of reactive nitrogen in the stratosphere. *Journal of Geophysical Research*, 103:3571–3586.

Simon-Miller, A. A., Conrath, B. J., Gierasch, P. J., Orton, G. S., Achterberg, R. K., Flasar, F. M., and Fisher, B. M. (2006). Jupiter's atmospheric temperatures: From Voyager IRIS to Cassini CIRS. *Icarus*, 180:98–112.

Singer, R. B., Clark, R. N., McCord, T. B., Adams, J. B., and Huguenin, R. L. (1979). Mars surface composition from reflectance spectroscopy - A summary. *Journal of Geophysical Research*, 84:8415–8426.

Skok, J. R., Mustard, J. F., Murchie, S. L., Wyatt, M. B., and Ehlmann, B. L. (2010). Spectrally distinct ejecta in Syrtis Major, Mars: Evidence for environmental change at the Hesperian-Amazonian boundary. *Journal of Geophysical Research (Planets)*, 115:0.

Smith, M. D. (1998). Estimation of a Length Scale to Use with the Quench Level Approximation for Obtaining Chemical Abundances. *Icarus*, 132:176–184.

Smith, N. S. and Raulin, F. (1999). Modeling of methane photolysis in the reducing atmospheres of the outer solar system. *Journal of Geophysical Research*, 104:1873–1876.

Smith, P. L., Yoshino, K., Parkinson, W. H., Ito, K., and Stark, G. (1991). High-resolution, VUV (147-201 nm) photoabsorption cross sections for C2H2 at 195 and 295 K. *Journal of Geophysical Research*, 96:17529.

Sneep, M. and Ubachs, W. (2005). Direct measurement of the Rayleigh scattering cross section in various gases. *J. Quant. Spectrosc. Radiat. Transfer.*, 92:293–310.

Snellen, I. A. G., de Kok, R. J., le Poole, R., Brogi, M., and Birkby, J. (2013). Finding Extraterrestrial Life Using Ground-based High-dispersion Spectroscopy. *Astrophysical Journal*, 764:182.

Sobolev, V. V. (1975). *Light scattering in planetary atmospheres.*

Southam, G., Rothschild, L. J., and Westall, F. (2007). The Geology and Habitability of Terrestrial Planets: Fundamental Requirements for Life. *Space Science Review*, 129:7–34.

Sprague, A. L. (2000). Thermal Emission Spectroscopy and Data Analysis of Solar System Regoliths. *Thermal Emission Spectroscopy and Analysis of Dust, Disks, and Regoliths*, 196:167–186.

Sprague, A. L., Emery, J. P., Donaldson, K. L., Russell, R. W., Lynch, D. K., and Mazuk, A. L. (2002). Mercury: Mid-infrared (3-13.5 micron) observations show heterogeneous composition, presence of intermediate and basic soil types, and pyroxene. *Meteoritics and Planetary Science*, 37:1255–1268.

Stark, G., Yoshino, K., Smith, P. L., and Ito, K. (2007). Photoabsorption cross section measurements of CO_2 between 106.1 and 118.7 nm at 295 and 195 K. *J. Quant. Spectrosc. Radiat. Transfer.*, 103:67–73.

Strobel, D. F. (1969). The Photochemistry of Methane in the Jovian Atmosphere. *Journal of Atmospheric Sciences*, 26:906–911.

Strobel, D. F. (1973). The Photochemistry of Hydrocarbons in the Jovian Atmosphere. *Journal of Atmospheric Sciences*, 30:489–498.

Sunshine, J. M. and Pieters, C. M. (1998). Determining the composition of olivine from reflectance spectroscopy. *Journal of Geophysical Research*, 103:13675–13688.

Suto, M. and Lee, L. C. (1984). Photoabsorption and photodissociation of HONO2 in the 105-220 nm region. *Journal of Chemical Physics*, 81:1294–1297.

Swift, J. J., Johnson, J. A., Morton, T. D., Crepp, J. R., Montet, B. T., Fabrycky, D. C., and Muirhead, P. S. (2013). Characterizing the Cool KOIs. IV. Kepler-32 as a Prototype for the Formation of Compact Planetary Systems throughout the Galaxy. *Astrophysical Journal*, 764:105.

Taylor, S. R. (1989). Growth of Planetary Crusts. *Tectonophysics*, 161:147–156.

Thompson, B. A., Harteck, P., and Reeves, Jr., R. R. (1963). Ultraviolet Absorption Coefficients of CO_2, CO, O_2 H_2O, N_2O, NH_3, NO, SO_2, and CH_4 between 1850 and 4000 A. *Journal of Geophysical Research*, 68:6431.

Tian, F. (2009). Thermal Escape from Super Earth Atmospheres in the Habitable Zones of M Stars. *Astrophysical Journal*, 703:905–909.

Tian, F., Claire, M. W., Haqq-Misra, J. D., Smith, M., Crisp, D. C., Catling, D., Zahnle, K., and Kasting, J. F. (2010). Photochemical and climate consequences of sulfur outgassing on early Mars. *Earth and Planetary Science Letters*, 295:412–418.

Tian, F., Kasting, J. F., and Zahnle, K. (2011). Revisiting HCN formation in Earth's early atmosphere. *Earth and Planetary Science Letters*, 308:417–423.

Tian, F., Toon, O. B., Pavlov, A. A., and De Sterck, H. (2005). Transonic Hydrodynamic Escape of Hydrogen from Extrasolar Planetary Atmospheres. *Astrophysical Journal*, 621:1049–1060.

Tinetti, G., Beaulieu, J. P., Henning, T., Meyer, M., Micela, G., Ribas, I., Stam, D., Swain, M., Krause, O., Ollivier, M., Pace, E., Swinyard, B., Aylward, A., van Boekel, R., Coradini, A., Encrenaz, T., Snellen, I., Zapatero-Osorio, M. R.,

Bouwman, J., Cho, J. Y.-K., Coudé de Foresto, V., Guillot, T., Lopez-Morales, M., Mueller-Wodarg, I., Palle, E., Selsis, F., Sozzetti, A., Ade, P. A. R., Achilleos, N., Adriani, A., Agnor, C. B., Afonso, C., Allende Prieto, C., Bakos, G., Barber, R. J., Barlow, M., Batista, V., Bernath, P., Bézard, B., Bordé, P., Brown, L. R., Cassan, A., Cavarroc, C., Ciaravella, A., Cockell, C., Coustenis, A., Danielski, C., Decin, L., De Kok, R., Demangeon, O., Deroo, P., Doel, P., Drossart, P., Fletcher, L. N., Focardi, M., Forget, F., Fossey, S., Fouqué, P., Frith, J., Galand, M., Gaulme, P., Hernández, J. I. G., Grasset, O., Grassi, D., Grenfell, J. L., Griffin, M. J., Griffith, C. A., Grözinger, U., Guedel, M., Guio, P., Hainaut, O., Hargreaves, R., Hauschildt, P. H., Heng, K., Heyrovsky, D., Hueso, R., Irwin, P., Kaltenegger, L., Kervella, P., Kipping, D., Koskinen, T. T., Kovács, G., La Barbera, A., Lammer, H., Lellouch, E., Leto, G., Lopez Morales, M., Lopez Valverde, M. A., Lopez-Puertas, M., Lovis, C., Maggio, A., Maillard, J. P., Maldonado Prado, J., Marquette, J. B., Martin-Torres, F. J., Maxted, P., Miller, S., Molinari, S., Montes, D., Moro-Martin, A., Moses, J. I., Mousis, O., Nguyen Tuong, N., Nelson, R., Orton, G. S., Pantin, E., Pascale, E., Pezzuto, S., Pinfield, D., Poretti, E., Prinja, R., Prisinzano, L., Rees, J. M., Reiners, A., Samuel, B., Sánchez-Lavega, A., Forcada, J. S., Sasselov, D., Savini, G., Sicardy, B., Smith, A., Stixrude, L., Strazzulla, G., Tennyson, J., Tessenyi, M., Vasisht, G., Vinatier, S., Viti, S., Waldmann, I., White, G. J., Widemann, T., Wordsworth, R., Yelle, R., Yung, Y., and Yurchenko, S. N. (2012). EChO. Exoplanet characterisation observatory. *Experimental Astronomy*, 34:311–353.

Toon, O. B. and Farlow, N. H. (1981). Particles above the tropopause - Measurements and models of stratospheric aerosols, meteoric debris, nacreous clouds, and noctilucent clouds. *Annual Review of Earth and Planetary Sciences*, 9:19–58.

Toon, O. B., Kasting, J. F., Turco, R. P., and Liu, M. S. (1987). The sulfur cycle in the marine atmosphere. *Journal of Geophysical Research*, 92:943–963.

Toon, O. B., McKay, C. P., Ackerman, T. P., and Santhanam, K. (1989). Rapid calculation of radiative heating rates and photodissociation rates in inhomogeneous multiple scattering atmospheres. *Journal of Geophysical Research*, 94:16287–16301.

Traub, W. A. (2012). Terrestrial, Habitable-zone Exoplanet Frequency from Kepler. *Astrophysical Journal*, 745:20.

Traub, W. A., Kaltenegger, L., and Jucks, K. W. (2008). Spectral characterization of Earth-like transiting exoplanets. In *Society of Photo-Optical Instrumentation Engineers (SPIE) Conference Series*, volume 7010 of *Society of Photo-Optical Instrumentation Engineers (SPIE) Conference Series*.

Traub, W. A., Levine, M., Shaklan, S., Kasting, J., Angel, J. R., Brown, M. E., Brown, R. A., Burrows, C., Clampin, M., Dressler, A., Ferguson, H. C., Hammel, H. B., Heap, S. R., Horner, S. D., Illingworth, G. D., Kasdin, N. J., Kuchner, M. J., Lin, D., Marley, M. S., Meadows, V., Noecker, C., Oppenheimer, B. R., Seager, S., Shao, M., Stapelfeldt, K. R., and Trauger, J. T. (2006). TPF-C: status and recent

progress. In *Society of Photo-Optical Instrumentation Engineers (SPIE) Conference Series*, volume 6268 of *Society of Photo-Optical Instrumentation Engineers (SPIE) Conference Series*.

Trauger, J. T. and Traub, W. A. (2007). A laboratory demonstration of the capability to image an Earth-like extrasolar planet. *Nature*, 446:771–773.

Tuomi, M., Anglada-Escudé, G., Gerlach, E., Jones, H. R. A., Reiners, A., Rivera, E. J., Vogt, S. S., and Butler, R. P. (2013). Habitable-zone super-Earth candidate in a six-planet system around the K2.5V star HD 40307. *Astronomy & Astrophysics*, 549:A48.

Tyler, A. L., Kozlowski, R. W. H., and Lebofsky, L. A. (1988). Determination of rock type on Mercury and the moon through remote sensing in the thermal infrared. *Geophysical Research Letters*, 15:808–811.

Udry, S., Bonfils, X., Delfosse, X., Forveille, T., Mayor, M., Perrier, C., Bouchy, F., Lovis, C., Pepe, F., Queloz, D., and Bertaux, J.-L. (2007). The HARPS search for southern extra-solar planets. XI. Super-Earths (5 and 8 $M_\oplus$) in a 3-planet system. *Astronomy & Astrophysics*, 469:L43–L47.

Vaghjiani, G. L. (1993). Ultraviolet absorption cross sections for N_2H_4 vapor between 191-291 nm and $H(^2S)$ quantum yield in 248 nm photodissociation at 296 K. *Journal of Chemical Physics*, 98:2123–2131.

van Boekel, R., Benneke, B., Heng, K., Hu, R., Madhusudhan, N., Quanz, S., Bétrémieux, Y., Bouwman, J., Chen, G., Decin, L., de Kok, R., Glauser, A., Güdel, M., Hauschildt, P., Henning, T., Jeffers, S., Jin, S., Kaltenegger, L., Kerschbaum, F., Krause, O., Lammer, H., Luntzer, A., Meyer, M., Miguel, Y., Mordasini, C., Ottensamer, R., Rank-Lueftinger, T., Reiners, A., Reinhold, T., Schmid, H. M., Snellen, I., Stam, D., Sun, Z., and Vandenbussche, B. (2012). The Exoplanet Characterization Observatory (EChO): performance model EclipseSim and applications. In *Society of Photo-Optical Instrumentation Engineers (SPIE) Conference Series*, volume 8442 of *Society of Photo-Optical Instrumentation Engineers (SPIE) Conference Series*.

van de Hulst, H. C. (1981). *Light scattering by small particles*.

Vandaele, A. C., Hermans, C., Simon, P. C., Carleer, M., Colin, R., Fally, S., Mérienne, M. F., Jenouvrier, A., and Coquart, B. (1998). Measurements of the NO_2 absorption cross-section from 42,000 cm^{-1} to 10,000 cm^{-1} (238-1000 nm) at 220 K and 294 K. *J. Quant. Spectrosc. Radiat. Transfer.*, 59:171–184.

Vilas, F. (1985). Mercury - Absence of crystalline Fe(2+) in the regolith. *Icarus*, 64:133–138.

Visscher, C. and Moses, J. I. (2011). Quenching of Carbon Monoxide and Methane in the Atmospheres of Cool Brown Dwarfs and Hot Jupiters. *Astrophysical Journal*, 738:72.

Visscher, C., Moses, J. I., and Saslow, S. A. (2010). The deep water abundance on Jupiter: New constraints from thermochemical kinetics and diffusion modeling. *Icarus*, 209:602–615.

Vogt, S. S., Wittenmyer, R. A., Butler, R. P., O'Toole, S., Henry, G. W., Rivera, E. J., Meschiari, S., Laughlin, G., Tinney, C. G., Jones, H. R. A., Bailey, J., Carter, B. D., and Batygin, K. (2010). A Super-Earth and Two Neptunes Orbiting the Nearby Sun-like Star 61 Virginis. *Astrophysical Journal*, 708:1366–1375.

Wagner, V., von Glasow, R., Fischer, H., and Crutzen, P. J. (2002). Are ch2o measurements in the marine boundary layer suitable for testing the current understanding of ch4 photooxidation?: A model study. *Journal of Geophysical Research: Atmospheres*, 107(D3):ACH 3–1–ACH 3–14.

Walker, J. C. G. (1977). *Evolution of the atmosphere.*

Wallace, P. J. and Edmonds, M. (2011). The sulfur budget in magmas: evidence from melt inclusions, submarine glasses, and volcanic gas emissions. *Reviews in Mineralogy & Geochemistry*, 73:215–246.

Walter, L. S. and Salisbury, J. W. (1989). Spectral characterization of igneous rocks in the 8- to 12-micron region. *Journal of Geophysical Research*, 94:9203–9213.

Warren, P. H. (1985). The magma ocean concept and lunar evolution. *Annual Review of Earth and Planetary Sciences*, 13:201–240.

Watts, S. F. (2000). The mass budgets of carbonyl sulfide, dimethyl sulfide, carbon disulfide and hydrogen sulfide. *Atmospheric Environment*, 34(5):761 – 779.

Winn, J. N., Matthews, J. M., Dawson, R. I., Fabrycky, D., Holman, M. J., Kallinger, T., Kuschnig, R., Sasselov, D., Dragomir, D., Guenther, D. B., Moffat, A. F. J., Rowe, J. F., Rucinski, S., and Weiss, W. W. (2011). A Super-Earth Transiting a Naked-eye Star. *Astrophysical Journal Letters*, 737:L18.

Wong, M. H., Mahaffy, P. R., Atreya, S. K., Niemann, H. B., and Owen, T. C. (2004). Updated Galileo probe mass spectrometer measurements of carbon, oxygen, nitrogen, and sulfur on Jupiter. *Icarus*, 171:153–170.

Wordsworth, R. (2012). Transient conditions for biogenesis on low-mass exoplanets with escaping hydrogen atmospheres. *Icarus*, 219:267–273.

Wu, C. Y. R. and Chen, F. Z. (1998). Temperature-dependent photoabsorption cross sections of H_2S in the 1600-2600 Å region. *J. Quant. Spectrosc. Radiat. Transfer.*, 60:17–23.

Wu, R. C. Y., Yang, B. W., Chen, F. Z., Judge, D. L., Caldwell, J., and Trafton, L. M. (2000). Measurements of High-, Room-, and Low-Temperature Photoabsorption Cross Sections of SO_2 in the 2080- to 2950-Å Region, with Application to Io. *Icarus*, 145:289–296.

Wu, Y.-J., Lu, H.-C., Chen, H.-K., Cheng, B.-M., Lee, Y.-P., and Lee, L. C. (2007). Photoabsorption cross sections of NH_3, NH_2D, NHD_2, and ND_3 in the spectral range 110-144 nm. *Journal of Chemical Physics*, 127(15):154311.

Wyatt, M. B., Christensen, P. R., and Taylor, L. A. (2001). Analysis of terrestrial and Martian volcanic compositions using thermal emission spectroscopy: 1. Determination of mineralogy, chemistry, and classification strategies. *Journal of Geophysical Research*, 106:14711–14732.

Yelle, R., Lammer, H., and Ip, W.-H. (2008). Aeronomy of Extra-Solar Giant Planets. *Space Science Review*, 139:437–451.

Yelle, R. V. (2004). Aeronomy of extra-solar giant planets at small orbital distances. *Icarus*, 170:167–179.

Yoshino, K., Esmond, J., Cheung, A.-C., Freeman, D., and Parkinson, W. (1992). High resolution absorption cross sections in the transmission window region of the schumann-runge bands and herzberg continuum of {O2}. *Planetary and Space Science*, 40(23):185 – 192.

Yoshino, K., Esmond, J. R., Sun, Y., Parkinson, W. H., Ito, K., and Matsui, T. (1996). Absorption cross section measurements of carbon dioxide in the wavelength region 118.7-175.5 nm and the temperature dependence. *J. Quant. Spectrosc. Radiat. Transfer.*, 55:53–60.

Yoshino, K., Parkinson, W. H., Ito, K., and Matsui, T. (2005). Absolute absorption cross-section measurements of Schumann Runge continuum of O_2 at 90 and 295 K. *Journal of Molecular Spectroscopy*, 229:238–243.

Young, A. T. (1973). Are the Clouds of Venus Sulfuric Acid? *Icarus*, 18:564.

Yung, Y. L., Allen, M., and Pinto, J. P. (1984). Photochemistry of the atmosphere of Titan - Comparison between model and observations. *Astrophysical Journal Supplement Series*, 55:465–506.

Yung, Y. L. and Demore, W. B. (1982). Photochemistry of the stratosphere of Venus - Implications for atmospheric evolution. *Icarus*, 51:199–247.

Yung, Y. L. and Demore, W. B., editors (1999). *Photochemistry of planetary atmospheres.*

Yung, Y. L., Drew, W. A., Pinto, J. P., and Friedl, R. R. (1988). Estimation of the reaction rate for the formation of CH3O from H + H2CO - Implications for chemistry in the solar system. *Icarus*, 73:516–526.

Zahnle, K., Claire, M., and Catling, D. (2006). The loss of mass-independent fractionation in sulfur due to a palaeoproterozoic collapse of atmospheric methane. *Geobiology*, 4(4):271–283.

Zahnle, K., Haberle, R. M., Catling, D. C., and Kasting, J. F. (2008). Photochemical instability of the ancient Martian atmosphere. *Journal of Geophysical Research (Planets)*, 113:11004.

Zahnle, K., Marley, M. S., and Fortney, J. J. (2009a). Thermometric Soots on Warm Jupiters? *ArXiv e-prints*.

Zahnle, K., Marley, M. S., Freedman, R. S., Lodders, K., and Fortney, J. J. (2009b). Atmospheric Sulfur Photochemistry on Hot Jupiters. *Astrophysical Journal Letters*, 701:L20–L24.

Zahnle, K. J. (1986). Photochemistry of methane and the formation of hydrocyanic acid (HCN)in the earth's early atmosphere. *Journal of Geophysical Research*, 91:2819–2834.

Zeng, L. and Sasselov, D. (2013). A Detailed Model Grid for Solid Planets from 0.1 through 100 Earth Masses. *Publications of the Astronomical Society of the Pacific*, 125:227–239.

Zhang, X., Liang, M. C., Mills, F. P., Belyaev, D. A., and Yung, Y. L. (2012). Sulfur chemistry in the middle atmosphere of Venus. *Icarus*, 217:714–739.

Zsom, A., Seager, S., and de Wit, J. (2013). Towards the Minimum Inner Edge Distance of the Habitable Zone. *ArXiv e-prints*.